City Research Online

City, University of London Institutional Repository

City, University of London

School of Mathematics, Computer Science & Engineering

Department of Mechanical Engineering & Aeronautics

Separating flows around swept and unswept wings with laminar and turbulent free stream conditions

PhD in Aeronautical Engineering

PhD student: Carlo Alessio Suardi

Supervisor   Prof. Alfredo Pinelli

Co-Supervisor: Dr. Mohammad Omidyeganeh

February 2020

If I have seen further,

it is by standing on the shoulders of giants.

Sir Isaac Newton

Abstract

The comparison of the three-dimensional (3D), subsonic flows past an infinite wing equipped with a $NACA-4412$ profile is presented considering an unswept and a 30° swept-back wing at incidence values that induce flow separation. The Reynolds number based on the aerofoil chord C and the free stream velocity in the chord plane Q_∞ is fixed at a common value $Re_c = CQ_\infty/\nu = 50 \times 10^3$. The investigation is carried out using highly-resolved-LES (Large Eddy Simulations) of the incompressible Navier-Stokes equations. The comparison between swept and unswept wings is undertaken considering both laminar and turbulent free stream conditions.

One of the two central objectives of the research has concerned the assessment of the *Simple Sweep Theory* when flow separation takes place. The *Simple Sweep Theory* is a commonly used tool that is frequently deployed in designing swept wings by a simple extension of the baseline flow around the corresponding straight wing. Another objective is the accurate and detailed characterisation of both the laminar and the turbulent flow separation behaviours on the swept and unswept wings at incidence. Especially in the turbulent boundary layer scenario, separation is still an open research topic that lately is receiving particular attention.

In the laminar inlet condition, only one incidence namely $\alpha = 5^o$ has been considered for both the wing configurations. The wings suction sides will be shown to experience laminar boundary layer separation forming a typical laminar separation bubble (LSB). The separating shear layer bounding the separated region breakdowns to turbulence, without any reattachment taking place downstream on the wings.

When comparing the flows between the unswept and the swept wing configurations, it is found that they satisfy the *Simple Sweep Theory* prediction along the wing, until the boundary layer starts to detach from the wings surface. When flow separation occurs, the emerging large-scale flow structures participate in the breakdown to turbulence presenting different features in the two wing configurations, thus leading to a violation of the *Simple*

Sweep Theory violation. The laminar separation mechanism for both wing configurations has been statistically characterised, allowing to shed some additional light to this process. The laminar separation is found to be a 3D process right from its detachment location.

Within the turbulent free stream framework, achieved by the introduction of free stream turbulence (FST) in the incoming flow, two wing incidences are considered, namely $\alpha = 5^o$ and $\alpha = 10^o$. For both the wing configurations, the FST triggers a very early transition towards turbulent boundary layer thus inhibiting the formation of an LSB, which is replaced by a fully 3D and time dependent boundary layer separation. The turbulent separation of the boundary layer is found to be a stochastic process that builds up moving downstream along the chord. The early formation of localised reversed flow spots in the upstream portion of the wing merge downstream to form the so-called *stall cells*, regions of reversing flow with a size comparable to the chord. The location of the mean turbulent separation can be defined only when considering the time averaged flow and it does not manifest in the instantaneous flow realisations.

As already seen for laminar regimes, the *Simple Sweep Theory* is observed when attached mean boundary layer takes place. In regions that present a statistically mean separation, it is violated. The regions of mean separation are characterised by large-scale fluctuating flow structures, which present some analogies to those found in the laminar separation.

It is therefore conjectured that a similar mechanism leads to the formation of the separating flow structures in the laminar and in the turbulent separation processes. It is also observed that in both boundary layer scenarios, the breakdown mechanism is similarly modified by the crosswind caused by the sweep. This observation suggests a common reason for the *Simple Sweep Theory* violation that occurs only when a global mean separation is established for both the boundary layer regimes. It also explains the fact that the theory holds for those wing portions affected by localised reversed spots that lie before the mean separation line. A formal correction of the *Simple Sweep Theory* when mechanisms of flow separation take place is also proposed in this thesis.

As a finale note, it is observed that the structure of the outer flow and of wall turbulence is always modified by the introduction of a constant crosswind, particularly inside the recirculating areas.

Key words: swept wing, simple sweep theory, laminar separation, turbulent separation, NACA-4412, highly-resolved LES.

Contents

x

Nomenclature

Notation

$(a, b, \dots)$	Functional dependency on variables a, b, $\dots$
$\partial\{\cdot\}/\partial a$	Partial derivative operator with respect to variable a
$<\cdot>_a$	Average operator with respect to a
$\lvert\cdot\rvert$	Absolute value operator
$\overline{\{\cdot\}}$	Complex conjugate operator
$\Delta\{\cdot\}$	Difference operator
$\mathcal{F}\{\cdot\}$	Fourier transform operator
$\vec{\{\cdot\}}$	Three-dimensional vector
$\{\cdot\}^*$	Value made non dimensional by Q_∞ and C
$\{\cdot\}^+$	Value made non dimensional by u_τ and ν
$\{\cdot\}'$	Fluctuation
$\{\cdot\}_\infty$	Value of the free stream flow
$\{\cdot\}^w$	Value at the wall
$\{\cdot\}_x$	Value in the chordwise direction
$\{\cdot\}_z$	Value in the spanwise direction
$\{\cdot\}_y$	Value in the y-direction
$\hat{\{\cdot\}}$	Value in the Fourier domain
$\sim O(\cdot)$	Order of magnitude

Physical and Fourier domains

x, y, z	Cartesian reference system
x	Chordwise direction
z	Spanwise direction

$x - y$	Chord plane
$x - z$	Wing plane
r	Radial coordinate of the polar reference system
s, n, z	Curvilinear coordinate system based on the aerofoil outline
Λ_z	Wavelength in the spanwise direction
k_z	Wavenumber in the spanwise direction
t	Time
T	Time period of an harmonic wave
f	Frequency

Computational geometry

i, j, k	Orthogonal mesh-element based reference system
N_i, N_j, N_k	Number of computational nodes along the three directions of the mesh basis
N_{tot}	Total number of computational nodes
ν_t	Subgrid viscosity

Wing and flow configuration

α	Angle of attack or incidence, defining the wing loading condition
Λ	Angle of sweep, defining the amount of crosswind on the wing
C	Aerofoil chord in the chordwise direction
ν	Kinematic viscosity of the fluid
ρ	Density of the fluid
P	Pressure of the fluid
u, v, w	Velocity components of the fluid in x, y and z
Q_∞	Velocity of the free stream in the chord plane
$U_\infty, V_\infty, W_\infty$	Velocity components of the free stream in x, y and z
Re_c	Reynolds number based on C, Q_∞ and ν
u_{tg}	Velocity component tangent to the foil wall, along direction s
τ	Shear stress
τ_{sn}	Shear stress component in direction s acting on surface with normal n

τ_{zn}	Shear stress component in direction z acting on surface with normal n
C_l	Coefficient of lift
C_d	Coefficient of drag
C_p	Coefficient of pressure
C_f	Coefficient of friction
ω	vorticity

Boundary layer related quantities

δ_{99}	Boundary layer edge considering $u/Q_\infty = 0.99$
δ^*	Displacement thickness
θ	Momentum thickness
H	Shape factor
β	Clauser parameter
u_τ	Friction velocity
w_τ	Spanwise friction velocity
Re_τ	Reynolds number based on δ^*, u_τ and ν

Turbulence related quantities

k	Turbulent kinetic energy, t.k.e.
$\mathcal{P}$	Production of t.k.e.
ε	Dissipation of t.k.e.
I	Turbulence intensity
$\mathcal{L}$	Integral length scale
$\wp$	Probability
σ	Standard deviation
R_{aa}	Spanwise two point autocorrelation of variable a
$\hat{E}$	t.k.e. spanwise energy spectrum
$u'u', v'v', w'w'$	Normal Reynolds stresses
$u'v', u'w', v'w'$	Cross-component Reynolds stresses

Acronyms

BL	Boundary layer
DNS	Direct numerical simulation
LES	Large eddy simulations
LSB	Laminar separation bubble
TSB	Transitional separation bubble
FST	Free stream turbulence
LE	Leading edge
TE	Trailing edge
IBM	Immersed boundary method
SUSA	In-house developed solver name
2D	Two-dimensional
3D	Three-dimensional
PSD	Power spectral density
HPC	High performance computing
K-H	Kelvin Helmholtz
TS	Tollmien–Schlichting
Re	Reynolds number
t.k.e.	Turbulent kinetic energy

Glossary

Chordwise	Direction along the wing chord
Spanwise	Direction along the wing span
Streamwise	Direction aligned with the mean velocity
Crosswind	Wind aligned with the spanwise direction
Crossflow	Flow perpendicular to the streamwise inviscid velocity direction
Swept wing	Wing adopting a sweep angle different that 0 with respect to the approaching wind
Unswept wing	Wing with a sweep angle $\Lambda = 0$, also referred as straight wing
Wavenumber	Literal abbreviation of wave number

List of Figures

xxx

List of Tables

Acknowledgements

If you want to go fast, go alone.
If you want to go far, go together.
Unknown author

First of all, I would like to thank all the parties which collaborated to make possible the present research and gave me the opportunity to take part in it. In particular, Prof. Alfredo Pinelli and Dr. Mohammad Omidyeganeh on behalf of *The School of Mathematics Computer Science and Engineering* at City, University of London and Dr. Stephen Rolston on behalf of *Airbus Group Innovations, Filton* at Airbus Group Limited. My *PhD* studies have been jointly funded by the School of Mathematics, Computer Science and Engineering of City, University of London and Airbus Group Limited, that I both gratefully acknowledge. The acknowledgement is extended to the people of the High Performances Computing (HPC) infrastructures where the most of present numerical simulations have been carried out. In particular: Sylvain Laizet (Imperial College) on behalf of the *U.K. Turbulent Consortium* (grant EPSRC EP/L000261/1) and the EPSRC (Engineering and Physical Sciences Research Council) (grant Resource Allocation Panel Summer 2017), both granting the access to the *ARCHER U.K. National Supercomputing Service*; Chris Marshall (City, University of London) for the access to the City, University of London HPC *ARION* and *SOLON*. I thank Nathalie Chatelain of the Post-Graduate-Research office at City, University of London for the administrative support provided throughout my PhD program. Also, I am grateful to Prof. Maurizio Quadrio (Politecnico di Milano) who first told me about the opportunity of the present PhD project in London and Dr. Alessandro Monti who contributed to make smooth my transition to London.

I am extremely grateful to Alfredo and Omid for the continuous supervision gifted to me during my PhD journey. The time, patience and care invested in both my personal and professional growth, gave me the momentum to recognise, accept, learn and re-start from my

own limits. Their unquestionable discipline towards the production of high quality, scientific research has impressed me in numerous occasions. I feel very lucky for the opportunity to have been trained by your brilliant minds, widely open, creative, awake and always aware. Although the arguments from time to time, I have ultimately found your teachings, not restricted to the scientific perspective, inestimable.

I praise all my closest friends and their partners for the continuous support they showed me during this adventure, especially when I needed it the most: Campa, Pippo, Benji, Carlo, Cupof, Chicco, Caste, Fabry, Salvo, Simo and Tento. I praise the members of my family. Their love, admiration and advice has always been there to help me move forward: my mum Rita, my dad Bepi, Roby, Fabry, Baby, Cla, Ale and Simo. The same gratitude is extended to all my relatives, who cheered me with a big smile and a warm hug every time I stepped in Leffe. A seriously not exhaustive list (i.e. really big and united Italian family here!) comprehends: ziaMina&zioAldo, ziaGiuliana&zioRoberto, ziaMaria&zioStefano, ziaLuciana&zioLuciano, ziaDelia&zioBepi and zioLuciano. A thought goes to the family members I lost during the present journey, NonnaMaria and Lana, and just before it, NonnaLina. I warmly thank all the peers who became good friends along the way. Particularly: Michael, Yana, Marche, Alex, Gio, Bomba and Ricky. I wish to harvest our friendship even further in the times ahead. I thank the research community at City that often turned colourful my grey-days in the no-windows-office. Particularly Ale, Ed, Isabella, Narghes, Tobi, Shane, Nik, Marco, Chetan and Richard. I thank the students I have taught and supported, particularly the brilliant Rafay and Kelly, for that sense of self reward I experienced contributing to their growth, which sometimes pushed me forward in my own journey. A thought goes to those who have not only been close to me but especially to my parents after I moved to London: Nadia&Max, Nives&Richi, Doni&Fra, Maria Rosa, Sig.raMarinella&Sig.Giovanni, VilleggiantiCamping30passi, Fero&Angela and Dott.Campostrini. Another thought goes to Roberta, Letizia&Claudio, ElenaRoma, LondonFootyPeers, Nico, Frasco, Fulla, Cumbe', JessToronto, Mirza, Dims, SamJupe, AleRossi, Kikka, Lele, Ele, Jamie, Gerson and to those I met for just an instant but made me think for long, that I did not mention explicitly here.

I found my doctorate in London, perceptible as a mental marathon as Maurizio once told me, seriously tough. Large amplitude, high frequency ups and downs paved the way, but I am really honoured to have made it, ultimately. Probably it was the right challenge I had longed for. My mind has been re-constructed and my perspective widened in ways I could not have imagined or predicted looking back. Awesome. For this, I do also praise myself for the courage and resilience I demonstrated to get exactly *hic et nunc* to *carpe diem*.

Chapter 1

Introduction

If we knew what it was we were doing,

it would not be called research,

would it?

Albert Einstein

In recent years there has been a renewed interest and new technological motivations towards the research of lifting surfaces adopting a sweep angle in a wide ranging variety of flow conditions, including flow separation scenarios. In the case of commercial aircraft, an increased aerodynamic optimisation of swept wings in subsonic, high loading conditions (i.e. take off and landing phases) has become of interest in response to the recently introduced severe normative on emissions and noise-generation in landing and take off configurations (European Union Aviation Safety Agency et al. 2019). Although the majority of commercial airborne vehicles is characterised by very high Reynolds number flows ($Re \sim O(10^6 - 10^8)$), the use of swept aerodynamic surfaces is not restricted to commercial aviation. More general examples include: sophisticated turbo-machinery with swept blades aiming to increase efficiency; micro-revolution-machinery with swept blades used in bio-engineering and renewable energies applications; drones mounting swept wings and blades flying in highly gusty conditions requiring a high degree of manoeuvrability. Differently from traditional aeronautics, almost all these recently introduced applications are characterised by low to moderate Reynolds number regimes ($\sim O(10^4 - 10^5)$). The large variations in the Reynolds number characterising different lifting surfaces implies that the corresponding boundary layers present different regimes: turbulent for the high Reynolds number cases, laminar and/or transitional in the other conditions. A phenomenon that is common to all the mentioned

regimes is the flow detachment from the wall that may be experienced when a sufficient adverse pressure gradient condition is reached along the wing chord.

The present contribution aims to provide a systematic comparison between the flows developing around straight and swept infinite wings in both laminar and turbulent regimes with the eventual presence of a separated region. For the wings with an infinite spanwise extension, the mechanism of the boundary layer separation, in both laminar and turbulent regimes, is a research subject that has not been completely understood yet. Despite the fact that this topic represents a still active area of investigation, during the last half century a large number of aerodynamicists have explored the separation phenomenon in both laminar and turbulent regimes. In the laminar regime, Gaster (1967) and Jones et al. (2008) and for the turbulent regime, Simpson (1989) can be mentioned as reference investigations. Other researchers have also tackled the analysis of the crosswind effect (e.g Black (1952) and Broadley (1998)). However, as mentioned above the flow mechanisms leading to the separation formation, and determining its dynamic characteristics, remain open subjects.

The major part of the flight mission for a commercial aircraft is within the transonic regime (Roberson & Johns 2008), which is characterised by a high Reynolds number attached flow. The lifting surfaces which are required for all the other flight phases (manoeuvring, take off and landing) have been previously designed within a safe and pre-established flow scenario where flow separation was avoided. The eventual appearance of flow separation in off-design condition would have eventually been mitigated with the use of passive control technique (for some examples see Lin (2002)). Thus, fundamental research aiming to fully unveil the separation mechanism has not been an industrial priority until recent days. The flow analogy between man made wings or blades in loading conditions, with feathered wings found in nature that actively control the vortex shedding process and eventually separation (e.g. Bechert et al. (2006), Carruthers et al. (2007) and Brücker & Weidner (2014)) have encouraged further fundamental research in the flow detachment mechanism. In particular, the dynamic character of the separation formation is of great interest for the development of active flow control devices to be engineered on the wings of aircraft and industrial machineries. A new generation of flow control devices should aim not only to mitigate flow separation, but eventually to exploit it in a beneficial manner.

The introduction of a sweep angle on engineered wings requires the analysis of its impact on the separation mechanism as well. When a swept wing is considered, often researchers and designers rely on the *Simple Sweep Theory* valid for attached flow condition, in both laminar and turbulent regimes (e.g. Sears (1948), Altman & Hayter (1951), Boltz et al.

(1960)). Although some authors have put forward preliminary results showing violations of the *Simple Sweep Theory* when the separation mechanism takes place (Broadley 1998, Uranga et al. 2011, De Tullio & Sandham 2017) many designers extend its use even with separated flow conditions. The detailed characterisation of the separation mechanism on a swept wing and the comparison to its straight wing counterpart is therefore a topic that goes beyond scientific curiosity having a potential impact on the industrial, aerodynamic design of wings.

The assessment and the eventual cause of the violation of the *Simple Sweep Theory* when a flow detachment mechanism takes place is one of the primary research goal of the present thesis. Alongside, the fundamental characterisation of the trailing edge separation mechanisms for both the straight and swept infinite wings in laminar and turbulent regimes is also a central topic of this doctoral work. The methodology that has been used to pursue these research challenges is based on high fidelity numerical simulations of moderate Reynolds number, incompressible, flows past infinite wings with a cambered profile at an incidence with or without a sweep angle with either laminar or turbulent incoming flow. For both these inflow conditions, the suction side of the foil is characterised by the presence of a variable adverse pressure gradient that increases gradually moving towards the trailing edge. This side presents a boundary layer that may eventually detach in the region close to the trailing edge. The flow field around the wing, in all the considered configurations, will be characterised in details exploiting the level of detail delivered by the adopted numerical methodology. One of the original contributions of this thesis, concern a profound assessment of the *Simple Sweep Theory* whose validity is evaluated not only for flow quantities considered in previous investigations (i.e. mean flow and global aerodynamic coefficients) but also for those characterising the fluctuating content of the flow (i.e. Reynolds stresses and perturbation energy spectra). Furthermore, the mechanisms leading to flow separation and the effects of the crosswind will also be addressed in details. In particular, the central role played by flow modes on the evolution of the separation, in both laminar and turbulent regimes, on both swept and unswept wings, will be illustrated by combining analysis of perturbation energy spectra, instantaneous flow field visualisations and the probabilistic scrutiny of the reversed flow.

Among the results of the present thesis, the validity of the *Simple Sweep Theory* will be shown to hold in both laminar and turbulent regimes as long as an attached flow establishes on the whole wing. On the other hand, it is found to be violated as soon as any form of separation takes place. Alongside, the separation mechanism, in laminar or turbulent condi-

tions, is found to be inherently three-dimensional and unsteady with topological differences between the flows developing around straight and swept wings. A probabilistic approach is therefore employed in order to characterise quantitatively the flow detachment mechanism, especially in the turbulent cases. The probabilistic approach has been previously proposed in a similar fashion by the pioneering observations of Simpson (1989). Some analogies in the flow modes driving the evolution of the detachment mechanism are found to be shared in the laminar and the turbulent separation processes.

Considering the numerical methodology used to tackle the mentioned physical processes, an in-house developed Navier-Stokes solver running on large, parallel computing infrastructures has been modified and massively employed. The simulations have been mostly executed on the supercomputer *ARCHER* owned and maintained by the Engineering and Physical Sciences Research Council (EPSRC 2020). The flow predictions are extremely demanding due to their high level of detail: hundreds of millions of computational nodes have been used to discretise the virtual flow field. The number of the simultaneous processors used is in the order of the hundreds and the wall clock computation time required to achieve statistically significant results is in the order of weeks. A single simulation has a nominal cost in the order of thousands of pounds, depending on the time required to capture the evolution of the flow fields. The recent attention to eco-friendly engineering designs justifies the high cost required to carry out highly resolved computational aerodynamics research, as the present one. Improving aerodynamic efficiency has become a key aspect of aeronautics research challenged by the concurrent needs of reducing the amount of emitted green-gases and the increasing demand for flights (Graver et al. 2018, European Union Aviation Safety Agency et al. 2019). In 2017 the CO_2 emissions from the transport sector accounted for the 24.48% of the worldwide total (International Energy Agency 2017), with the commercial aviation responsible for approximately the 11% of the transport share (data of the shares only available for the year 2018 in Graver et al. (2018)). In the power production sector, in which turbo-machineries are largely used (in some cases with a flow regime similar to the ones investigated in this thesis) the benefit obtained through detailed aerodynamic research could be even greater. Indeed, since the electricity and heat production sector accounted for almost the 40% of the CO_2 emissions in 2017 (International Energy Agency 2017), it is clear that even a modest increase in the efficiency of a turbo-machine experiencing flow separation could be enormously beneficial. Similar reasoning could be extended to the improved design of the blades used in wind turbines.

The thesis synopsis is arranged as follows. Chapter 2 presents the literature review rel-

evant to the topics tackled in the present work. The adopted, numerical methodology is detailed in chapter 3, where preliminary tuning of the simulation settings (spanwise domain numerical extension and numerical grid refinement study) are also presented. Chapter 4 presents the results of the investigation obtained in the laminar regime mainly illustrated using a systematic comparison between the unswept and the swept wing configurations. Chapter 5 focuses on the results obtained in the turbulent regime using a similar approach. Finally, conclusions and suggestions on future research close the thesis.

Chapter 2

Literature review

Learning never exhausts the mind.

Leonardo da Vinci

This chapter contains a generic literature review on the aerodynamics of swept wings which is the core topic of the thesis. First, an historical outline on the adoption of the swept wing configuration on commercial aircraft is briefly summarised in section 2.1. Section 2.2 presents a technical literature survey about the *Simple Sweep Theory* , a baseline framework representing the working horse of swept wing design. Section 2.3 and 2.4 provide a review of the state-of-the art knowledge on the separation of both laminar and turbulent boundary layers exposed to an adverse pressure gradient with special emphasis on the comparison between swept and unswept wing configurations.

2.1 Brief history of the swept wing configuration

The *infinite swept wing* configuration has been proposed in the early conceptual work of Adolf Busemann first presented at the Volta Congress 1935. This pioneering concept aimed at delaying the shock induced drag divergence of the transonic flight conditions (Vos & Farokhi 2015), in which a sharp drag increase occurs when the speed of sound is approached. At that time, the increasing thrust power made available by the evolution of aircraft engines opened the opportunity to widen the flight envelope beyond the speed of sound. This new scenario introduced a series of new aerodynamic challenges and in particular scientist and engineers had to tackle the drag divergence appearing at sonic flight condition (Vos & Farokhi 2015). The phenomenon consists in an abrupt increase of the drag experienced by
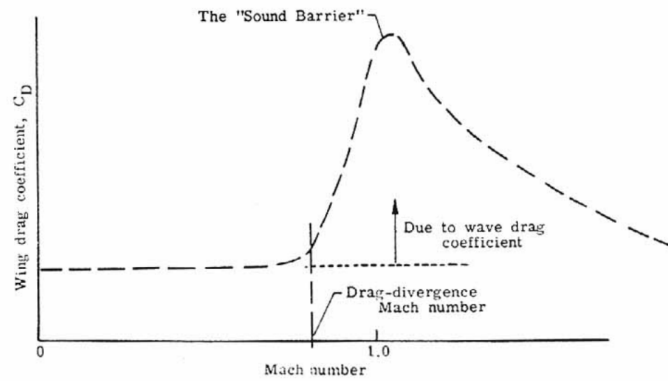
Figure 2.1: Distribution of the wing drag coefficient as function of the Mach number. Taken from Talay (1975).

a flying object when the speed of sound is approached. Nowadays, the behaviour of the total wing drag with the increase of the Mach number (ratio between the flight speed and the speed of sound in the fluid surrounding the moving object) is well understood and can be graphically depicted as in figure 2.1. The steep gradients in the transonic regime, visible in the figure, are due to the formation of a shock wave on the wing (Talay 1975, Anderson Jr 1990), which intensity can be controlled designing the wing for the transonic flight. The shock wave delimits an upstream region of supersonic flow on the wing. After the shock, the flow is abruptly compressed and slowed down via a non reversible process (Anderson Jr 1990). The extra drag induced by the appearance of a shock wave goes under the name of *wave drag*. Busemann proposed to rotate the wing with respect to the fuselage to reduce the component of the flow velocity normal to the leading edge. The rationale behind this idea was the hypothesis that the major aerodynamic features of the wing and the shock wave formation were mainly connected to the wind flow component perpendicular to the wing leading edge (Busemann 1935). Later, this idea was verified by the experimental measurements of Ludwieg (Ludwieg 1940) (here proposed by the reproduced version of Schlichting & Truckenbrot (1960) as reported by Vos & Farokhi (2015) in figure 2.2) and by many other authors (e.g. Ackeret et al. (1951)).

The infinite swept wing configuration allows to approach the speed of sound delaying the appearance of the shock wave, thus avoiding the extra wave drag and effectively making the wing to behave like an infinite unswept wing at reduced flight speed (Vos & Farokhi 2015). Rotating (not shearing) the wing with respect to the flow, not only increases the value of the critical Mach number (i.e. the value of Mach at which a local shock wave appears on the wing) but also weakens the intensity of eventual shock wave and the induced drag as
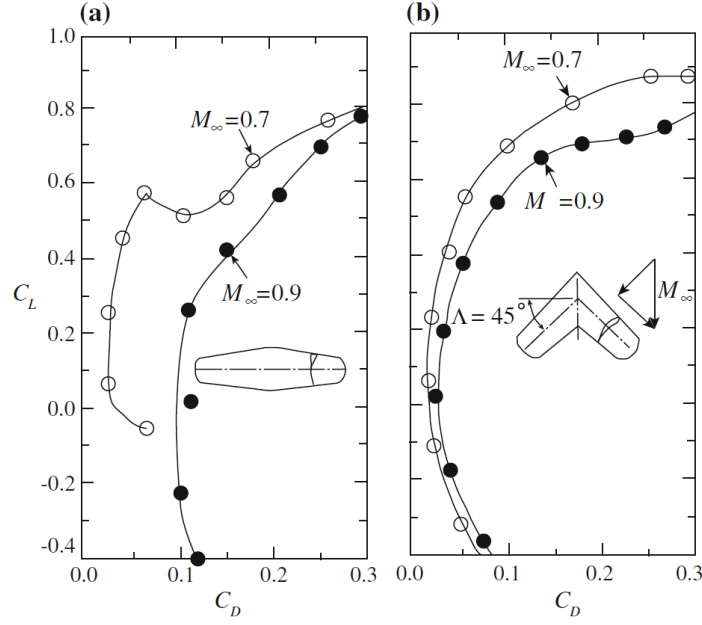
Figure 2.2: Wing polar varying the Mach number for a straight (Left) and swept (Right) wing. Reproduction of the Ludwieg (1940) measurements by Schlichting & Truckenbrot (1960), taken from Vos & Farokhi (2015).

compared to the corresponding unswept wing. These observations constitute the backbone of the formulation of the *Sweep Independence Principle* (which is nowadays referred as the *Simple Sweep Theory*) currently extended for the design of subsonic swept wings: the characteristics of the central part of the wing (far from root and tip) are determined solely by the component of the flow normal to the leading edge (note that it was not possible to find the original work of Busemann (1935) and here an elaborations of his theory found in Jones (1989) has been used as a reference). For uniform inflow conditions, the drag decreases even for swept wings that share the same aspect ratio (i.e. spanwise dimension over wing chord) with their straight counterparts (Vos & Farokhi 2015). When the wing is swept back, the chordwise component of the wind velocity decreases and as a consequence the lift decreases. Therefore, to obtain the same global lift of the straight wing counterpart without changing the flying speed, the swept wing needs a larger span. (Vos & Farokhi 2015, Anderson Jr 1999).

A detailed account on the historical stages that have led to the actual swept wing configuration goes beyond the scope of this thesis. However, an interested reader can find more information in Vos & Farokhi (2015) or Anderson Jr (1999).

2.2 *Simple Sweep Theory* for subsonic wings

The *Simple Sweep Theory* for the flow past a wing can be formulated in two equivalent manners: *the swept wing characteristics are the same of those of an unswept wing when scaled with a simple trigonometric function of the sweep* Λ *(e.g. chordwise distribution of pressure,* $C_{p_x,\Lambda=0} = C_{p_x,\Lambda}\cos^2(\Lambda))$ (Altman & Hayter 1951); or alternatively *when the chordwise flow condition is matched, a swept and an unswept infinite wings share the same aerodynamic characteristics* (Jones 1947).

For fully laminar regimes Cooke (1950), using as a starting point the pioneering work of Prandtl (1946) and Sears (1948), employed a modification of the Falkner-Skan solution to show that the *Simple Sweep Theory* was applicable to the case of yawed, infinite cylinders. Nowadays, the Falkner-Skan-Cooke three-dimensional boundary layer equations are widely used to describe the boundary layer resulting from the superposition of a constant crosswind to the otherwise two-dimensional boundary layer developing on a surface with an infinite spanwise extension. The profile of the additional spanwise velocity component is found after that of the two-dimensional flow is determined. Wild (1949) also showed the integral behaviour of a three dimensional boundary layer on a laminar swept back wing to be directly related to the solution of the von Kármán-Polhausen integral equation on a straight wing. All these analyses were carried out under the hypothesis of attached boundary layers.

In the fifties, various wind tunnel measurements of subsonic flows past infinite wings at relatively high chord Reynolds numbers (i.e. $Re_c = Q_\infty C/\nu = O(10^6)$; Q_∞ being the free-stream velocity in the chord plane, C the aerofoil chord and ν the kinematic viscosity) showed that several aerodynamic quantities are well predicted by the *Simple Sweep Theory* when measured along the aerofoil section of a swept wing (e.g. pressure coefficients or boundary layers thicknesses) (Altman & Hayter 1951, Boltz et al. 1960). In particular, these experiments considered a high Reynolds number condition with an almost undisturbed free stream rapidly transitioning to turbulence in the very early stage of the wing due to the high Reynolds number or the incidence (Allen & Burrows 1956).

Altman & Hayter (1951) verified the applicability of the *Simple Sweep Theory* for the chordwise pressure coefficient, for the velocity profiles inside the boundary layer and consequently for the chordwise boundary layer integral quantities (displacement thickness, momentum thickness and shape factor). In their experiments, the boundary layer transitioned to turbulence naturally and quickly in the very early stage of the wing, without experiencing any large-scale separation along the wing for all the loading cases. In figure 2.3 their chord-
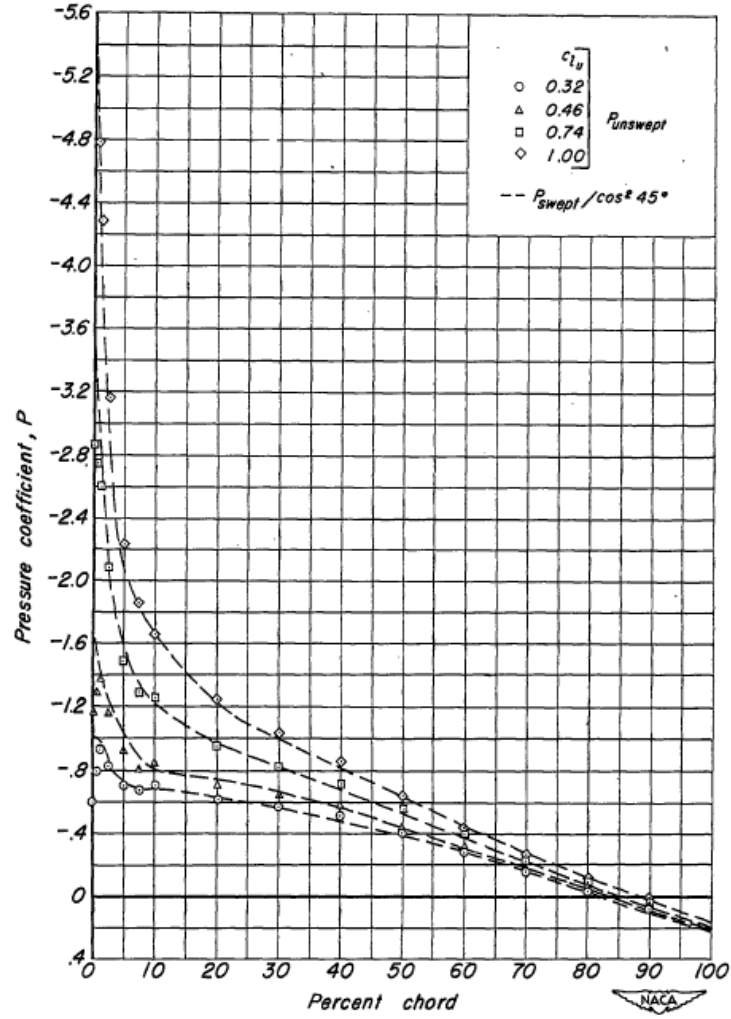
Figure 2.3: Chordwise distributions of the pressure coefficient along the upper wing surface as a function of the sweep at different loading conditions (C_{l_y}). Taken from Altman & Hayter (1951).

wise pressure distributions on the wing upper side are proposed for increasing values of the angle of attack, showing a quite perfect match between the swept and the unswept wing and thus validating the *Simple Sweep Theory* predictions.

Boltz et al. (1960) proved the robustness of the theory by showing that although a set of crossflow vortices formed on the subsonic swept wing, with a strong influence on the transition mechanisms, the overall chordwise wing performances were left unchanged with respect to their straight wing counterpart. In figure 2.4 their measurements of the chordwise pressure distributions on the wing upper side are proposed for different angles of attack, showing a reasonably good match between the swept and the unswept wing. Alongside the verification of the applicability of the *Simple Sweep Theory* , this work also clearly showed a different transition mechanism for the swept wing as compared to the same unswept one.

The different transition scenario between straight and swept wings have also been re-

11
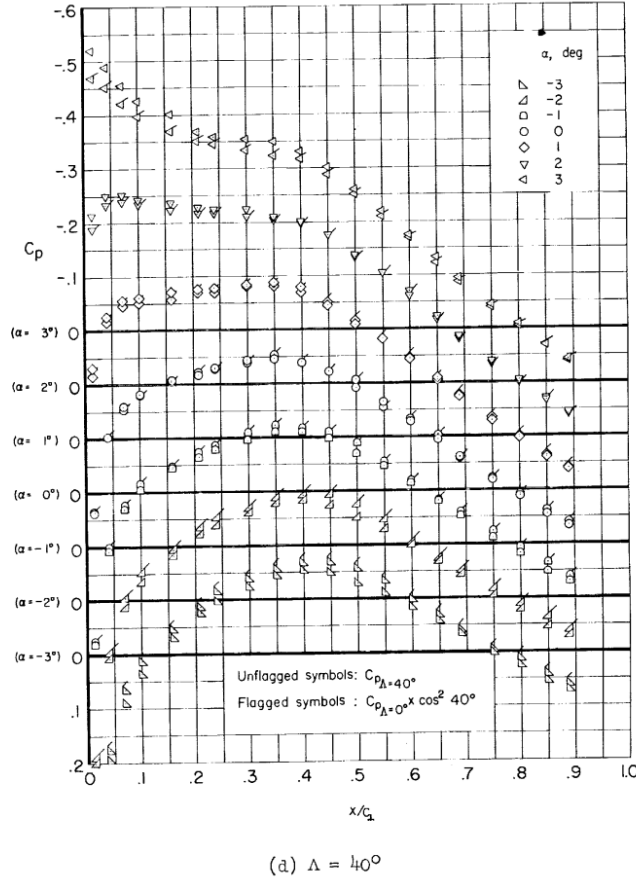
Figure 2.4: Chordwise distributions of the pressure coefficient along the upper wing surface as a function of the sweep for different angles of attack α. Taken from Boltz et al. (1960).

ported by several other investigations (e.g. Black (1952), Anscombe & Illingworth (1952)), also promoting more recent works focused on a deeper understanding of the swept wing transition mechanism when no disturbances are considered (see for example Reed & Saric (1989), Dagenhart (1992), Wassermann & Kloker (2003), Bonfigli & Kloker (2007), Duan et al. (2014)). In summary, when the transition mechanism is dominated by the primary modes (Morkovin 1993), the transition process leading to a turbulent boundary layer on a swept wing may be radically different to its straight wing counterpart (Dagenhart 1992). In particular, on a straight wing, the most common transition mechanism is related with the amplification of the Tollmien-Schlichting (T-S) instability; for the swept case is the amplification of the crossflow instability that plays a dominant role. Furthermore, the transition on a swept wing is often driven by the interaction between the crossflow and the T-S instabilities. The interested reader may find a detailed discussion regarding the possible transition scenarios on a swept wing in the works of Dagenhart (1992), Reed & Saric (1989), R. & Saric (1999) and White et al. (n.d.).

Although the transition mechanism of the swept wing may vary with respect to that of

the straight wing, many of the mentioned researches still report an overall aerodynamic performance of swept wings, in the chordwise direction, identical to those of the corresponding unswept wings. The research and measurements accumulated during the years have helped in making *Simple Sweep Theory* the work horse of the preliminary design of infinite swept wings at aeronautically relevant Reynolds number (i.e. real commercial flight conditions).

Despite its increasing technological importance, the validity of the *Simple Sweep Theory* in flow conditions that may lead to boundary layer separation has not received the same attention and more controversial results are reported in the literature for both the high and low Reynolds number regimes (e.g. Selby (1982), Uranga et al. (2011)). The early experimental work of Selby (1983) discussed the applicability of the *Simple Sweep Theory* in the case of a turbulent separation in high Reynolds number regimes. In particular, he considered the flow separation caused by a forward facing step with and without a sweep. The author has focused on the determination of the maximum sweep for which the reattachment position remains independent of the crosswind (of course, in this configuration the separation location is fixed by the edge of the step). He found that up to $\Lambda = 38^o$, within a range of Re_h ($Re_h = U_\infty h/\nu$ with h the height of the step and U_∞ the free stream velocity perpendicular to the step edge), the reattachment position stays independent of Λ.

In the framework of low Reynolds number flows featuring a laminar separation, Jones (1947) proposed to extend the *Simple Sweep Theory* introducing a correlation between the size of the recirculation region in an unswept and a swept wing. Recent high fidelity numerical investigations at low chord Reynolds number ($i.e. 10^2 - 10^4$) seem to contradict the proposed extensions of the *Simple Sweep Theory* (Uranga et al. 2011, De Tullio & Sandham 2017). In particular, the implicit Large Eddy Simulation (LES) of Uranga et al. (2011) has shown that while the pathway towards separation of the laminar boundary layer on the suction side of a wing does not seem to be affected by the sweep, the whole reattachment process, embedding a turbulence transition of the shear layer enveloping the separated region, is modified by the sweep. In their investigation the boundary layer on the suction side of the wing separates, transitions to turbulence and reattaches to the wall before the trailing edge. In figure 2.5a their chordwise pressure distribution for different sweep angles is presented and the variation caused by the crosswind on the transition location is highlighted. In figure 2.5b, the distribution of the boundary layer integrals as a function of the sweep is also proposed, showing their change caused by the sweep. De Tullio & Sandham (2017) using direct numerical simulations (DNS) have provided additional evidence of the different transition mechanisms that takes place in the detaching shear layer of the separated region
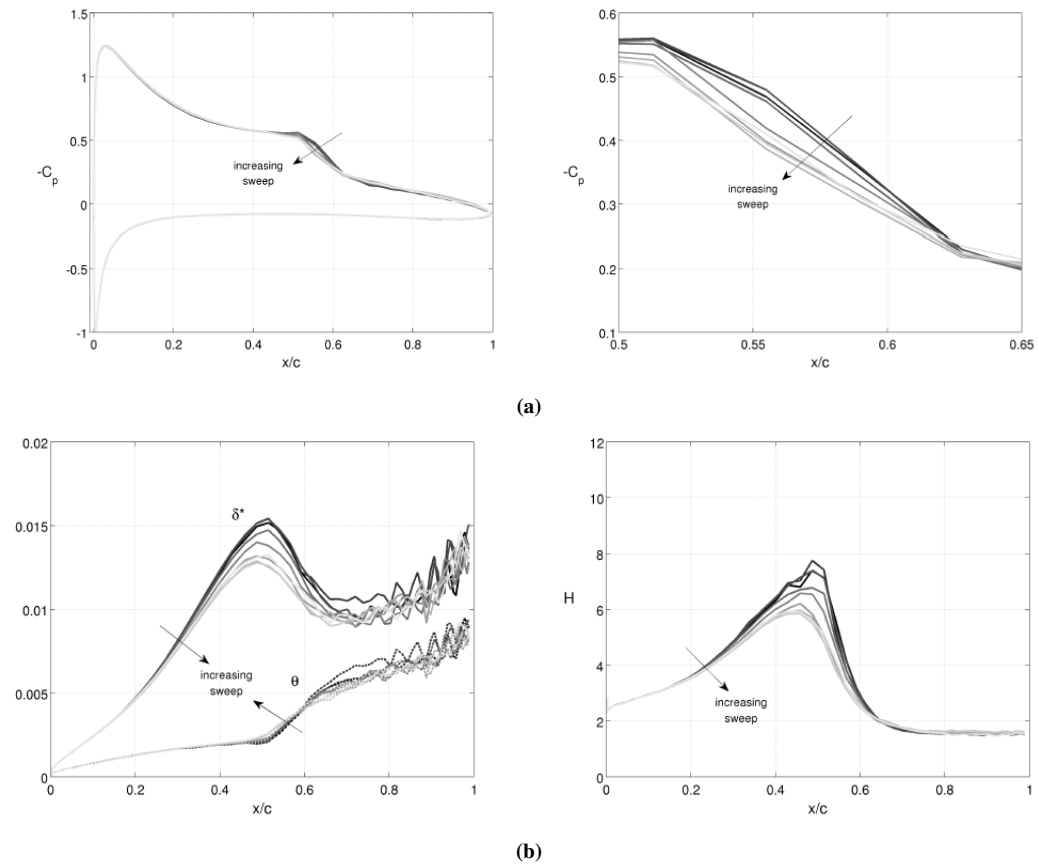
Figure 2.5: Chordwise distributions of (a) pressure and (b) momentum and displacement thicknesses along the upper side of the wing where laminar separation takes place for all the considered sweep angles. Taken from Uranga et al. (2011)
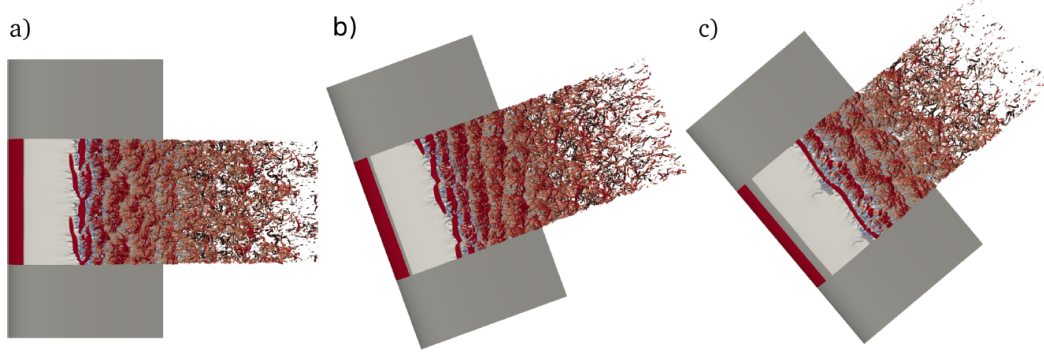
Figure 2.6: Flow visualisations of the upper side of wings with different sweep angles ((a) $\Lambda = 0^o$, (b) $\Lambda = 20^o$, (c) $\Lambda = 40^o$). All cases experience boundary layer laminar separation and transition to turbulence on the upper side of the wing. Taken from De Tullio & Sandham (2017).

when a sweep is introduced. Through a number of visualisations of swept wings (here proposed in figure 2.6) they have shown how the crosswind influences the separation-transition process, leading to different flow structures. The orientation and the structure of the flow with respect to the flow direction is changed when the sweep is introduced.

The current contribution aims to provide a systematic and extensive comparison between flows around swept/unswept infinite wings considering both laminar and turbulent separation scenarios. The following two sections will mainly report literature results available in the specific topics.

2.3 Laminar boundary layer separation

When an undisturbed low Reynolds number flow approaches a cambered wing it may separate from the wall under the action of the adverse pressure gradient. Often, the separation is followed by a transition to turbulence. This scenario is typical of the so called *laminar separation bubble* (LSB) or transitional separation bubble (TSB) (Gaster 1967, Horton 1968, O'Meara & Mueller 1987, Jones et al. 2008, Hain et al. 2009, Yarusevych et al. 2009). Several researches have outlined the stages of this process: the magnitude of Tollmien–Schlichting (TS) waves are amplified in the upstream portion of the laminar attached flow under the action of the aerofoil curvature; due to the adverse pressure gradient the flow may separate, and in this case the separation of the shear layer simultaneously with the amplification of a Kelvin–Helmholtz (KH) instability are observed; the KH instability leads to a development of three-dimensional (3D) structures in the shear layer and to its turbulent transition (Watmuff 1999, Alam & Sandham 2000, Lang et al. 2004, Marxen et al. 2004, Jones et al. 2008, Hain et al. 2009, Marxen et al. 2012). In some cases the boundary

layer reattaches to the wall in a time-averaged sense, either in a laminar or in a turbulent state, in some others it does not and the separated region merges directly in the wake. The flow region bounded by the separating shear layer is characterised by the presence of reversed flow and is often referred to as the *dead air region* (Alam & Sandham 2000). The described flow field is highly unsteady and once time-averaged it takes the shape of a bubble of recirculating fluid sitting above the aerofoil.

The LSB has been shown to be very sensitive to a number of parameters (such as the Reynolds number, the external disturbances, the pressure gradient, . . .) (O'Meara & Mueller 1987, Jones et al. 2008). To understand the basic mechanism that governs its phenomenology often researcher had to consider simplified condition to avoid the interference of extended factors. In particular, some authors have studied the flow on a flat plate subject to a controlled adverse pressure gradient and level of external disturbances (Gaster 1967, Marxen & Henningson 2011, Jagadeesh et al. 2013, Hosseinverdi & Fasel 2015, Balzer & Fasel 2016, Hosseinverdi & Fasel 2019). Others focused on the flow past a backward facing step that sets the condition of the separation on the edge of the step (Kaltenbach & Janke 2000, Schafer et al. 2009). Concerning the numerical predictions of the LSB scenario, some authors have showed that a high fidelity methodology (DNS or highly resolved LES) is required to capture its physical behaviour (Cadieux et al. 2012). Using a set of resolved simulations, Marxen et al. (2013) showed how the LSB structure and stability are strongly conditioned by the level of the external perturbations contained in the free stream flow. Through companion experimental investigations, they showed that the characteristics of the LSB may change abruptly even for the slightest perturbation present in the free stream.

Although a complete description of the LSB is still lacking even for the case of a two-dimensional mean flow, some authors have extended their research considering the effect of a crosswind on the flow (Kaltenbach & Janke 2000, Hetsch & Rist 2009, Uranga et al. 2011, De Tullio & Sandham 2017). These investigations are particularly relevant to the present thesis that in chapter 4 covers the LSB scenario when a sweep angle is introduced in the approaching uniform flow.

Kaltenbach & Janke (2000) considered the effect of the crosswind on the LSB, investigating the laminar flow past a step varying the sweep Λ of its edge. They found that the *Simple Sweep Theory* holds up to $\Lambda = 40^o$ for several mean quantities characterising the LSB in the direction normal to the step edge, among them the location of the reattachment line past the step. These measurements and conclusions were obtained for a moderate Reynolds number leading to a natural transition to turbulence only inside the separated shear layer behind the

step. They also reported that an increase in turbulence intensity can modify the effect of the sweep on the transition process, although with negligible effects on the normal-to-the-step mean flow behaviour. Figure 2.7 proposes some snapshots taken from Kaltenbach & Janke (2000) representing the instantaneous wall pressure perturbations obtained by varying the sweep. The footprints of newly emerging flow structures are observed from the separation location onwards, even tough the reattachment location remains fixed. The aforementioned article also provides some details about the separation bubble topology and the effect of the crosswind on it. The descriptions are in qualitatively agreement with those reported for the finite separation observed on a comparable swept wing flow considered in the doctoral thesis of Broadley (1998).
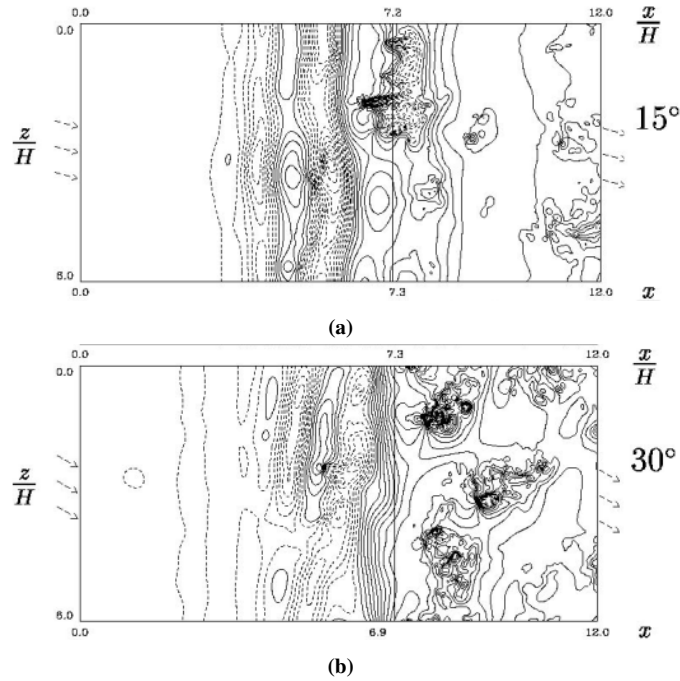
Figure 2.7: Snapshots of the separation and reattachment past a step swept-back flow by means of wall instantaneous pressure fluctuations. (a) Case at $\Lambda = 15^o$ sweep and (b) at $\Lambda = 30^o$ sweep. The step edge is at $x/H = 0.0$ while the solid vertical lines mark the location of reattachment. Taken from Kaltenbach & Janke (2000).

In a more recent research, Hetsch & Rist (2009) focused on the determination of the proper scaling for the crossflow (the latter is defined as the flow perpendicular to the inviscid streamline, and must not be confused with the crosswind which is along the spanwise direction) using a quasi-3D DNS simulations of a laminar separation bubble with and without a mean crosswind. The bubble formation is generated by imposing an appropriate adverse pressure gradient at the top edge of their computational box. Their principal findings, presented in Figure 2.8 and 2.9, show that is possible to collapse the crosswind and crossflow

profiles for different sweep angles independently of the chordwise flow. These findings are of great interest, but the use of an approximate DNS formulation suggests some care in their extension to *real world* three-dimensional scenarios.
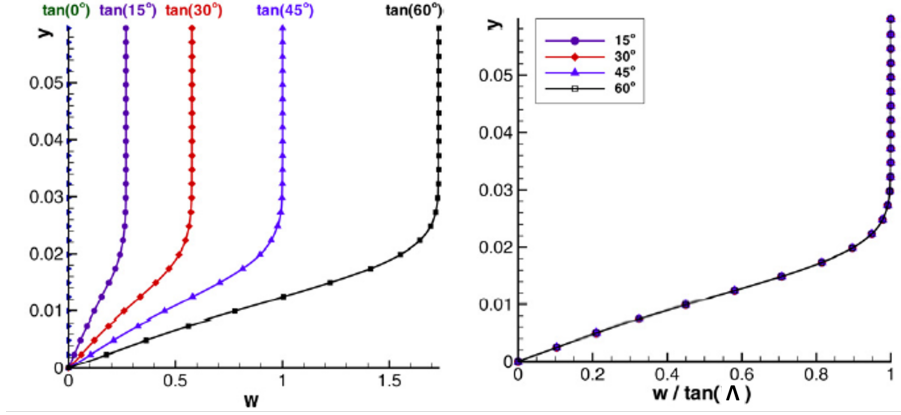
Figure 2.8: (Left) Mean profiles of the crosswind velocity component at the separation location for different sweep angles Λ. (Right) Same as in the left panel but premultiplied by $\tan(\Lambda)$. Taken from Hetsch & Rist (2009).
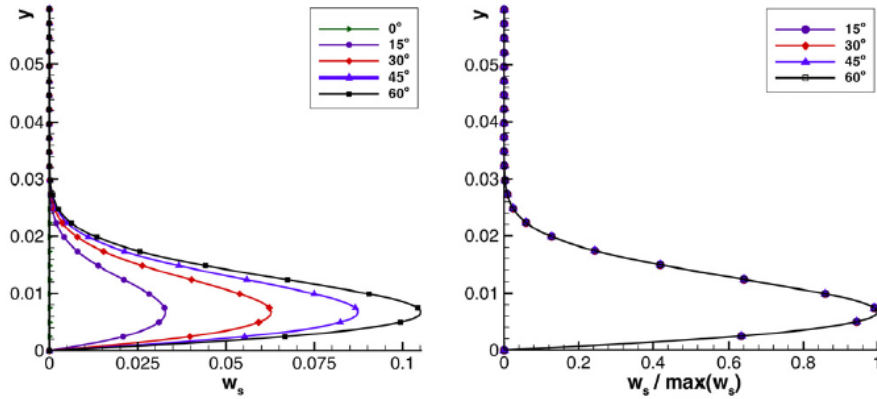
Figure 2.9: (Left) Mean profiles of the crossflow (flow perpendicular to the local 3D inviscid streamline on the wing) at the separation location for different sweep angles Λ. (Right) Same as in the left panel but premultiplied by the respective maximum crossflow velocity. Taken from Hetsch & Rist (2009).

As already mentioned, the work of Uranga et al. (2011) and De Tullio & Sandham (2017) represent the most up-to-date numerical investigations on the LSB scenario. These contributions have already been reported in section 2.2.

2.4 Turbulent boundary layer separation

Next, the flow separation in the case of a turbulent boundary layer subject to an adverse pressure gradient is reviewed. This phenomenon (Howe 1968, Simpson 1989), is widely known in the aeronautics industry as it often occurs by the trailing edge region of a subsonic

wing at high Reynolds number, even when a fully turbulent boundary layer establishes from a very early stage. In general, a stronger adverse pressure gradient needs to be applied to cause a turbulent boundary layer detachment as compared to the one required for a laminar boundary layer separation. The reason behind this increase is related with the enhanced energy produced by the turbulent fluctuations (Orlandi & Jiménez 1994, Schlichting & Gersten 2000, Fukagata et al. 2002). Furthermore, the intensity of the adverse pressure gradient required to produce a separation on a given geometry increases with the Reynolds number. In particular, the stall angle of an aerofoil exhibiting turbulent boundary layers increases when the Reynolds number of the incoming flow is increased (Jacobs & Sherman 1937, Pinkerton 1938, Abbott et al. 1945). Although some passive control devices have been investigated to delay the appearance of turbulent separation (Simpson 1996, Lin 2002, Ashill et al. 2005), the intimate mechanisms that determine the separation and its phenomenology are not totally clear yet. The literature covering fundamental investigations on the turbulent separation mechanism is scarce (e.g. Simpson (1989), Dmitriev (1990)).

Kitsios et al. (2017) reported that the Reynolds stress production and dissipation profiles in presence of a strong adverse pressure gradient turbulent boundary layer exhibit a second outer peak aside from the one observed for the zero pressure gradient case. This extra maximum becomes more pronounced and more spatially concentrated when increasing the pressure gradient. Also, the authors noted that this outer peak matches the location of the inflection point of the mean velocity profiles (in their case the adverse pressure gradient was quite severe, causing a confined turbulent boundary layer detachment from the wall). This shared position suggests the emergence of an outer shear flow instability.

Recently, other authors have put forward some evidences of an eventual participation in the separation mechanism of the coherent structures populating the inner sublayer of the turbulent boundary layer. Indeed, those flow structures sustaining wall turbulence (low/high speed streaks and quasi-streamwise vortices, (Smith et al. 1991, Smith 1996, Jiménez & Pinelli 1999)) have been found to be affected by the presence of an adverse pressure gradient on both a flat plates (Lee & Sung 2009, Monty et al. 2011, Kitsios et al. 2017) and on unswept wings at an incidence (Vinuesa, Hosseini, Hanifi, Henningson & Schlatter 2017, Vinuesa et al. 2018). Lee & Sung (2009) found that when a strong adverse pressure gradient is applied, near-wall streaks are weakened and the spanwise spacing between them becomes irregular and increases significantly up to 400 viscous wall units (approximately four times larger than that of the zero pressure gradient flow). Simultaneously, some researchers have pointed out the existence of confined backflow nuclei (localised blobs of instantaneous veloc-

ity opposite to the direction of the free stream), narrowed within the low speed wall streaks in high Reynolds number turbulent boundary layer of wall bounded flows even when no pressure gradient is applied (Johansson 1988, Lenaers et al. 2012). Lenaers et al. (2012) have employed DNS to systematically assess and quantify the controversial detention of backflow events in zero pressure gradient turbulent boundary layer. They observed that backflow occurs more often and farther away from the wall as the Reynolds number increases. Recently, Brücker (2015), using an original technique based on the imaging of deflecting micropillar in a zero pressure gradient turbulent boundary layer at a high Reynolds number, found that backflow regions are located in areas of a high spanwise gradient of wall-shear stress, with strong sweeps towards the wall. The effect of an adverse pressure gradient to the backflow phenomena observed in the turbulent boundary layer has been investigated by Vinuesa, Örlü & Schlatter (2017), who proposed a link between the increasing backflow nuclei detection and the incipient separation occurring at the trailing edge of a wing at an incidence. The flow that they have numerically simulated via DNS featured a tripped suction side boundary layer at a chord Reynolds number of about half a million along a NACA-4412 at 5° incidence. The regions of backflow were assumed to correlate with the local flow structures and in particular with the instantaneous and local distribution of the streamwise velocity streaks deformed under the effect of an adverse pressure gradient. A statistical analysis of the distribution of these backflow regions also revealed that the probability of finding a separated spot increases along the suction side as the trailing edge of the wing is approached, i.e. increasing the intensity of the adverse pressure gradient. A qualitative evidence of the effect of an increasing probability to find a backflow event moving towards the trailing edge is reproduced here in figure 2.10. Along the same line of research, recent results produced by our group confirmed the existence of localised regions of separated flow appearing in a turbulent boundary layer developing along the suction side of a wing (Suardi et al. 2019). In this thesis this observations and corresponding discussions are extended to the case of a swept wing.

Indeed, the effect of a constant crosswind to the formation mechanism of a turbulent boundary layer separation caused by a chordwise adverse pressure gradient has not yet received much attention, not even in the simplified case of an infinite wing flow condition. The detailed analysis of the crosswind effect to the outer and wall layer flow structures can certainly lead to new understanding that can inspire new localised flow control techniques limiting or suppressing the separation of turbulent boundary layers. The study on the separation mechanism of a turbulent boundary layer on a swept wing is one of the original

(a)

(b)
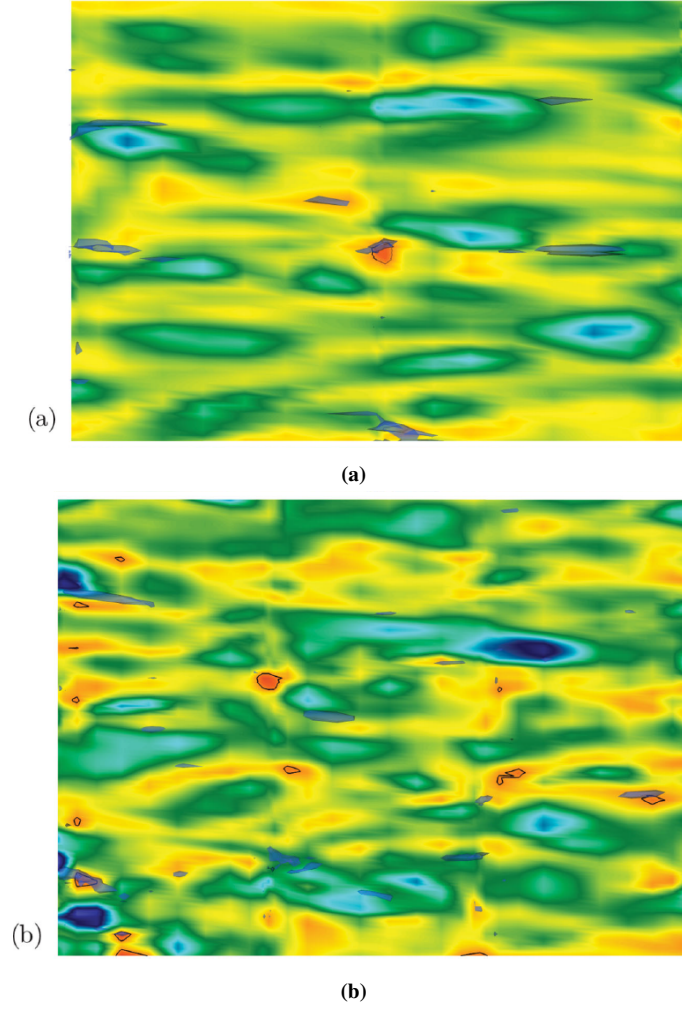
Figure 2.10: Snapshots of the instantaneous wall friction on the suction side of a $NACA-4412$ at 5° incidence. Positive friction (towards trailing edge) is represented in blue, negative friction in red. The two graphs represent the same quantity in two regions in the neighbourhood of $x/C \approx 0.4$ (a) and $x/C \approx 0.8$ (b). Taken from Vinuesa, Örlü & Schlatter (2017).

contribution brought by the current investigation. Although the recent literature is quite rich in reporting several investigations on the drag reduction effects that unsteady or spatially not-uniform crosswind oscillations of the mean flow can produce by altering the structure of the close-to-the-wall turbulence and inducing the appearance of a local unsteady Stoke's layer (see for example Jung et al. (1992), Choi (2002), Du et al. (2002), Viotti et al. (2009), Quadrio et al. (2009), Auteri et al. (2010), Lardeau & Leschziner (2013)), not much information is available on the effect of a mean steady crosswind. In the present thesis, this effect and its combination with a variable pressure gradient distribution are considered. In particular, emphasis will be given on the stretching and tilting of the near wall structures and their influence on the appearance and topology of local regions of reversed flow on a wing suction side.

Chapter 3

Methodology

Where the senses fail us,

reason must step in.

Galileo Galilei

The flow conditions are those of a three-dimensional, incompressible flow around an infinite swept and unswept wing with the $NACA - 4412$ profile. This profile has been chosen for several reasons: its non-symmetric geometry, its wide adoption in turbomachineries and the available literature reporting its performances (Jacobs & Sherman 1937). The methodology employs high-fidelity, numerical simulations of the incompressible Navier-Stokes equations. In particular, an highly resolved LES (Large Eddy Simulations) approach is adopted.

The present chapter is constituted as follows. The problem identification is presented in section 3.1, and the governing equations in section 3.2. Section 3.3 contains the numerical formulation deployed to discretise the governing equations. Sections 3.5 and 3.6 present the steps taken to guarantee the independence of the predicted flow from the particular numerical settings considered, namely the grid refinement study and the computational domain size study. Lastly, section 3.7 presents an insight of the chosen numerical free stream condition to simulate the desired laminar and the turbulent flow scenarios.

In the following sections, a trade off between clarity and readability has been made with the symbolic formula. In particular, the specification of the independent variables of each mathematical function has been stated explicitly when this is introduced for the first time only. Also, the present chapter contains numerous symbols (i.e. subscripts and superscripts) and mathematical operators required to precisely describe both the analytical and the numerical models adopted to carry out the investigation. Although an effort of consistency has been

made, the notation of some symbols, subscripts or superscripts in sections 3.2 and 3.3 may differ with respect to that used throughout the thesis.

3.1 Problem identification

In the adopted Cartesian coordinate system, centred at the $NACA - 4412$ leading edge (LE), x (sometime indicated as x_1 and referred as the chordwise direction) is aligned with the aerofoil chord (C) and it points towards the trailing edge (TE). y (or x_2) lies in the foil plane and it is normal to x, pointing upwards. z (or x_3 and referred as the spanwise direction) is deployed along the bi-normal direction with respect to the $x - y$ plane. The plane $x - y$ is referred as the aerofoil or chord plane, the plane $x - z$ is referred as the wing plane. u, v and w (or u_1, u_2 and u_3) will denote the components of the velocity vector field along the x, y and z direction, respectively. The reference system is sketched in figure 3.1. The axis r is part of a polar reference system with origin at the aerofoil leading edge. Alongside, it is also defined the curvilinear reference system based on the foil shape. To this end, s is the curvilinear direction following the foil shape, while n is the direction normal to s and lying in the chord plane.
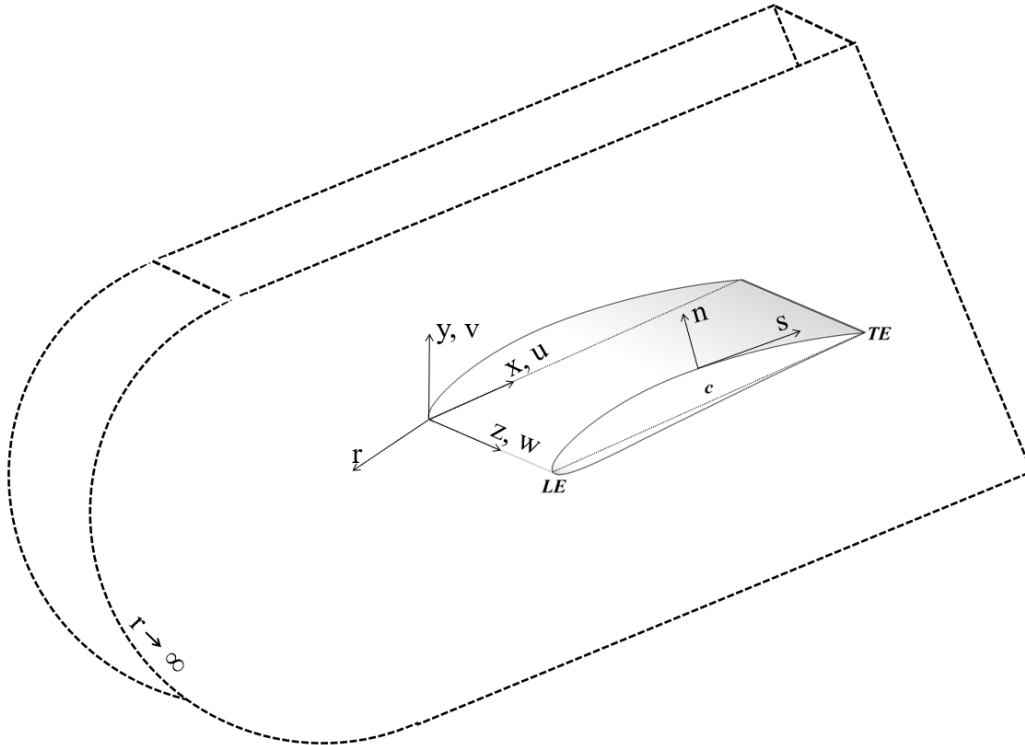
Figure 3.1: Sketch of the reference systems used.

The free stream wind approaches the wing leading edge from the upstream far-away

location formally indicated with $r \to \infty$. The free stream pressure is indicated with P_∞. Its density with ρ_∞ and its kinematic viscosity with ν_∞, both constant in space and time as implied by the incompressible fluid assumption. The free stream wind velocity is the vector $\vec{Q}_\infty$ with the magnitude indicated as $|\vec{Q}_\infty|$. The components of the free stream velocity along the directions x, y and z are indicated with U_∞, V_∞ and W_∞. When the free stream vector lies on the $x - y$ plane, the included angle between the free stream and the x-axis is the angle α, called the aerofoil incidence or angle of attack. The incidence sets the loading condition on the wing. When the free stream vector lies on the $x - z$ plane, the included angle between the free stream and the x-axis is indicated with Λ and it is defined as the sweep angle of the wing. The sweep angle sets the amount of crosswind on the wing imposing a non zero value of W_∞. The free stream velocity value in the chord plane (which would be formally written as $|\vec{Q}_\infty^{xy}|$, being $\vec{Q}_\infty^{xy}$ the projection of the free stream velocity vector $\vec{Q}_\infty$ on the chord plane) is indicated as Q_∞ for simplicity throughout the text. As a consequence, $U_\infty = Q_\infty \cos(\alpha)$ and $V_\infty = Q_\infty \sin(\alpha)$. Note that when the swept wing is considered, $Q_\infty = |\vec{Q}_\infty^{xy}| = |\vec{Q}_\infty| \cos(\Lambda)$, while in the unswept case $Q_\infty = |\vec{Q}_\infty^{xy}| = |\vec{Q}_\infty|$. A schematic representation of the free stream definition and notation is shown in figure 3.2.

Although the results for different wing configurations varying the sweep will be presented, it is remarked that all of them share the same value of the chord-based Reynolds number, fixed to the value of $Re_c = 5 \times 10^4$ (defined as $Re_c = Q_\infty C / \nu$). The choice has been made to follow the prescription of the *Simple Sweep Theory* (described in section 2.2) in order to assess its capabilities. As a consequence, the magnitude of total free stream $|\vec{Q}_\infty|$ changes between the different sweep configurations.

3.2 Governing equations

The equations of the model are the three-dimensional LES equations (Ferziger & Peric 2002). These are obtained by filtering out the velocity and pressure fluctuations taking place below a cut-off length scale, chosen within the inertial range of turbulence. Using the index $i = 1 \dots 3$ to switch among the components of a three-dimensional vector, the spatial filtering operation is formally defined as

$$u_i = \tilde{u}_i + u_i' \quad \text{with} \quad \tilde{u}_i = \int_{-\infty}^{\infty} u_i(r_i) G(x_i - r_i) dr_i \tag{3.1}$$
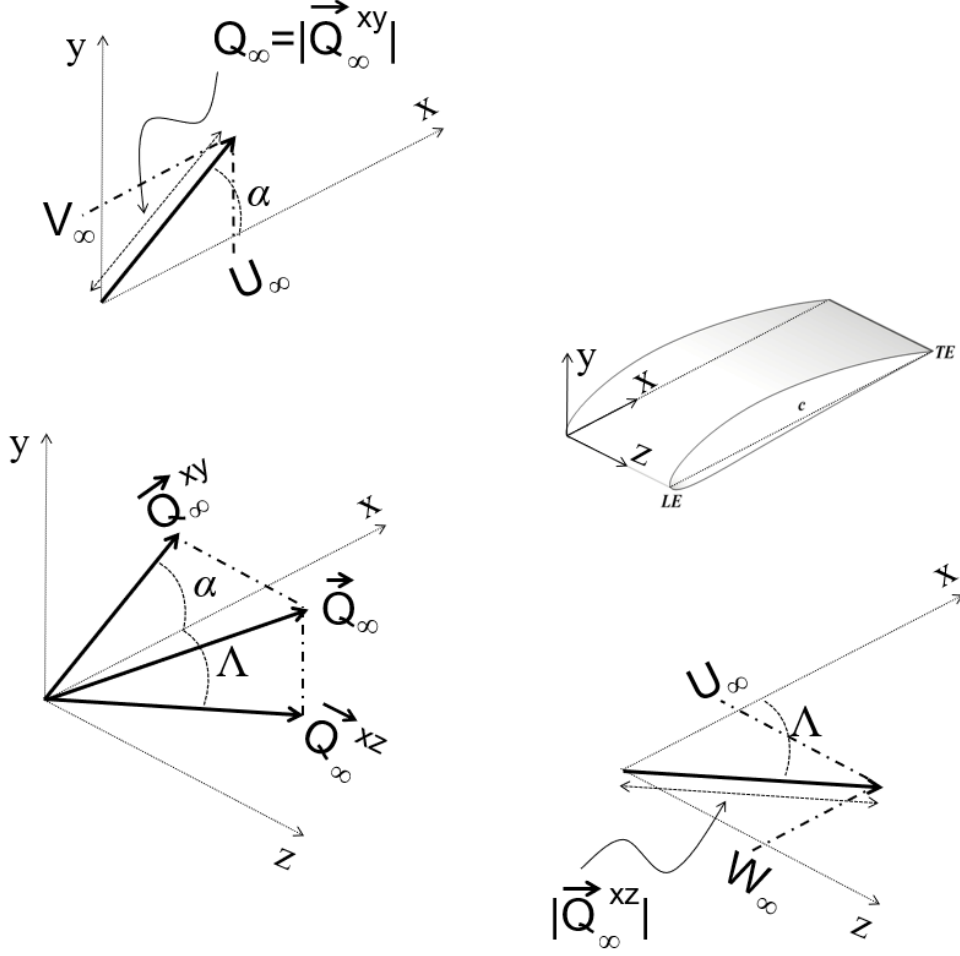
Figure 3.2: The reference free stream notation.

where $u_i(x, y, z, t)$ represents the velocity, $\tilde{u}_i(x, y, z, t)$ and $u'_i(x, y, z, t)$ its resolved and sub-grid scales (the reader is warned that this notation is adopted in the present section and in section 3.3 only, since anywhere else u'_i indicates the velocity fluctuation) and G is a representative low band pass filter in the space domain. Using the tensor notation (i.e. $i = 1 \ldots 3$ and $j = 1 \ldots 3$) and adopting the Einstein notation for the summation on repeated indices, the governing equations read

$$\frac{\partial \tilde{u}_i}{\partial t} + \tilde{u}_j \frac{\partial \tilde{u}_i}{\partial x_j} = -\frac{1}{\rho} \frac{\partial \tilde{P}}{\partial x_i} + \frac{1}{Re_c} \frac{\partial^2 \tilde{u}_i}{\partial x_j x_j} + \frac{\partial \tau_{ij}}{\partial x_j}, \qquad \frac{\partial \tilde{u}_j}{\partial x_j} = 0. \tag{3.2}$$

with ρ the fluid density, $\tilde{P}(x, y, z, t)$ the resolved pressure field and $\partial / \partial \cdot$ is used to indicate the partial derivative operator. The equations have been made non-dimensional by introducing the reference length scale C (aerofoil chord) and reference velocity Q_∞ (free stream in the chord plane). To make the notation lighter, the superscript used to indicate a non dimensional

26

quantity, $\{\cdot\}^*$, has not been specified here. In the given set (3.2), $Re_c = Q_\infty C/\nu$ is the chord Reynolds number and $\tau_{ij} = \widetilde{u_i u_j} - \tilde{u}_i \tilde{u}_j$ is the subgrid Reynolds stress tensor (Leonard 1975).

The unresolved stresses constitute the well-known central closure problem in LES. These stresses represent the drainage of momentum done by the unresolved small scales over the actually resolved ones. To close the given system of equation the subgrid stresses are related with the deformation rate tensor of the resolved field using an eddy-viscosity assumption, i.e.

$$\tau_{ij} - \delta_{ij}\tau_{kk}/3 = -2\nu_t \widetilde{S}_{ij} \tag{3.3}$$

where ν_t is the turbulent viscosity and $\tilde{S}_{ij} = (\partial \tilde{u}_i/\partial x_j + \partial \tilde{u}_j/\partial x_i)/2$ is the resolved strain-rate tensor of magnitude $|\tilde{S}|$. A traditional grid-dependent closure for the eddy viscosity would be $\nu_t = (C_t \tilde{\Delta})^2 |\tilde{S}|$, where $\tilde{\Delta} = 2(\Delta x \, \Delta y \, \Delta z)^{1/3}$ is the grid-dependent filter size (with Δx, Δy and Δz a measure of the resolution of the numerical grid in the three directions, respectively) and C_t would be determined using a certain model (e.g. Dynamic model, Germano et al. (1991)). Instead, in this study the closure for the eddy viscosity is provided by the ILSA method (Integral Length-Scale Approximation) where the eddy viscosity is formulated as in Piomelli et al. (2015), i.e.

$$\nu_t = (C_{ILSA} L_{ILSA})^2 |\tilde{S}| \tag{3.4}$$

where C_{ILSA} is a coefficient introduced by the model and L_{ILSA} the model length scale. As mentioned by Piomelli et al. (2015), L_{ILSA} should be a fraction of the local, instantaneous integral scale of turbulence. In particular, the formulation of L_{ILSA} contained in Rouhi et al. (2016) is adopted here, i.e.

$$L_{ILSA} = \frac{<\tilde{k}^{3/2}>_z}{<\varepsilon>_z} \tag{3.5}$$

where $\tilde{k}(x, y, z, t)$ is the local, resolved turbulent kinetic energy ($\tilde{k} = 1/2\tilde{u}_i'\tilde{u}_i'$, with $\tilde{u}_i'$ the fluctuating part of the resolved velocity field) and $\varepsilon(x, y, z, t)$ the local, total dissipation rate ($\varepsilon = 2(\nu + \nu_t)\tilde{S}_{ij}'\tilde{S}_{ij}'$, with $\tilde{S}_{ij}'$ the fluctuating part of the resolved strain-rate tensor, given by the resolved $\tilde{\varepsilon} = 2\nu\tilde{S}_{ij}'\tilde{S}_{ij}'$ and subgrid $\varepsilon_t' = 2\nu_t\tilde{S}_{ij}'\tilde{S}_{ij}'$ dissipation rates). Both $\tilde{k}$ and ε are calculated locally and instantaneously. However, since L_{ILSA} is an integral quantity representing the average size of an ensemble of eddies, an averaging operation has been used along the homogeneous, spanwise direction (indicated with $<\cdot>_z$) in equation 3.5, as recommended in Rouhi et al. (2016). This results in L_{ILSA} that varies in the directions x and y and in time.

The definition of the length scale based on turbulence quantities implies some advan-

tages. The LES filter is independent from the resolution of the computational grid used, as specified in Piomelli et al. (2015). Also, the filter allows to switch automatically, without any presumption on the local flow state, from a LES to a fully resolved, DNS (Direct Numerical Simulations) approach. This feature is particularly important when the fluid domain encompasses turbulent, laminar and transitional regions which can be tackled without the intervention of any numerical artefact with a single formulation. When no energy is accumulated by the subgrid fluctuations, the set of equations (3.2) switch automatically to the three dimensional, unsteady, incompressible Navier-Stokes equations:

$$\frac{\partial u_i}{\partial t} + \frac{\partial u_i u_j}{\partial x_j} = -\frac{1}{\rho}\frac{\partial P}{\partial x_i} + \frac{1}{Re_c}\frac{\partial^2 u_i}{\partial x_j x_j}, \qquad \frac{\partial u_j}{\partial x_j} = 0 \tag{3.6}$$

where $P(x, y, z, t)$ is the fully resolved pressure fields.

Furthermore, the adoption of a small coefficient of the ILSA method ($C_{ILSA} = 0.002$) determines the filter to act only on the smallest scales of the turbulent activity (Piomelli et al. 2015). Ultimately, the fidelity of the methodology can be practically considered that of a standard DNS.

3.2.1 Initial and boundary conditions

The differential equations (3.2) are equipped with boundary and initial conditions (indicated B.C. and I.C.) to deliver a well posed differential problem. The boundary conditions are expressed formally as

$$\begin{cases} u_i = 0 \text{ at the wall, no slip condition} \\ \partial P/\partial n = 0 \text{ at the wall, impermeability condition} \\ \text{Inflow/Outflow at } r \to \infty, \text{ free stream condition} \end{cases} \tag{3.7}$$

where n is used to indicate the normal-to-the-wing-surface direction. The initial condition for the velocity field $u_i^o(x, y, z)$ may be chosen in multiple ways. It can be as simple as the no-motion condition everywhere in the domain or fixed to the solution of a potential, inviscid flow condition. In the latter case the Laplace equation for the velocity potential around the aerofoil has to be solved for the specified incidence α and sweep Λ with $no - slip$ condition at the wall and free stream velocity $\vec{Q}_\infty$ at the outer boundary $r \to \infty$. Using $\chi(x, y, z)$ for the velocity potential of the inviscid flow ($u = \partial\chi/\partial x$, $v = \partial\chi/\partial y$ and $w = \partial\chi/\partial z$), the

potential problem can be written as

$$\frac{\partial^2 \chi}{\partial x_j x_j} \quad = \quad 0 \qquad \text{with} \qquad \begin{cases} \partial \chi / \partial n = 0 \ \text{ at the wall} \\[6pt] \frac{\partial \chi}{\partial x} \check{x} + \frac{\partial \chi}{\partial y} \check{y} + \frac{\partial \chi}{\partial z} \check{z} = \\[6pt] |\vec{Q}_\infty| cos(\alpha) cos(\Lambda) \check{x} + \\[6pt] + |\vec{Q}_\infty| sin(\alpha) cos(\Lambda) \check{y} + \\[6pt] + |\vec{Q}_\infty| sin(\Lambda) \check{z} \ \text{ for } r \to \infty \end{cases} \qquad (3.8)$$

where $\{\check{\ }\}$ has been used to indicate the unit vectors of the reference system.

3.3 Numerical formulation

The equations 3.2 with their boundary and initial conditions are discretised on a three-dimensional, structured, conformal mesh occupying the flow domain around the wing. Their time evolution is solved by an in-house-developed software called *SUSA*. Hereafter, alongside to the required mesh details, the numerical formulation implemented into *SUSA* is briefly presented. The numerical code is mostly written in the language FORTRAN-77. Further details on the code, its parallelisation and the extensive validation campaign can be found in previous publications (e.g. Lopes et al. (2006), Omidyeganeh & Piomelli (2011), Rosti et al. (2016), Rosti (2016), Monti et al. (2019), Monti (2019)).

Equations 3.2 are further elaborated before proceeding with the discretisation in time and space. The convective term is written in the conservative form (i.e. $\tilde{u}_j \frac{\partial \tilde{u}_i}{\partial x_j} = \frac{\partial \tilde{u}_i \tilde{u}_j}{\partial x_j}$). Also, thanks to the incompressible formulation that simplifies the expression of $\tilde{S}_{ij}$, the subgrid stresses (here modelled with the artificial viscosity hypothesis) and the viscous diffusion can be collected together (i.e. $\frac{1}{Re_c} \frac{\partial^2 \tilde{u}_i}{\partial x_j x_j} + \frac{\partial \tau_{ij}}{\partial x_j} = \left(\frac{1}{Re_c} + \frac{1}{Re_t} \right) \frac{\partial^2 \tilde{u}_i}{\partial x_j x_j}$, where $Re_t = CQ_\infty / \nu_t$). After the mentioned elaborations, the formulation to be discretised reads

$$\frac{\partial \tilde{u}_i}{\partial t} + \frac{\partial \tilde{u}_i \tilde{u}_j}{\partial x_j} + \frac{1}{\rho} \frac{\partial \tilde{P}}{\partial x_i} + \left(-\frac{1}{Re_c} - \frac{1}{Re_t} \right) \frac{\partial^2 \tilde{u}_i}{\partial x_j x_j} = 0, \qquad \frac{\partial \tilde{u}_j}{\partial x_j} = 0. \qquad (3.9)$$

3.3.1 Time discretisation

The time discretisation is obtained via a fractional step method as in (Kim & Moin 1985), breaking the time-advancement in two steps. The first one is the prediction step, which provides the not-divergence-free $\tilde{u}_i^*(x, y, z)$ based on the known velocity and pressure fields

29

at the previous instant of time n, $\tilde{u}_i^n(x, y, z, t = t^n)$ and $\tilde{p}^n(x, y, z, t^n)$. The second is the projection step, where the pressure correction $\tilde{\phi}$ is found enforcing on $\tilde{u}_i^*$ the divergence free constraint. $\tilde{\phi}$ is the correction required to be applied to $\tilde{u}_i^*$ in order to find the updated divergence-free velocity field at the time instant $n + 1$, $\tilde{u}_i^{n+1}(x, y, z, t = t^{n+1})$. The updated pressure $\tilde{P}^{n+1}(x, y, z, t^{n+1})$, containing the correction, is ultimately found. This procedure formally reads

a) Prediction step $\dfrac{\tilde{u}_i^* - \tilde{u}_i^n}{\Delta t} + \dfrac{\partial \tilde{u}_i^n \tilde{u}_j^n}{\partial x_j} + \dfrac{1}{\rho}\dfrac{\partial \tilde{P}^n}{\partial x_i} + \left(-\dfrac{1}{Re_c} - \dfrac{1}{Re_t}\right)\dfrac{\partial^2 \tilde{u}_i^n}{\partial x_j x_j} = 0$

b) Projection step $\dfrac{\partial^2 \tilde{\phi}}{\partial x_j x_j} = -\dfrac{1}{\Delta t}\dfrac{\partial \tilde{u}_i^*}{\partial x_i}$ (3.10)

c) Final update $\tilde{u}_i^{n+1} = \tilde{u}_i^* + \dfrac{1}{\Delta t}\dfrac{\partial \tilde{\phi}}{\partial x_i}$; $\tilde{P}^{n+1} = \tilde{P}^n + \tilde{\phi}$

where Δt is the chosen time advancement interval. The projection step is a Poisson equation and thus an elliptic differential problem.

The prediction step formulated in 3.10 is totally explicit. This would impose stricter constrains to the span of the time advancement interval to avoid numerical divergence of the scheme. To relax the span of the time interval, a semi-implicit formulation is considered using the implicit Crank-Nicolson scheme for the wall-normal diffusive terms (the one containing the expected higher shear stresses nearby the foil wall) and the explicit Adams-Bashforth scheme for all the other terms. The actual prediction step formulation becomes

a) $\dfrac{\tilde{u}_i^* - \tilde{u}_i^n}{\Delta t} +$

$+ \dfrac{1}{2}\left(-\dfrac{1}{Re_c} - \dfrac{1}{Re_t}\right)\left[\dfrac{\partial^2 \tilde{u}_i^*}{\partial y^2} + \dfrac{\partial^2 \tilde{u}_i^n}{\partial y^2}\right] +$

$+ \dfrac{3}{2}\left\{\dfrac{\partial \tilde{u}_i^n \tilde{u}_j^n}{\partial x_j} + \dfrac{1}{\rho}\dfrac{\partial \tilde{P}^n}{\partial x_i} + \left(-\dfrac{1}{Re_c} - \dfrac{1}{Re_t}\right)\left[\dfrac{\partial^2 \tilde{u}_i^n}{\partial x^2} + \dfrac{\partial^2 \tilde{u}_i^n}{\partial z^2}\right]\right\} +$ (3.11)

$- \dfrac{1}{2}\left\{\dfrac{\partial \tilde{u}_i^{n-1} \tilde{u}_j^{n-1}}{\partial x_j} + \dfrac{1}{\rho}\dfrac{\partial \tilde{P}^{n-1}}{\partial x_i} + \left(-\dfrac{1}{Re_c} - \dfrac{1}{Re_t}\right)\left[\dfrac{\partial^2 \tilde{u}_i^{n-1}}{\partial x^2} + \dfrac{\partial^2 \tilde{u}_i^{n-1}}{\partial z^2}\right]\right\} = 0$

where $\tilde{u}_i^{n-1}(x, y, z, t = t^{n-1})$ and $\tilde{P}^{n-1}(x, y, z, t^{n-1})$ have been used. However, in the following section the space discretisation will be shown for the simpler fully explicit prediction step contained in equations 3.10. This choice is made to avoid an otherwise lengthier description of the discretisation, that would not introduce anything formally different.

3.3.2 Space discretisation

The LES equations (3.10) are space discretised using a second-order accurate, cell-centred finite volume method inside the computational domain generated and meshed as follows. Each wing cross section mounts a two-dimensional ($2D$), $NACA-4412$ aerofoil. The computational domain on a generic chord plane, accommodating the $2D$ aerofoil, is sketched in figure 3.3a. On the chord plane, the domain is meshed using a body fitted $C-$grid generated with the axis i along aerofoil surface s and j always normal to i. The term $C-$grid refers to the C letter shape of the structured mesh that wraps the foil. For the first j layer of the mesh, the direction j and n coincide along the aerofoil. The computational size of the $C-$grid around the aerofoil (constituting the computational box) are graphically shown in figure 3.3b. The virtual wake plane, shown in the figure causes the $C-$shape of the mesh and
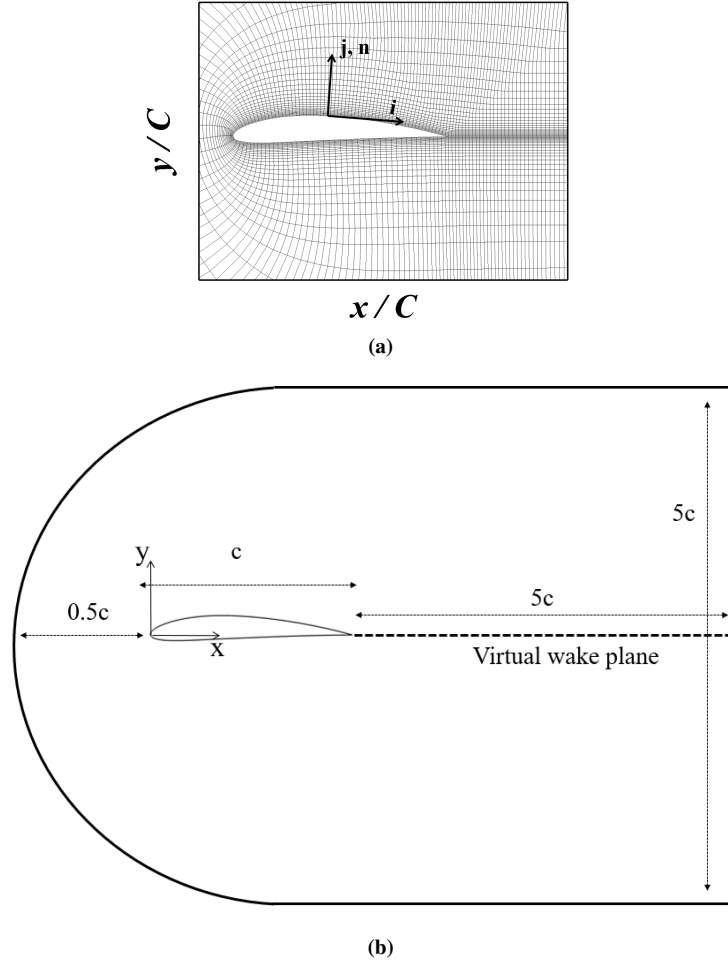
Figure 3.3: (a)Planar view of a wing section showing a sample of the mesh adopted. i and j constitute the mesh basis. n is the normal of the wing surface. $n$exactly coincides with the mesh axis j for the cell layer embracing the aerofoil. (b) Size of the computational box used for the flow predictions.

is defined as the extension of the chord behind the aerofoil. It is remarked that the virtual

wake plane is a technical artifice used to create a $C-$type structured mesh surrounding the aerofoil, but does not have any physical meaning and it will be treated as a continuum space. The i axis continues from the wall surface to the virtual wake plane. For the space discretisation that will be presented in the following lines, a mesh composed by quasi-orthogonal elements is required. To achieve such a goal, a minimum requirement is implicitly set for the number of points used for the spatial discretisation in order to approximate the curvilinear foil geometry with quasi-orthogonal elements. It is not an easy matter to quantify the minimum requirement. This is because the eventually generated numerical error has a variable impact on the accuracy of the global flow prediction depending on the particular level of the flow momentum and its gradients across each mesh element. In general, a severe quasi-orthogonality has to be imposed for those mesh elements in locations where there is a concurrent high flow momentum combined with sharp gradients. As a consequence, the mesh has to be increasingly fine (using a smooth spacing distribution) approaching the foil by any direction, especially where the wall presents great curvature (i.e. nose and trailing edge). Also, the grid resolution has to increase at high gradients presence (i.e. boundary layer and recirculation locations). An iterative process is usually required to originate a suitable mesh which does not affect the accuracy of the flow prediction, as it will be presented in section 3.5. It is mentioned that there is a geometrical non zero angle between the aerofoil wall on the upper side at the trailing edge and the virtual wake plane. The mesh elements nearby this location presents a constrained level of non-orthogonality depending on the mentioned angle. The proximity to the wall and the downstream location with respect to the foil, usually determine a low momentum flow (i.e. low gradients at the wall vicinity) that helps to maintain negligible the originated numerical error.

The $3D$ mesh extension is achieved by extruding the $2D$ mesh in k, corresponding to the z direction using a uniform spacing Δz. The resulting computational domain is constituted by quasi-cuboid cells, which are referred with the discrete notation in the mesh basis (i, j, k). Each cell has a specific volume $V(i, j, k)$ and surface area $S(i, j, k)$ with outward normal $\vec{n}$.

According to the finite volume method, each cell of the mesh corresponds to the control volume where the equations 3.10 have to be satisfied. The discretisation method is conservative for the mass and flow momentum by construction, since the cells are all contiguous, not overlapping and sharing an equal surface between each other in all the directions. The computational solutions of the discretised equations (P^{n+1} and u_i^{n+1}) are defined at the centroid of each cell, thus the name co-located cell centred approach. The number of computational nodes is N_i, N_j and N_k in the three axes forming the mesh basis. The co-located approach

has some advantages (e.g. a simplified coding formulation and minimized memory and computational impact), but also drawbacks (it may lead to the occurrence of spurious oscillations in the pressure field). The specific approach of Rhie & Chow (1983) is used to avoid fictitious pressure oscillations eventually generated by the co-located formulation. A discussion of its implementation can be found in Rosti (2016).

To find the finite volume formulation, the equations 3.10 are integrated on each control volume. Here, the procedure is shown for the generic cell (i, j, k) with centroid called P. The integrated equations read

a) $\int_V \frac{\tilde{u}_i^* - \tilde{u}_i^n}{\Delta t} dV + \int_V \frac{\partial \tilde{u}_i^n \tilde{u}_j^n}{\partial x_j} dV + \int_V \frac{1}{\rho} \frac{\partial \tilde{P}^n}{\partial x_i} dV + \left(-\frac{1}{Re_c} - \frac{1}{Re_t} \right) \int_V \frac{\partial^2 \tilde{u}_i^n}{\partial x_j x_j} dV = 0$

b) $\int_V \frac{\partial^2 \tilde{\phi}}{\partial x_j x_j} dV = -\frac{1}{\Delta t} \int_V \frac{\partial \tilde{u}_i^*}{\partial x_i} dV$ (3.12)

c) $\tilde{u}_i^{n+1}(i, j, k) = \tilde{u}_i^* + \frac{1}{\Delta t} \frac{\partial \tilde{\phi}}{\partial x_i}$; $\tilde{P}^{n+1}(i, j, k) = \tilde{P}^n + \tilde{\phi}.$

The gauss theorem $\int_V \frac{\partial F_i}{\partial x_i} dV = \oint_S F_i n_i dS$, with F_i generic differentiable vector field, is used to obtain the formulation showing the fluxes across the cell boundaries as intended by the finite volume method,

a) $\int_V \frac{\tilde{u}_i^* - \tilde{u}_i^n}{\Delta t} dV + \oint_S \tilde{u}_i^n \tilde{u}_j^n n_j dS + \oint_S \frac{1}{\rho} \tilde{P}^n n_i dS + \left(-\frac{1}{Re_c} - \frac{1}{Re_t} \right) \oint_S \frac{\partial \tilde{u}_i^n}{\partial x_j} n_j dS = 0$

b) $\oint_S \frac{\partial \tilde{\phi}}{\partial x_j} n_j dS = -\frac{1}{\Delta t} \oint_S \tilde{u}_i^* n_i dS$ (3.13)

c) $\tilde{u}_i^{n+1}(i, j, k) = \tilde{u}_i^* + \frac{1}{\Delta t} \frac{\partial \tilde{\phi}}{\partial x_i}$; $\tilde{P}^{n+1}(i, j, k) = \tilde{P}^n + \tilde{\phi}.$

To solve the equations, a numerical approximation for the surface and volume integrals have to be introduced. The volume integral is approximated considering the value of a generic quantity $q(x, y, z)$ as constant within the cell and equal to the value at the cell centre P. This allows a second-order accuracy for the integral approximation, which reads

$$\int_V q dV \approx q_P(i, j, k) V_p(i, j, k). \tag{3.14}$$

The same second-order accuracy is desired for the surface integrals, thus the integrand functions are approximated with the value at the centre of each surface, referred with the surface name. Thanks to the cuboid shape of each cell, the cell surface is the sum of the six contributions in the three directions. In figure 3.4 a generic cell is sketched with its local axes. To
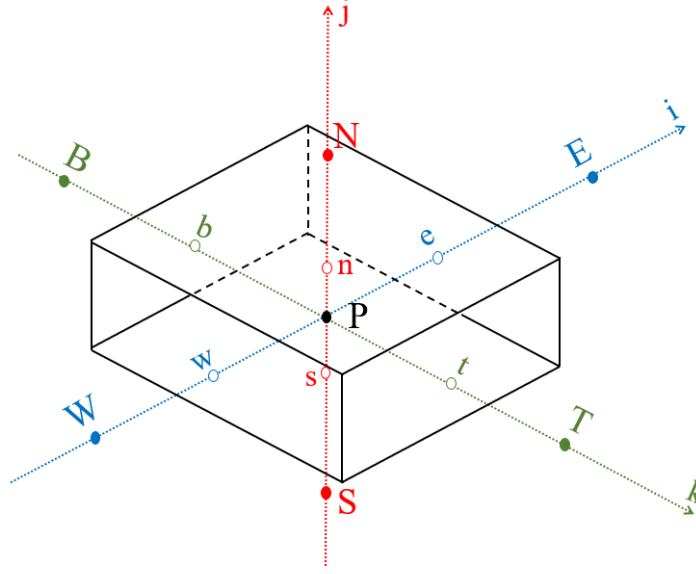
Figure 3.4: Three dimensional sketch of the generic cell (i,j,k) with cell centre P. The local basis i, j, k is shown. The centres of the cell faces are indicated with e, n, t, w, s, b, while the centres of the adjacent cells composing the global structured mesh with E, N, T, W, S, B.

guide the reader, the common nomenclature adopted in the following lines for the surfaces and cell centres is shown in the three-dimensional space (the nomenclature is similar to that in Ferziger & Peric (2002)). The surfaces are referred as $e(i, j, k)$ and $w(i, j, k)$ in the i direction; $n(i, j, k)$ and $s(i, j, k)$ in the j direction; $t(i, j, k)$ and $b(i, j, k)$ in the k direction. The cell centre of the adjacent cell across surface e is referred as $E(i, j, k)$ (also, thanks to the structured property of the mesh it can be referred as cell centre $(i + 1, j, k)$). That one across n as $N(i, j, k)$ (or cell centre of the global mesh $(i, j + 1, k)$) and across t as $T(i, j, k)$ (or cell centre $(i, j, k + 1)$). The same applies for the remaining neighbouring cells. The approximation of the surface integral of the generic flux $f(x, y, z)$ (which can be any of the convective fluxes $\tilde{u}_i^n \tilde{u}_j^n n_j$, the diffusive fluxes $\frac{\partial \tilde{u}_i^n}{\partial x_j} n_j$, the pressure fluxes in the prediction step $\tilde{P}^n n_i$ or the pressure-correction gradient fluxes in the projection step $\frac{\partial \tilde{\phi}}{\partial x_j} n_j$) across the surface e, for instance, is obtained as

$$\int_{S_e} f \, dS_e \approx f_e(i, j, k) S_e(i, j, k). \tag{3.15}$$

The value of the fluxes at the surface centre is obtained interpolating the values of the two nearest computational nodes, in the direction of the surface normal, i.e.

$$f_e = f_E \lambda_e + f_P (1 - \lambda_e) \tag{3.16}$$

with $\lambda_e(i, j, k)$ being the linear interpolative factor based on the positions of e, P and E. The

interpolation reads

$$\lambda_e = \frac{|\vec{r}_e - \vec{r}_P|}{|\vec{r}_E - \vec{r}_P|}. \tag{3.17}$$

The surface centred derivative is elaborated via the use of the directional derivative property $((\partial f(x, y, z)/\partial x_j)n_j = \partial f/\partial n_j)$ and subsequently approximated with a central difference scheme centred at the surface centre. Thus the diffusive contribution in the prediction step or the pressure one in the projection step become

$$\begin{aligned}
\left(\frac{\partial \tilde{\phi}}{\partial x_j} n_j\right)_e &= \left(\frac{\partial \tilde{\phi}}{\partial n_i}\right)_e &\approx \frac{\tilde{\phi}_E - \tilde{\phi}_P}{|\vec{r}_E - \vec{r}_P|} \\
\left(\frac{\partial \tilde{u}_i^n}{\partial x_j} n_j\right)_e &= \left(\frac{\partial \tilde{u}_i^n}{\partial n_j}\right)_e &\approx \frac{\tilde{u}_{iE}^n - \tilde{u}_{iP}^n}{|\vec{r}_E - \vec{r}_P|}.
\end{aligned} \tag{3.18}$$

This approach does not introduce spurious oscillations as long as the points P, e and E lie on the same line, and the latter corresponds to the outward normal of the surface centred in e. This is valid for an orthogonal mesh, composed by orthogonal elements (Ferziger & Peric 2002). Otherwise, the deferred correction (Böhmer et al. 1984) is used via the formulation proposed by Muzaferija (1994). A discussion of its implementation can be found in Ferziger & Peric (2002) or in Rosti (2016). Extra care has been taken to generate the current mesh embracing the foil in order to avoid strongly non-orthogonal cells (more details are given in section 3.5), but the correction has been implemented to reduce the numerical error in specific mesh locations and to allow for a relaxation of the resolution, where possible. Note that this correction slightly reduces the second-order accuracy of the present method as assessed by Rosti (2016).

3.3.3 Numerical boundary conditions

The flow condition to be simulated is that of the infinite wing, i.e. indefinitely extended wing in the spanwise direction. Due to the finite size of the computational box, a periodic boundary condition is enforced at the virtual surfaces bounding the box in the spanwise direction. This is a common practice for the numerical simulations of infinite wings, adopted by many authors (e.g. Jones et al. (2008), Hain et al. (2009)).

The $C-$type mesh introduces an additional numerical boundary as already mentioned in section 3.3.2 at the so called virtual wake plane. Such a mesh assembly is required to generate a structured mesh surrounding the curvilinear foil. The flow field on the virtual wake plane is not known and is part of the flow prediction. However, the virtual plane is numerically constituted by two separate but coinciding planes using the structured character

of the mesh. On these two planes, a numerical boundary condition of continuity of the flow field is enforced across the virtual wake plane.

On the outer computational boundary, an inlet/outlet condition is set. To determine which portion of the boundary in all the parallel chord planes (or k planes in the discretised space) is either an inlet or an outlet, a local spanwise average of the fluid velocity is evaluated in a tiny region close to the boundary at each time step. When the averaged flow direction points outward, the corresponding portion of the boundary is assumed to be an outlet, and is treated using a convective *non-reflective* boundary condition. Conversely, if the flow direction is directed inward, the corresponding boundary surface is considered to be an inlet, and a Dirichlet type condition based on an irrotational flow approximation is employed. In particular, the value to be assigned to the velocity is determined by solving a companion potential equation (similar to that formulated in equation 3.8) discretised via a Hess-Smith panel method (Hess & Smith 1967). The boundary condition for the potential equation is the free stream condition, i.e.

$$
\begin{cases}
U_\infty = |\vec{Q}_\infty| cos(\alpha) cos(\Lambda) \\
V_\infty = |\vec{Q}_\infty| sin(\alpha) cos(\Lambda) \\
W_\infty = |\vec{Q}_\infty| sin(\Lambda)
\end{cases}
\tag{3.19}
$$

where α and Λ are the specific incidence and sweep for each of the wing configuration simulated. Once the potential flow is solved, the resulting flow condition is enforced on the inlet portion of the outer boundary as a Dirichlet condition. A sketch graphically showing the outer boundary treatment is shown in figure 3.5. The adoption of this adaptive inlet/outlet condition based on a potential flow solution allows to consider more compact $x - y$ domains without compromising the quality of the predicted solution Rosti (2016).

As can be noticed, the free stream condition is modified by the introduction of a constant spanwise velocity (dependent on the value of the sweep) to model the swept wing configuration.

At the foil wall is implemented the no-slip and impermeability boundary conditions as formulated in section 3.2.1.
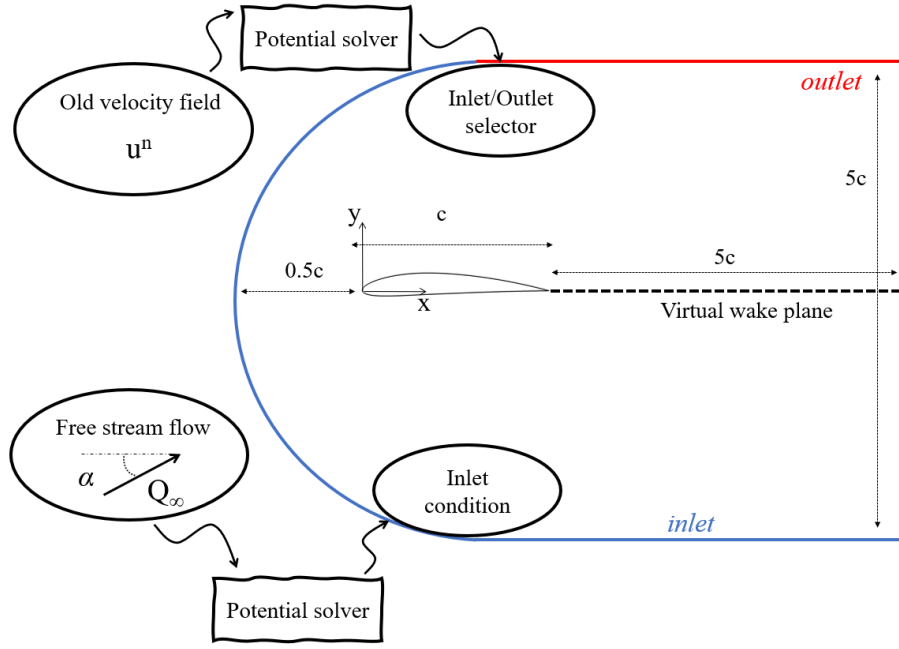
Figure 3.5: Sketch graphically showing the outer boundary treatment and computational dimensions.

3.3.4 Solution of the discretised equations

Substituting all the approximation schemes in equations 3.13, the solving discretised equations for the unknowns $\tilde{u}_i^*$ and $\tilde{\phi}$ of the cell (i, j, k) become

Prediction step (3.20)

$$a_S^I \tilde{u}_i^*(i, j - 1, k) + a_P^I \tilde{u}_i^*(i, j, k) + a_N^I \tilde{u}_i^*(i, j + 1, k) = b^I(i, j, k)$$

Projection step (3.21)

$$a_B^{II} \tilde{\phi}(i, j, k - 1) + a_W^{II} \tilde{\phi}(i - 1, j, k) + a_S^{II} \tilde{\phi}(i, j - 1, k) + a_P^{II} \tilde{\phi}(i, j, k) +$$
$$+ a_T^{II} \tilde{\phi}(i, j, k + 1) + a_N^{II} \tilde{\phi}(i, j + 1, k) + a_E^{II} \tilde{\phi}(i + 1, j, k) = b^{II}(i, j, k)$$

where the known coefficients $a_P^I \dots$, $a_P^{II} \dots$ have been named accordingly to the computational node they are referred to; b^I and b^{II} are the known right-hand-side of the equations. The superscript $\cdot^I$ has been used for any coefficient of the prediction step, while $\cdot^{II}$ for those of the projection step. Conversely with respect to the coefficients, the indices notation is kept for the unknowns. This choice is made to make an easier connection with the matrix notation that will follow when assembling the discretised equations from the cells.

When all the cells are considered at the same time, the problem can be described as the search for the solutions of two separate linear systems (one for the prediction step and one for the correction step) in the discrete unknowns $\tilde{u}_i^*(i, j, k)$ and $\tilde{\phi}(i, j, k)$ with $i = 1 \dots N_i$, $j =$

$1 \ldots N_j$ and $k = 1 \ldots N_k$. The problem can be written using the matrices formulation. To this aim, each of the discrete unknowns and right-hand-side terms of the equations for all the cells are organised in two vectors. The resulting size of each vector is $[N_i N_j N_k \times 1]$, while that of the matrices (A) containing the coefficients of the unknowns is $[N_i N_j N_k \times N_i N_j N_k]$. The linear systems can be formally written as,

$$\text{Prediction step} \quad [A^I]\{\tilde{u}^*\} = \{b^I\} \tag{3.22}$$

$$\text{Projection step} \quad [A^{II}]\{\tilde{\phi}\} = \{b^{II}\} \tag{3.23}$$

where $[\cdot]$ has been used to indicate a matrix and $\{\cdot\}$ for a vector. The boundary condition are simply enforced modifying specific rows of the matrices corresponding to the boundaries locations (Ferziger & Peric 2002).

The two matrices (A^I and A^{II}) are different and the corresponding linear systems require different computational power to be solved. A^I is quasi-three-diagonal. The partially implicit formulation used only along the j direction would imply a three-diagonal matrix for each sector of the matrix representing the solution into the computational mesh along a $j = 1, \ldots, N_j$ cell-column for all i and k locations. The j columns would be totally independent to each other since no implicit formulation is used along i and k. This is valid for those j-columns starting from the wing surface. In the wake this is not valid, due to the boundary condition of continuity across the virtual wake plane. The j-column starting from the virtual wake and extending below it is tied to the base cell of the j-column starting from the same location on the virtual wake plane but extending above it, and vice versa. Since the two spatially-adjacent j-columns (below and above the virtual wake plane) do not correspond to adjacent sectors in the A^I matrix, the consequence is the appearance of some sparse values in the matrix. The number of sparse values is proportional to the number of i points used to discretise the virtual wake plane. To avoid the factorisation of a sparse matrix, which would be computationally more expensive (Quarteroni et al. 2014), the solution of the linear system linked to the A^I matrix is re-arranged in blocks: one block is constituted by those values corresponding to the j-columns starting from the aerofoil surface in the computational mesh (number of elements in i and k referred as N_i^{FOIL} and N_k^{FOIL}); the second is that formed by those columns having their base on the virtual wake plane (number of elements in i and k referred as N_i^{WAKE} and N_k^{WAKE}). The former block is composed by $N_i^{FOIL} N_k^{FOIL}$ three-diagonal matrices of size $[N_j \times N_j]$ and it is factorised without further elaborations via the Thomas factorisation (Quarteroni et al. 2014). The latter is re-arranged in order to have

38

numerically contiguous columns across the virtual wake plane and allow for a faster factori-sation. Thanks to the re-arrangement, the block initially constituted by $N_i^{WAKE} N_k^{WAKE}$ sparse matrices of size $[N_j \times N_j]$ results composed by $1/2 N_i^{WAKE} N_k^{WAKE}$ three-diagonal matrices of size $[2N_j \times 2N_j]$. The block is ultimately solved via the Thomas factorisation (Quarteroni et al. 2014).

A^{II} is quasi-seven-diagonal due to the implicit formulation in all the three directions (consequence of the elliptic character of the Poisson equation in the projection step) and the virtual wake plane treatment. It represents the most expensive part of the computation. To cut down on the computational cost, the Fourier expansion along the spanwise, periodic direction is deployed.

3.3.5 Fourier expansion deployed

To ease the computational cost required to obtain the solution of the linear system represent-ing the projection step, the discrete Fourier expansion in the spanwise, periodic direction is adopted. The expansion, using J for the imaginary unit and $\{\hat{\cdot}\}$ to refer to a quantity in the frequency domain, reads as

$$\tilde{\phi}(i,j,k) = \frac{1}{N_k} \sum_{i_k=0}^{N_k-1} \hat{\tilde{\phi}}_{i_k}(i,j) e^{\frac{2\pi J i_k k}{N_k}} \tag{3.24}$$

Examples of the effect of the Fourier expansion introduction to the expression of the com-putational unknowns are provided:

$$\tilde{\phi}(i,j,k+1) = \frac{1}{N_k} \sum_{i_k=0}^{N_k-1} \hat{\tilde{\phi}}_{i_k}(i,j) e^{\frac{2\pi J i_k (k+1)}{N_k}} \qquad = \frac{1}{N_k} \sum_{i_k=0}^{N_k-1} \hat{\tilde{\phi}}_{i_k}(i,j) e^{\frac{2\pi J i_k k}{N_k}} e^{\frac{2\pi J i_k}{N_k}}$$

$$\tilde{\phi}(i+1,j,k) = \frac{1}{N_k} \sum_{i_k=0}^{N_k-1} \hat{\tilde{\phi}}_{i_k}(i+1,j) e^{\frac{2\pi J i_k k}{N_k}} \tag{3.25}$$

$$\tilde{\phi}(i,j+1,k) = \frac{1}{N_k} \sum_{i_k=0}^{N_k-1} \hat{\tilde{\phi}}_{i_k}(i,j+1) e^{\frac{2\pi J i_k k}{N_k}} \, .$$

When the Fourier transform is introduced in equation 3.21, representing the projection step of the cell (i,j,k), the spatially-dependent ϕ unknowns along the k direction can be

reduced to an independent summation of unknowns in the wavenumber space, i.e.

$$
\begin{aligned}
a_T^{II}\tilde{\phi}(i,j,k+1) + a_P^{II}\tilde{\phi}(i,j,k) &+ a_B^{II}\tilde{\phi}(i,j,k-1) = \\
&= a_T^{II}\frac{1}{N_k}\sum_{i_k=0}^{N_k-1}\hat{\tilde{\phi}}_{i_k}(i,j)e^{\frac{2\pi J i_k k}{N_k}}e^{\frac{2\pi J i_k}{N_k}} + a_P^{II}\frac{1}{N_k}\sum_{i_k=0}^{N_k-1}\hat{\tilde{\phi}}_{i_k}(i,j)e^{\frac{2\pi J i_k k}{N_k}} + \\
&+ a_B^{II}\frac{1}{N_k}\sum_{i_k=0}^{N_k-1}\hat{\tilde{\phi}}_{i_k}(i,j)e^{\frac{2\pi J i_k k}{N_k}}e^{-\frac{2\pi J i_k}{N_k}} = \\
&= \frac{1}{N_k}\sum_{i_k=0}^{N_k-1}\hat{\tilde{\phi}}_{i_k}(i,j)e^{\frac{2\pi J i_k k}{N_k}}\left(a_T^{II}e^{\frac{2\pi J i_k}{N_k}} + a_P^{II} + a_B^{II}e^{-\frac{2\pi J i_k}{N_k}}\right) = \\
&= \frac{1}{N_k}\sum_{i_k=0}^{N_k-1}\hat{\tilde{\phi}}_{i_k}(i,j)e^{\frac{2\pi J i_k k}{N_k}}\left(a_P^{II} + 2a_T^{II}\cos(\frac{2\pi i_k}{N_k})\right).
\end{aligned}
\tag{3.26}
$$

Note that $a_T^{II} = a_B^{II}$ due to uniform mesh in the k direction, therefore $\left(a_P^{II} + 2a_T^{II}\cos(\frac{2\pi i_k}{N_k})\right)$ is a real number.

When the same elaboration is applied for all the cells of the mesh, the global system of the projection step can be assembled again using the matrix formulation. The quasi-seven-diagonal linear system is transformed in N_k independent quasi-five-diagonal linear systems for all the wavenumbers $i_k = 0 \dots N_k - 1$ in the wavenumber space.

3.3.6 Parallel computing implementation

When hundreds of millions of computational nodes are used to discretise the computational domain (as in the present case), the computational power and fast-access-memory required for the solution of the projection step cannot be provided by a single computer. Therefore the code is parallelised using the MPI message passing protocol (Forum 1994) and run on a TIER-1 high performance computational machine (HPC) with distributed memory and ultraband communication. The technique of the domain decomposition is deployed in the i direction and each block is assigned to a different computational core in the parallel infrastructure. A typical parallel configuration to carry out the three-dimensional, high-fidelity flow prediction of the present investigation employs hundreds of computational cores. The contiguous blocks exchange planes at the interfaces, which are needed to compute convective and viscous derivatives with a second order finite volume formulation. Communication between neighbouring blocks is handled by means of MPI Sendrecv directives by exploiting the topological connectivity, which is directly implemented with MPI.

The parallelisation implies additional complications when the implementation of both

the prediction and projection steps is considered. In the prediction step, an efficient communication between the cores across the domain blocks on the virtual wake plane is required. This as a consequence of the continuity boundary condition enforced between the two sides of the plane. In *SUSA*, the linear systems corresponding to the j-columns in the aerofoil wake are reduced before the MPI communication is established in order to lower the number of information to be exchanged in the communication. In the projection, the elliptic character of the Poisson equation poses a serious threat to the parallel computation performances. A classic implementation would use each computational core to solve each of the independent quasi-five-diagonal system associated with a specific wavenumber. This method implies an MPI communication across all the decomposed blocks to assign a global problem for each wavenumber (representing the discretisation in the i and j direction of whole computational domain) to each core. The communication would pose serious scalability issues when the number of core of the distributed machine is in the order of the hundreds, even when ultraband communication is available. The actual implementation does not adopt this methodology. Instead, the parallel data structure of the N_k independent, quasi-five-diagonal systems from each i block is passed to the PETSc library (Balay et al. 2019). The library directly deals with the solution of the global, spectral Poisson problem using high performances methods (Krylov methods) implemented ad-hoc for the solution of spectral elliptic problems with distributed memory computing architectures (Balay et al. 2019). In particular, the iterative Biconjugate Gradient Stabilized (BiCGStab) method is used during the current investigation. The scalability of the Krylov solver with increasingly larger parallel machines strongly depends on the preconditioner that is selected among the suite offered by PETSc (Crone & Munday 2014). In particular, the *Euclid* preconditioner (Balay et al. 2019) is found to be the most beneficial for the parallel computations carried out by the present investigation.

3.4 Flow evolution and statistically steady state

When the flow predictions are computed, an initial transient evolution and a dynamic equilibrium are observed for each prediction. The initial transient can be representative of a fictitious dynamic (e.g. numerical transient from an inviscid initial condition to a viscous flow condition or from a two-dimensional initial condition to a three-dimensional flow) or a physical dynamic (e.g. transient from one incidence condition to another). In any case, for each steady boundary and flow conditions (i.e. Reynolds number, angle of attack, sweep)
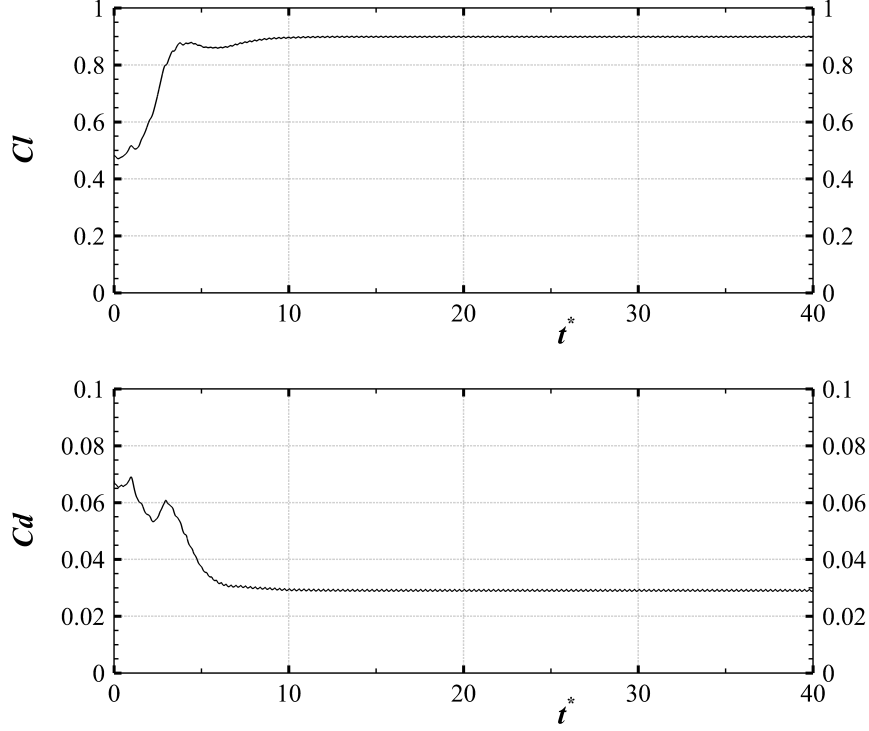
Figure 3.6: Time evolution of the wing integral performances during a two-dimensional flow prediction. (Top) C_l; (Bottom) C_d.

considered, each flow prediction is observed to evolve from the initial transient to a dynamic equilibrium state. The equilibrium state allows to define a statistically steady state of the flow condition, which implies a statistically steady flight condition of the wing. Figure 3.6 shows a typical two-dimensional flow prediction by looking at the time evolution of the wing integral performances, namely the coefficient of lift C_l and that of total drag C_d. The initial transient can be seen until $t^* = tQ_\infty/C \simeq 10$ (the superscript $\{\cdot\}^*$ is used to indicate a quantity made non dimensional using Q_∞ and C). After, the dynamic system can be considered to be statistically steady.

The transient evolution of the flow condition is not of interest during the present investigation, which provides a swept/unswept comparison within the statistically steady state framework. All the statistical results that will be presented refer to the flow field once the statistically steady state is reached. Whenever a time average is computed, it is intended for a time window outside the initial transient.

A typical flow prediction requires roughly a day to march for a time interval $\Delta t^* = \Delta t Q_\infty/C \simeq 1$, using a parallel computing infrastructure composed by hundreds of cores. The daily nominal cost of a typical flow prediction, as estimated by the *ARCHER* calculator (HPC mostly used for the current investigation, ARCHER (2020)), is about £100.

42

Therefore, shortening any transient solution can be enormously beneficial to the total computational time required for the simulations. For this reason, a preliminary two-dimensional flow condition of the unswept wing at 5° incidence is carried out using the potential flow as initial condition. The resulting flow field is subsequently used as initial condition for the corresponding three-dimensional simulation. Once the statistically steady state is achieved, the flow field is used as initial condition for all the other cases simulated (swept wing and 10° incidence case). Whilst the adopted strategy, an initial transient with a time scale $\Delta t^* \sim O(5)$ is observed (but not considered) for all the simulated cases.

3.5   Grid refinement study

To assure the independence of the resolved scales from the computational grid used to discretise the domain, a grid refinement study for the flow case of an infinite straight wing with a spanwise domain extension of $20\%C$ has been carried out. This consideration becomes particularly stringent when a laminar free-stream condition is specified as this condition may lead to unsteady separation and a later turbulent transition of the shear layer along the aerofoil, as mentioned in section 2.3. This phenomena set local, unsteady gradients that are difficult to estimate a-priori. In these conditions, no universal or accepted empirical criteria on the mesh requirements are available and an *iterative* grid refinement must be unavoidably carried out.

A starting mesh has been selected following the guidelines in Rosti (2016) and then a roughly 50% finer grid (in j and k directions) has been generated to allow for a comparison. As a target guideline, the aspect ratio of the mesh cells where the flow recirculation was expected has been kept close to 1. In this location the shear stress seems not to have a preferential direction, due to the chaotic flow pattern of the three-dimensional vortices breakdown to turbulence (Yarusevych et al. 2009). Not having achieved satisfactory convergence (difference between the time and spanwise average of the flow fields smaller than 10%, especially for the velocity profiles), another grid has been generated. The latter has been refined mostly in the area where the separating and recirculating flow takes place. Due to the structured character of the mesh, the refinement of a specific domain area in the j direction implies the same refinement everywhere in the domain for that j layer of cells. A smooth variation of spacing is assured between these differently refined area. For the j layer coinciding with the aerofoil wall, the same spacing in the i direction is used for the adjacent elements at the trailing edge (one per each side of the foil and one per each side of the virtual
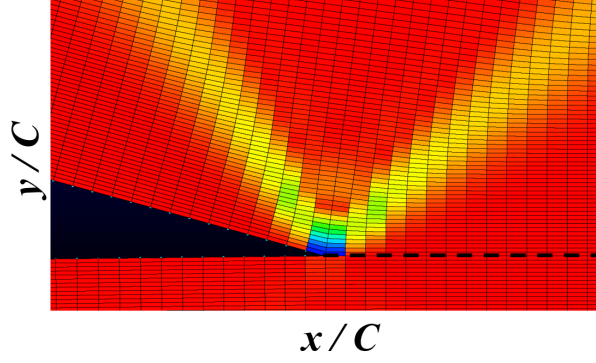
Figure 3.7: Distribution of the minimum included angle between 90° (red) and 82° (blue) of the quasi-orthogonal mesh elements nearby the trailing edge. The virtual wake plane is indicated with a thick dashed line.

	Ni	Nj	Nk
Coarse	2773	191	87
Medium	2881	279	165
Fine	3361	379	301

Table 3.1: Number of computational nodes in the three directions for the meshes considered during the grid refinement study.

wake plane). The stretching along the i and j directions is kept below 2% everywhere in the close surrounding of the foil (proximity in the order of the chord size, formally $\sim O(C)$), but for a few elements above the trailing edge. In this location, due to the virtual wake plane angle, the stretching for some elements increases to almost 12% in the i direction and 4% in the j direction. In general, the spacing in the i direction on the upper side of the foil is smaller than that on the bottom side, since the highest velocity gradients will be shown to appear above the wing. The spacing in the i direction is smoothly distributed in order to avoid any sharp discontinuity anywhere along the foil, on the virtual wake plane or at the interface between the two. To achieve a structured mesh around the curvilinear foil geometry composed by quasi-orthogonal elements, as required for the present numerical formulation, the minimum included angle of each element has been kept everywhere greater than 85° (note that all the included angles of an element in an orthogonal mesh are 90°). The elements on top of the trailing edge, adjacent to it, are exceptional and constrained by the foil geometry. The minimum included angle decreases as low as 82° for these elements. Figure 3.7 shows the distribution of the minimum included angle of the elements nearby the trailing edge.

The number of computational nodes for the three meshes (referred as Coarse, Medium and Fine) can be found in table 3.1. In particular, the number of points on the upper foil side for the *Coarse* mesh is 616, the *Medium* mesh is 653 and for the *Fine* mesh is 1002. On the bottom side, 444 points are used for the *Coarse* mesh, 466 points are used for the *Medium*

mesh, while 528 for the *Fine* mesh.

The preliminary mesh design process was carried out by using as a metric the convergence of mean velocity profiles $< u_{tg} >_{z,t} (x, y)$ (the notation $< \cdot >_{z,t}$ is used to indicate the time and spanwise average operation) and of the fluctuating kinetic energy production $< \mathcal{P} >_{z,t} (x, y)$ (with $\mathcal{P} = u_i' u_j' \partial < u_i >_z / \partial x_j$ where u_i' is the perturbation velocity field and $< u_i >_z$ the spanwise averaged one). For the time average, the evolution of the system in a statistical steady state (defined in section 3.4) has been considered using a time window of over $30 Q_\infty / C$ time units, sampling it with a frequency of $f = 2000 C / Q_\infty$. The comparison in arbitrary locations along the chord and into the wake of mean wall-tangent velocity profile resulting from the computation with different meshes is shown in figure 3.8. The almost perfect match of the profiles with the *Medium* and *Fine* meshes can be appreciated, while a clear mismatch is observed when the *Coarse* grid is adopted. Quantitatively, considering the profiles extracted at the chord location $x/C = 0.30$, the velocity difference at the wall normal location $n/C = 0.01$ (n being the normal to the wall direction) is 12.5% between *Coarse* and *Medium* (having defined the difference as $|u^{Medium} - u^{Coarse}|/|u^{Coarse}|$) and 6% between *Medium* and *Fine* (having defined the difference as $|u^{Fine} - u^{Medium}|/|u^{Medium}|$). The comparison of the fluctuating kinetic energy production profiles obtained with different meshes is presented in figure 3.9. A good agreement is found between the profiles obtained with the *Medium* and the *Fine* meshes, while the profile obtained with the *Coarse* grid presents several differences. Not only the peak value appears wrongly estimated, but also its vertical location. Considering the profiles extracted at the location $x/C = 0.55$, the difference of the predicted wall normal location of the fluctuating kinetic energy production is 11% between *Coarse* and *Medium* and 3% between *Medium* and *Fine*. Hence, the mesh *Medium* has been adopted to carry out the present investigation.
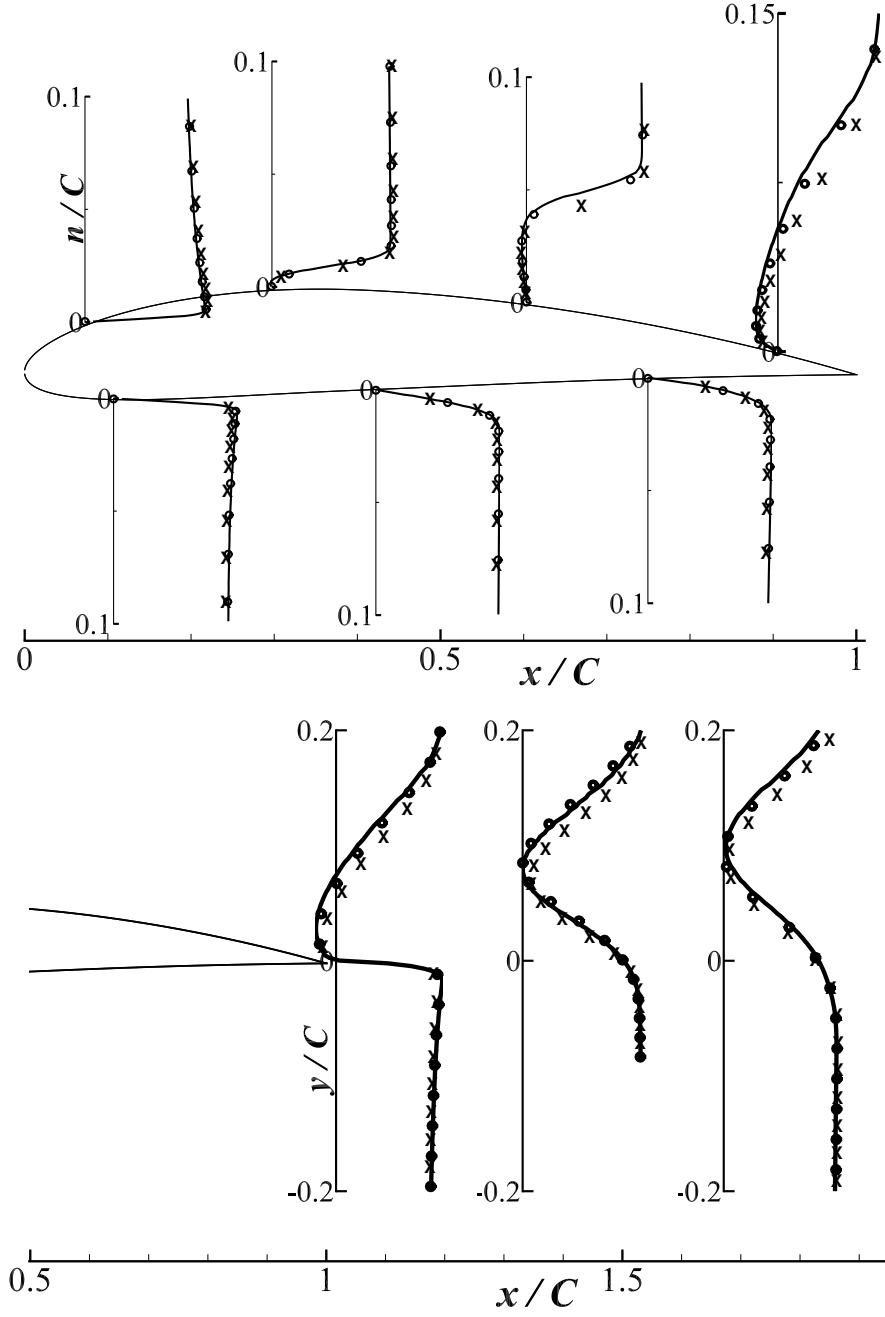
Figure 3.8: Profiles of $< u_{tg} >_{z,t} /Q_\infty$ extracted along the aerofoil (Top) and into the wake (Bottom) for the three meshes compared. $\times$ for the *Coarse* mesh, $\circ$ for the *Middle* and solid line for the fine one. Flow condition: $Re_C = 50 \times 10^3, \alpha = 5^o, \Lambda = 0^o$, laminar inlet.
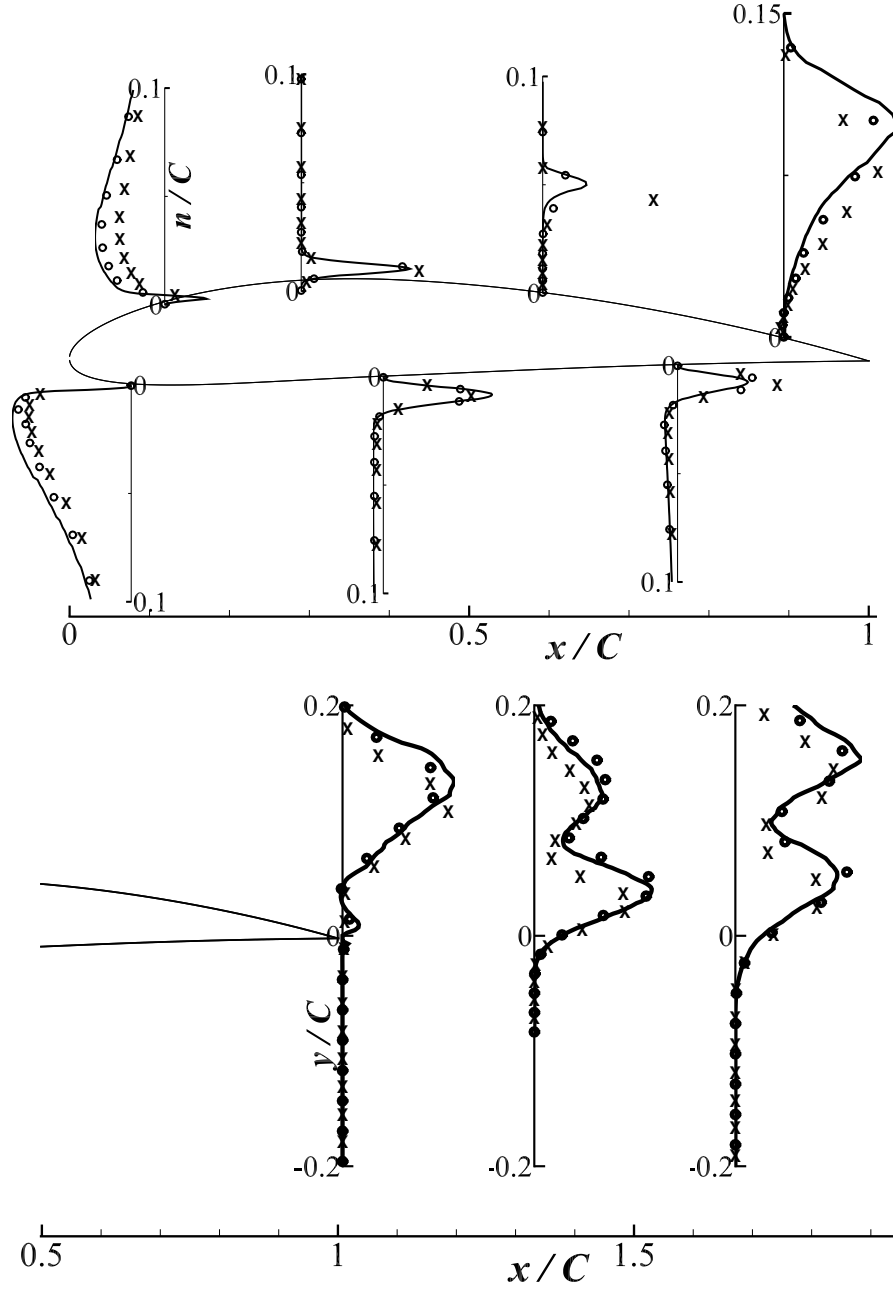
Figure 3.9: Profiles of $< \mathcal{P} >_{z,t} C/Q_\infty^3$ extracted along the aerofoil (Top) and into the wake (Bottom) for the three meshes compared. Legend as in figure 3.8

3.6 Extension of the computational domain study

Aiming to numerically simulate flow conditions of infinite wings, an analysis on the impact of the spanwise size of the computational domain has been carried out. Previous numerical studies on similar flow conditions (i.e. flow around infinite straight or swept back wings simulated via LES or DNS) lack a clear rationale on the selected domain size. Some have simulated the transitional and turbulent flows past an infinite wing using a spanwise domain extension of $0.1C$ (Vinuesa et al. (2018), flow at $Re_c = 100 \times 10^3$, tripped), some have used $0.2C$ (Uranga et al. (2011), flow at $Re_c = 60 \times 10^3$; Vinuesa et al. (2018), flow at $Re_c = 200 \times 10^3$, tripped). Others have used a larger domain size of $0.4C$ (De Tullio & Sandham (2017), flow at $Re_c = 50 \times 10^3$).

Therefore, it has been preferred to conduct a preliminary assessment rather than relying on parameters suggested by other authors before undertaking the investigation that is the object of the thesis. The spanwise domain size has been assessed by considering the variations of the statistical features of the flow field. In particular, the results obtained when considering two infinite straight wings with a spanwise extension of $0.2C$ and $0.4C$ have been considered within an incoming laminar flow frame. The time average has been collected through $50 Q_\infty/C$ time units, after the condition of statistically steady flow (as defined in section 3.4) has been achieved. Figure 3.10 shows a comparison between the two cases in terms of the mean velocity $< u_{tg} >_{z,t}$ (the notation $< \cdot >_{z,t}$ is used to indicate the time and spanwise average operation). A satisfying match between the two cases is observed both along the aerofoil and in the wake. Quantitatively, when considering the profiles extracted at the chord location $x/C = 0.30$, the velocity difference at the wall normal location $n/C = 0.01$ (n being the normal to the wall direction) is 5.5% between the two simulated cases with different spanwise extension. Differently, when considering $< \mathcal{P} >_{z,t} (x, y)$ (shown in figure 3.11) and the turbulent dissipation $< \varepsilon >_{z,t} (x, y)$ (where $\varepsilon = 1/Re_c \partial u_i'/\partial x_j \partial u_i'/\partial x_j$, shown in figure 3.12), the effect of the spanwise size of the domain becomes clear. In particular, in the narrow case $< \mathcal{P} >_{z,t}$ seems to be over-predicted along the foil surface, whilst almost uninfluenced by the domain size in the wake region. Considering the profiles extracted at the location $x/C = 0.55$, the difference of the predicted peak of the fluctuating kinetic energy production is overestimated by 40% at the smaller computational box. Turbulence dissipation in the narrower domain presents a complementary behaviour with a similar distribution on the wing and a short prediction in the wake. When the profiles extracted at the location $x/C = 1.25$ are quantitatively compared, the difference at the vertical location $y/C = 0.08$

is found to be 22%, underestimated by the narrower computational box. A vertical shift in the profiles of both $< \mathcal{P} >_{z,t}$ and $< \varepsilon >_{z,t}$ is also noticed in the rear part of the suction side when comparing the differently extended boxes. This implies a wrong estimation of the shear stress layer location by the narrower box.

In view of the non-negligible difference in the distribution of the production and dissipation of the turbulent kinetic energy, all the flow field predictions that will be presented were obtained considering the wider spanwise domain extension (i.e. $0.4C$). This domain configuration increases the level of confidence in the conclusions that arise when comparing swept vs unswept wings. Due to the larger extension, the number of computational nodes in the spanwise direction for the mesh (*Medium* as defined in section 3.5) used throughout the investigation object of the thesis becomes $N_k = 330$. The ultimate size of the mesh considered for the swept/unswept flow comparison is therefore $N_i = 2881$, $N_j = 279$ and $N_k = 330$. The number of resulting computational nodes discretising the computational flow domain is $N_{tot} \approx 250 \times 10^6$.

The present investigation did not consider a larger computational box due to the even more demanding computational cost that would be faced. Therefore, a spanwise extension of $0.4C$ has to be considered a minimum requirement for the numerical investigation of the flow scenarios considered here, but may not be a sufficient extension when a higher order of accuracy is targeted.
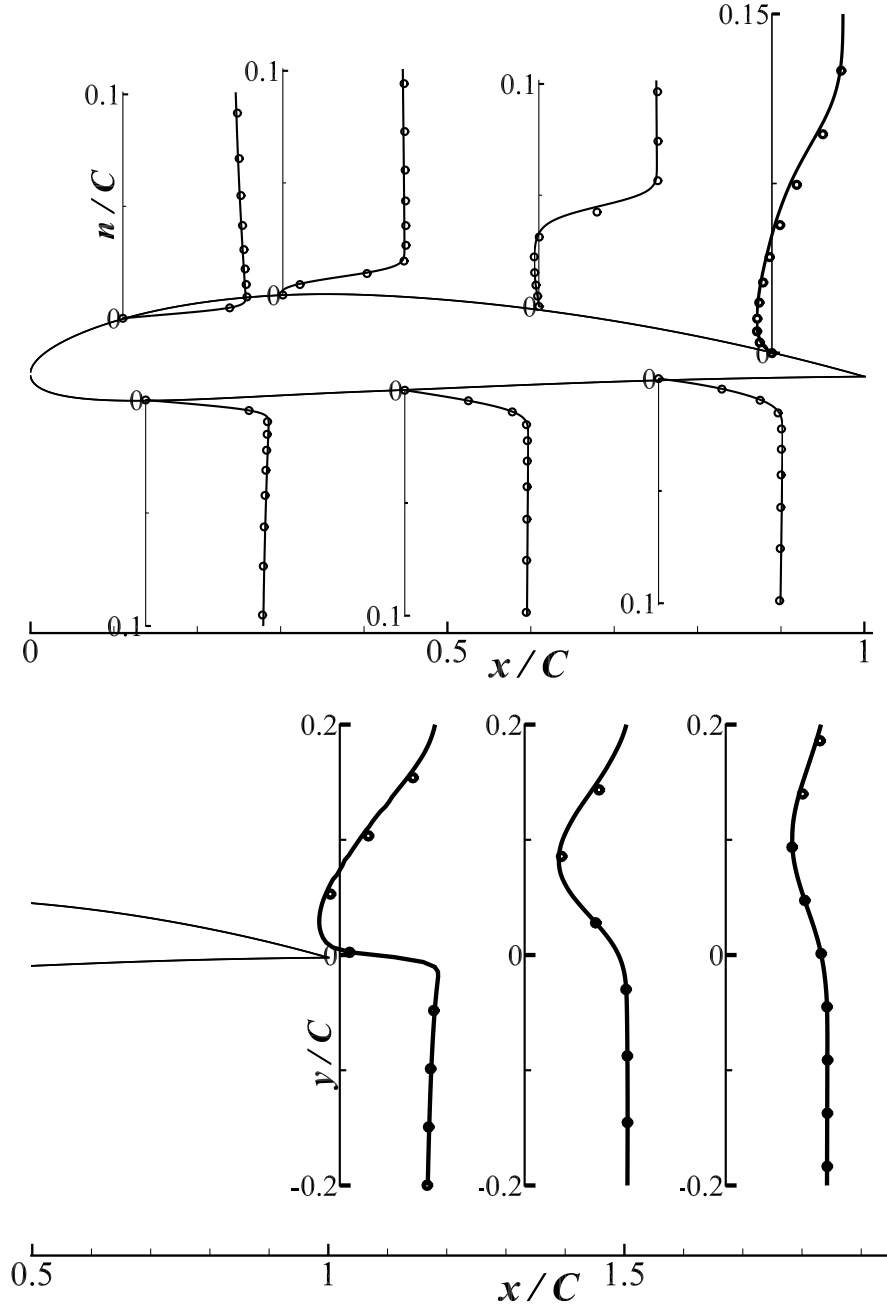
Figure 3.10: Profiles of $< u_{tg} >_{z,t} /Q_\infty$ extracted along the aerofoil (Top) and into the wake (Bottom) for the 0.2*C* and 0.4*C* spanwise extended domain. ∘ corresponds to the 0.2*C* case, while the solid line is the 0.4*C* case. Flow condition: $Re_C = 50 \times 10^3, \alpha = 5^o, \Lambda = 0^o$, laminar inlet.
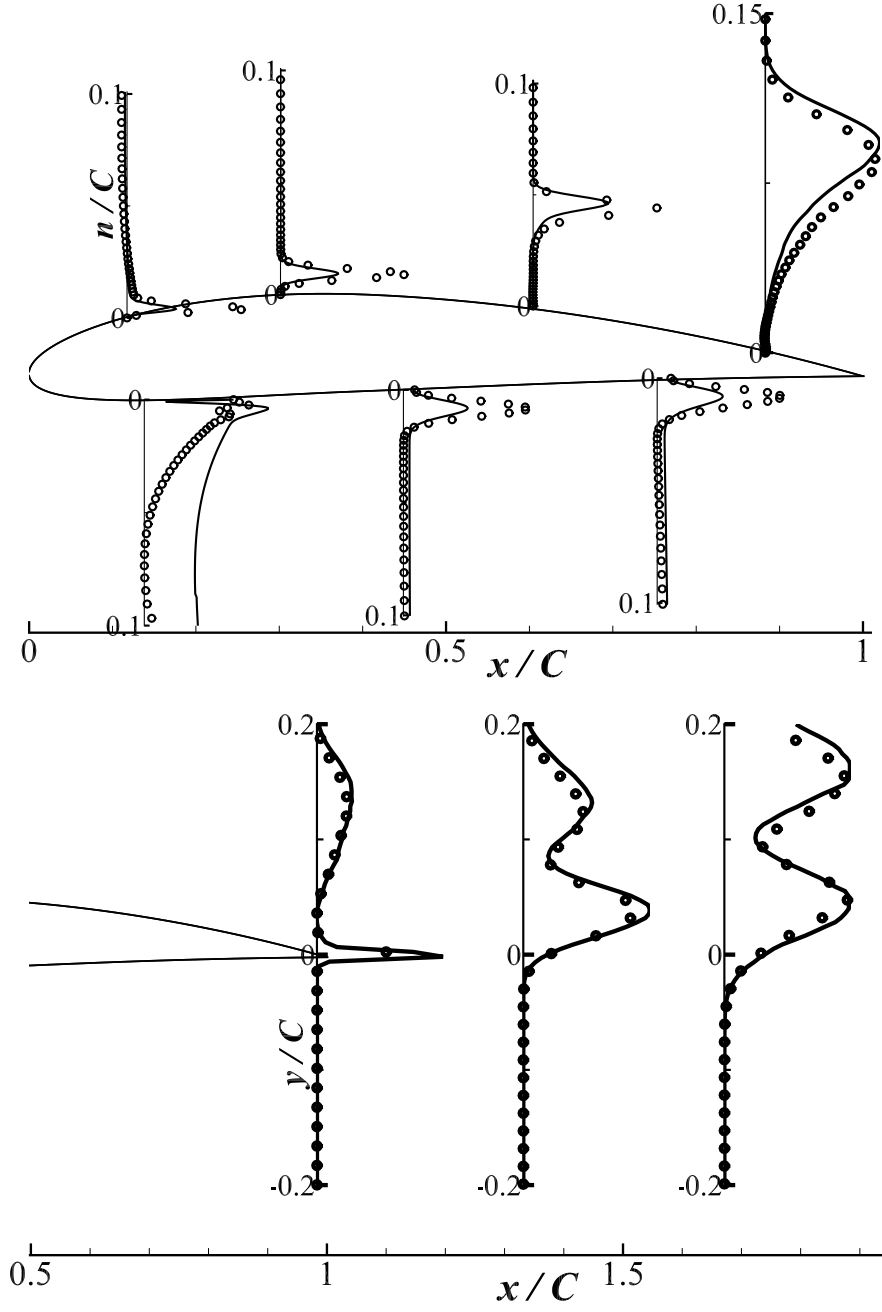
Figure 3.11: Profiles of $< \mathcal{P} >_{z,t} C/Q_\infty^3$ extracted along the aerofoil (Top) and into the wake (Bottom) for the $0.2C$ and $0.4C$ spanwise extended domain. Flow condition and symbols as in figure 3.10.
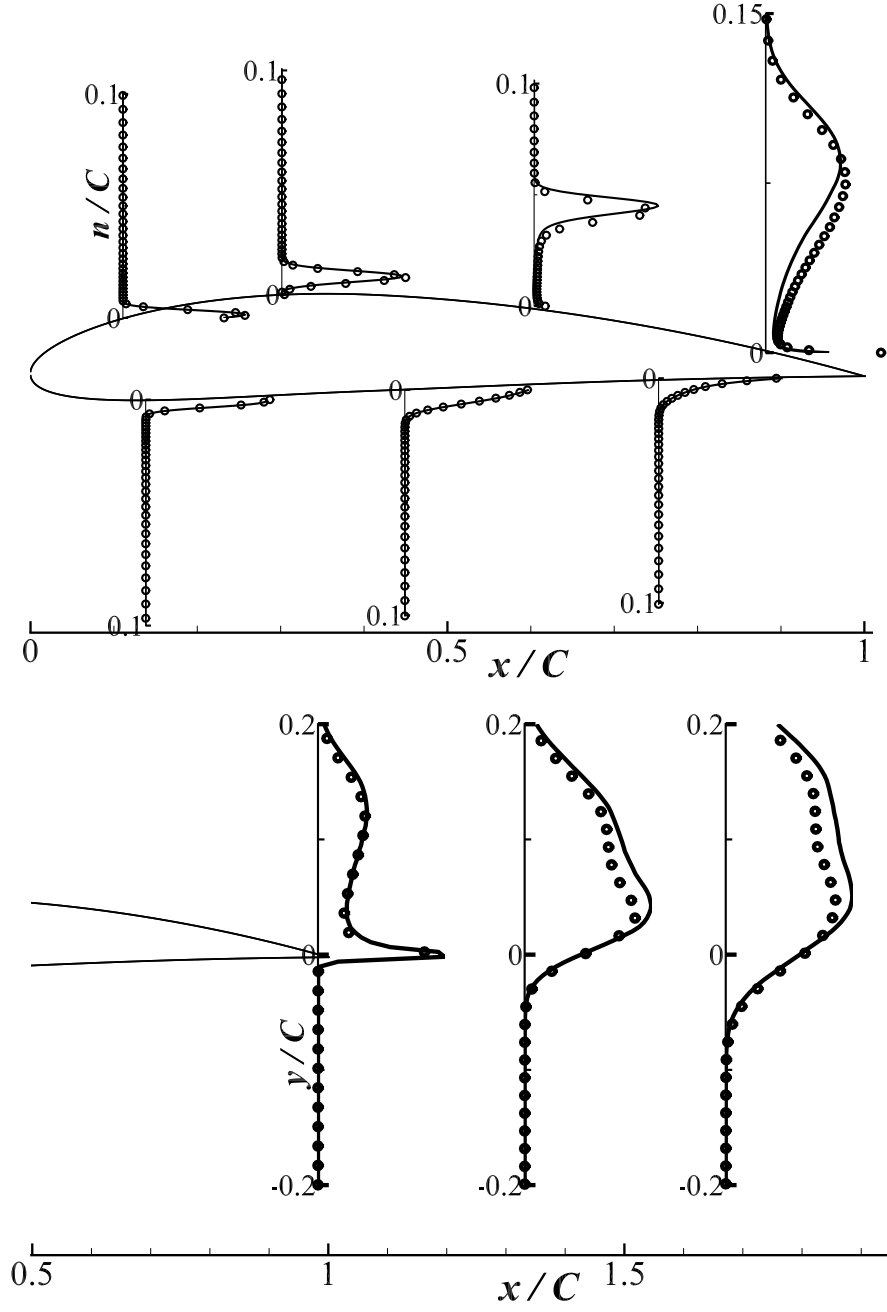
Figure 3.12: Profiles of $< \varepsilon >_{z,t} C^2/Q_\infty^2$ extracted along the aerofoil (Top) and into the wake (Bottom) for the 0.2C and 0.4C spanwise extended domain. Flow condition and symbols as in figure 3.10.

3.7 Inflow configurations

For the present comparison between swept and unswept wing configurations, two scenarios of the free stream flow approaching the wing have been considered to simulate the laminar and the turbulent boundary layer separation.

To investigate a laminar boundary layer separation on the wing at incidence, an undisturbed inlet has been considered similarly as into the literature (e.g. Jones et al. (2008), Yarusevych et al. (2009)). Within this frame, the $NACA - 4412$ at an incidence of $\alpha = 5^o$ will be shown in section 4.1 to naturally host a laminar separation on the suction side, independent of the sweep.

At the moderate Reynolds number considered here, the boundary layer has been tripped using strong perturbations in the free stream. This allows to force an early transition and to form a developing turbulent boundary layer on the verge of separation on the wing. This approach allows to mimic higher Reynolds flow turbulent separation with a limited numerical cost. The tripping approach adopted here presents some similarities to that investigated by Brandt et al. (2004) for the case of the transition to turbulence of a Blasius profile on a flat plate. Specific flow perturbations (representative of a free stream turbulence, FST) have been injected upstream of the wing to trigger a developing turbulent boundary layer from a location nearby the wing leading edge (see section 5.1). The superimposed disturbances may trigger the boundary layer transition through a by-pass mechanism (Morkovin 1993) governed by the Klebanoff modes (Schlatter et al. 2008), as it will be further discussed in section 5.1.3. The characteristics of the perturbations are discussed with further detail in the following section. A detailed comparison between the flow fields with and without the injected perturbation field will be presented among the results in section 5.1. Two static incidences have been separately tested for both the wing configurations, namely $\alpha = 5^o$ and $\alpha = 10^o$. The selection of the two loading conditions have allowed for a wider characterisation of the turbulent separation mechanism, thanks to the consequently different amount of flow detachment on the wing suction side.

3.7.1 Free stream turbulence generation and injection

As already mentioned, a turbulent boundary layer developing on the wing at the considered low Reynolds number is achieved by superimposing to the incoming laminar flow a turbulence field. The latter is obtained through an independent DNS of grid generated turbulence performed prior to the computations of the wing fields. The strong incoming disturbances
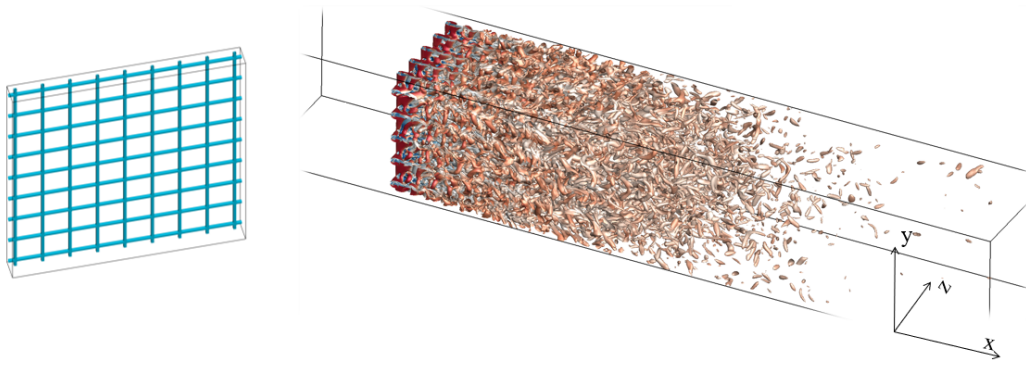
Figure 3.13: Illustrations of the virtual net (Left) and the flow structures generated when the unidirectional flow goes past it (Right). The flow is aligned with the x direction. By the courtesy of Dr. Muhammad Farrukh Shahab who developed the baseline method to generate the grid turbulence in *SUSA* and provided the figure.

trigger the initially laminar boundary layer to turbulence in the proximity of the leading edge by the by-pass mechanism (Morkovin 1993). The perturbations mimic the presence of isotropic turbulence (Pope 2000) behind a uniform grid when a uniform unidirectional flow condition crossing an orthogonal indefinitely-extended virtual net is considered. Figure 3.13 shows a representative illustration of the virtual grid and the flow structures generated when the unidirectional flow goes past it (the flow structures are identified by the Q-criterion (Hunt et al. 1988)). The virtual net is implemented via the immersed boundary method (Peskin 1972). The Immersed Boundary Method (IBM) is a numerical technique used to simulate flow fields past bodies that do not necessarily conform with the computational grid. In the *SUSA* code, a number of IB methods have been implemented and validated. The interested reader can find the implementation details and the validations of the IBM methods in *SUSA* in Omidyeganeh & Piomelli (2011), Rosti et al. (2016), Rosti (2016), Monti et al. (2019), Monti (2019). By tuning the geometry of the virtual grid, it is possible to generate a grid turbulence with a satisfying spectra and pre-specified integral scales. For the grid turbulence computation, the flow condition is set with $Re_M = 2000$ (based on the free stream velocity approaching the grid and the grid spacing $M = 0.045C$) and $Re_B = 210$ (based on the rod size $B = 0.005C$; corresponding solidity equal to 0.21). The resolution of the uniform-grid has been tuned to preserve the targeted turbulent spectra (grid resolution matching the generated Kolgomorov's scale). Similarly, also the spacing of the nodes where the body forces mimic the presence of the virtual grid has been tuned to resolve all the flow scales of the grid turbulence.

The unsteady perturbed flow field is introduced upstream of the aerofoil at each time-

step. The location of the plane where the grid turbulence is introduced in the flow field is quite critical. One would like to inject a homogeneous and isotropic turbulent kinetic energy spectrum while avoiding a too strong decay of the turbulence intensity before impacting on the aerofoil. For long time integrations the injected turbulent signal is recycled through stored solutions. To avoid the introduction of artificial time scales into the turbulent field, the perturbation coherence is completely broken via the introduction of white noise on top of each turbulent field injected. It is noted that the prediction-projection approach helps to reduces the eventual generation of spurious oscillation where the fictitious perturbations are introduced. An illustration of the introduced perturbation can be found in picture 3.14.
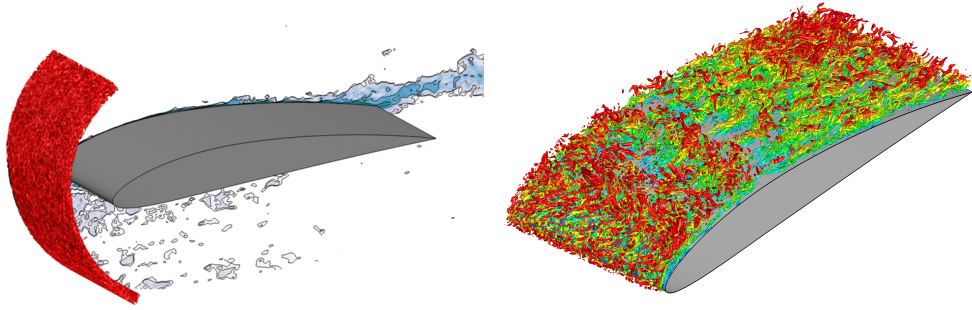
Figure 3.14: Illustrations of the introduced free stream turbulence (Left) and its effect on the flow past the aerofoil (Right).

The power spectral density of the non-dimensional turbulent kinetic energy time signal (i.e. $PSD\{k\} = \mathscr{F}\left\{k(t)/Q_\infty^2\right\}\overline{\mathscr{F}\left\{k(t)/Q_\infty^2\right\}}$, where the turbulent kinetic energy is $k(t) = 1/2\left[u'u'(t) + v'v'(t) + w'w'(t)\right]$, the symbol $\{\bar{\cdot}\}$ indicates the complex conjugate operator and the symbol $\mathscr{F}\{\cdot\}$ indicates the Fourier transform operator) of the perturbation field extracted from the twin DNS of grid generated turbulence is shown in figure 3.15. In the same figure, the PSD of the remaining disturbances downstream of the foil (i.e. $x/C \approx 2$) is included. Considering the spectrum of the introduced disturbances, a reasonably extended inertial scale band (frequencies band $1 < f^* = fQ_\infty/C < 50$) can be observed.

The turbulent intensity (defined in the three Cartesian directions summarised with the i-index as $I_i = \sigma_{ui}/Q_\infty$, where σ_{ui} is the standard deviation of the ith velocity component time signal) of the extracted perturbation field is $I_u = I_v = I_w = I \approx 10\%$. Such high intensity provided at the injection points has been chosen to overcome the substantial viscous decay of the FST convected downstream, which is a consequence of the considered low Reynolds number. In figure 3.15 the qualitative characterisation of the FST decay can be observed by comparing the PSD of the injected perturbation with the surviving disturbances
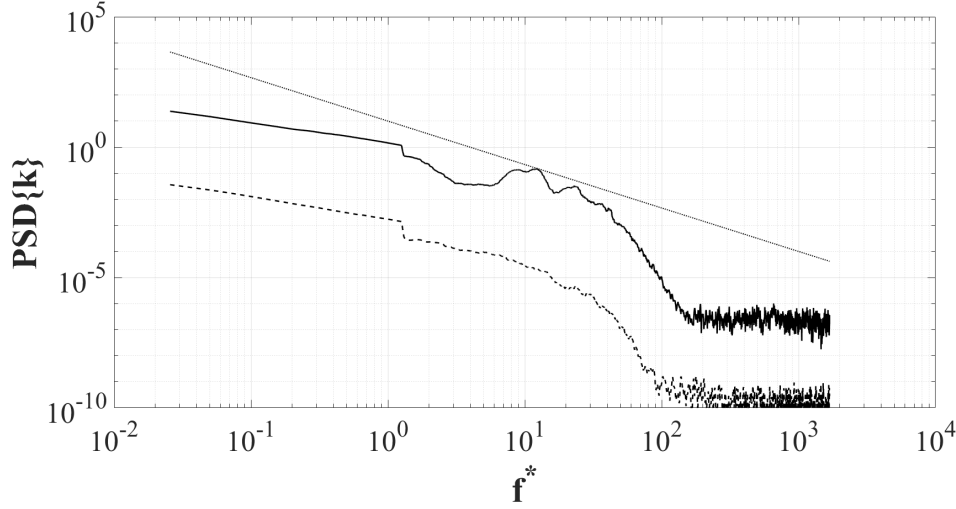
Figure 3.15: Power spectral density of the non-dimensional turbulent kinetic energy time signal $PSD\{k\}$ of the introduced perturbation (solid line) and its intensity at a distance $2C$ behind the foil (dashed line). The dotted line corresponds to the $-5/3$ power law. Flow condition: $Re_C = 50 \times 10^3, \alpha = 5^o, \Lambda = 0^o$, inlet with FST.

sampled downstream of the foil. Furthermore, an intense FST (i.e. $I > 6.5$) has been prescribed when a dominant by-pass transition is sought, to avoid an early laminar boundary layer separation (Zaki et al. 2010). The integral length scale of the perturbation field is $\mathcal{L}_u = \mathcal{L}_v = \mathcal{L}_w = \mathcal{L} \approx 0.045C$, leftover of the virtual grid spacing. When the perturbation is introduced upstream of the aerofoil simulation, the inertial scale band is observed to further enlarge before approaching the profile (as it will be shown in section 5.1) thanks to the $0.13C$ distance between the injection plane and the aerofoil leading edge. Conversely, the turbulent intensity decays before approaching the boundary layer of the aerofoil. An intensity of $I \approx 7\%$ is recorded just outside the boundary layer edge by the aerofoil nose (in this location the boundary layer thickness is in the order of $0.1\%C$).

A representative measure of the decay of the FST intensity is measured along the convective direction outside the suction side boundary layer and it is compared with literature data of turbulence behind a grid. The FST intensity in the chordwise plane (i.e. $I_Q = \sigma_Q^2/Q^2$) is $I_Q = (7.6, 6.0, 3.4)$ at $[(x/C, y/C)] = [(0.24, 0.18), (0.85, 0.19), (1.96, 0.18)]$, respectively. The spectra extracted in the three locations are shown in figure 3.16, while the corresponding turbulence intensities are plotted in figure 3.17. The rate of decay of the intensity follows an algebraic trend with decay exponent n_{FST} (Mohamed & Larue 1990). For the turbulent decay behind a uniform grid without a pressure gradient, the decay exponent is $n_{FST} \approx 1.3$ (Mohamed & Larue 1990). In the present case $n_{FST} \approx 0.5$ is observed over the suction side along the chord, while $n_{FST} \approx 1.3$ behind the foil.
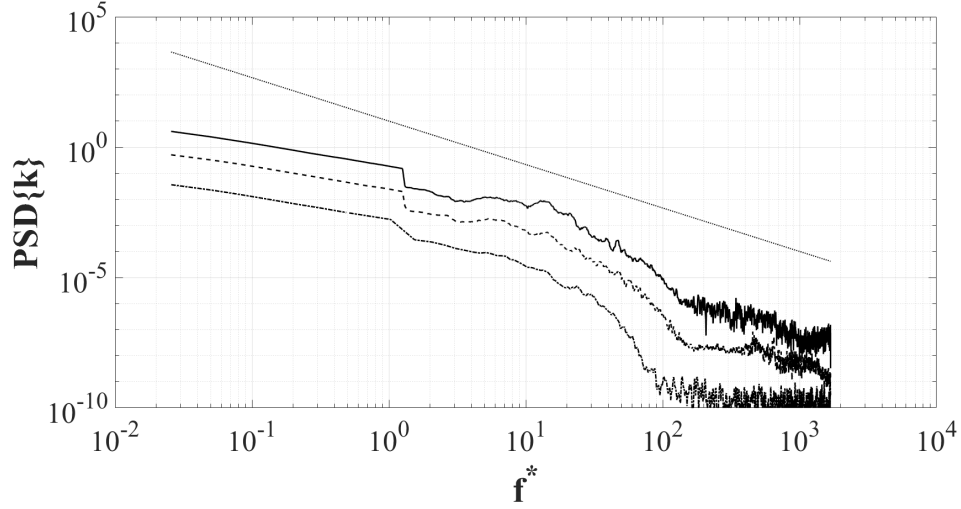
Figure 3.16: $PSD\{k\}$ of the FST at $(x/C, y/C) = (0.24, 0.18)$ with the solid line; $(x/C, y/C) = (0.85, 0.19)$ with the dashed line; $(x/C, y/C) = (1.96, 0.18)$ with the dot-dashed line. The dotted line corresponds to the $-5/3$ power law. Flow condition: $Re_C = 50 \times 10^3$, $\alpha = 5^o$, $\Lambda = 0^o$, inlet with FST.

The present FST condition has been modelled in analogy to that used by the experimental research group at the University of Southampton in the frame of the project *Quiet aerofoil of the next generation* (EPSRC grant No.$ZP/N020413/1$). The present investigation is related to the project and the details of the free stream turbulence have been discussed during informal presentation between the research groups and companies involved (universities: University of Southampton, University of Nottingham, City, University of London, Brunel University and Technion-Israel Institute of Technology; companies: Airbus Group Limited and Vestas).
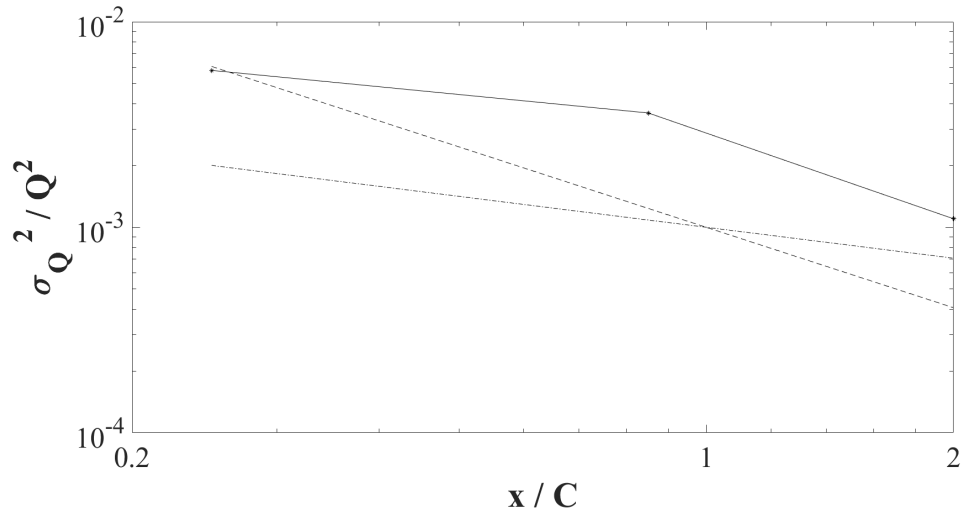
Figure 3.17: Turbulent intensity $I_Q = \sigma_Q^2/Q^2$ probed at $[(x/C, y/C)] = [(0.24, 0.18), (0.85, 0.19), (1.96, 0.18)]$. The solid line connecting the intensities represents the measured decay exponent (Mohamed & Larue 1990). As a matter of comparison, the dot-dashed line a decay exponent of 0.5, while the dashed line of 1.3. Flow condition: $Re_C = 50 \times 10^3, \alpha = 5^o, \Lambda = 0^o$, inlet with FST.

Chapter 4

Laminar separation

The chapter contains the comparison between the swept and unswept laminar boundary layer experiencing the flow separation mechanism, after the baseline unswept flow condition is presented. The flow scenario is obtained in the frame of a laminar incoming free stream.

The statistical quantities have been accumulated within a time window $\Delta t^* = \Delta t Q_\infty / C$ $\simeq 100$ for both the wing configurations throughout the statistical steady state of the flow as defined in section 3.4. Roughly, this period corresponds to 15 full domain flow-through cycles. In accordance with the *Simple Sweep Theory* , the comparison between swept and unswept wing is made considering statistical values accumulated along the x direction only.

4.1   Mean two-dimensional unswept field

For the unswept wing case and laminar incoming flow, the distribution of the mean (i.e. time and spanwise averaged, indicated with $< \cdot >_{z,t}$) chordwise velocity component $< u >_{z,t}$ (x, y) is shown in figure 4.1. The figure shows a recirculating region covering a large portion of the foil suction side. Conversely, the whole pressure side is characterised by a fully attached boundary layer. The average separation point on the suction wall, tagged with a symbol in figure 4.1, is located at $x/C = 0.26$. The iso-line of the mean chordwise velocity that can be used to identify the shape of the laminar separation bubble is referred as the limit (or dividing) streamline (Alam & Sandham 2000) and it is also plotted in the same figure. The LSB is observed to close at the trailing edge (i.e. there is no mean reattachment point on the suction side) presenting an extension comparable with that of the aerofoil. In particular, its chordwise length is $0.852\,C$ and its wall-normal height is $0.143\,C$. The bubble appears to be stretched above the aerofoil reaching a streamwise location of $0.112\,C$ downstream of the trailing edge at a distance from the chord line (i.e. at $y/C = 0$) of $0.075\,C$. On the suc-
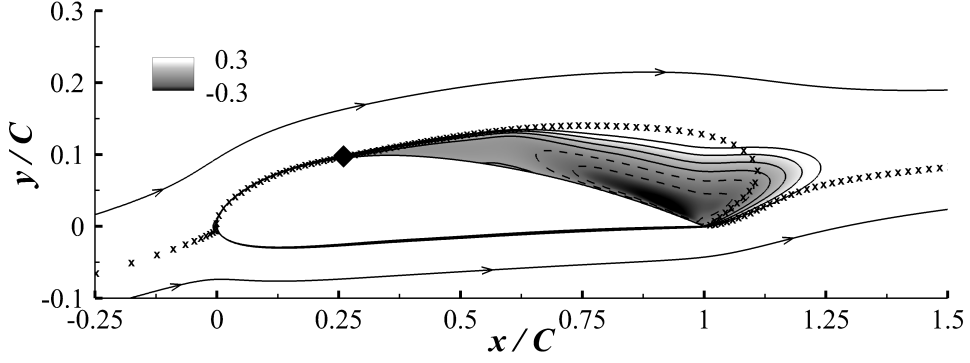
Figure 4.1: Contours of $< u >_{z,t} /Q_\infty$. Solid iso-lines represent positive values: $< u >_{z,t}=$ $[0, 0.1, 0.2, 0.3]Q_\infty$; dashed ones are used for negative iso-values $< u >_{z,t}= [-0.3, -0.2, -0.1]Q_\infty$. The limiting streamline is represented using the $\times$ symbols. The $\blacklozenge$ symbol tags the mean flow separation point on the wall (i.e. location with zero mean wall shear stress). Flow condition: $\alpha = 5^o, \Lambda = 0^o$, laminar inlet.

tion side, inside the bubble, a small secondary separation region is visible within the interval $x/C = [0.55-0.65]$ at approximately $y/C = 0.8$. As discussed later, this secondary recirculation envelops a region characterised by positive mean velocity (i.e. velocity vector directed downstream). Some other authors have reported the presence of this secondary bubble indicating the interaction of the primary recirculating flow with the no-slip wall condition as the physical mechanism responsible for its generation (Marxen & Henningson 2011).

Figure 4.2 displays the iso-contours of the mean spanwise vorticity $< \omega_z >_{z,t} (x, y) = \partial < u >_{z,t} (x, y)/\partial y - \partial < v >_{z,t} (x, y)/\partial x$ for the same flow configuration. From the figure, it is possible to observe a thin and intense separating shear layer developing along the limit streamline. This shear layer originates at $x/C \simeq 0.26$, in correspondence with the point of separation, developing away from the wall, along the outer edge of the primary recirculating zone. This intense shear layer is the origin of the instability that triggers a
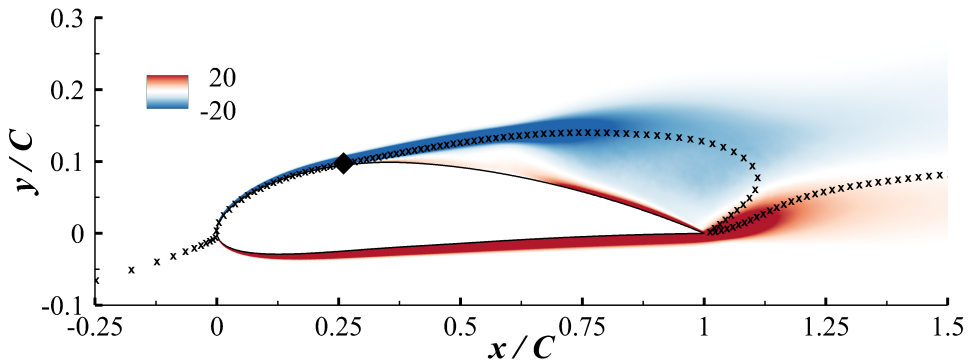
Figure 4.2: Contours of $< \omega_z >_{z,t} C/Q_\infty$. Blue shading indicates a negative vorticity, while the red is for the positive vorticity. As in figure 4.1, the symbol $\blacklozenge$ is used to tag the separation point while the line with $\times$ symbols is the limiting streamline. Flow condition: $\alpha = 5^o, \Lambda = 0^o$, laminar inlet.

turbulence transition further downstream, above the aerofoil, as observed by several authors in similar circumstances (e.g. Jones et al. (2008), Yarusevych et al. (2009)).

4.2 Influence of the sweep on the flow field

4.2.1 2D flow and pressure fields

The mean field corresponding to the swept wing (sweep $\Lambda = 30^o$) does not present any substantial difference with the straight wing case. This almost perfect match appears clearly from figure 4.3 where a direct comparison between some selected $< u >_{z,t}$ iso-lines are displayed for both wing configurations. In particular, the mean location of the boundary layer separation point is unaffected by the presence of the steady crosswind separation location $x/C = 0.26$. The robustness of the mean location of the laminar boundary separation point to an imposed spanwise flow has already been reported by other authors (Hetsch & Rist 2009). It is also observed that the leading edge stagnation point (which for the swept case should be referred as an attachment line due to the out-of-the plane mean flow component (Vos & Farokhi 2015)) is not affected by the sweep either. The anyway small differences between the two flow fields can only be detected inside the recirculating region.

Figure 4.4a provides a comparison between the two wing configurations in terms of mean chordwise pressure coefficient distribution, i.e. $< C_{p_x} >_{z,t} (x, y) = 2(< P >_{z,t} (x, y) - P_\infty)/\rho Q_\infty^2$. In both cases, the suction side presents two local maxima: one close to the wall at $x/C = 0.10$ (the *suction peak*) and another one on the dividing streamline. It is noticed that the locations of the second maximum is shifted downstream of about 10% in the swept wing case (unswept wing coordinates of second peak: $(x/C, y/C) = (0.75, 0.14)$; swept
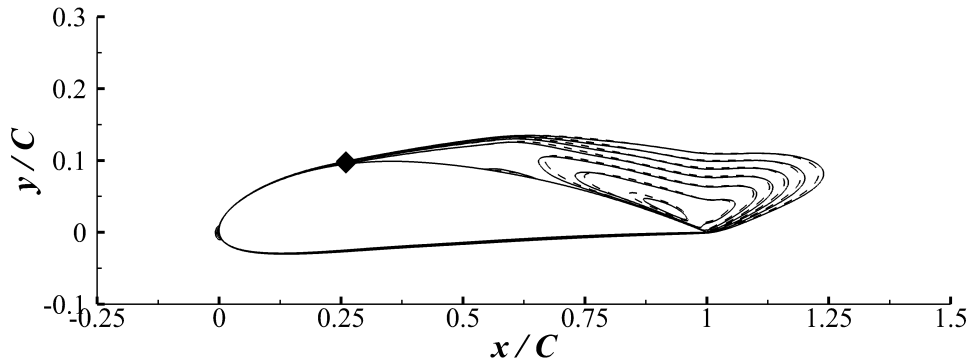
Figure 4.3: Comparison between iso-lines of $< u >_{z,t} /Q_\infty$. Iso-lines have been extracted in the range $< u >_{z,t} \in [-0.3Q_\infty$ and $0.3Q_\infty]$ with a uniform sampling of $\Delta < u >_{z,t} = 0.1 \ Q_\infty$. Solid lines refer to the straight wing case, the dashed ones to the swept one. As in figure 4.1, the symbol ◆ is used to tag the separation point. Flow condition: $\alpha = 5^o$, laminar inlet.
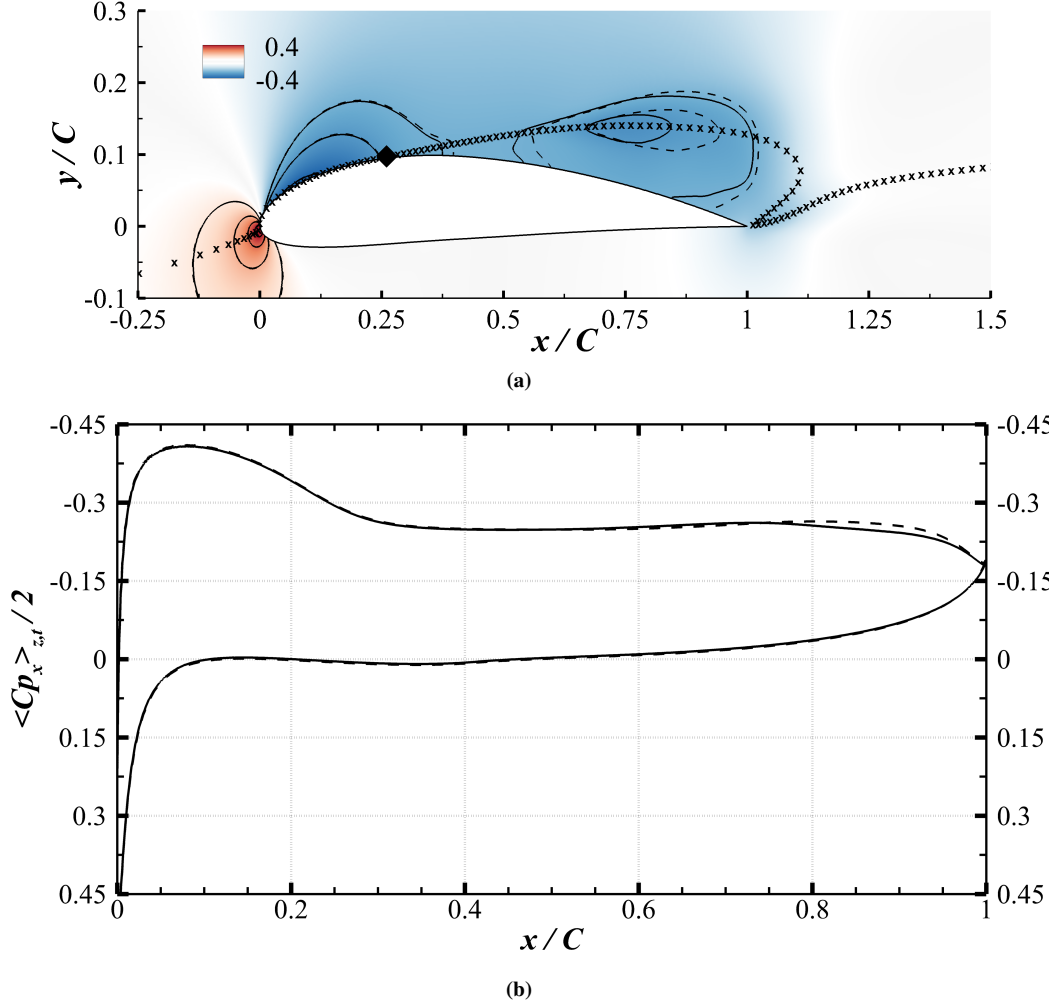
Figure 4.4: Flow condition: $\alpha = 5^o$, laminar inlet. (a) Contours of $< C_{p_x} >_{z,t}$. Blue shading indicates negative values while red is for positive ones. The solid iso-lines corresponds to the values $< C_{p_x} >_{z,t} = (-0.4, -0.3, -0.25, 0.1, 0.2, 0.3, 0.4)$ for the straight wing, while the dashed line is used for the correspondent swept wing iso-lines. As in figure 4.1, the line with $\times$ symbols is used to identify the dividing streamline. (b) Wall distribution of $< C_{p_x} >_{z,t}$. Solid line: straight wing; dashed line: swept wing.

case: $(x/C, y/C) = (0.83, 0.14))$. This downstream translation that can be also noticed from the distribution of the suction side wall $< C_{p_x} >_{z,t}$ (see figure 4.4b), is consistent with the general modification of the LSB shape. Indeed, in the first half of the aerofoil, the $< C_{p_x} >_{z,t}$ distribution is unaffected by the sweep. From $x/C = 0.5$ onwards, the *separation* plateaus share a similar pressure coefficient value (i.e. $< C_{p_x} >_{z,t} /2 = -0.25$) but extending further downstream reaching the location $x/C = 0.9$ in the swept case. Uranga et al. (2011) have also reported a variation in the pressure distribution along the suction wall of a straight and a swept wing. In particular, they performed a LES of infinite wings mounting the cambered $SD - 7003$ foil at similar incidence, in both swept and unswept conditions. Differently from the current results, the pressure plateau is found to shrink when a sweep is introduced.

This different behaviour can be attributed either to an insufficient resolution or to a lack of statistical convergence. As explained in the methodology section, an extensive a-priori assessment have been conducted on the required resolution and domain sizes that was not performed in Uranga et al. (2011). Finally, it is remarked that the $< C_{p_x} >_{z,t}$ distribution on the pressure side of the foil is observed to be independent of the sweep.

4.2.2 Flight condition

Next, the lift and drag coefficients are compared between the two wing configurations. The time averaged lift and chordwise drag coefficients and the associated root mean square values in the straight wing case are $C_l = 0.536 \pm 0.0263$ and $C_{d_x} = 0.067 \pm 0.0015$, respectively. The data are in agreement with those found by other authors: an $Xfoil$ (Drela 1989) prediction at $Re_C = 50 \times 10^3$, with Mach number equal to zero and $N_{critic} = 9$ (representing laminar inlet in $Xfoil$) finds $C_l \simeq 0.7$ and $C_{d_x} \simeq 0.055$; the experimental campaign of Jacobs & Sherman (1937) at $Re_C = 42.1 \times 10^3$ with laminar inlet reports $C_l \simeq 0.8$ and $C_{d_x} \simeq 0.03$ (the authors mention a low accuracy for the measurement at low Reynolds number). In the swept wing case, considering the chordwise plane, the obtained values are $C_l = 0.540 \pm 0.0292$ and $C_{d_x} = 0.068 \pm 0.0018$. To characterise the unsteady behaviour of the wings, the power spectral density (PSD) associated to the time series of the lift and the chordwise drag coefficients has been considered, i.e. $PSD\{C_l\} = \mathscr{F}\left\{C_l(t)\right\} \overline{\mathscr{F}\left\{C_l(t)\right\}}$ and $PSD\{C_{d_x}\} = \mathscr{F}\left\{C_{d_x}(t)\right\} \overline{\mathscr{F}\left\{C_{d_x}(t)\right\}}$. Here, the overline indicates the complex conjugate operator and the symbol $\mathscr{F}\left\{\cdot\right\}$ indicates the Fourier transform operator. The resulting spectra are shown in figure 4.5. The distribution of the most energetic modes when considering the lift coefficient is very similar, although the frequencies seem to be shifted to the right (higher frequency) and the energy content of the dominating modes to be increased in the swept wing case. The spectrum associated with the drag coefficient shows a similar behaviour presenting a frequency shift. Altogether, all the spectra show a complex dynamic behaviour rich of different harmonics and sub-harmonics. An energy peak around $f^* \approx 0.06$ (corresponding to $T^* \approx 16$) is noticed for all the spectra. This is believed to be linked to the finite size of the computational domain, since the time period has a similar scale of the flow-through cycle (i.e. $\simeq 6$). However, the focus of the thesis concerns a systematic comparison between the straight wing and its swept counterpart with identical chordwise inflow condition. It is opinion of the author that the same numerical effect appears in all cases and that does not interfere with the comparative analysis.

As already observed from the spectra of the lift and drag coefficients also the correspond-
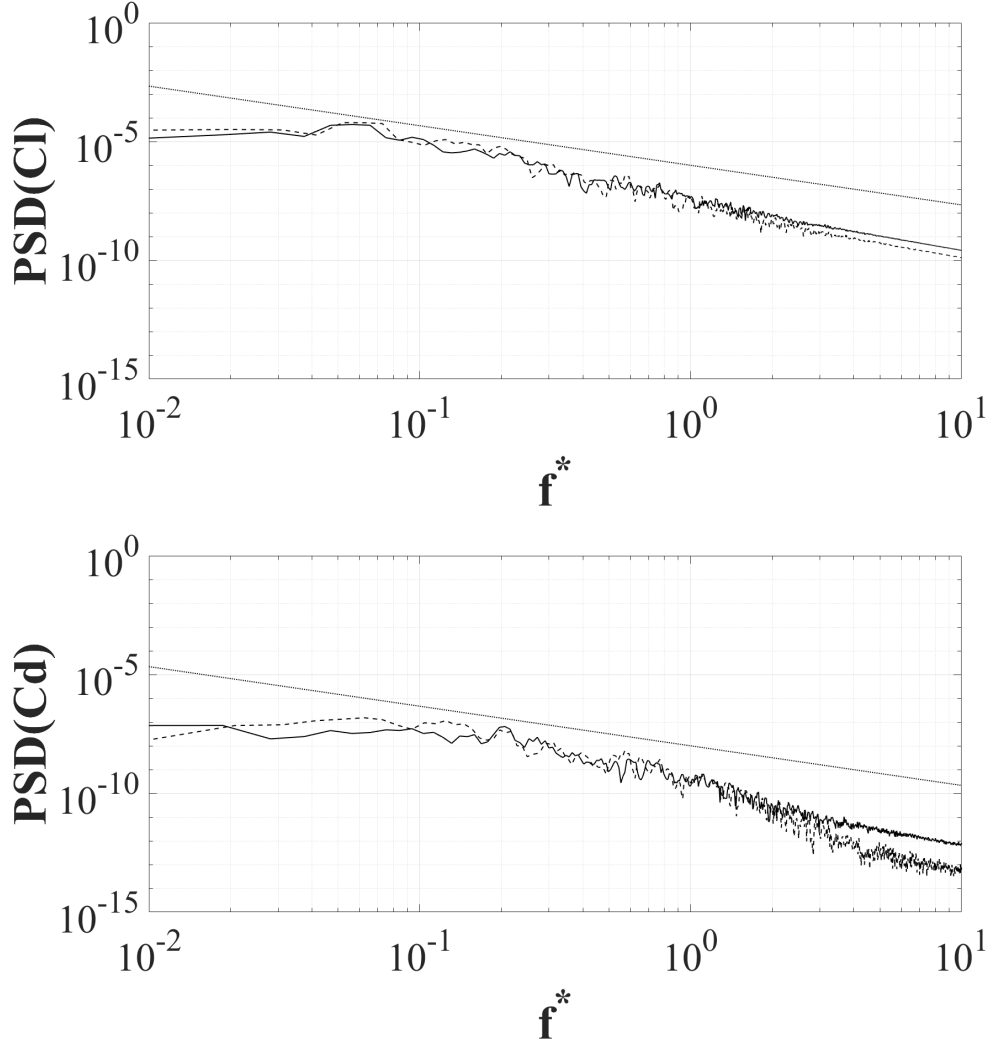
Figure 4.5: Power spectra of (Top) C_l and (Bottom) C_{d_x}. The solid line is used for the unswept wing, the dashed line for the swept configuration.

ing time series of the two quantities, displayed in figure 4.6, is not easy to interpret. However, a clear modulation of fast flow dynamics with non-dimensional period $T^*_{\text{fast}} = T_{\text{fast}} Q_\infty / C \sim O(0.1)$ (corresponding to non-dimensional frequency $f^*_{\text{fast}} = f_{\text{fast}} C / Q_\infty \sim O(10)$) appears to be produced by a much larger non dimensional time period ($T^*_{\text{slow}} = T_{\text{slow}} Q_\infty / C \sim O(10)$, $f^*_{\text{slow}} \sim O(0.1)$) for both the C_l and C_{d_x} recorded in the swept and unswept cases. Considering the lift coefficient in figure 4.6a, its time history can be assumed to be the result of a superposition of short scale dynamics with a large scale oscillation: between the non dimensional time interval $\Delta t^* = [40 - 60]$ two waves with a non dimensional time period of $T^* \approx 10$ and an excursion on the C_l of $\approx 5\%$ appear for the straight wing, while $T^* \approx 20$ and $\Delta C_l \approx 5\%$ for the swept case; on top of both, one can also observe smaller oscillations appearing within a non dimensional period of $T^* \approx 1$. In the same time interval ($\Delta t^* = [40 - 60]$) the large time period variation of the drag coefficient C_{d_x} recorded for the
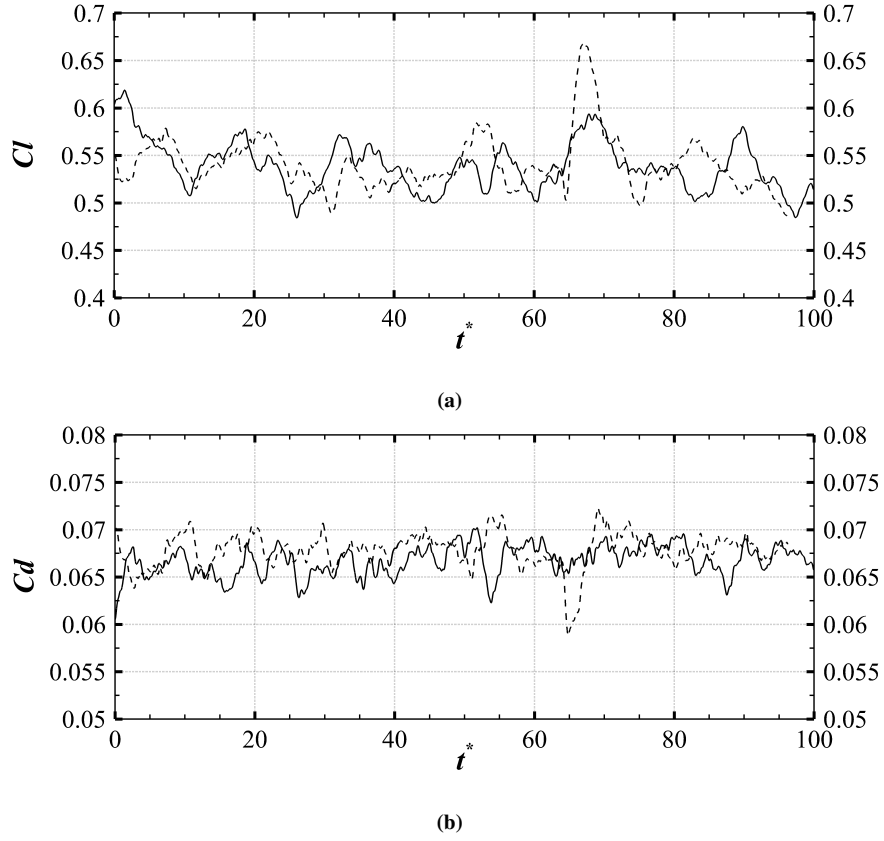
Figure 4.6: (a) Time history of the lift coefficient. The solid line is used for the straight wing, the dashed for the swept configuration. (b) Time history of the drag coefficient. Lines style meaning is the same as for the C_l.

swept wing in figure 4.6b appears to be halved as compared to the unswept case.

In an attempt to understand the role of the structures embedded in the flow on the dynamical behaviour of the overall aerodynamic field, some instantaneous snapshots of the flow around the unswept wing have been sampled out and presented in figure 4.7. The snapshots qualitatively portray some of the most typical flow characteristics. In particular, several $3D$ unsteady large scale flow structures (size being $\sim O(C)$) have been observed (e.g. in the range $x/C = [0.75 - 1.10]$, $y/C = [0 - 0.1]$ in figure 4.7a). Some of them develops moving downstream through a roll-up of the separating shear layer. Other structures are embedded in the wake arising as a result of the merging of the suction and pressure side boundary layers after the trailing edge. Structures of smaller size (size $\sim O(\delta_{99})$, with δ_{99} being the distance from wall where the mean velocity attains the $99\% Q_\infty$ value) are also detected. These are mainly generated from the interaction of the recirculating flow and the wing wall. The aforementioned structures can be detected by considering a sequence of instantaneous snapshots of the iso-contours of the chordwise velocity component extracted in one of the cross plane (shown in figure 4.7). In particular by comparing 4.7a and 4.7b, the presence

65
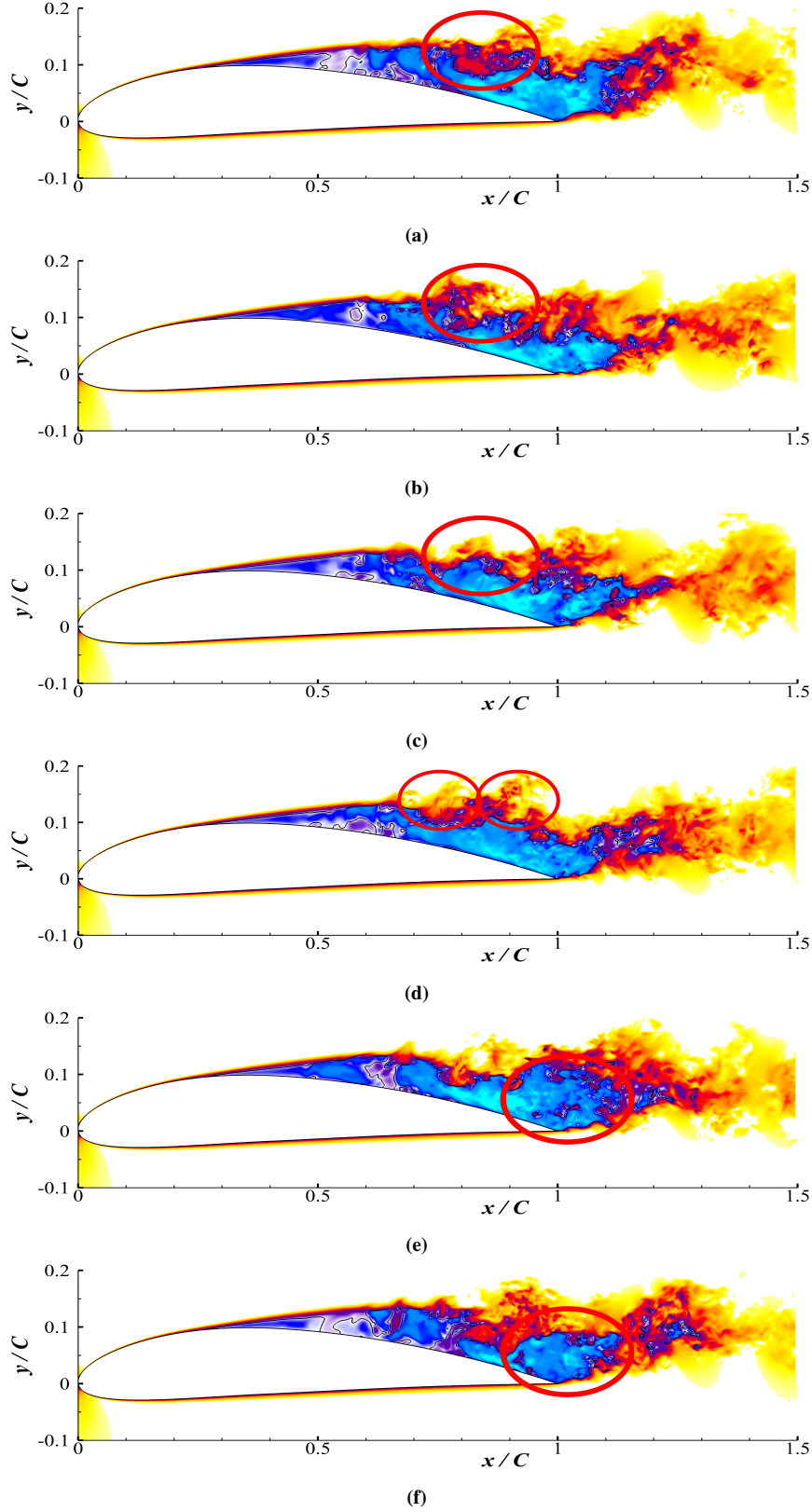
Figure 4.7: Instantaneous contours of $u(x, y, z, t)/Q_\infty$. The contours result from a non-linear colour map using red scale for positive values and blue for negatives. The white colour is used for the velocity close to zero and beyond $u/Q_\infty = 0.75$. The iso-line corresponding to the zero value is drawn with a black solid line. The snapshots are taken with a not-constant time interval in the range $\Delta t^* = [0.008 - 0.004]$ from the straight wing time evolution. Flow condition: $\alpha = 5^o$, $\Lambda = 0^o$, laminar inlet.

of a flow structure originating at $x/C = 0.75$ is noticed by the edge of the separated shear layer at $y/C \approx 0.1$ (circled in red in the figures). The time lag between the two images is $\Delta t_b^* = (t_b - t_a)Q_\infty/C = 0.054$ (from now on the non dimensional time lag between the snapshot at time t_j and the initial time t_a is defined as $\Delta t_j^* = (t_j - t_a)Q_\infty/C$). The snapshots of the two following frames (figures 4.7c and 4.7d), captured at $\Delta t_c^* = 0.109$ and $\Delta t_d^* = 0.185$, respectively show the continuation of the clock-wise roll-up of the shear layer and its downstream displacement that reaches $x/C = 0.8$ and $x/C = 0.9$ in the two frames (flow structure circled in red in the figures). In 4.7d the upper limit of the separation bubble is $y/C \simeq 0.2$, reducing in size as the trailing edge is approached. However, no specific energy peak can be observed in the spectra for $f^* \simeq 6$ (frequency given by the time scale of the vortex generation appearing between frame b and d). Finally, by comparing the last two frames (i.e. 4.7e and 4.7f), captured at $\Delta t_e^* = 0.288$ and at $\Delta t_f^* = 0.378$, the generation of a new eddy that starts to roll-up by the trailing edge is noticed at $(x/C, y/C) = (1.0, 0.5)$. The roll-up occurs in an anti-clock-wise fashion, and the eddy is ultimately shed into the wake. The latter is characterised by vortex shedding that develops in a quite chaotic von Kármán street. The snapshots also reveal the transition process of the shear layer bounding the separation region that quickly increases its thickness downstream.

When considering a similar qualitative analysis based on successive snapshots, the swept wing configuration shows a time evolution of the flow topology very similar to the one described for the straight wing case.

4.2.3 Perturbation field and transition

In figure 4.8, the iso-contours of the mean turbulent kinetic energy,

$$< k >_{z,t} (x, y) = 1/2 \, [< u'u' >_{z,t} (x, y)+ < v'v' >_{z,t} (x, y)+ < w'w' >_{z,t} (x, y)] \quad (4.1)$$

are displayed for both wing configurations. $< k >_{z,t}$ is observed to take on larger values in two specific regions of the flow domain, both extending through the limit streamline. The leftmost region envelops the separating shear layer, with the maximum $< k >_{z,t}$ value attained at $(x/C, y/C) = (0.80, 0.14)$ and with an elongated shape that develops along a direction parallel to the chord, spanning almost 35% of it. The other region grows from a location downstream of the trailing edge and with the maxima of $< k >_{z,t}$ aligned along a direction forming an angle with the chord similar to the foil incidence. The x-extension of the second region is about 25% of the chord and its absolute maximum is located at $(x/C, y/C) = (1.15, 0.34)$. The two regions eventually merge downstream into the wake with a weaker intensity. From figure 4.8 it is also possible to analyse the difference between the distribution of $< k >_{z,t}$ in the swept and unswept case by considering the iso-lines. They overlap in the two regions, but then deviate when entering the merging zone moving downstream into the wake.

In both cases transition occurs in a bounded region. To quantify the transition and the turbulent nature that the flow assumes when moving downstream along the wing, the power spectrum of the non-dimensional turbulent kinetic energy time signal acquired at specific
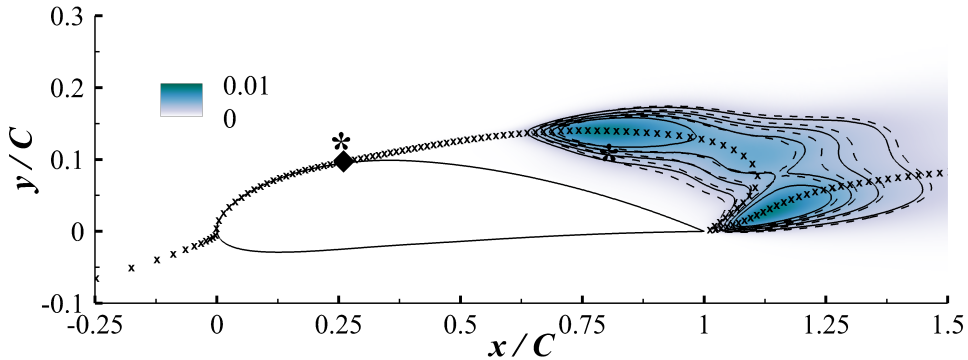
Figure 4.8: Iso-contours of $< k >_{z,t} /Q^2_\infty$ with a colour map using the green colour for the maximum value and the white for the minimum. Iso-lines for $< k >_{z,t} /Q^2_\infty$ between 0.002 and 0.005 using 4 levels are shown. The solid lines is used for the straight case, the dashed otherwise. The $\times$ symbols identify the limiting streamline, whereas the symbol ◆ is used for the location of mean separation. The symbol ✳ marks where the spectra shown in figure 4.9 are taken. Flow condition: $\alpha = 5^o$, laminar inlet.

locations (x, y, z) is computed, i.e.

$$PSD\{k\} = PSD\{k(x, y, z, t)/Q_\infty^2\} = \mathscr{F}\left\{k(x, y, z, t)/Q_\infty^2\right\}\overline{\mathscr{F}\left\{k(x, y, z, t)/Q_\infty^2\right\}} \quad (4.2)$$

The time signal is acquired at mid span (i.e. $z/C = 0.2$) for the two $(x/C, y/C)$ locations identified with a $*$ symbol in figure 4.8. The $PSD\{k\}$ is displayed in figure 4.9 for both the chosen locations in the flow field. In the upstream location, at $(x/C, y/C) = (0.25, 0.11)$, the flow still presents a clear laminar character, while further downstream at $(x/C, y/C) = (0.80, 0.10)$, the flow features a spectrum that includes a portion of inertial range (i.e. $1 < f^* = fQ_\infty/C < 50$). It is also noticed that in both locations, the spectra obtained for the swept and unswept case do not show any significant difference. It has to be mentioned that the data for the swept wing are affected by noise at high frequency, for $f^* > 10^2$, due to some duplicated values in the data series which have not been filtered out from the data set.
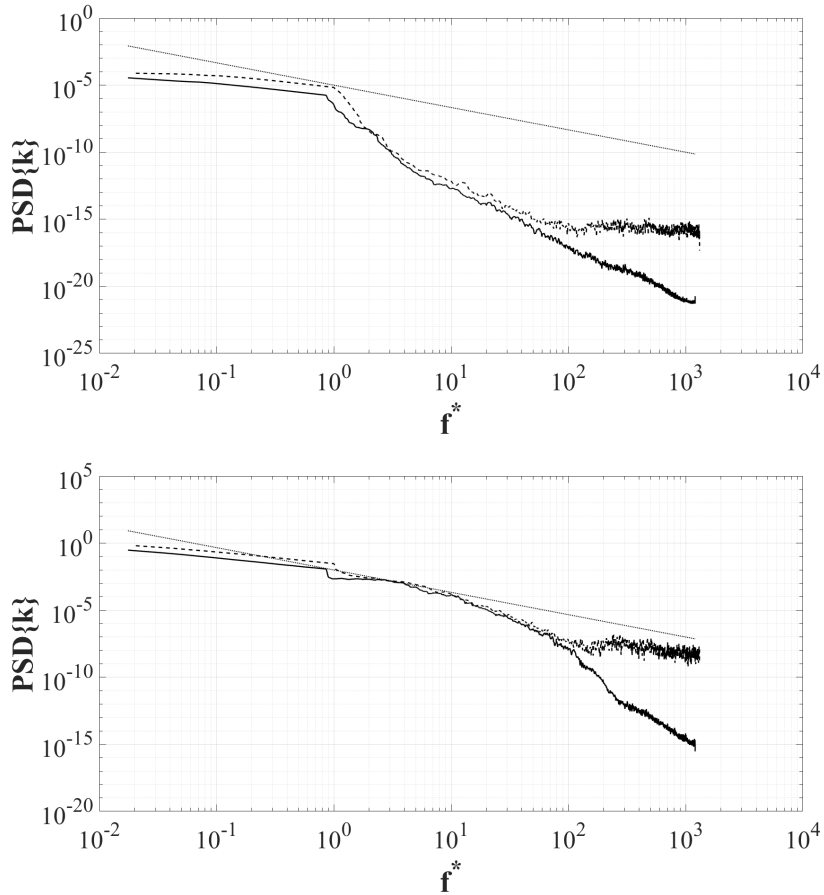
Figure 4.9: $PSD\{k\}$ obtained at (Top) $(x/C, y/C, z/C) = (0.25, 0.11, 0.2)$ and at (Bottom) $(x/C, y/C, z/C) = (0.80, 0.10, 0.2)$. The two locations in the chord plane are identified with a $*$ in figure 4.8. The solid line is used for the straight wing, the dashed for the swept wing and the dotted line correspond to the $-5/3$ power law.

4.2.4 Boundary layer structure

Some classical definitions of the boundary layer and of related integral quantities require a modification when dealing with an APG boundary layer that may eventually feature a mean separation. The δ_{99} BL thickness requires to specify a free stream velocity outside of the boundary layer for each location on the foil. To make a case, the velocity profiles extracted from the suction side of the straight wing at $x/C = 0.05$ and $x/C = 0.2$ can be considered, provided in figure 4.10a. It can be observed that the mean tangent to the wall velocity profile, $< u_{tg} >_{z,t} (x, n)$ (note that n indicates the direction normal to the foil wall, while tg corresponds to the direction s. Thus, $u_{tg}(x, n)$ is a velocity lying in the chord plane, combination of the Cartesian components $u(x, y)$ and $v(x, y)$), does not approaches the $< u_{tg} >_{z,t} /Q_\infty = 1$ limit monotonically. Instead, it increases up to a value larger than the free stream, at about $n/C = 0.01$, and then decreases asymptotically to match the free stream value. Thus, the standard definition of boundary layer thickness would deliver a height much lower than the actual boundary layer depth. Since the boundary layer is a measure of the region where viscosity plays a role, it has also been suggested to consider the maximum velocity as a criterion to establish the height of the BL. However, when the same convention is applied along the whole foil, unrealistic values of the various thicknesses
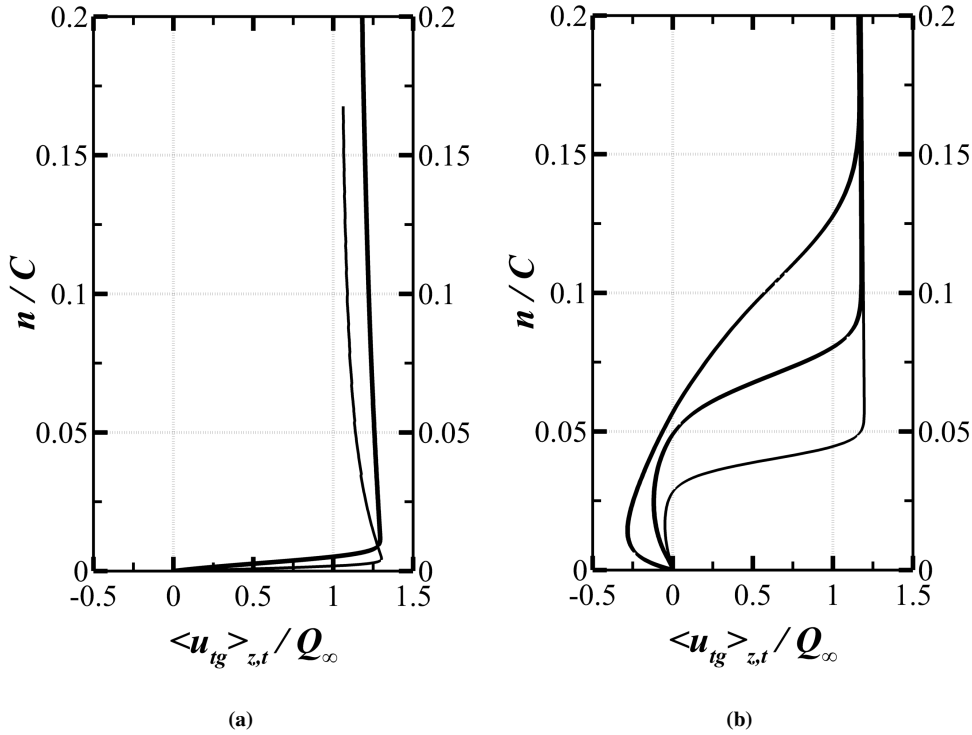
Figure 4.10: (a) Example of the velocity profile inside an attached boundary layer. (b) Example of the velocity profile in a boundary layer presenting a mean separation.

would be obtained. This difficulty has been discussed by several authors and in particular by Vinuesa and collaborators (Vinuesa et al. 2016) that have finally adopted the *zero vorticity* criterion to establish the location of the BL edge and to compute the integral quantities. In this work the same vorticity-vanishing criterion is used, considering the vorticity component perpendicular to the mean flow plane (i.e. the spanwise vorticity component $< \omega_z >_{z,t}$ (x,n)), to tag the BL edge and thus to find the value of the external velocity. The vanishing vorticity criterion has shown to be an effective tool to determine regions where both velocity gradients and a viscosity dissipation play a role.

Furthermore, in the present thesis an extension to the criterion has also been considered to deal with the eventual mean flow separation on the wing. Although in an instantaneous flow realisation, the conventional decomposition of the flow into a boundary layer and an external inviscid field cannot be applied when separation takes place, the concept can be extended to the mean separated flow field. In this case the external inviscid flow would match a boundary layer developing on a virtual wing made of the union of the actual physical wing and the separated region. In the latter, *inner* region, a complex condition develops where both the viscous and inviscid effects have comparable importance. The extension of the vanishing vorticity criterion applied above the separated flow, has been found useful to to re-establish the BL-*Euler* flow decomposition along the portion of the foil affected by the mean separation. Typical mean velocity profiles extracted within the region affected by mean separation are displayed in figure 4.10b. In particular, following the aforementioned general idea, the edge of the boundary layer has been obtained by considering the region above the inflection point of the mean chordwise velocity (caused by the separation and discussed with further detail later into section 4.3.2) to detect the zero-crossing of the out-of-plane vorticity linked to the *extended* boundary layer edge. The line marking the edge of the layer obtained with this methodology is similar in shape to the limit streamline. The formal definitions of the BL thicknesses (the displacement thickness δ^* and the momentum thickness θ (Schlichting 1979)) obtained with the adopted methodology are:

$$\delta^*(x) = \int_0^{\breve{n}} [1 - < u_{tg} >_{z,t} (x,n) / < \breve{U}_{tg} >_{z,t} (x,\breve{n})] dn \qquad (4.3)$$

$$\theta(x) = \int_0^{\breve{n}} [1 - < u_{tg} >_{z,t} (x,n) / < \breve{U}_{tg} >_{z,t} (x,\breve{n})][< u_{tg} >_{z,t} (x,n) / < \breve{U}_{tg} >_{z,t} (x,\breve{n})] dn$$

$$\text{with } < \breve{U}_{tg} >_{z,t} (x,\breve{n}) = < u_{tg} >_{z,t} (x,n) \Big|_{[n=\breve{n}: <\omega_z>_{z,t}(x,\breve{n})=0]}$$

When comparing the two wing configurations, it is found that upstream of the separated

region all the integral boundary layer quantities match, while further downstream the sweep plays a non negligible role for some of them. Figure 4.11b shows that the distribution of θ of the swept configuration deviates from the straight wing case especially in the rightmost portion of the separated region, beyond $x/C \simeq 0.6$. The pressure side does not show any effect due to the sweep with θ/C bounded with the range $\Delta\theta = [2 - 3]C \times 10^{-3}$ within the interval $\Delta x/C = [0.20 - 1.00]$. In the mean separation location on the suction side is recorded $\theta = 0.0017C$. On the suction side the distribution of θ is interesting even in the simpler straight wing case, as it increases monotonically until $x/C = 0.30$ and then it almost levels off completely until $x/C = 0.75$, showing a change in curvature around $x/C = 0.50$. In the range from $x/C = 0.75$ to $x/C = 0.85$, θ/C suddenly increases, deviating from the pressure side. From $x/C = 0.85$ to $x/C \approx 0.90$, it settles to a constant value of 4×10^{-3} and finally in the last portion of the foil it strongly increases again attaining a value of 8×10^{-3} by the trailing edge. The distribution of the swept wing momentum thickness deserves some additional comments, since it deviates from that of the unswept case beyond $x/C \simeq 0.6$. The distribution takes on the shape of an upside down bell, with its minimum at $x/C \approx 0.75$, thus not presenting the kink that characterises θ/C of the straight wing at $x/C = 0.75$. The distributions of the two wing configurations match again beyond the location $x/C = 0.9$. In summary, it is observed that on the suction side the distribution of the momentum thickness is not only affected by the separation, but also by the sweep when the former occurs. This observation has a clear consequence on the applicability of the *Simple Sweep Theory* that should be limited to the prediction of attached flows, at least when laminar free-stream conditions are considered.

Figure 4.11a shows that although the displacement thickness of the chordwise boundary layer is greatly affected by the separation, its values is almost unaffected by the sweep. In particular, the suction side boundary layer thickness grows monotonically from $2 \times 10^{-3}C$ to $1.5 \times 10^{-1}C$ moving from 10% of the chord location until the trailing edge. On the pressure side the boundary layer thickness increases in a much more moderate way ranging within the $\Delta\delta^* = [2 - 5] \times 10^{-3}C$ interval. It is noted a similarity of the suction side distributions behaviour with respect of the separation and transition location as in Brendel & Mueller (1988). The pressure and suction side thickness growth rates start to differentiate beyond the location $x/C = 0.20$. On the pressure side, after this location, the BL height levels off reaching an asymptotic value of 1×10^{-1}. Conversely, on the suction side the monotonic increase of the BL size is linked to the appearance of the mean separation zone where a complex viscid-inviscid interaction takes place. In the mean separation location, the dis-
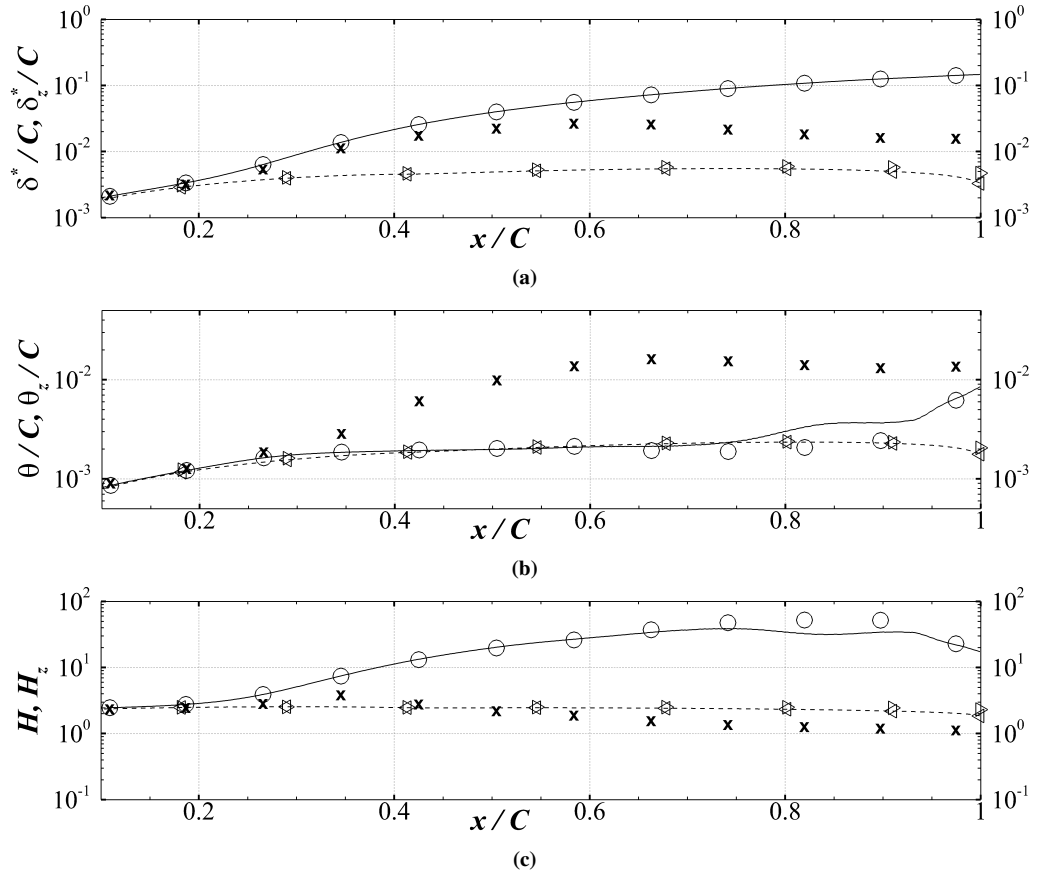
Figure 4.11: a: chord distribution of the non dimensional displacement thickness. b: non dimensional momentum thickness distribution. c: shape factor distribution. The chordwise boundary layer developing on the suction side of the straight wing is indicated with the solid lines, while o refer to the swept wing. The chordwise boundary layer developing on the pressure side of the straight wing is indicated with the dashed lines, while ◁ refer to the swept wing. The spanwise flow correspondent integrals are shown with × on the suction side and ▷ on the pressure side.

placement thickness is found to be $0.006C$.

In the case of the swept wing another, crosswind, boundary layer develops along the chord. To characterise this cross boundary layer, the same integral quantities defined above in equations 4.3 are used. Here too, the edge of the boundary layer is identified using the vanishing vorticity criterion, this time applied to the mean x- vorticity component $< \omega_x >_{z,t}$ (x, y). The following definition are thus introduced for the boundary layer thicknesses of the spanwise flow,

$$\delta_z^*(x) = \int_0^{\check{n}} [1 - < w >_{z,t} (x,n)/ < \check{W} >_{z,t} (x,\check{n})]dn \qquad (4.4)$$

$$\theta_z(x) = \int_0^{\check{n}} [1 - < w >_{z,t} (x,n)/ < \check{W} >_{z,t} (x,\check{n})][< w >_{z,t} (x,n)/ < \check{W} >_{z,t} (x,\check{n})]dn$$

$$\text{with } < \check{W} >_{z,t} (x,\check{n}) = < w >_{z,t} (x,n)\big|_{[n=\check{n} : <\omega_x>_{z,t}(x,\check{n})=0]}.$$

The obtained distributions are shown in figures 4.11a and b. The distribution of both δ_z^* and θ_z on the pressure side are found to match those of the chordwise flow indicating that in the lower foil side a unique boundary layer develops. The suction side presents an interesting behaviour which is worth to be described carefully. The distribution of δ_z^* is found to follow that of δ^* until $x/C \simeq 0.4$, while beyond a clear difference is recorded: instead of increasing monotonically, it decreases and almost level out at $\delta_z^* = 1.5 \times 10^{-2}C$. The fact that the chordwise distribution does not match the spanwise one indicates that the second half of the upper portion of the foil is characterised by two distinct boundary layers. The distribution of the cross momentum thickness on the suction side also presents a clear difference with the chordwise one, from as early as the mean separation location. Indeed, θ_z increases monotonically over the mid chord location where θ_z attains a maximum value an order of magnitude higher than the one predicted for the chordwise boundary layer (i.e. $1 \times 10^{-2}C$ at $x/C = 0.65$). After, it almost levels out until the trailing edge, where a comparable to the chordwise thickness value is recorded. Next, the distribution of the shape factors H and H_z (given by the ratio between the displacement and the momentum thickness of the chordwise and spanwise flows) is given, respectively. Figure 4.11c shows the distribution along the chord of H for both wing sides and also for the crosswind boundary layer in the swept wing case. On the pressure side all the distributions (H of the chordwise flow on the straight and swept wing and H_z of the spanwise flow on the swept wing) coincide along the whole chord with an almost constant value of about 2.5, thus close to the value of a Blasius boundary layer (for which $H = 2.59$ Schlichting (1979)). The spanwise shape

factor on the suction side mildly oscillates around this same value, reaching a maximum value of ≈ 4 at $x/C \approx 0.35$ and a minimum of ≈ 1 at $x/C \approx 0.7$. These distributions suggest that the boundary layers on the pressure side and the crosswind one developing on the suction side behave as attached, laminar boundary layers. As expected the chordwise boundary layers developing the suction side for both the wings show a completely different character. From the leading edge until about 70% of the chord, the distribution of H is identical for the swept and the unswept wings showing a monotonic increase that becomes steeper after $x/C \simeq 0.26$. In the last third portion of the foil, the unswept wing value of H levels off presenting a final drop as the trailing edge is approached. Differently, in the swept wing case there is no plateau and the value of H continues to increase albeit a final fall in the trailing edge region where it matches again the value attained in the straight wing configuration. Thus, by comparing the swept and unswept, chordwise distribution of H, it appears that the sweep only affects the separation taking place beyond 70% of the chord.

4.3   Sweep effect to specific flow features

So far, the aerodynamic quantities that have been considered seem to reinforce the *Simple Sweep Theory* in almost all the locations along the foil but in the surroundings of the separation and consequent transition to turbulence. Indeed, in proximity of the separated region and in particular across the shear layer that bounds the recirculating bubble, where transition occurs, the swept and the unswept wings have been shown to present different behaviours.

In this section the focus will be put more on the mechanisms involved in the boundary layer separation, trying to shed some more light on the differences between the two wing configurations. The spectral analysis carried out in the following sections is based on a database obtained out of the flow simulations spanning $\Delta t^* \simeq 6$ for both the wing configurations.

4.3.1   Separation of the laminar boundary layer

Although the basic mechanisms of separation in an APG boundary layer are well understood, an exact description of its occurrence and the development of an accurate predictive model for the inception of separation are still active research topics. For the case of the straight wing with a laminar free-stream condition, at moderate Reynolds numbers, some models have been developed in the past. These models deliver fairly good descriptions, especially for the prediction of the location of the mean separation. Some authors, relying on the *Simple Sweep Theory* , have extended these models to swept wing configurations showing their applicability also when a crosswind is present (e.g. (Davis et al. 1987, Selby 1983)).

Here, the focus is more in describing in details the physical phenomena behind separation in the two wing configurations providing an informed ground for the critical assessment of the models available in literature. As an example of the information that can be gained by detailed simulations, the effect of the spanwise modulated perturbation on the separation and how the sweep play a role in modifying these modulations and their energy content is anticipated.

Figure 4.12a presents the time-averaged spanwise energy spectrum of the non dimensional velocity fluctuations field premultiplied by the spanwise wavenumber k_z (Pope 2000), i.e.

$$
\begin{aligned}
k_z & < \hat{E}^* >_t (x, y, k_z) = \\
& 1/2 k_z \left[< \hat{R}^*_{u'u'} >_t (x, y, k_z) + < \hat{R}^*_{v'v'} >_t (x, y, k_z) + < \hat{R}^*_{w'w'} >_t (x, y, k_z) \right].
\end{aligned}
\tag{4.5}
$$

Note that $< \hat{R}^*_{u'u'} >_t (x, y, k_z)$ (and the same for the others components, $\hat{R}^*_{v'v'}$ and $\hat{R}^*_{w'w'}$) is

the energy content of the k_z wave number of the Fourier transform of the two-point autocorrelation in the spanwise direction of the non dimensional fluctuations of the x-wise velocity component. The two-point autocorrelation function of a non dimensional fluctuating velocity component in the spanwise direction is defined as:

$$< R_{u'u'}^* >_t (x, y, r) =$$
$$\left\langle \int [u(x,y,z,t)- <u>_{z,t} (x,y)][u(x,y,z+r,t)- <u>_{z,t} (x,y)]/Q_\infty^2 dr \right\rangle_t . \tag{4.6}$$

Therefore, the iso-contours of $< \hat{E}^* >_t (x, y, k_z)$ quantify the energy content of a specific spanwise mode (having spanwise wavelength λ_z) at a specific x/C and y/C location. In figure 4.12a, the spectrum obtained for the straight wing, is shown as a function of the distance from the wing suction side in correspondence of the x/C location where the mean separation takes place. The perturbation energy is observed to be mostly contained within a specific layer surrounding the edge of the boundary layer at $y/C = 0.101$. In this energy containing strip, the spectrum presents a peak associated with a spanwise wavelength λ_z/C corresponding to the spanwise dimension on the computational box. This result is not surprising since this region still behaves in a laminar fashion and therefore locally almost 2D. However, a non negligible energy content is also found to be associated with spanwise modes having a wavelength as short as $0.20C$ suggesting the development of a spanwise modulated perturbation. To determine which velocity component (i.e. the directionality) of this spanwise modulation, the attention is turned to the energy content of the velocity components directly, shown in figures 4.12b, c and d. From the figures, it appears that the energy is mainly associated with the x-wise velocity fluctuations with a weaker content corresponding to the spanwise velocity fluctuations.

To evaluate the effect of the sweep on the spanwise modulated energy content detected, in figure 4.12e the same quantity as in 4.12a is presented, sampled at the same location but for the swept configuration. From the figure, it is clear that the sweep does not affect the vertical location of the maxima of the energy content, however it seems to induce a decrease in the energy content associated with the smaller wavelengths (i.e. $\lambda_z/C < 0.3$).

To shed some further light on the structure of the spanwise perturbation field, two snapshots of the instantaneous x-velocity component $u'(x, y, z, t)$ iso-values are considered on a x-z plane, captured above the wing suction side at $y/C = 0.101$ (shown in figures 4.13a and c for the unswept case, while in panels 4.13b and d for the swept one). Via the view from the top proposed in panel a, one can appreciate a clear spanwise modulation of the x-wise veloc-
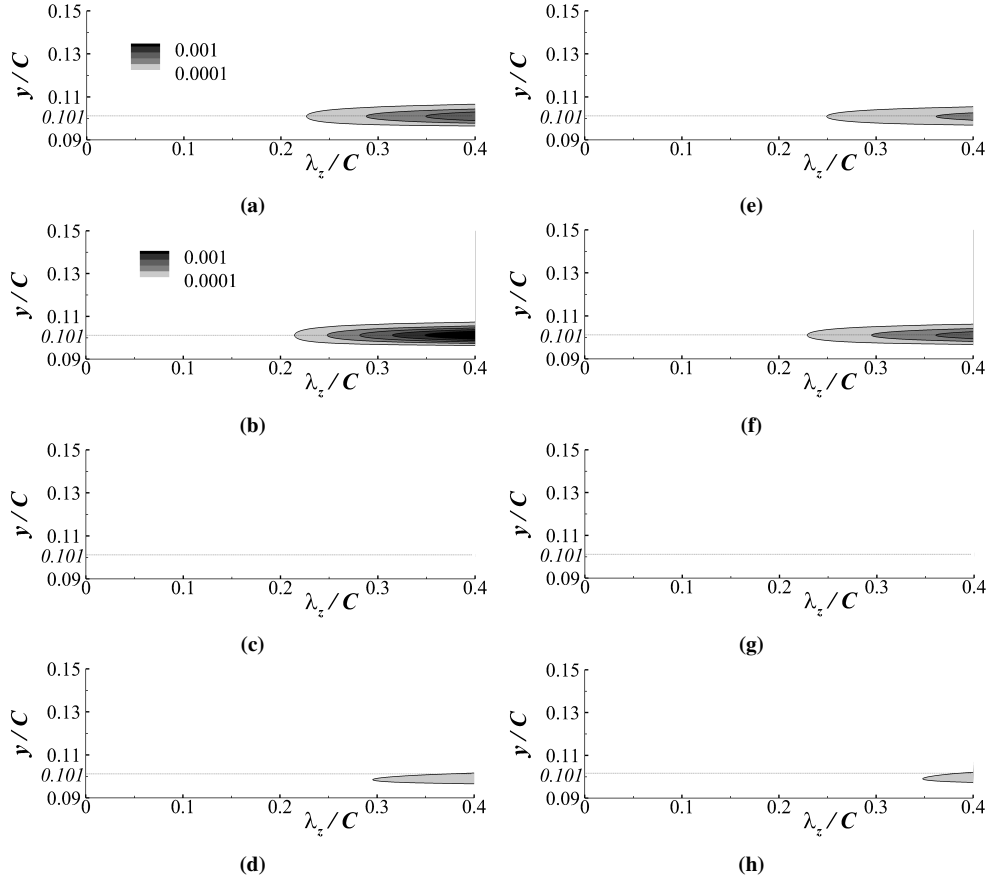
Figure 4.12: Spanwise energy content of the fluctuating velocity field. The straight wing is illustrated in the left column, the swept one in the right column. The spectra are extracted at the chord location of mean separation, $x/C = 0.26$. Panels (a) and (e) correspond to iso-contours of $k_z < \hat{E}^* >_t C$. The grey-scale colour map is distributed non-linearly with the black regions corresponding to $k_z < \hat{E}^* >_t C > 0.001$. The iso-lines are sampled with an increment of $k_z < \Delta\hat{E}^* >_t C = 0.000225$ starting from $k_z < \hat{E}^* >_t C = 0.0001$. (b) and (f) Iso-contours of $< \hat{R}^*_{u'u'} >_t$. The grey-scale colour map is distributed non-linearly with the black regions corresponding to $< \hat{R}^*_{u'u'} >_t > 0.001$. The iso-lines are sampled with an increment of $< \hat{R}^*_{u'u'} >_t = 0.000225$ starting from $< \hat{R}^*_{u'u'} >_t = 0.001$. (c) and (g) Iso-contours of $< \hat{R}^*_{v'v'} >_t$. Same legend as for $< \hat{R}^*_{u'u'} >_t$. (d) and (h) Iso-contours of $< \hat{R}^*_{w'w'} >_t$. Same legend as for $< \hat{R}^*_{u'u'} >_t$.

ity perturbation field taking place in the neighbourhood of the separation line of the mean flow. The view allows for a qualitative observation of the spatial character of the perturbation in the wall parallel plane. The modulation wavelength in both the x and z directions corresponds to about half spanwise domain size. To better understand the three-dimensional character of the flow perturbation, with the panel c the iso-values of the x-velocity fluctuations are also shown on a y-z plane extracted at $x/C = 0.26$. Again, a spanwise modulation can be recognized within a strip centred at $y/C = 0.101$, having the location of maximum amplitude at $z/C = 0.20$. The wall normal modulation is revealed to have a size comparable with the boundary layer thickness. When the swept wing is considered, panels b and d, an increased coherence of the spanwise modulation is revealed, which energy is now concentrated on a wavelength of almost the spanwise size of the computational box. Although the perturbation field appears to be modified by the sweep, as already mentioned the mean separation occurs in the same exact location for both wing configurations. Thus as a preliminary conclusion, it can be stated that the sweep has very little impact on the flow field upstream of the separation line and does not even set the location of the latter; however it seems to have a clear effect on the three dimensional evolution of the fluctuating field that takes place downstream the separation point. By looking at the leading edge region ($i.e. x/C \simeq [0-0.1]$) of the straight wing perturbation field in figure 4.13a, a fluctuating energy accumulation can be observed. The same pattern is not visible in the swept wing field shown in 4.13b. The fluctuation is linked to the very low frequency cycle (i.e. $T^* \simeq 10$) of the unsteady flow as already discussed when commenting the C_l and C_{d_x} time series, in figure 4.6. By looking at the fluctuating field in another cross plane, shown in Figure 4.13c, the perturbation can be seen to affect the entire domain around the aerofoil. The absence of a positive fluctuating velocity in the swept case (panel 4.13b or 4.13d) is due to the wing being in another instantaneous state of the unsteady flow cycle with respect to the straight wing counterpart. In particular, the straight wing snapshot has been extracted at $t^* \simeq 100$, which can be seen from the C_l time series being after an ascending trend of the oscillation cycle (look at figure 4.6); while the snapshot of the swept wing has been extracted at $t^* \simeq 95$ that corresponds to another state of the oscillating cycle (as seen in figure 4.6).

Finally, it is highlighted that the present simulation study on the swept wing did not show any *crossflow* transition and the transition seems to take place along the canonical straight wing route, i.e. through an instability of the shear layer emanating above the recirculation bubble. The lack of crossflow instability has also a clear impact on the separation that, in the present framework, is driven solely by the chordwise flow and the adverse pressure gradient

as initially envisaged in the conceptual scenario proposed by Jones (1947).
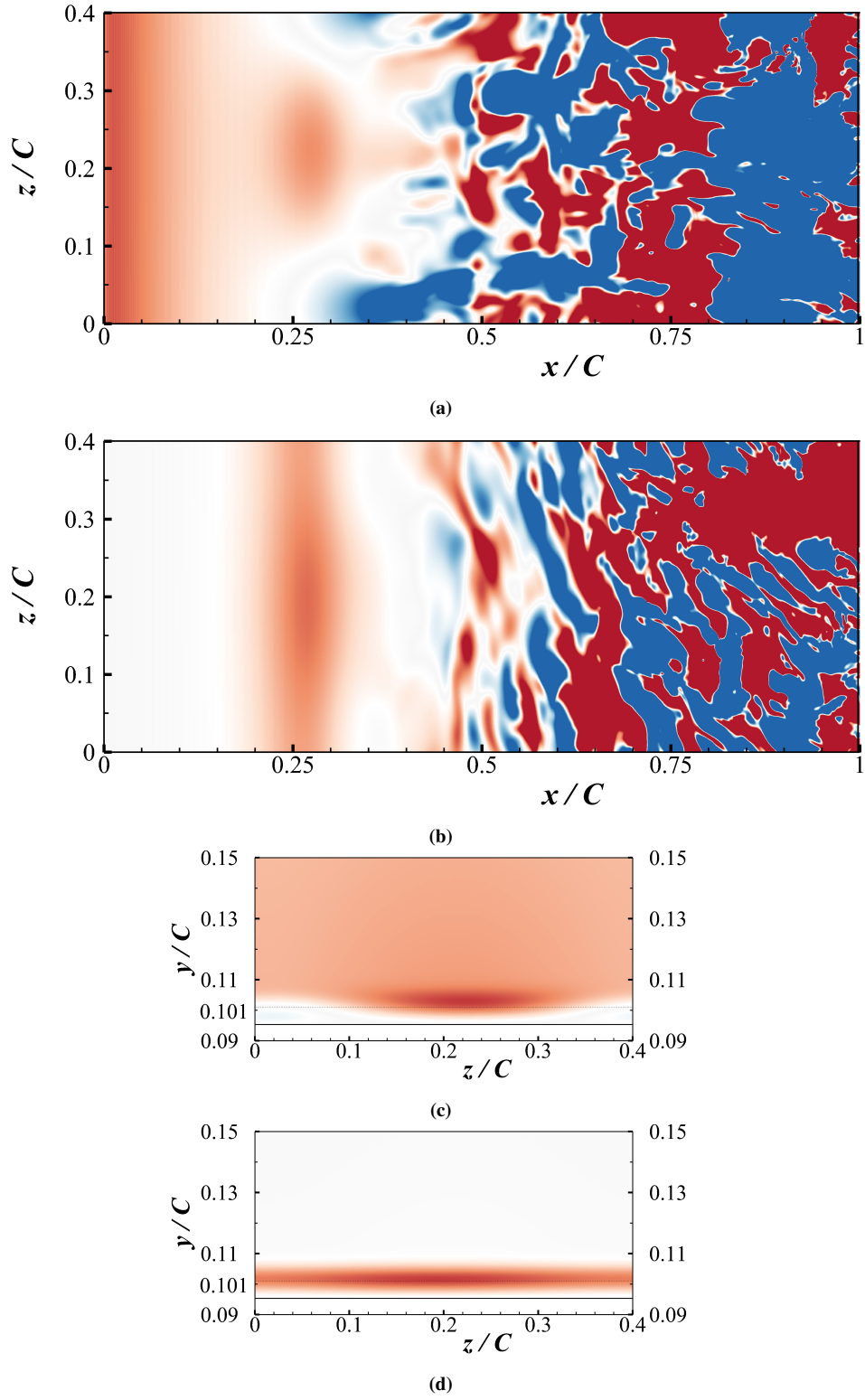
Figure 4.13: Flow condition: $\alpha = 5^o$, laminar inlet. (a) and (b) Iso-contours of u'/Q_∞ on a plane parallel to the aerofoil suction wall. The selected plane passes through $y/C = 0.101$ at the separation location $x/C = 0.26$. (c) and (d) Iso-contours of u'/Q_∞ on a normal-to-the-wall plane at the location of separation. (a) and (c) refer to the straight wing, while (b) and (d) to the swept one. The colour map shows $u'/Q_\infty > 0.1$ in red, $u'/Q_\infty < -0.1$ in blue and a fluctuation close to zero in white.

4.3.2 Instability of the detached shear layer

The separating shear layer hosts the growth of the inviscid Kelvin-Helmholtz (K-H) instability (Marxen et al. 2013) and this feature in its early stage is unaffected by the introduction of the spanwise mean flow. The instantaneous snapshots of the y component of the fluctuating velocity field $v'(x, y, z, t)$ extracted on a plane parallel to the foil reveals the overall behaviour of the shear layer. Two of those snapshots are shown in in figures 4.14a and 4.14b for both the wing configurations.Above the suction wall, the footprints of the K-H instability are observed as region of alternating positive and negative fluctuations of $v'(x, y, z, t)$. The region containing the development of the convective instability grows moving downstream. The described instability originates about the location where the shear layer starts to detach from the wall. This location approximately corresponds to the coordinates where the chordwise mean velocity profiles are observed to develop an inflection point (the location is specified in the following lines). The latter is a clear consequence of the mean recirculation bubble forming on the suction side of the wing and its location does not seem to be affected by the sweep.

An interesting observation concerns the mean spanwise velocity profile of the swept
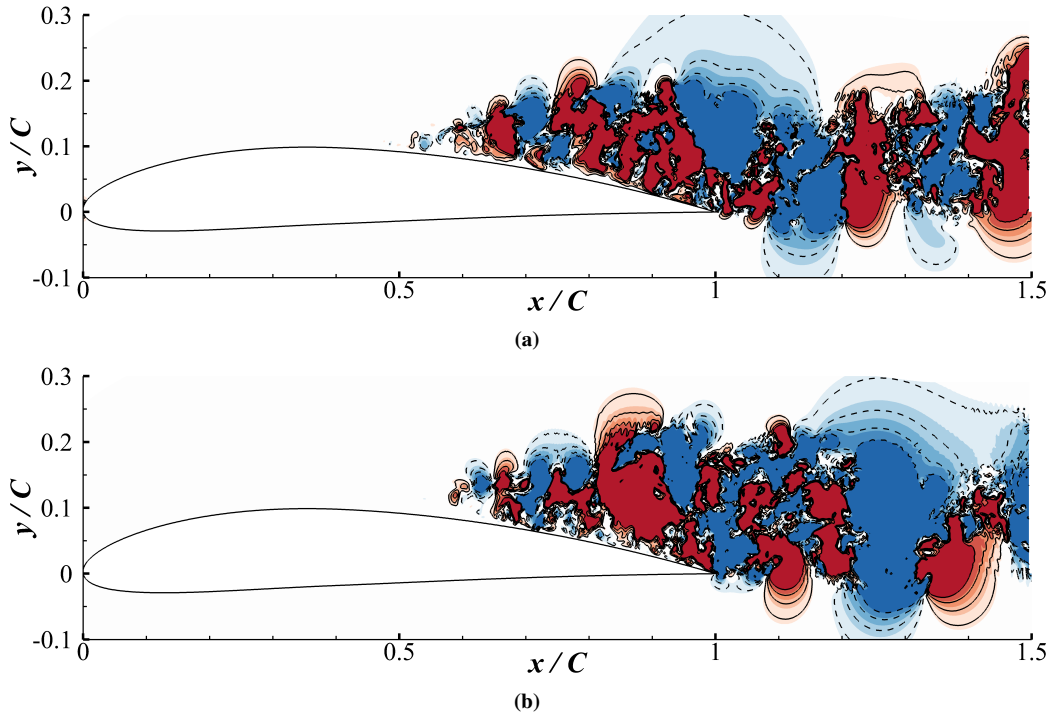
Figure 4.14: Contours of v'/Q_∞ at wing mid-span, on a plane parallel to the foil. Red regions correspond to positive perturbations (i.e. $v'/Q_\infty > 0.1$). 4 solid iso-lines between $v' = 0.025Q_\infty$ and $v' = 0.1Q_\infty$ have also been sampled. Blue regions correspond to negative values (i.e. $v'/Q_\infty < -0.1$) and the sampled negative iso-lines are the dashed ones. Thw white colour is used for a fluctuation close to zero. Flow condition: $\alpha = 5^o$, laminar inlet. (a) Straight wing case. (b) Swept wing case.

wing case showing an inflection point sharing the same location as that of the mean chord plane flow. This common inflectional location is visible from figure 4.15, showing the mean wall-tangent and spanwise velocity profiles of the swept wing configuration ($< u_{tg} >_{z,t}$ (x,n) and $< w >_{z,t}$ (x,n)) and their corresponding curvature distributions ($\partial^2 < u_{tg} >_{z,t}$ $(x,n)/\partial n^2$ and $\partial^2 < w >_{z,t}$ $(x,n)/\partial n^2$) extracted at two subsequent chordwise locations (at $x/C = 0.3$ and $x/C = 0.6$, respectively). At the upstream station, i.e. at $x/C = 0.3$ just downstream of the mean separation point, the velocity profiles in 4.15a, reveal an almost completely attached flow. The curvature distributions, given in figure 4.15b, shows a more intense curvature variation for the wall-tangent profile (the non dimensional excursion in this case is between ± 5, while for the spanwise component is ± 2). As already anticipated, the inflection point is found in the same normal-to-the wall location for both the profiles, at $n/C = 0.0076$, roughly corresponding to the local displacement thickness. When considering the profiles of figures 4.15c and d, in the downstream chord location this correspondence is almost exact for the wall-tangent mean velocity profile, while the spanwise velocity inflection point is slightly shifted upward. The presence of an inflection point also in the mean spanwise profile has the potential to trigger another instability originating from its location. The eventual, additional instability due to the inflection of the mean spanwise velocity distribution may provide an explanation for the modification of breakdown process of the K-H vortices observed in the swept wing case.

In both wings configurations, the flow structures generated by the K-H instability take the shape of spanwise coherent vortices moving away from the wall while growing and convecting downstream (Yarusevych et al. 2009). As they detach from the wall, the effect of viscosity becomes less important and the inviscid K-H instability triggers the aforementioned spanwise vorticity rollers. The situation is equivalent to the one of a plane mixing layer where initial 2D structure becomes fully 3D downstream as turbulent transition develops.

Although the described phenomena are qualitatively similar in the two wings configurations, in the swept case the wavenumber associated with the rollers breakdown process is different. The Q-criterion (Hunt et al. 1988) with a non dimensional threshold of 50 has been used to identify the K-H rollers and their evolution in a region of significance for the detection of their breakdown process (range $\Delta x/C = [0.5 - 0.75]$). Instantaneous snapshots of the Q iso-surfaces are shown using different cross planes in figures 4.16a and c for the straight wing, while in figure 4.16b and d the equivalent surfaces are given for the swept case. In all the figures, the flow structures are coloured according to the chordwise vorticity fluctuations, $\omega'_x(x,y,z,t)$, using the red colour for positive values. Figures 4.16a and
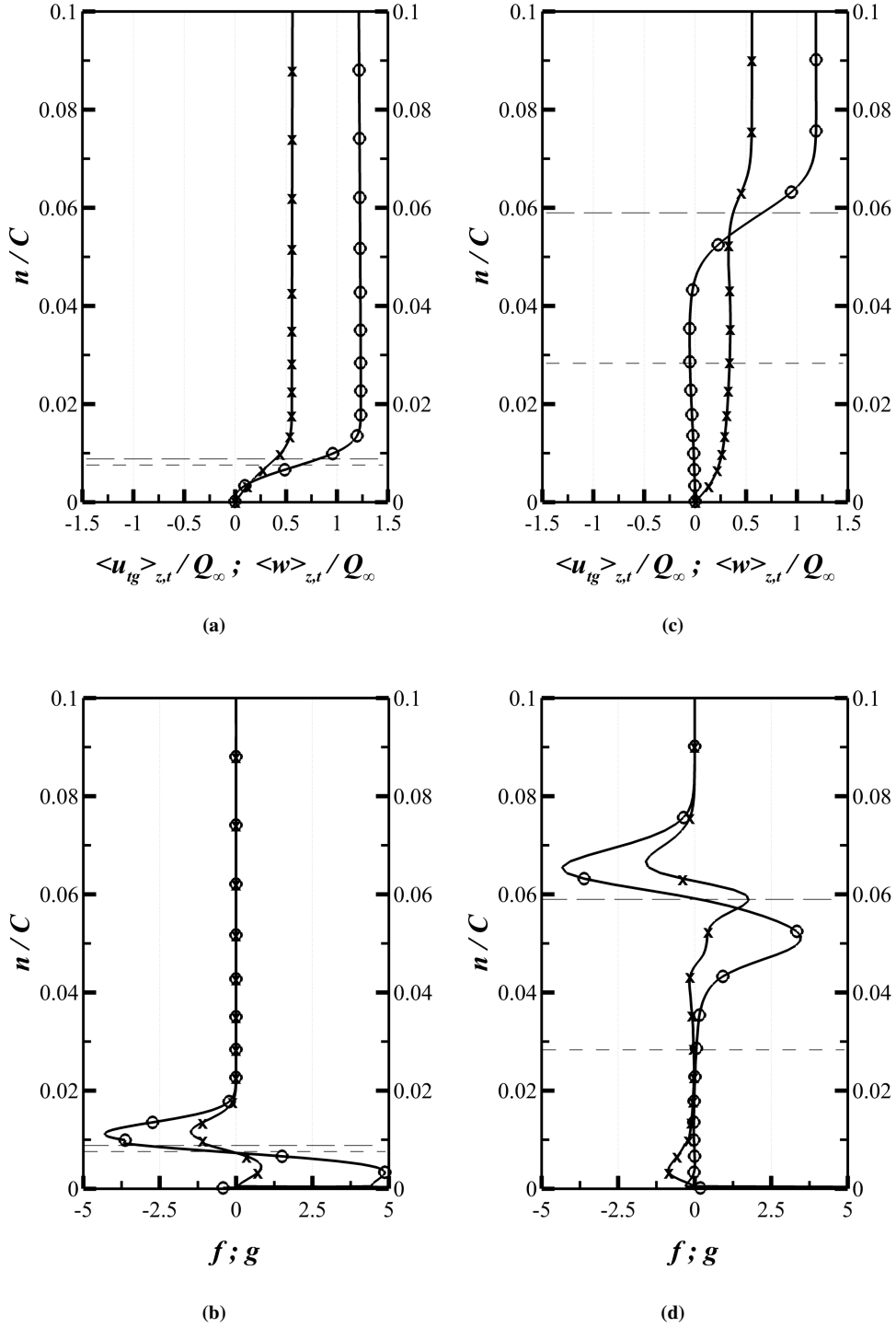
Figure 4.15: Wall normal distribution of $< u_{tg} >_{z,t} /Q_\infty$ and $< w >_{z,t} /Q_\infty$ in (a and c). The corresponding curvature distributions $f = (C^2/Q_\infty)\partial^2 < u_{tg} >_{z,t} /\partial n^2$ and $g = (C^2/Q_\infty)\partial^2 < w >_{z,t} /\partial n^2$ are given in (b and d). All the profiles have been extracted from the suction side of the swept wing, in particular (a and b) at $x/C = 0.30$ and (c and d) at $x/C = 0.60$. The chordwise quantities are shown with the circled line while the spanwise ones with the crossed lines. The long dashed line indicates the chordwise displacement thickness at the specific location, while the dashed line the spanwise displacement thickness.

84
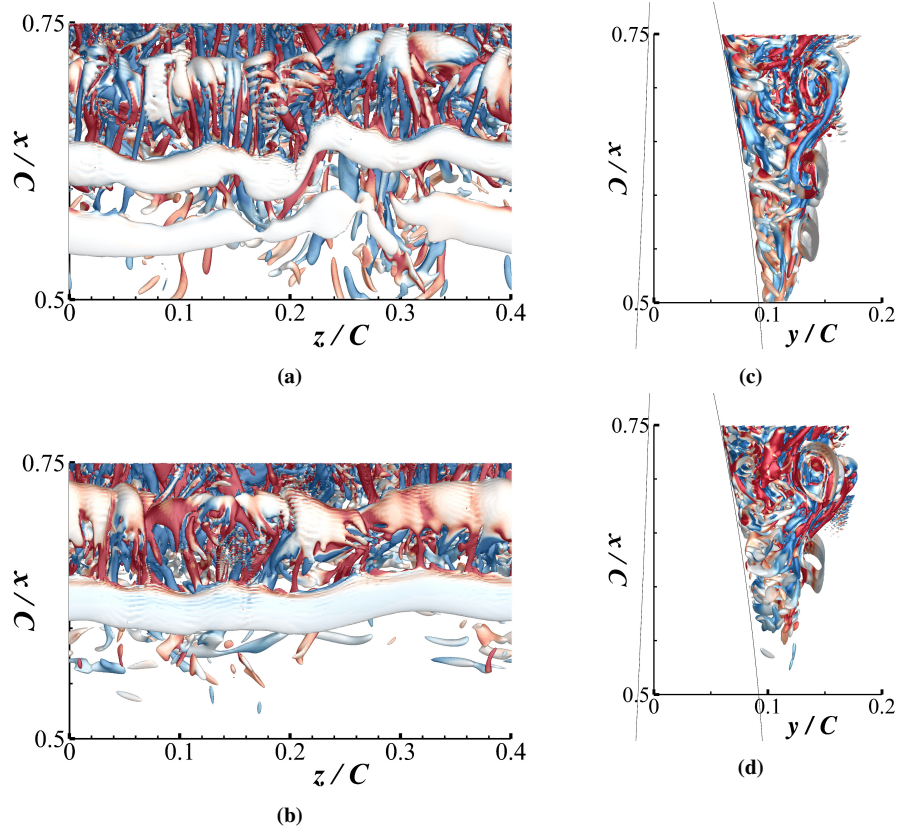
Figure 4.16: Iso-surfaces of Q-criterion with a non dimensional threshold fixed at 50. Flow condition: $\alpha = 5^o$, laminar inlet. Panels (a) and (c) concern the straight wing, while (b) and (d) correspond to the swept case. (a and b) top views, flow from the bottom to the top; (c and d) side views, flow from the bottom to the top.

4.16b offer the same iso-surfaces from a different perspective using a view from the top of the suction side. From the figures, it is possible to notice that the spanwise rollers seem to be modulated along z with a wavenumber that differs in the two wings configurations. In particular, in the swept wing case the spanwise structures appear to be more rectilinear extending along the whole span. Differently, in the straight wing case the spanwise coherence of the rollers at $x/C \approx [0.55 - 0.60]$ is clearly interrupted. The strong spanwise coherence of the rollers in the case of the swept wing can also be appreciated in figures 4.16b and 4.16d that allow to identify the full spanwise coherency of a particular roller centred at $(x/C, y/C) = (0.6 - 0.65, 0.13 - 0.15)$. Indeed, in this location it is possible to to look through a straight roller that clearly deploys along the whole wing span.

The different flow structure that the two wings exhibit in the breakdown region of the separating shear layer can also be appreciated by considering the iso-contours of $\omega'_x(x, y, z, t)$ on z-y cross planes extracted on the suction side. The aforementioned contours are reported for both wings in figure 4.17 at different cross planes obtained by slicing the domain at four

85
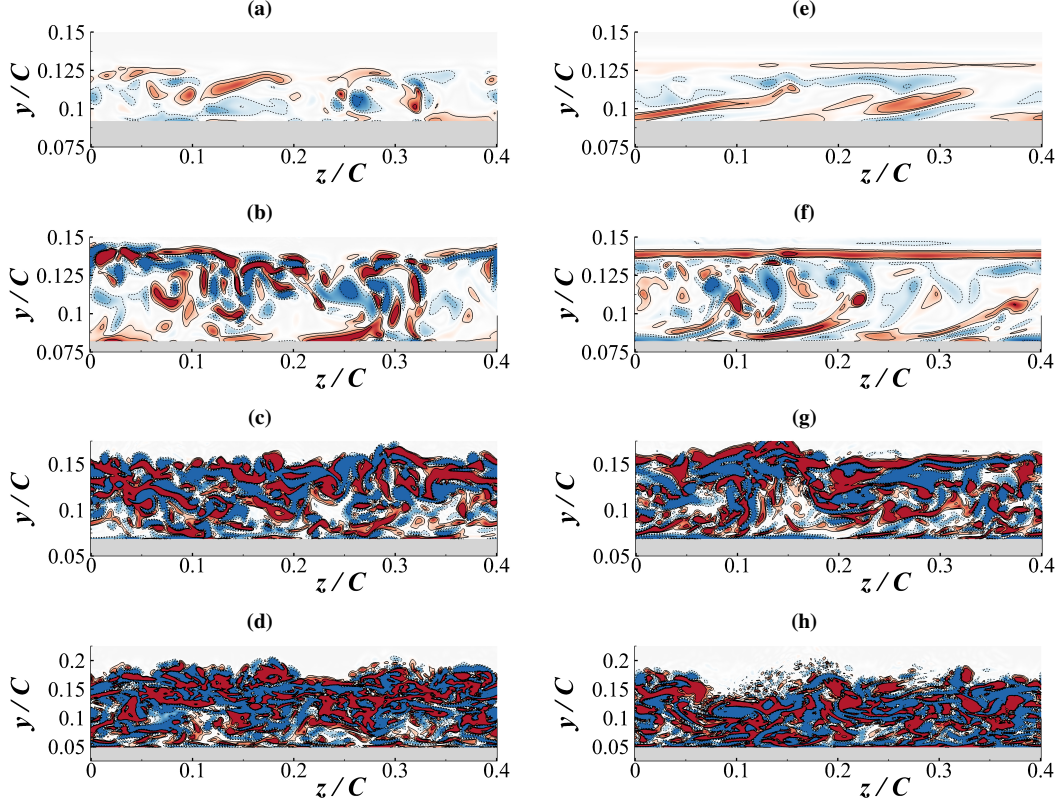
Figure 4.17: Flow condition: $\alpha = 5^o$, laminar inlet. (Left column) Straight wing, (Right Column) Swept wing. Instantaneous contours of $\omega'_x C/Q_\infty$ pictured on z-aligned slices for subsequent chordwise locations on the wing suction side. Location respectively at $x/C = [0.50, 0.60, 0.70, 0.80]$ in [(a-e), (b-f), (c-g), (d-h)]. Colour map such as positive perturbations in red with solid iso-lines at $\omega'_x = [5, 10, 20]Q_\infty/C$, blue and dashed lines for negative perturbations.

different streamwise locations (i.e. $x/C = [0.50, 0.60, 0.70, 0.80]$). The difference in the streamwise vorticity field between the two wings, becomes particularly clear when comparing its spanwise coherence in the region spanned by the detached shear layer especially within the x- range $\Delta x/C = [0.50, 0.60]$ at $y/C = 0.125$, visible in figures 4.17a and 4.17e, and at $y/C = 0.1375$, as it is shown in figures 4.17b and 4.17f.

For a more quantitative comparison of the shear layer structure and its instability in the two wings configurations, in figure 4.18 the spectrum of the fluctuating energy (defined in equation 4.5) extracted at $x/C = 0.55$ and premultiplied by the spanwise wavenumber k_z is considered. Similarly to figure 4.12, the figure shows the energy content as a function of the spanwise wavelength λ_z and the y/C coordinate. When comparing the distributions of the two wings within the interval $\Delta y/C = [0.125 - 0.150]$ (selected because containing the spatial region occupied by the shear layer at this particular streamwise location), in the unswept case the energy is noticed to spread for $\lambda_z > 0.2C$ with a rather isolated peak located at $\lambda_z = 0.05C$. Differently, in the swept case the energy is confined in the spanwise

(a)

(b)
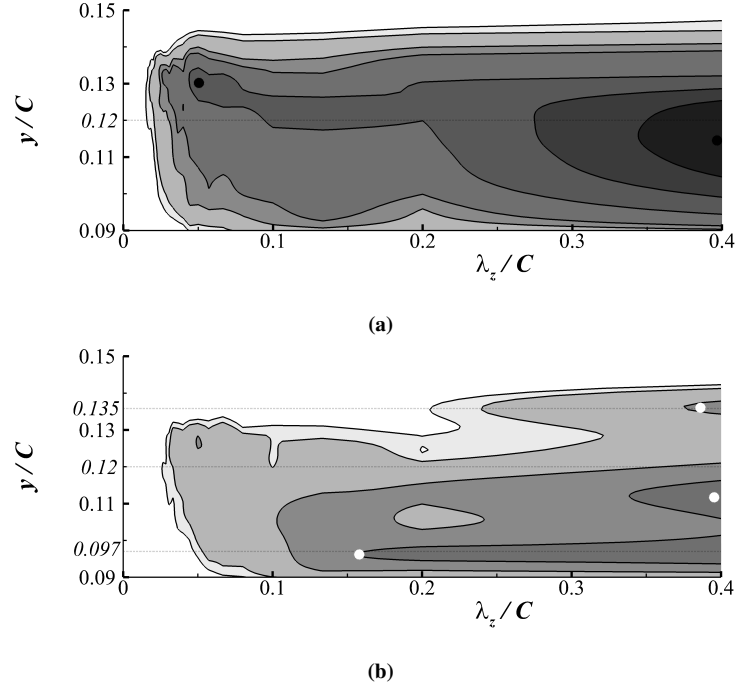
Figure 4.18: Iso-contours of $k_z < \hat{E}^* >_t C$ extracted at $x/C = 0.55$. The grey-scale colour map is distributed non-linearly with the black regions corresponding to $k_z < \hat{E}^* >_t C > 0.001$ as in figure 4.12a. The iso-lines are sampled for $k_z < \hat{E}^* >_t C = [0.02, 0.03, 0.07, 0.1, 0.2, 0.35, 0.5, 1]$. Panel (a) Straight wing case; black dots are used to highlight the maxima. Panel (b) Swept wing case; white dots used to indicate the maxima.

wavelengths interval $\lambda_z > 0.25C$. This observation suggests that in the two wings, the K-H rollers are broken by a spanwise modulation of different wavelengths. In particular, in the case of the swept wing the spanwise modulation takes place at a larger wavelength λ_z.

4.3.3 Regions violating the *Simple Sweep Theory*

The three-dimensional breakdown of the shear layer that envelops the recirculating regions has been shown to present different features in the swept and the unswept wing cases. It is therefore expected that beyond the location at which the shear layer undergoes a laminar/turbulent transition (i.e. at $x/C \approx 0.6$), also the average portrait of the two flow fields will be different and the *Simple Sweep Theory* won't hold locally any more. In figure 4.4b, showing the wall pressure distribution, a difference between the chord-aligned $< C_{p_x} > z, t$ of the two wings is seen to become non negligible downstream of the mentioned location and definitely clear beyond $x/C \simeq 0.75$. From this location on, it is also possible to notice a difference in the value and distribution of the boundary layer shape factor reported in figure 4.11c. The chordwise distribution of the mean skin friction coefficient $< C_{f_x} > z, t$ is also affected by the sweep as visible in figure 4.19. Concerning this last quantity, it is important to highlight that when dealing with a mean crosswind, the skin friction coefficient can be
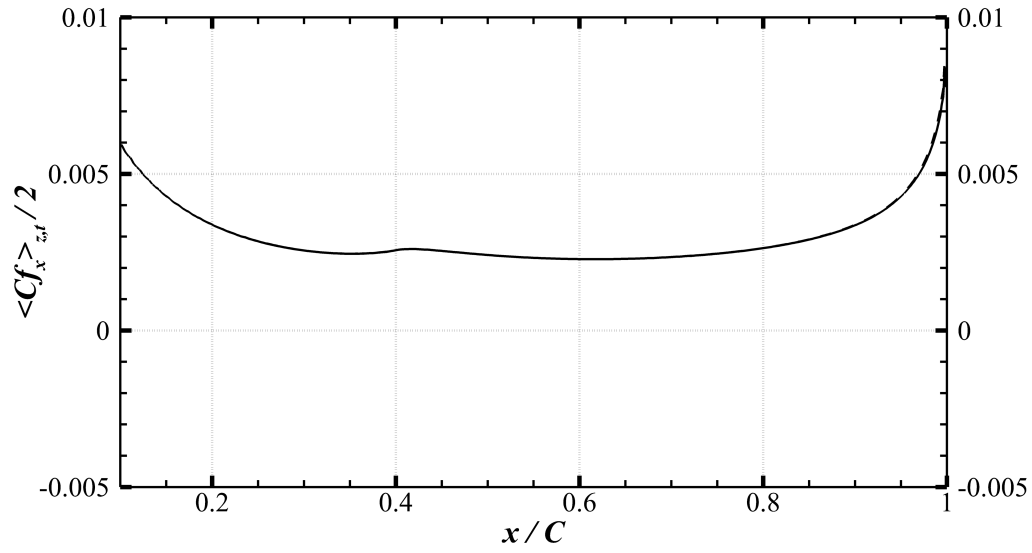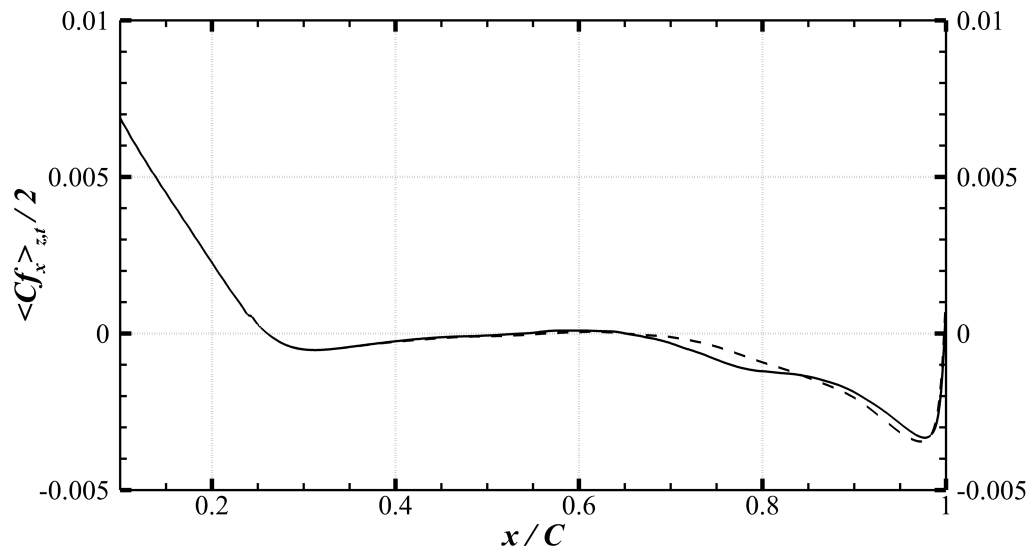
Figure 4.19: Distribution of $< C_{f_x} > z, t$ on the pressure (a) and suction (b) sides of the wings. Solid lines are used to represent the straight wing case; dashed lines refer to the swept wing case.

defined in different ways depending on the chosen value of the scaling pressure (i.e. the selection of the free stream velocity forming the dynamic pressure) and on the component of the wall stress vector $\vec{\tau^w}$ that in the swept case is oblique to the chord. Here, in order to provide a direct insight on the validity of the *Simple Sweep Theory*, only the mean chordwise friction coefficient is considered, $< C_{f_x} >_{z,t} (x,y) = 2 < \tau^w_{sn} >_{z,t} (x,y)/\rho Q^2_\infty$ (note that τ^w_{sn} is the component in the chord plane, along the direction s (outlining the foil) of the wall stress vector $\vec{\tau^w}$ acting on the wing surface with normal n). The distribution of this quantity along the suction side of the foils is shown in figure 4.19b. Once more, it is noticed that the $< C_{f_x} >_{z,t}$ distributions of the two wings start deviating beyond the chord location at $x/C = 0.75$. Consistently with the values of the pressure and skin friction coefficients, also the mean vertical velocity component $< v >_{z,t} (x,y)$ in the two cases does not match any more when evaluated downstream of the mentioned chord location. The variation in the distribution of $< v >_{z,t}$ when the sweep is introduced can be appreciated by looking at three selected profiles shown in figure 4.20a. From these wall-normal profiles extracted at chord locations $x/C = [0.65, 0.8, 1.0]$, it is possible to notice that the sweep induced difference of the velocity profiles at $x/C = 0.8$ becomes larger than 15% at the distance of $0.025 \, C$ from the wall.

When considering higher order statistical quantities the variations in their distributions become even more remarkable indicating that for the last quarter of the foil the *Simple Sweep Theory* is considerably violated. In figure 4.20b the wall-normal profile of the mean vertical component of the Reynolds stress tensor, $< v'v' >_{z,t} (x,y)$, is presented for three chord locations at $x/C = [0.65, 0.8, 1.0]$. At $x/C = 0.8$ the difference between the profile is observed to be larger than 15%. A similar deviation is observed when considering the off-diagonal Reynolds stresses $< u'v' >_{z,t} (x,y)$ and $< v'w' >_{z,t} (x,y)$, shown in figures 4.20c and 4.20d, respectively. For both quantities, the difference between the two chordwise flows takes on larger values upstream of the location previously indicated for the diagonal $< v'v' >$ component (see the profiles at $x/C = 0.65$). Once more, the difference in the distribution of the Reynolds stresses downstream of the separation point indicates that the three dimensional breakdown of the shear layer and the consequent turbulence transition are driven by different instability mechanisms in the two wings configurations.
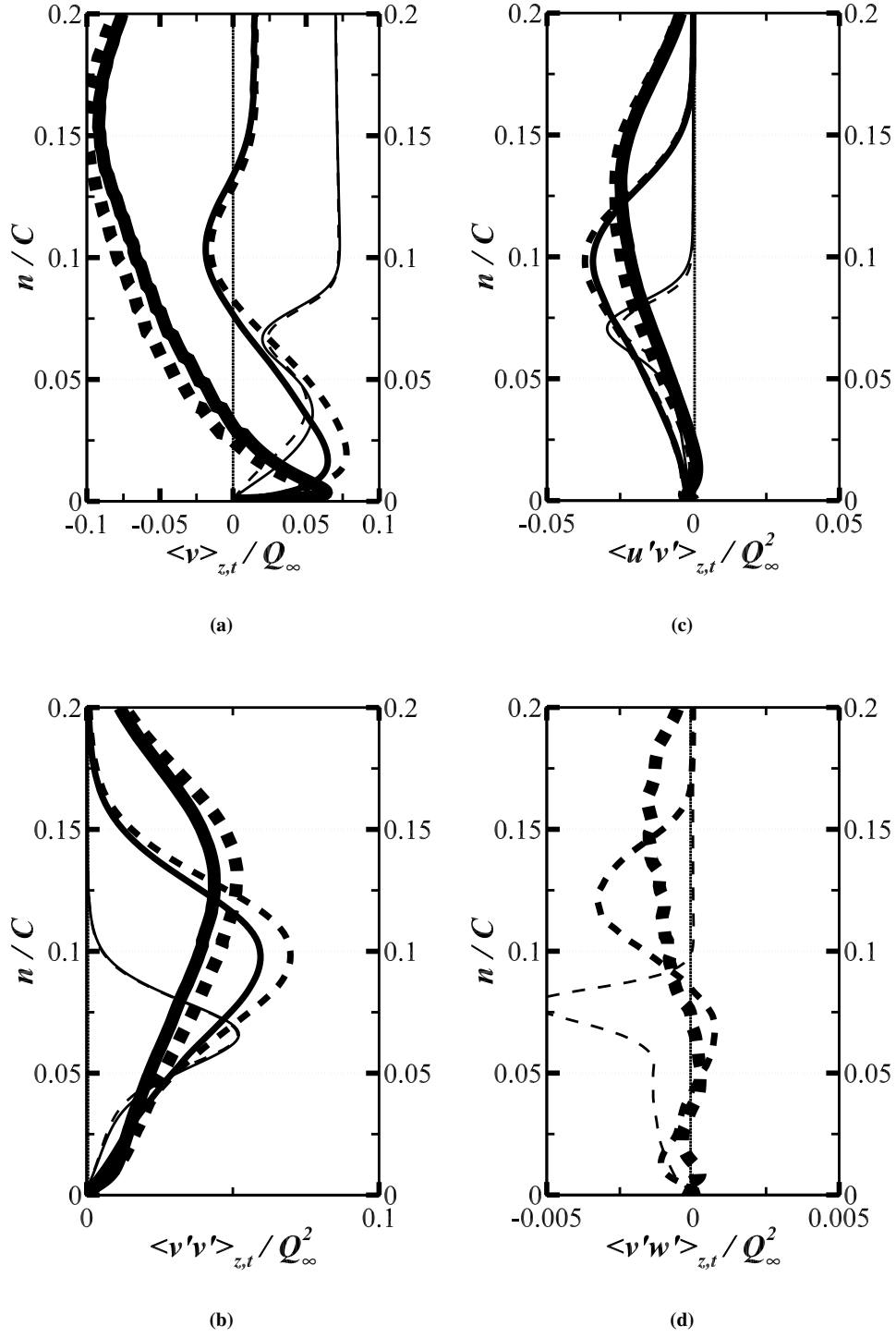
Figure 4.20: Wall normal distribution of (a) $< v >_{z,t} /Q_\infty$, (b) $< v'v' >_{z,t} /Q^2_\infty$, (c) $< u'v' >_{z,t} /Q^2_\infty$ and (d) $< v'w' >_{z,t} /Q^2_\infty$. Solid line refers to the straight wing case, the dashed one for the swept wing. In (d) the values for the straight wing are not presented because trivially equal to zero. Profiles extracted at $x/C = [0.65, 0.8, 1.0]$ and drawn with a thicker line moving downstream.

4.3.4 Flow structure inside the mean reversed flow region

Since the separating shear layer breakdown occurs following different routes in the wings configurations, the flow close by the wall in the recirculating region is expected to be characterised by different flow features. A qualitative support to this estimate can be drawn from figure 4.17 showing an instantaneous snapshot of the $\omega'_x(x, y, z, t)$ distribution visualised on spanwise slices at $x/C = [0.50, 0.60, 0.70, 0.80]$. One can easily see that already in the first chordwise location at $x/C = 0.5$ (see figures 4.17a and e for the straight and the swept wing, respectively) the flow pattern is quite dissimilar in the two wings configurations, especially in the range $\Delta y/C = [0.09 - 0.11]$. In the straight wing case, the footprints of the vortex cores aligned in the streamwise directions with alternating signs can be easily detected. These vortices appear to be quite coherent spanning a lateral size of about $0.05C$ and with an height of $2\%C$ which corresponds to half the displacement thickness of the boundary layer at this x location. Differently, in the swept case the streamwise vortices appear to be stretched in the spanwise direction (showing a width of $0.1C$) and also tilted with respect to the wall. Further downstream, at $x/C = 0.6$, corresponding to figures 4.17b and f, the above described flow patterns seem to develop on a shorter wavelength although keeping the same structure. Marching even further downstream at $x/C = 0.7$ (see figures 4.17c and g), the different flow organisation of the two wings is still clear, at least within a narrow layer of about $20\%\delta^*$ thickness neighbouring the wall. From the snapshots extracted at this location, in the swept wing case the inclined and spanwise stretched vortices have a spanwise size of $\approx 0.05C$ and an height of $\approx 0.20\delta^*$. At the final cross section considered, at $x/C = 0.8$, shown in figures 4.17d and h, the iso ω'_x contours take on a much more complex topology that corresponds to a turbulent state. In this condition it becomes impossible to detect any significant difference between the two cases without resorting to a more quantitative analysis.

A confirmation of the qualitative observations, that have been put forward above, come from the premultiplied energy spectrum of the fluctuating field $k_z < \hat{E}^* >_t$ which has been defined in equation 4.5. In particular, figure 4.18 shows that close to the first considered chordwise location (i.e. at $x/C = 0.55$) the energy content in the vertical range of interest here (i.e. in the interval $y/C = [0.09 - 0.120]$) is topologically different in the two wings scenarios. In the swept case an energy maximum appears at $y/C = 0.097$ with the energy content spread in the range $\Delta \lambda_z = [0.15 - 0.4]$. Differently this energy peak is not detected in the straight wing counterpart.

In the swept case, at this same y location the mean spanwise velocity profile does not appear to be inflected. This can be noticed from figure 4.15d showing the curvature of the spanwise mean velocity profile at the chord location $x/C = 0.6$, close to those mentioned earlier.

The absence of a mean inflection point might suggest that the vortex stretching in the z direction is not originated by an instability but it is rather due to the combined action of the chordwise flow and the mean spanwise flow. These combined actions generate a family of quasi-spanwise, spiralling vortices. This conjecture has already been put forward in previous studies that highlighted the presence of these coherent vortices with a spiralling topology within the core of a separated region when a swept wing flow is considered (e.g. Davis et al. (1987), Broadley (1998), Kaltenbach & Janke (2000), Hetsch & Rist (2009)). An heuristic explanation for the emergence of spiralling vortices is based on the recognition that the momentum in the recirculation region in the cross plane x-y has no privileged directionality and that the crosswind can locally have a dominant effect deviating the roll-up of the recirculating bubble in the spanwise direction. The mean flow deviation in the spanwise direction is also visible from the mean spanwise velocity $< w >_{z,t}$ profiles sampled within the early portion of the mean separated region. In figure 4.15c, the mean spanwise velocity profile at $x/C = 0.6$ clearly shows a changing behaviour above and below of $n/C = 0.059$ that resembles the one of two superimposed boundary layers. The upper one is caused by the outer spanwise flow that sees the underneath recirculating flow as a region of fluid of different effective viscosity. Similarly to the case of flows over a porous media, one could assign a separated, virtual origin to the outer flow and the mean crosswind may be predicted as an effective superposition of two boundary layers of different nature.

4.3.5   Statistical analysis of the reversed flow

For both the considered wing configurations, an instantaneous visualisation of the chordwise component of the wall friction is provided in figure 4.21. Using the same notation as in section 4.3.3, the instantaneous component of the wall stress vector $\vec{\tau^{w}}$ along the foil line s acting on the wing surface with normal n is referred as $\tau_{sn}^{w}(x, y, z, t)$. The separation location is easily detected for both wing configurations at $x/C \simeq 0.26$. The friction distribution on the portion of the wing interested by the reversed flow is noticed to be topologically different in the two configurations, with the iso-friction lines distorted by the action of the crosswind in the spanwise direction in the swept wing case. This is in agreement with the previous findings presented in section 4.3.4.

(a)

(b)
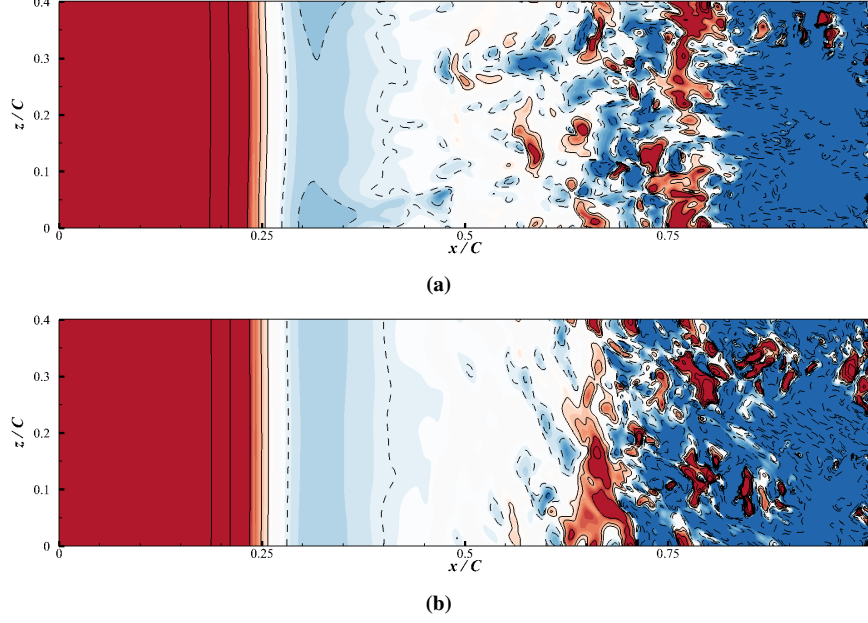
Figure 4.21: Iso-contours of $\tau^w_{sn}/(\rho Q^2_\infty)$ on the suction side wall. Flow condition: $\alpha = 5^o$, laminar inlet. Top: straight wing; Bottom: swept wing. The red colour is used for positive friction values (the y axis is pointing upwards), blue for negative ones.

Following Vinuesa, Örlü & Schlatter (2017) and Brücker (2015) to quantify the reversed flow one can compute the time averaged cumulative probability to observe a backflow event along the span for all the chord stations along the wing, i.e.

$$\wp(\tau^w_{sn} < 0)(x,n) = < \frac{1}{L_z} \int_0^{L_z} \epsilon \, dz >_t \quad \text{with} \quad \begin{cases} \epsilon = 1 \text{ if } \tau^w_{sn}(x,n,z,t) < 0 \\ \epsilon = 0 \text{ if } \tau^w_{sn}(x,n,z,t) \geq 0 \end{cases} . \quad (4.7)$$

The computed distribution of $\wp(\tau^w_{sn} < 0)$ along the chord is shown in figure 4.22. It is interesting to note that no locations have $\wp = 1$ (i.e. a guaranteed separation), but it has a certain chordwise probabilistic distribution. This suggests that the laminar separation front is not a two-dimensional process in the spanwise direction, but it is affected by a certain spanwise modulation. The three-dimensional effect is however fairly small, since the chordwise probabilistic distribution has a base of only $1\%C$ around the location $x/C = 0.26$.

Because of the introduction of a preferential flow direction, the sweep is found to reduce even further the three-dimensionality of the separation front observed in the straight wing case. The most likely location of separation is found with a probability of $\wp = 65\%$, higher than the $\wp = 56\%$ recorded in the unswept case. Consequently, the chordwise probabilistic distribution of the separation location is narrower in the swept case, being $0.7\%C$. Further downstream, the crosswind induced by the sweep has an effect on the probabilistic distribu-
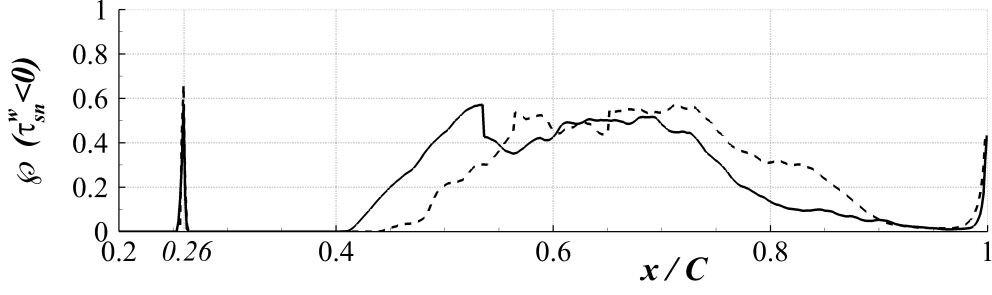
Figure 4.22: Distribution of $\wp(\tau_{sn}^w < 0)$ along the chord on the suction side wall. The solid line is used for the straight wing and the dashed line for the swept wing.

tion of the skin friction when the flow is reversed on the average. Overall, it is noticed that the probability distribution of having a separated flow is strongly affected by the sweep. In this case, all the separated area is shifted downstream giving a further confirmation that the *Simple Sweep Theory* does not apply (or at least not completely) when separation occurs on the wing.

A further characterisation of the sweep effect on the flow topology inside the reversed flow region can be obtained by considering the statistical analysis of the instantaneous flow direction. In particular, the time averaged cumulative probability along the span of observing a planar (parallel to the foil wall) instantaneous flow realisation aligned with the mean planar flow direction for all the chord stations along the wing is considered. The probability is defined as:

$$\wp((\bar{u} \bullet < \bar{u} >_{z,t}) < 0)(x,n) = < \frac{1}{L_z} \int_0^{L_z} \epsilon \, dz >_t \quad \text{with} \quad \begin{cases} \epsilon = 1 \text{ if } cond < 0 \\ \epsilon = 0 \text{ if } cond \geq 0 \end{cases} \quad (4.8)$$

and $cond = [u(x,n,z,t) < u >_{z,t} (x,n) + w(x,n,z,t) < w >_{z,t} (x,n)]$.

Figure 4.23 shows the resulting distribution of $\wp((\bar{u} \bullet < \bar{u} >_{z,t}) < 0)$ on different planes parallel to the foil suction side at a distance of $n/C = [0, 0.008, 0.018, 0.030, 0.050]$. The flow inside the reversed flow region in the wall vicinity (i.e. $n/C = 0, x/C > 0.4$, the thinnest line in figure 4.23) has a completely different probability distribution to be found in the direction of the mean flow when the two wings are compared. In the unswept case the flow has no a preferential direction, having an almost 50% probability to be found in the direction of the local mean flow. Conversely, the flow on the swept wing is the most of the time aligned with the mean local velocity. The mean velocity on the swept wing has been shown by the attached character of the spanwise boundary layer (see for example the
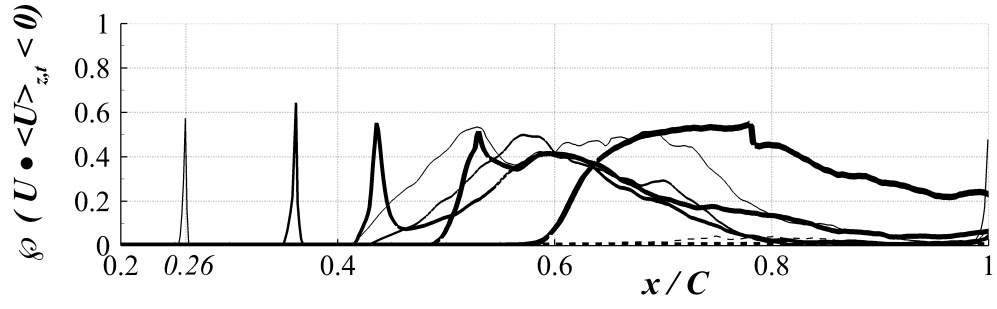
Figure 4.23: Distribution of $\wp(\bar{u} \bullet < \bar{u} >_{z,t} < 0)$ along the chord on different planes parallel to the foil suction side at a distance $n/C = [0, 0.008, 0.018, 0.030, 0.050]$. A thicker line is used for planes further away from the wall. The solid line is used for the straight wing and the dashed line for the swept wing.

spanwise shape factor H_z distribution in figure 4.11c) to have always a positive spanwise component. Similar observations can be made when the same analysis is extended to the other planes at increasing distances from the wall. This is a confirmation of the spanwise spiralling pattern of the reversed flow on a swept wing.

Chapter 5

Turbulent separation

Next, the comparisons between a swept and an unswept wing is presented when a turbulent incoming free stream is considered (FST) to trigger a developing turbulent boundary layer on the wing. Two different incidences have been investigated, namely 5° and 10°. The respective boundary layers that develop on the wing suction side present a different amount of flow detachment. The chapter is structured as follows. Section 5.1 focuses on the overall effect of the FST injection on a baseline laminar flow field for the unswept wing, for which the fully laminar behaviour was presented in section 4.1. The additional effect of the foil incidence variation is also considered in this section. Sections 5.2 and 5.3 present extensive comparisons between the swept and the unswept flow configurations for both incidences. In particular, in 5.2 the overall sweep effect on the flow field is considered, while in 5.3 some more specific flow mechanisms are discussed.

As already done in the previous chapter for the laminar incoming free stream condition, all the results that will be presented for both swept and unswept wings have been obtained by statistically averaging within a non-dimensional time period $\Delta t^* = \Delta t Q_\infty / C \simeq 70$ for the 5° incidence case, and $\Delta t^* \simeq 30$ for the 10° case. Roughly, the considered time window corresponds to 11 full domain flow-through cycles in the low incidence case and 5 in the higher one. The short time averaging window used for the higher angle of attack is justified by the stabilising character of the FST on the unsteady flow behaviour, which will be discussed in section 5.1.2. Once again, in accordance with the *Simple Sweep Theory* , the comparison between swept and unswept wing is made considering statistical values accumulated along the x direction only.

5.1 Unswept wing with free stream turbulence

5.1.1 Mean two-dimensional flow fields

When considering the 5° incidence, the injection of a 10%-intense free stream turbulence on the incoming laminar flow causes the full suppression of the suction side LSB, thanks to an enhanced mixing motion at the wall (Schlichting & Gersten 2000). The overall change between the flow with and without FST injection can be observed by comparing the contours of the mean chordwise velocity component $<u>_{z,t}(x, y)$ in the two conditions, as depicted in figure 5.1 and 4.1. It is recalled that in figure 4.1 (no FST), the iso-lines were used to identify low and negative values of the chordwise velocity component. By inspection of the figure, one can quantify a 10%C normal-to-the-wall size of the flow region with a velocity $<u>_{z,t} \leq 0.2$ at the trailing edge, indicating a thick boundary layer. Looking at figure 5.1 (with FST), it can be noticed that the LSB has been completely suppressed. Furthermore, from the figure one can quantify a thickness of 7%C for the region with velocity $<u>_{z,t} \leq 0.9$ at $x/C = 1.0$, indicating a critically thinner boundary layer on the suction side as compared to the one of the previous case. These preliminary observations already clearly show the different structure of the flow field when the FST is injected, especially on the suction side. The only common feature of the two flow fields is the mean location of the leading edge stagnation point, which is recorded for both cases at $(x/C, y/C) = (0.001, -0.003)$.

When the incidence is set to $\alpha = 10^o$ within the same FST intensity, a mean boundary layer separation appears to take place on the suction side. An overview of the flow field is presented qualitatively in figure 5.2 using iso-contours of the mean chordwise velocity component $<u>_{z,t}$. A first difference with respect to the 5° case with FST (presented in figure 5.1) is the estimated thickness of 10%C for the region with velocity $<u>_{z,t} < 0.9$ at $x/C = 1.0$. The boundary layer is found to be thicker than that in the lower incidence condition. Furthermore, the appearance of mean reversed flow in the very rear part of the wing suction side, beyond $x/C > 0.91$, can be observed. The mean separated area in figure 5.2, i.e. the flow region with negative chordwise velocity, has been coloured with a light green colour. The light green area on the top of the trailing edge indicates that the separated area is only 1%C in height. A more quantitative footprint of the mean turbulent separation is given by the comparison of the suction side $<C_{f_x}>_{z,t}$ distribution between the FST cases shown in figure 5.3b. In the highest loading condition, alongside a lower friction at the wall from $x/C \simeq 0.45$, a sign change at $x/C = 0.91$, marking the mean separation location, is also observed. Although the flow separation is fairly small, it suggests a different
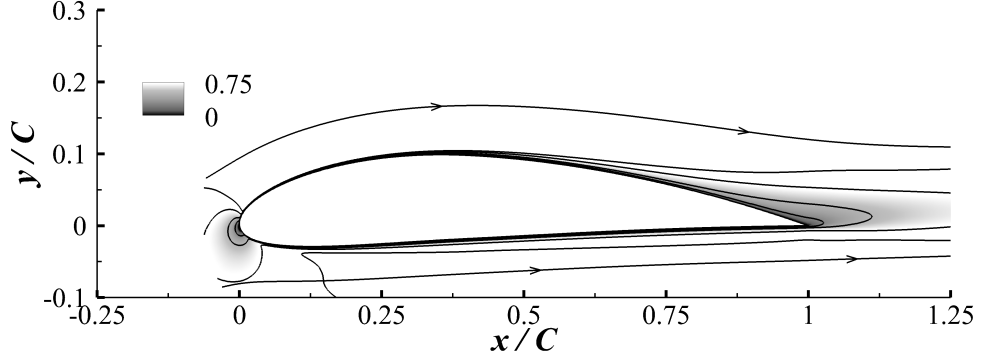
Figure 5.1: Contours of $< u >_{z,t}$ in the unswept wing configuration at 5° incidence with FST, quantified by iso-lines at $< u >_{z,t}= [0.25, 0.50, 0.75, 0.90]Q_\infty$. The grey-sale colour map is adjusted for having the white colour corresponding with values $< u >_{z,t} \geq 0.75Q_\infty$. Few streamlines are identified by the arrowed solid lines.
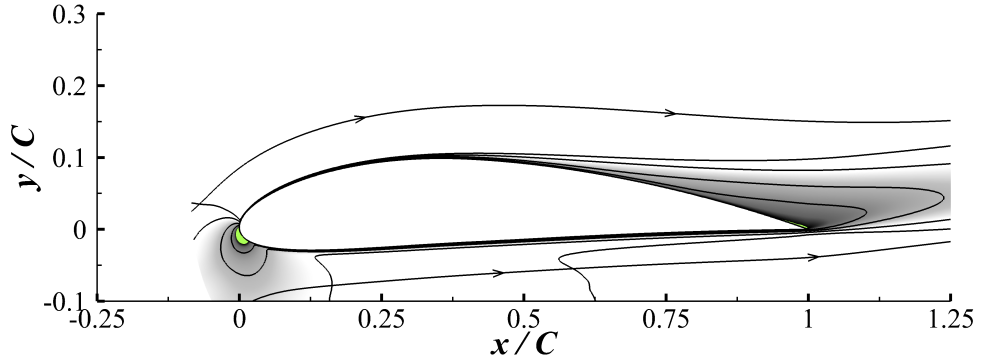
Figure 5.2: Contours of $< u >_{z,t}$ in the unswept wing configuration at 10° incidence with FST, quantified by iso-lines at $< u >_{z,t}= [0.25, 0.50, 0.75, 0.90]Q_\infty$. The grey-scale colour map is adjusted for having the white colour corresponding with values $< u >_{z,t} \geq 0.75Q_\infty$ and black colour corresponding with $< u >_{z,t}= 0Q_\infty$. Negative values of $< u >_{z,t} /Q_\infty$ are illustrated with light green contours. Few streamlines are identified by the arrowed solid lines.

flow dynamic process taking place at the trailing edge portion of the wing. The size of the separated region is tiny, if compared to that of the LSB discussed in chapter 4.

It is also noticed that at higher incidence, the mean location of the leading edge stagnation point moves at location $(x/C, y/C) = (0.002, -0.009)$ on the bottom side, downstream of the position recorded for the lower incidence case. It is remarked that the light green region on the profile nose $(x/C = 0)$ does not correspond to a boundary layer separation. In this location, the negative values of the chordwise velocity are caused by the fluid having to go past the profile nose flowing from the stagnation point to reach the suction side.

Concerning the numerical resolution used in the three directions of the structured mesh, the grid spacings have been kept below the standard values recommended for wall bounded turbulent flows (Kim et al. 1987) due to the turbulent character of the boundary layer that will be discussed in section 5.1.3. In particular, for both the incidences the following inequalities

are satisfied: $\Delta s^+ = \Delta s u_\tau / v < 5$, $\Delta n^+ = \Delta n u_\tau / v < 0.8$ and $\Delta z^+ = \Delta z u_\tau / v < 5$. Note that Δs, Δn and Δz indicate the spacing of the grid in the three directions of the mesh basis: s along the foil surface lying in the chord plane, n in the same plane and normal to s and z in the spanwise direction. $u_\tau = \sqrt{\tau_{sn}^w / \rho}$ is the friction velocity. This is based on τ_{sn}^w which is recalled to be the component in the chord plane, along the direction s (outlining the foil) of the wall stress vector $\vec{\tau^w}$ acting on the wing surface with normal n.

5.1.2 Pressure field and flight condition

The pressure distribution along the aerofoil in the unswept wing case changes radically when changing the incoming flow conditions (i.e. incidence and incoming turbulence level). Figure 5.3a shows the distribution of the pressure coefficient for the three flow scenarios that have been considered in the unswept wing configuration. Along the lower side of the aerofoil the pressure increases monotonically for all three cases: the laminar incoming flow case at 5° incidence, the case at same incidence with FST and the 10° incidence with FST. On the suction side, the wide plateau linked to the LSB of the laminar incoming case ($< C_{p_x} >_{z,t} /2 = -0.25$ for $\Delta x/C = [0.40 - 0.65]$) is completely suppressed for both the FST cases. The suction peak depression increases in strength and moves upstream when going from laminar to FST and when increasing the angle of attack: $< C_{p_x} >_{z,t} /2 = -0.4$ at $x/C = 0.07$ for the laminar incoming flow case, $< C_{p_x} >_{z,t} /2 = -0.6$ at $x/C = 0.03$ for the turbulent incoming flow case at 5° incidence and $< C_{p_x} >_{z,t} /2 = -1.5$ at $x/C = 0.01$ for the 10° incidence with FST.

In general, the wing lift is increased and the total drag decreased when FST is injected into the flow field. The lift coefficient is $C_l = 0.54$ for the laminar case, $C_l = 0.85$ for that at 5° with FST and $C_l = 1.27$ for 10° with FST. The chordwise drag coefficients are $C_{d_x} = 0.066$, $C_{d_x} = 0.032$ and $C_{d_x} = 0.049$ respectively for the three cases. In the 5° incidence FST case, the lift coefficient almost doubles thanks to the suppression of the LSB on the suction side of the foil and then further increases at higher incidence, although keeping below the stall limit value of the aerofoil. It is interesting to note that the drag coefficient decreases introducing the FST, for both angles of attack. It will be shown later that the FST triggers the boundary layer from a laminar to a developing turbulent condition from the very early stage of the wing. Thus, it is concluded that the overall drag reduction is directly linked to the LSB suppression: i.e. the reduction in pressure drag overrides the increased skin friction drag related to the developing turbulent boundary layer. To support this statement, the suction side, chordwise wall friction coefficient is presented in figure 5.3b
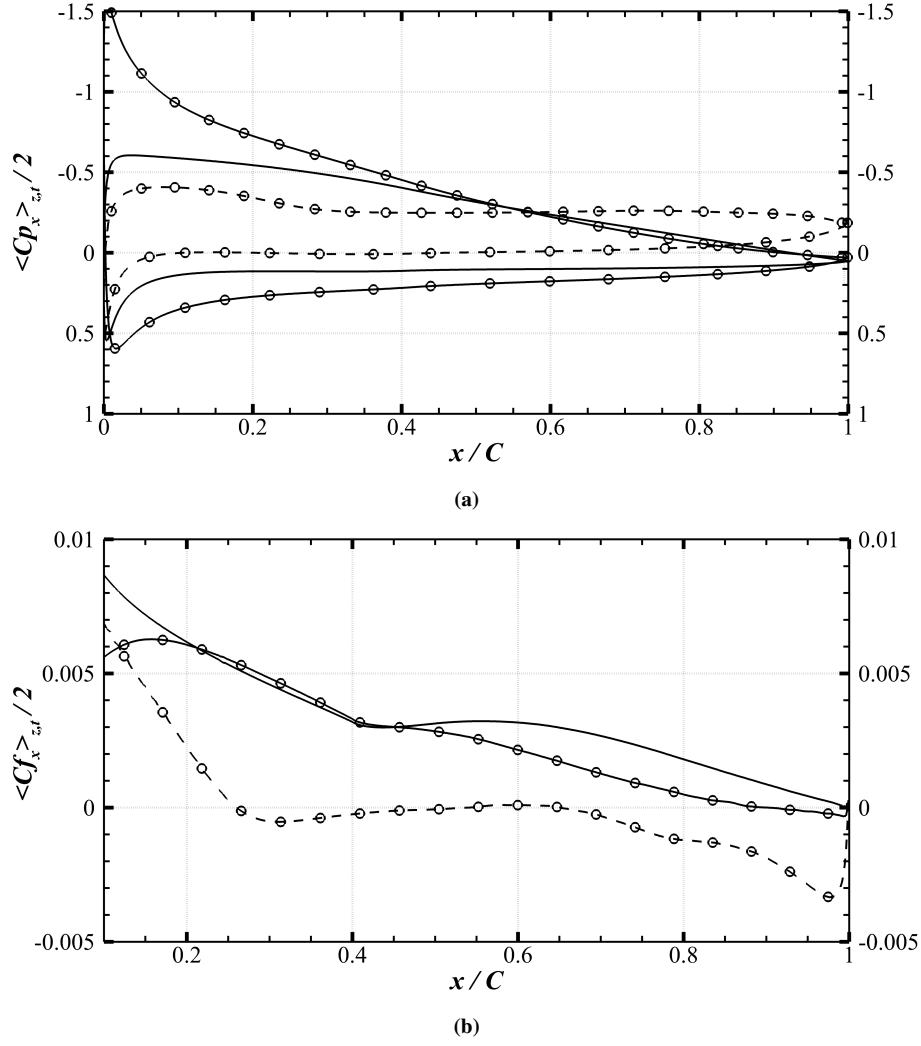
Figure 5.3: (a) Wall distribution of $< C_{p_x} >_{z,t}$ of the unswept wing for both aerofoil sides and incidences. In dashed circled line the laminar incoming case at 5° incidence, in solid line the turbulent incoming case at 5° incidence and in the solid circled line the turbulent incoming case at 10°. (b) Suction side wall friction coefficient of the chordwise flow of the unswept case for chord locations of major interest. Line styles same meaning as in panel (a).

for all the three cases discussed here. In the laminar case, the distribution of the friction is smaller than those of the turbulent cases, for any incidence, along the whole attached portion of the boundary layer. Thus, the overall drag reduction can be only explained with the LSB suppression and the consequent pressure drag reduction. This is just a confirmation of the widely known concept stating that an early and sudden transition to turbulence of the flow often brings an overall drag benefit for those cases where a fully attached laminar condition cannot be achieved.

Not only the mean values of the aerodynamic coefficients are modified in the three conditions, but also their fluctuating behaviours. A measure of this variation is given by the standard deviation of the lift and drag time history. In the laminar inflow condition, it is

found $\sigma_{LIFT} = 5\%$, while for both loading conditions in the FST case $\sigma_{LIFT} = 1\%$. Concerning the drag, it is found $\sigma_{DRAG} = 2.5\%$ for the laminar case, $\sigma_{DRAG} = 1\%$ for the turbulent case at the lower incidence and $\sigma_{DRAG} = 1.5\%$ for the higher angle of attack case. Although the lift and the drag are integral quantities, that do not provide information on the flow dynamics, their variations provide an initial insight on the FST effect. The reduced variance of the lift and drag is simply linked to the suppression of the LSB, that otherwise introduces highly variable and unpredictable dynamics being governed by several flow scales (some comparable to the wing chord, others to the boundary layer thickness) (Gaster 1967, Jones et al. 2008, Yarusevych et al. 2009, Marxen & Henningson 2011, Jagadeesh et al. 2013).

5.1.3 Boundary layer structure

The modalities by which the turbulent perturbations added at the free stream trigger the boundary layer transition to turbulence depend on the specific receptivity mechanisms of the boundary layer (Brandt et al. 2004, Balzer & Fasel 2016), thus ultimately on the properties of the added perturbations. Here, receptivity is defined as a measure of the energy transfer from the introduced perturbation to the energy content of the boundary layer. This transfer can take place in several ways and is bounded by an eventual saturation level in the boundary layer. Physically, this transfer occurs through the activation or modification of some flow structures and their interaction mechanisms, that persist until the appearance of a stable configuration. The saturated response of a laminar boundary layer is referred to as the *by-pass transition mechanism* (Morkovin 1993). When this condition is attained, the specific features of the boundary layer and that of the introduced perturbation are not crucial any more as turbulence is almost suddenly triggered.

In the present investigation, the injected perturbation is sufficiently intense, spanning a broad frequency spectrum to cause a by-pass transition mechanism as for the Blasius boundary layer in Brandt et al. (2004). The resulting, sudden inception of turbulence renders the foil boundary layer very different from the laminar one, even in its initial portion. In the previous chapter, the wing boundary layer was keeping its laminar character for a large extension of the wing and its transition to turbulence was taking place on the rear part of the wing. When FST is injected, regardless of the incidence, the boundary layer begins the transition to turbulence process from the very early stage of the wing via a by-pass mechanism, on both the aerofoil sides. More details on the by-pass mechanism taking place at the investigated incidences will be shown and discussed in 5.3.1. Here, it is anticipated that
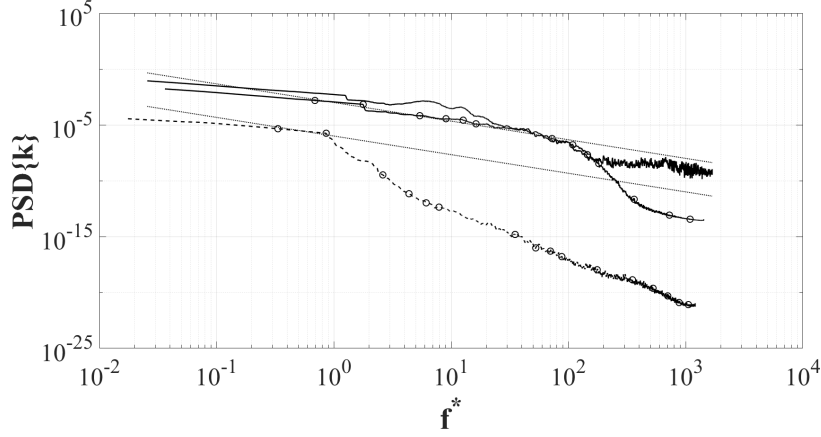
Figure 5.4: $PSD\{k\}$ obtained at $(x/C, y/C, z/C) = (0.25, 0.11, 0.20)$ from the unswept flow fields. The lines have the same meaning as in figure (5.3). The dotted lines correspond to the power law, duplicated and shifted for visualization purposes.

they resemble the Klebanoff modes as in Brandt et al. (2004). The different states of the boundary layer for the three considered configurations are clearly visible in figure 5.4. The figure shows the power spectrum of the non-dimensional turbulent kinetic energy time signal, $PSD(k)$, as defined in equation 4.2, acquired in the early wing location $x/C = 0.25$ at a normal-to-the wall distance of $n/C = 0.005$ at mid span $z/C = 0.2$. The fluctuating energy content of the laminar inlet case is negligible on the whole spectrum ($PSD(k) < 10^{-5}$ for all $f^* = fC/Q_\infty$), indicating a laminar condition. Both the turbulent free stream cases share a negligible energy content beyond $f^* > 100$ (keeping the same nominal threshold to consider negligible values as done for the laminar case) presenting a fairly extended inertial range of the spectrum which indicates a developing turbulent boundary layer ($1 < f^* < 100$).

The spectra in figure 5.4 show that the higher incidence case has a more developed spectrum that approaches the isotropic turbulence one, with a $-5/3$ power law for an extended range of frequencies. In the low incidence scenario the inertial range is not fully developed, with the large energetic scales, inherited from the grid turbulence superimposed at the inlet, leaving a footprint in the range between $2 < f^* < 20$. This could be interpreted as a slower receptivity dynamics of the energy injected by the FST in the lower incidence case.

To characterise the developing boundary layer along the suction side of the straight wings at the two incidences, some velocity profiles scaled with viscous quantities (i.e. ν and u_τ) are shown in figure 5.5. The profiles are extracted at the locations $x/C = [0.20, 0.65, 1.0]$ and show the distribution of $u^+ = u/u_{tau}$ as a function of $n^+ = nu_\tau/\nu$, where n is the wall normal direction. A developing turbulent boundary layer can be observed for both the incidences. In particular, at higher incidence an extended logarithmic region from an

103
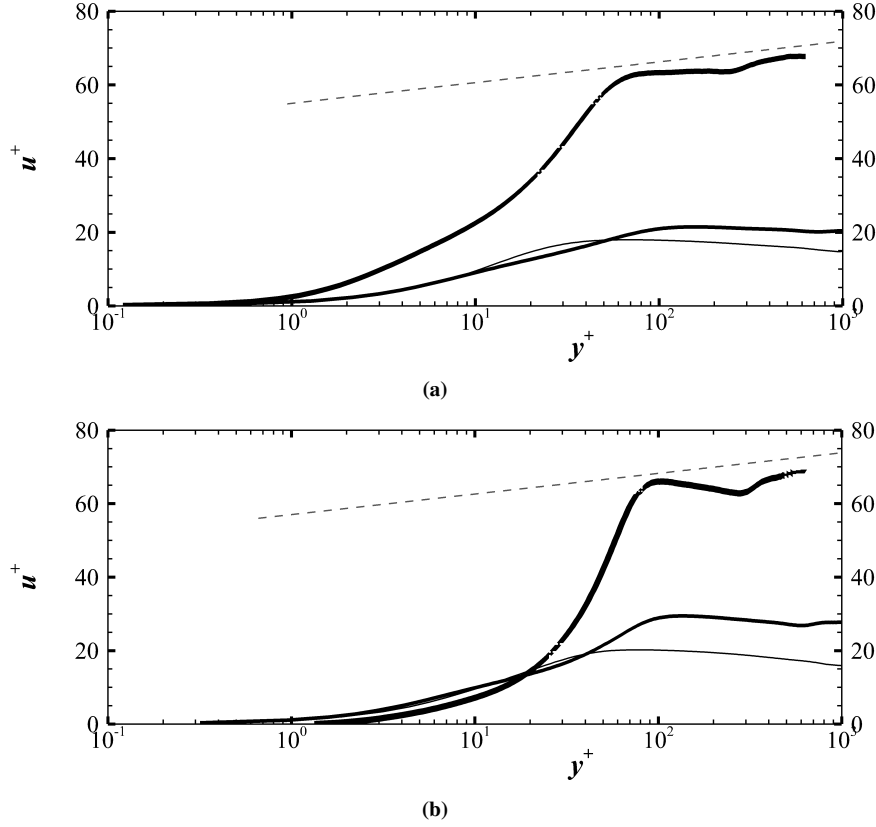
Figure 5.5: Wall normal velocity profiles scaled with viscous quantities (i.e. ν and u_τ) extracted at the locations $x/C = [0.20, 0.65, 1.0]$. A thicker solid line is used for further downstream locations. The dashed line represents the logarithmic law for zero pressure gradient, smooth wall turbulence. (a) 5° incidence case; (b) 10° incidence case.

earlier chord location with respect of the other incidence case is clearly visible. This is an indication of both a rapidly developing turbulent boundary layer in the higher incidence case, and also of the consistency with the spectra shown in figure 5.4 for the suction side location $x/C = 0.25$. It is also noticed that the logarithmic velocity profile (i.e. dashed line in the figures) is not maintained along the whole chord. This behaviour was expected because of the varying pressure gradient condition along the suction side (Mcdonald 1969), and also for the low value of Reynolds number considered in the present investigation. The trend is in agreement with that found by Vila et al. (2017) for a similar Re_τ condition. The logarithmic law does not extend along all the aerofoil when low Reynolds numbers are considered. This is also the case when a FST is applied to trigger an early boundary layer transition. As a consequence, the boundary layer for both the incidences simulated is to be considered in a developing turbulent state. However, the flow detachment mentioned in section 5.1.1, which is going to be considered for the straight-swept comparison, will anyway have a turbulent character.

5.2 Influence of the sweep on the turbulent flow field

5.2.1 2D flow and pressure fields

When considering a turbulent free stream, the introduction of a sweep does not change the mean chordwise velocity component distribution independently of the angle of attack. A comparison between the mean chordwise velocity field $< u >_{z,t} (x, y)$ of the straight wing case with the swept wing distribution is presented in figure 5.6. An almost perfect match of the velocity iso-lines around the foil for different values of the sweep is observed at both angles of attack. Only a fairly small mismatch is noted in the wake of the foil in the low incidence case (roughly half a chord downstream of the trailing edge). This difference can also be appreciated by looking at the deviation between the iso-line $< u >_{z,t} = 0.75Q_{\infty}$ of the two wing cases inside the aerofoil wake in figure 5.6a. However, this mismatch may be only due to the lack of statistical convergence and cannot be attributed to any specific physical phenomenon. The slow convergence rates of the flow statistics in the wake are produced by the presence of slow and large structures that require longer observation periods to deliver converged results. Figures 5.6c and 5.6d propose a further comparison between the wing configurations by considering the wall-normal distributions of the mean velocity tangent to the foil $< u_{tg} >_{z,t} (x, n)$ at several locations sampled along the suction side. All the profiles extracted along the profile are perfectly matching between the swept and unswept configurations.

Also the distribution of the pressure at the wall seems to be unaffected by the sweep in both the considered loading conditions, as revealed by figure 5.7c showing the distribution of the wall mean chordwise pressure coefficient $< C_{p_x} >_{z,t}$ at different sweep and incidence angles. This result is in agreement with what has been found in high Reynolds number flows past swept wings by other authors (Altman & Hayter 1951, Boltz et al. 1960). It is remarked that a consequence of this invariance is that the stagnation point (becoming the attachment line in the swept case) and the suction peak locations are left unchanged by the introduction of the sweep.

In the 5° incidence case, the mean pressure distribution attained for different sweep angles matches perfectly also away from the wall. This perfect collapse clearly appears when considering the pressure iso-lines around the foil for the swept and unswept pair which are provided in figure 5.7a. The match is almost perfect except below the pressure side where some deviation can be appreciated. This effect can probably be related with the slightly different imposed FST upstream of the two wing configurations (discussed in section 5.2.3).
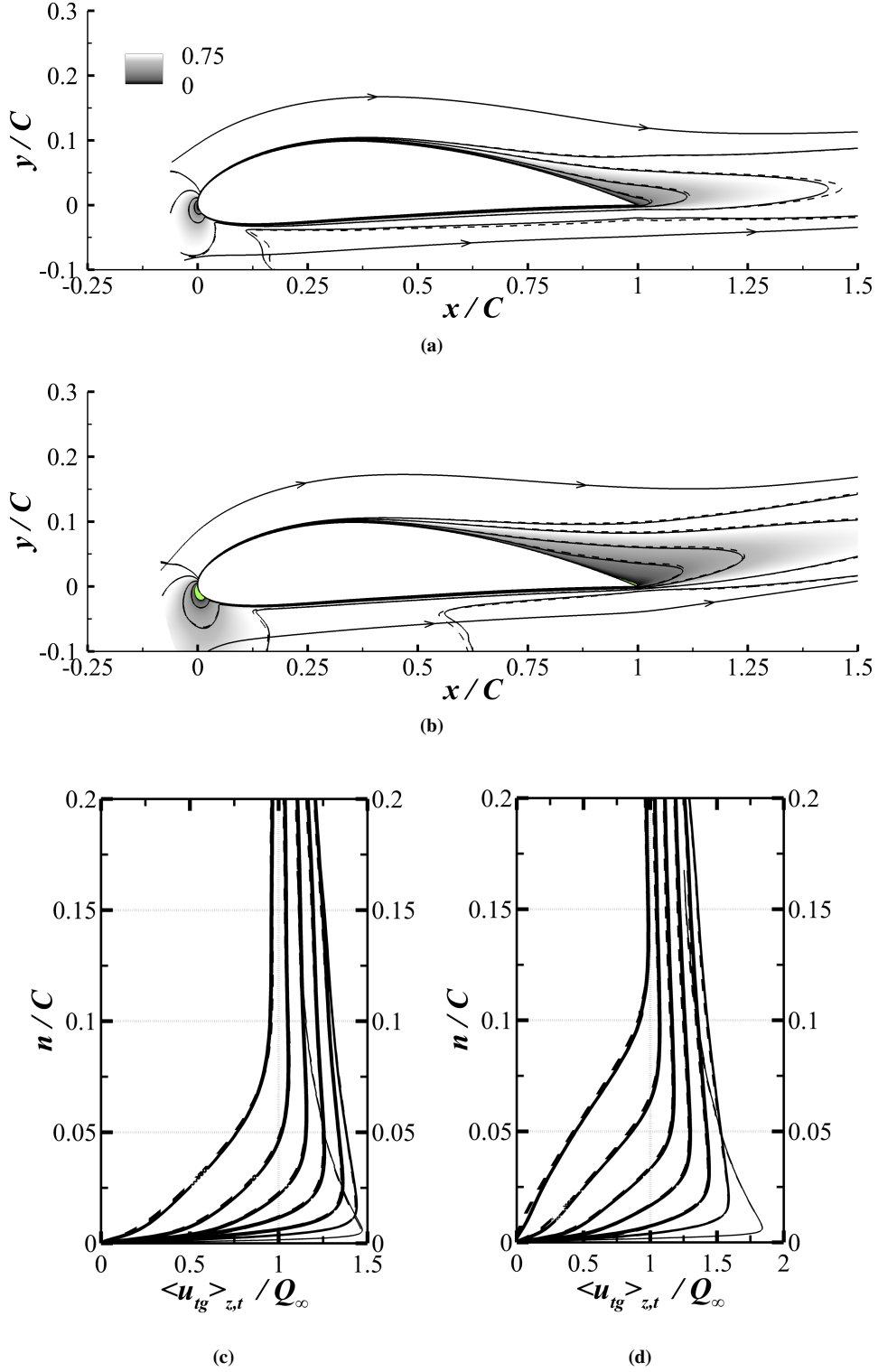
Figure 5.6: Contours of $< u >_{z,t} /Q_\infty$ quantified by iso-lines sampled at $< u >_{z,t} =$ $[0.25, 0.50, 0.75, 0.90]Q_\infty$. The solid line is used for the straight wing case, the dashed line for the swept one. The grey-scale colour map is calibrated to have the white colour matching $< u >_{z,t} \geq 0.75Q_\infty$. Examples of streamlines are identified by the arrowed solid lines. (a) 5° incidence with FST. (b) 10° incidence with FST; Negative values of $< u >_{z,t} /Q_\infty$ are illustrated with light green contours. (c) Wall-normal distribution of $< u_{tg} >_{z,t} /Q_\infty$ in the 5° incidence case for the chordwise locations $x/C =$ $[0.05, 0.2, 0.35, 0.5, 0.65, 0.8, 1.0]$, increasing the thickness of the line while moving downstream. Solid line for the straight wing, dashed otherwise. (d) Same as in (c) but for the 10° incidence.

Also, in the 10° case (illustrated in figure 5.7b) some small deviations of the pressure field can be observed on both wing sides by the trailing edge region. As for the 5° angle of attack, the deviation on the pressure side is probably related with the content of the FST in the two wing configurations (discussed in section 5.2.3). However, the deviation observed on the suction side (visible when comparing the iso-lines $< C_{p_x} >_{z,t} = -0.01$ in the surroundings of $x/C = 0.9$, in figure 5.7b) probably has a different origin and can be the consequence of the different structure of the flow fields in the vicinity of the separation location which is influenced by the sweep. This behaviour is analysed in more details later on in section 5.3.2.

5.2.2 Vorticity field

The structure of the mean vorticity field is obviously altered by the introduction of a mean crosswind. In the case of the straight wing the mean flow is two-dimensional, laying into the aerofoil plane, and therefore the only non-zero mean vorticity component is $< \omega_z >_{z,t}$ (x, y). In the swept case, the mean velocity field is three-dimensional and therefore the mean vorticity field is also three-dimensional with both $< \omega_x >_{z,t}$ (x, y) and $< \omega_y >_{z,t}$ (x, y) taking on non-zero values everywhere in the flow domain. These additional mean vorticity components, characteristic of the swept case, are presented in figure 5.8 in a region surrounding the aerofoil.

The chordwise vorticity field $< \omega_x >_{z,t}$, shown in figures 5.8a and 5.8b, does not change very much in the two loading conditions. Note that the upper and lower side of the foil are characterised by a vorticity field with a different sign. This is due to the rotation of the wall-normal vector on the two sides (on the bottom side is negative with respect to the y axis, while on the upper side is oriented as the y axis). The thickness of the vorticity layer around the foil will be quantified later keeping into account the presence of a spanwise boundary layer in section 5.2.4.

When introducing the crosswind, a local increase in the thickness of the $< \omega_x >_{z,t}$ vorticity layer is observed at about mid-chord on the suction side for both incidences, although with different shapes in the two cases. For the 5° case the layer thickening is localized within the range $\Delta x/C = [0.45 - 0.70]$, while for the higher incidence case in the range $\Delta x/C = [0.35 - 0.65]$. In the former case the thickening is smooth with a maximum height of $2\%C$ (having used the iso-line $< \omega_x >_{z,t} = 5$ as an estimator). In the 10° case the shape is more abrupt showing a maximum thickness of $3\%C$. This shape is related with the incipient turbulent boundary layer detachment process, as it will be further discussed in section 5.3.3.
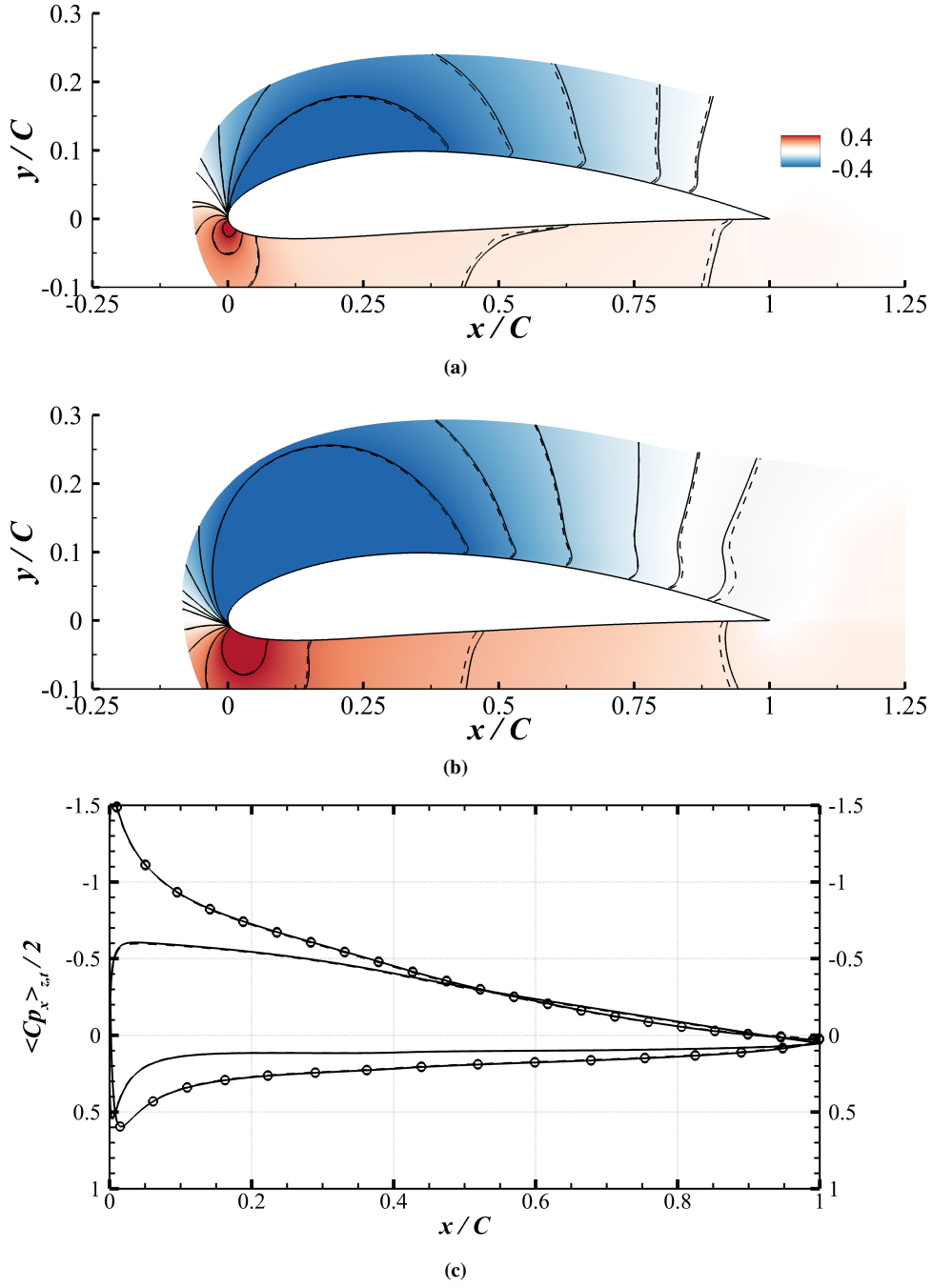
Figure 5.7: (a) Contours of $<C_{p_x}>_{z,t}$ quantified by iso-lines sampled at $<C_{p_x}>_{z,t}=$ $[-0.05, 0.075, \pm0.1, \pm0.2, \pm0.3, \pm0.4]$ for the 5° incidence case with FST. The solid line is used for the straight wing, the dashed for the swept configuration. The colour map shows zones of depression in blue and over-pressure in red. (b) Same as in (a) but for the 10° incidence case with FST. Iso-lines drawn for $<C_{p_x}>_{z,t}= [-0.01, -0.05, \pm0.1, \pm0.2, \pm0.3, \pm0.4]$. (c) Distribution of $<C_{p_x}>_{z,t}$ at the foil surface for both the aerofoil sides. Solid lines represent the straight case, dashed the swept one. Circled lines for the 10° incidence case, solid lines without symbols for those of the 5° case.

The mean vorticity component $< \omega_y >_{z,t}$, shown in figures 5.8c and 5.8d, does not show any significant difference between the two incidences. The corresponding wall layers are much thinner than the ones characterising the $< \omega_x >_{z,t}$ distribution (a smaller value for the contours needs to be selected to actually visualise the layer thickness). Also, $< \omega_y >_{z,t}$ shows a change in sign moving downstream along the foil accordingly to the variations of the wall normal unit vector. The change of sign takes place in correspondence with the point of maximum thickness with respect to the chord line on both sides of the wing: $x/C = 0.35$ on the upper side, $x/C = 0.13$ on the lower side for the $NACA - 4412$ profile.

The spanwise component of the mean vorticity field allows for a direct comparison between the swept and unswept configurations. Its sign distribution is determined by the location of the stagnation point (attachment line in the swept case), regardless of the incidence or the sweep. The distribution of $< \omega_z >_{z,t}$ is shown in figures 5.9a and 5.9b for the low and high incidence conditions respectively. In the same figures, solid and dashed iso-lines allow for a direct comparison between the swept and unswept cases.

By looking at these selected iso-lines, it is noticed that in the lower incidence case the spanwise vorticity field follows everywhere the *Simple Sweep Theory* , while the theory does not hold for the higher loading condition. Figure 5.9c shows a comparison for the 5° case of the wall-normal distribution of $< \omega_z >_{z,t} (x,n)$ in two subsequent locations on the suction side, $x/C = 0.8$ and $x/C = 1.0$. From the latter distribution, a 7% difference is measured in the peak region, at $n/C = 0.002$. Being the largest difference observed at the lower incidence, one may suggest that a negligible change is introduced by the spanwise flow on the mean spanwise vorticity distribution. Differently, the higher loading condition presents a substantial deviation of the spanwise vorticity field between the two wing configurations, as clearly observed considering the iso-lines provided in figure 5.9b. A quantitative measure of this deviation is given by the analysis proposed in figure 5.9d, comparing the wall-normal $< \omega_z >_{z,t} (x,n)$ profiles for two subsequent locations at $x/C = 0.8$ and $x/C = 1.0$, on the suction side. In the former a difference of 15% is already observed in the peak region ($n/C = 0.0017$), while in the latter a difference of 50% is achieved at the location $n/C = 0.004$. Clearly, in the higher incidence case the spanwise flow plays a non-negligible role in the distribution of the vorticity field, although its effect is mainly confined to the rear part of the wing suction side. In this region deeply affected by the crosswind, the *Simple Sweep Theory* becomes unreliable. As already mentioned, the cause of the modification of the mean vorticity field can be attributed to the formation of a turbulent separation region which will be discussed in more details in section 5.3.2.
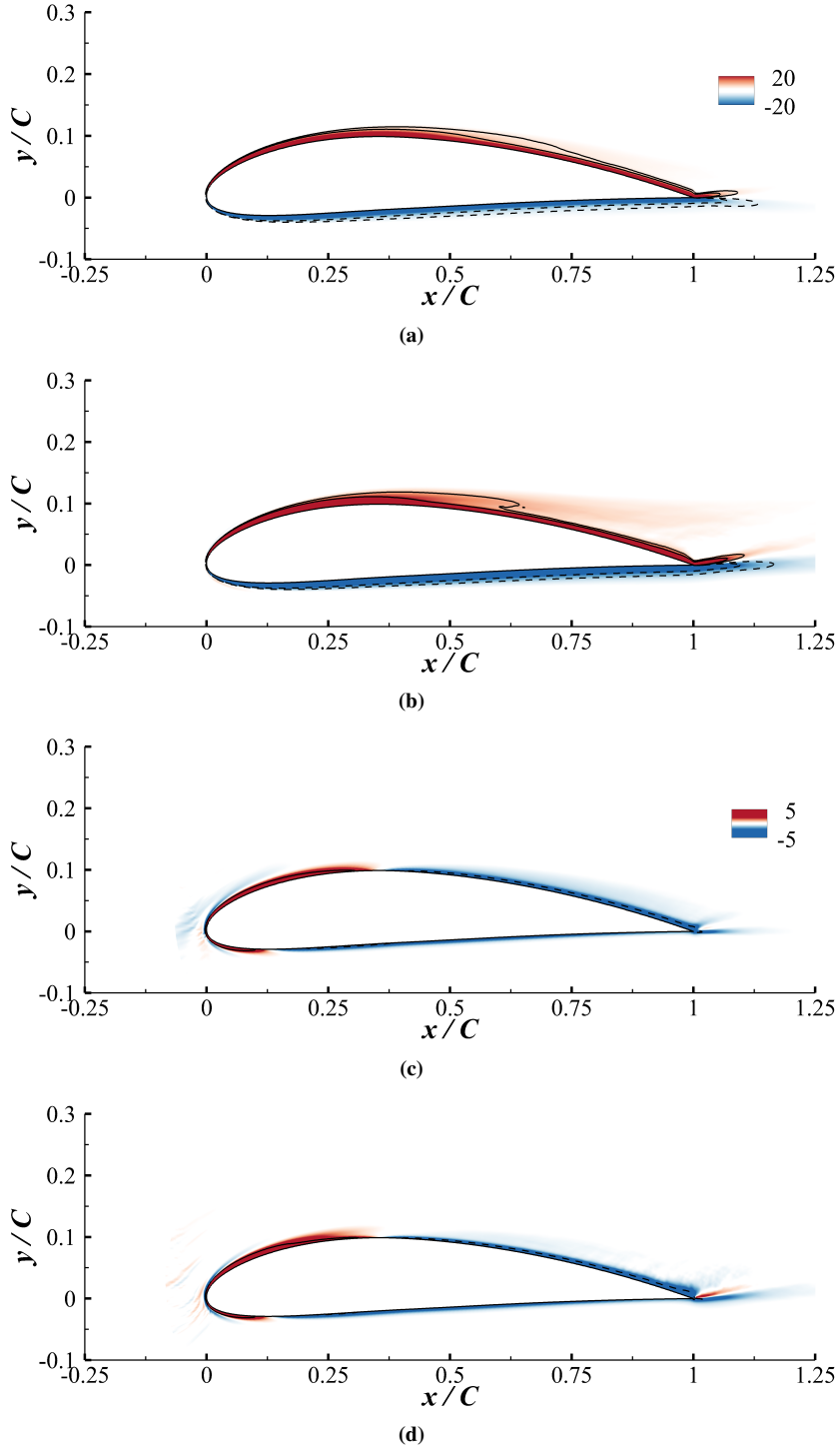
Figure 5.8: (a) Contours of $< \omega_x >_{z,t} C/Q_\infty$ at 5° angle of attack for the swept wing case with FST: red corresponds to positive values (aligned with x), in blue negative ones. Selected iso-lines at $< \omega_x >_{z,t} = [\pm 5 \pm 10]Q_\infty/C$ are represented with solid lines for positive values, dashed otherwise. (b) Same as in (a) but for the 10° incidence case with FST. (c) Contours of $< \omega_y C/Q_\infty >_{z,t}$ with a colour-map showing in red a vorticity aligned with y, in blue otherwise. Iso-lines at $< \omega_y >_{z,t} = [\pm 5]Q_\infty/C$, solid line for positive values, dashed otherwise. (d) Same as in (c) but for the 10° incidence case with FST.
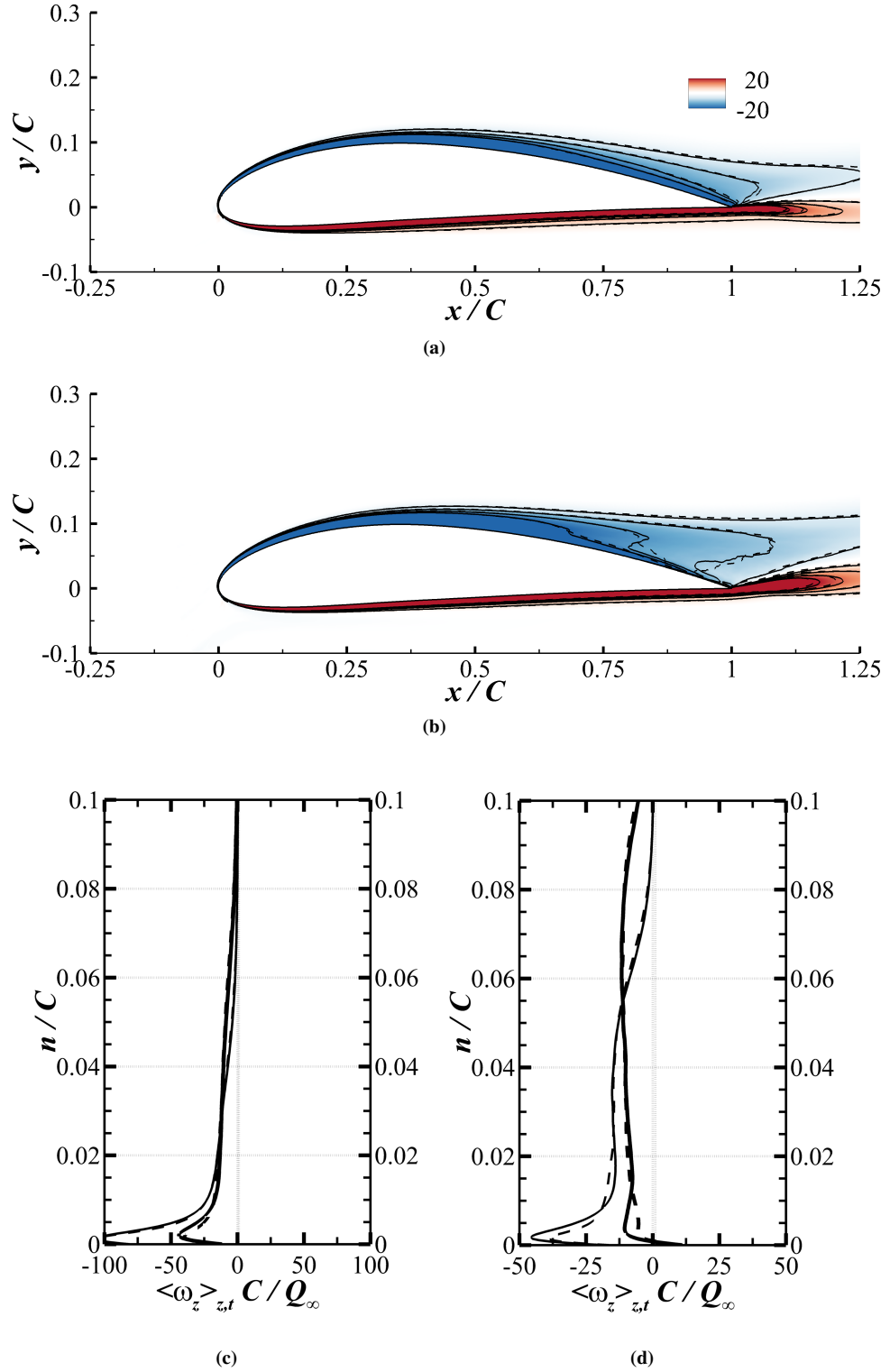
Figure 5.9: (a) Contours of $< \omega_z >_{z,t} C/Q_\infty$ in the 5° incidence cases with FST: positive vorticity in red, in blue otherwise. Selected iso-lines at $< \omega_z >_{z,t} = [\pm 5 \pm 10 \pm 15 \pm 20]Q_\infty/C$ are represented with solid lines for the straight wing, dashed for the swept one. (b) Same as in (a) but for the 10° incidence cases with FST. (c) Wall-normal distribution of $< \omega_z >_{z,t} C/Q_\infty$ in the 5° incidence case for the chordwise locations $x/C = 0.8$ and $x/C = 1.0$, using a thicker line for the latter case. Solid line for the straight wing, dashed otherwise. (d) Same as in (c) but for the 10° incidence.

5.2.3 Perturbation field

In the present investigation, a very intense FST level has been deliberately adopted to cause an early by-pass transition albeit the low Reynolds number considered for both the wing configurations, as described in section 3.7. The choice has been made to avoid the otherwise inherently different transition process between the straight and the swept wings (Morkovin 1993, Reed & Saric 1989, Saric et al. 2003) that would complicate a direct comparison of the perturbation fields around the foils. The intensity and the integral length scale of the FST have been kept invariant with respect to the direction of the mean incoming wind.

A first observation of the results suggests that the fluctuating components of the velocity field in the region surrounding the aerofoil are only mildly affected by the introduction of the sweep, although this similarity is not observed in regions interested by an eventual boundary layer separation. The influence of the FST on the perturbation field corresponding to the swept and unswept configurations is illustrated in figures 5.10a and 5.10b for both the low and high incidence cases. The plots show the mean perturbation field using $< k >_{z,t} (x, y)$ (i.e. the mean turbulent kinetic energy) as an estimator. In the far-field, the effect of the perturbation introduced upstream in the chordwise direction is revealed by the different deviation of the iso-lines observed for the two wing configurations. This variation is a consequence of the FST intensity that is preserved in the mean incoming direction but not along the chordwise one. Regardless of the far-field treatment, the velocity and pressure fluctuations close to the aerofoil surface do not show any relevant deviation when the swept and unswept wings are compared. The region neighbouring the aerofoil appears to follow the same dynamic response independently of the sweep and of the type of perturbation triggering the transition. This behaviour is quantified in figure 5.10c showing a comparison between the swept and unswept configurations for the normal-to-the-wall distributions of $< k >_{z,t} (x, n)$ extracted at $x/C = [0.8, 1.0]$ in the low incidence case. The difference between the two wings appears to be quite small with a deviation between the two distributions at the trailing edge below 5%, measured at the peak location ($n/C = 0.025$). Similar considerations can be made for the higher incidence case, shown in 5.10d, at the chord locations $x/C = [0.65, 0.8, 1.0]$. In this case the largest difference between the two chordwise flows is recorded for the energy distribution extracted at $x/C = 0.65$, where a difference of 6% is achieved at the peak location ($n/C = 0.018$). The maximum deviation between the two perturbation fields is localised at the trailing edge for the low incidence case, whereas it is found further upstream, at $x/C \approx 0.65$, for the higher incidence case.

112
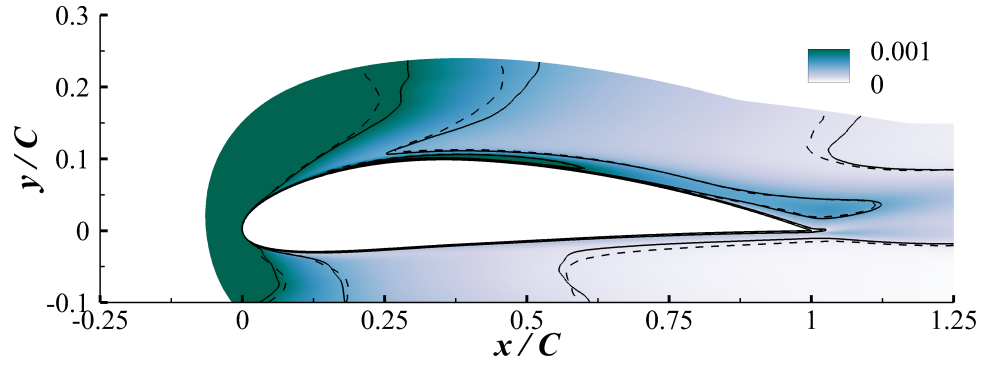
(a)
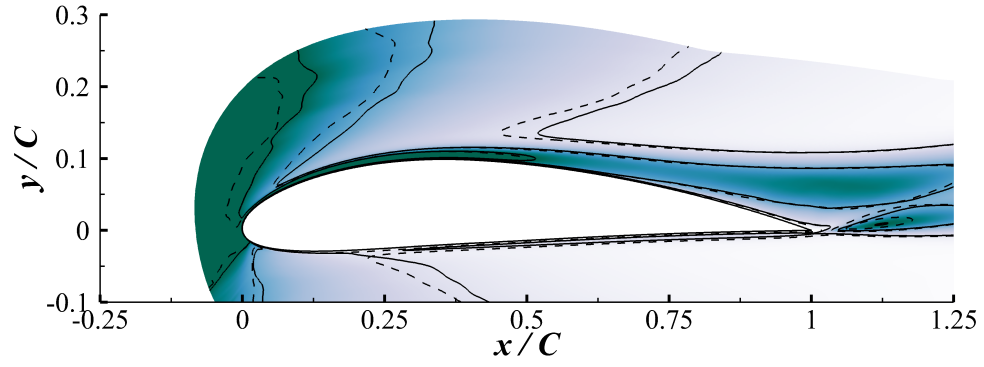
(b)
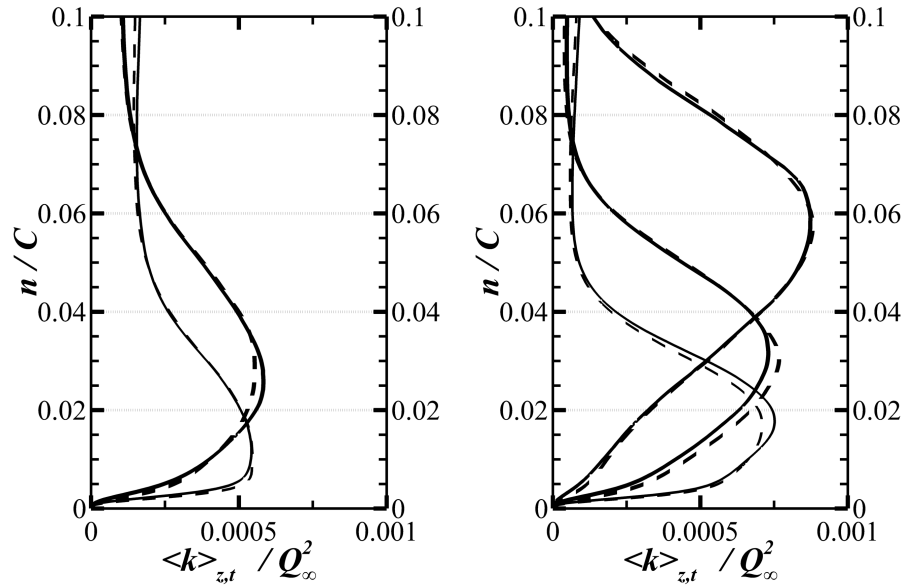
(c)
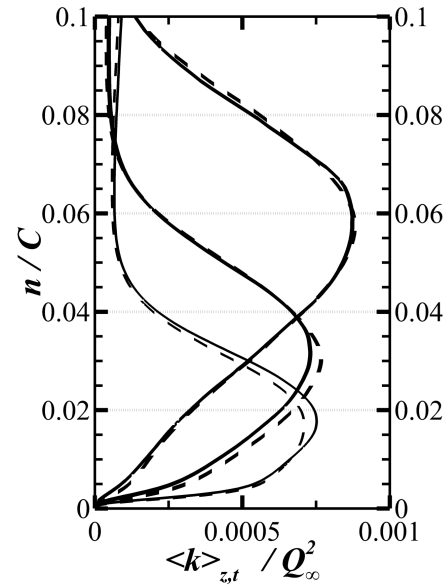
(d)

Figure 5.10: (a) Contours of $< k >_{z,t} /Q^2_\infty$ at 5° incidence cases with FST. The intensity increases from lighter to darker colours. Solid iso-lines represent $< k >_{z,t}= [0.0001, 0.0005, 0.001]Q^2_\infty$ for the straight case, dashed for the swept one. (b) Same as in (a) but for the 10° incidence case with FST. (c) Wall-normal distribution of $< k >_{z,t} /Q^2_\infty$ in the 5° incidence case for the chordwise locations $x/C = [0.8, 1.0]$, using a thicker line for the profile extracted at the trailing edge. Solid line for the straight wing, dashed otherwise. (d) Same as in (c) but for the 10° incidence and chordwise locations $x/C = [0.65, 0.8, 1.0]$. The profiles are plotted with an increasingly thicker line for increasing values of x.

113

5.2.4 Boundary layers characterisation

BL thicknesses in the low incidence case

The boundary layer thicknesses of the turbulent chordwise flow remain almost unchanged when a sweep is introduced. This observation is in agreement with the past literature covering the turbulent attached flows at high Reynolds number regimes (Altman & Hayter 1951, Boltz et al. 1960). The boundary layer chordwise integrals have been defined previously in equations 4.3. The chordwise displacement thickness for both wing configurations is shown in figure 5.11a for both the suction and the pressure sides. The distributions on the pressure side, which remains unaltered by the sweep, are bounded in the range $\Delta \delta^* = [2 \times 10^{-3} - 4 \times 10^{-3}]C$. Those on the suction side stay within the mentioned range until $x/C \approx 0.3$. Further downstream they increase monotonically, almost linearly, until the trailing edge, achieving a value $\delta^* = 2 \times 10^{-2}C$. The δ^* distribution also presents an inflection point at $x/C = 0.45$. The chordwise momentum thicknesses, shown in figure 5.11b, follows the same trend described for the displacement thicknesses. On the pressure side the values range is $\Delta \theta = [1 \times 10^{-3} - 3 \times 10^{-3}]C$. On the suction side the thickness goes from $\theta = 1 \times 10^{-3}C$ at the leading edge to $\theta = 1.5 \times 10^{-2}C$ at the trailing edge, for both sweep angles. The shape factor H distribution, shown in figure 5.11c, which is again almost independent of the sweep, takes on a value of almost 2 for both foil sides, while on the suction side they are both always slightly larger. However, in the trailing edge region, the distributions of the two sides start differentiating with the suction side values increasing to 2.8, and the pressure side decreasing to 1.6.

Next, the spanwise integral values δ_z^*, θ_z and H_z that characterise the crosswind boundary layer are considered in figures 5.11a, 5.11b and 5.11c, respectively. The distributions of the three integrals on the pressure side follow almost perfectly their respective chordwise flow counterparts. Differently, on the suction side beyond the location $x/C \simeq 0.35$ the distributions of the three spanwise flow integrals show a distinct behaviour as compared to the ones relative to the chordwise flow. This indicates that from the mentioned location the two boundary layers (chordwise and spanwise) present a different character. The boundary layer generated by the spanwise flow appears not influenced by the formation of the chordwise flow separation moving towards the wing trailing edge, as can be deduced from the suction side distribution of H_z in figure 5.11c: the z-shape factor distribution starts at the value $H_z = 2.1$ at $x/C = 0.1$ and decreases almost linearly to the value $H_z = 1.4$ at the trailing edge, clearly indicating an attached boundary layer. It is also noticed that the H_z distribution

on the suction side coincides with both the matching H and H_z on the pressure side from the leading edge until $x/C \simeq 0.45$. Beyond this point, H_z on the suction side is found to be always smaller than both H and H_z on the pressure side, which share an almost equal value.

BL thicknesses for the higher incidence case

The independence to the crosswind of the chordwise boundary layer integrals is observed along most of the span of the chord. However, a small variation is detected in correspondence with the beginning of flow separation. The comparisons between δ^*, θ and H is presented in figures 5.12a, 5.12b and 5.12c, respectively. It is noted that the H distribution shows a small deviation in the very rear part of the suction side between the swept and the unswept cases. This variation is caused by the presence of a separated region in this location (this will be further discussed in section 5.3.2).

When comparing the distribution of the integral values of the chordwise and spanwise flows, it is noticed that on the suction side the displacement thickness, shown in figure 5.12a, appears to increase almost linearly from the leading edge to the trailing edge, from $\delta^* = 3 \times 10^{-3}C$ to $\delta^* = 6 \times 10^{-2}C$. The δ^* variation along x appears to be even more linear than its lower incidence counterpart (figure 5.11a) along the whole chord extension. The suction side spanwise displacement thickness follows a similar trend, but it increases with a milder slope, reaching the value $\delta^* = 2 \times 10^{-2}C$ at the trailing edge. The momentum thicknesses generated by the two velocity components exhibit different features from mid-chord on. In particular, in figure 5.12b the largest difference between the two layers appear to be at about $x/C = 0.6$. From this location, the difference between the two boundary layers decreases moving downstream. The shape factors of the two boundary layer developing on the suction side, H and H_z shown in figure 5.12c, are appreciably different along the whole chord, highlighting their different predispositions towards an eventual separation. Indeed, the suction side distribution of H can be observed to deviate rapidly from that of an attached boundary layer moving towards the trailing edge. Conversely, the distribution on the same aerofoil side of H_z matches the distribution found for the lower incidence case (H_z bounded in the range $[2.1 - 1.4]$), indicating an attached flow. As for the lower incidence case, it is noticed that the H_z distribution on the suction side is always smaller than both the coinciding distributions of H and H_z on the pressure side.
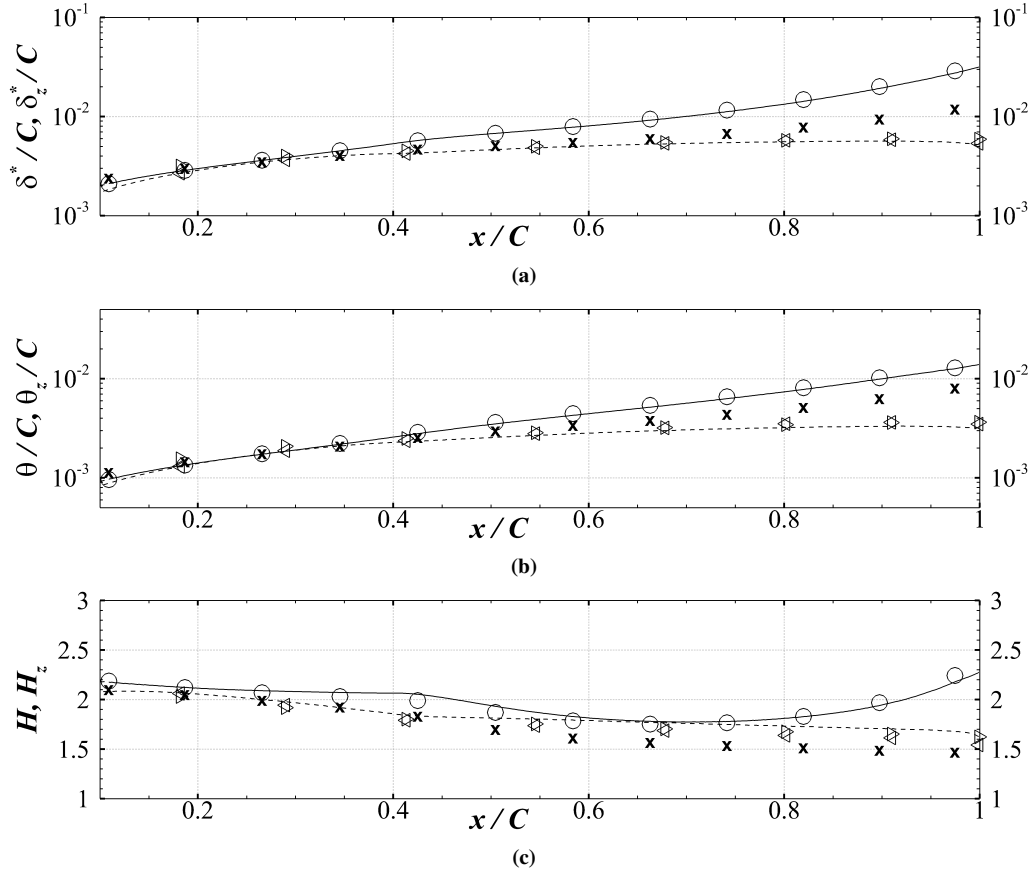
Figure 5.11: Distribution along the chord of the chordwise boundary layer mean non-dimensional thicknesses for the 5° angle of attack: (a) displacement thickness, (b) momentum thickness and (c) shape factor. The solid line is used for the suction side of the straight wing, while ∘ for the swept one. The dashed line is used for the pressure side of the straight wing, ◁ for the swept case. The spanwise corresponding boundary layer thicknesses are shown with ✕ on the suction side and ▷ on the pressure side.
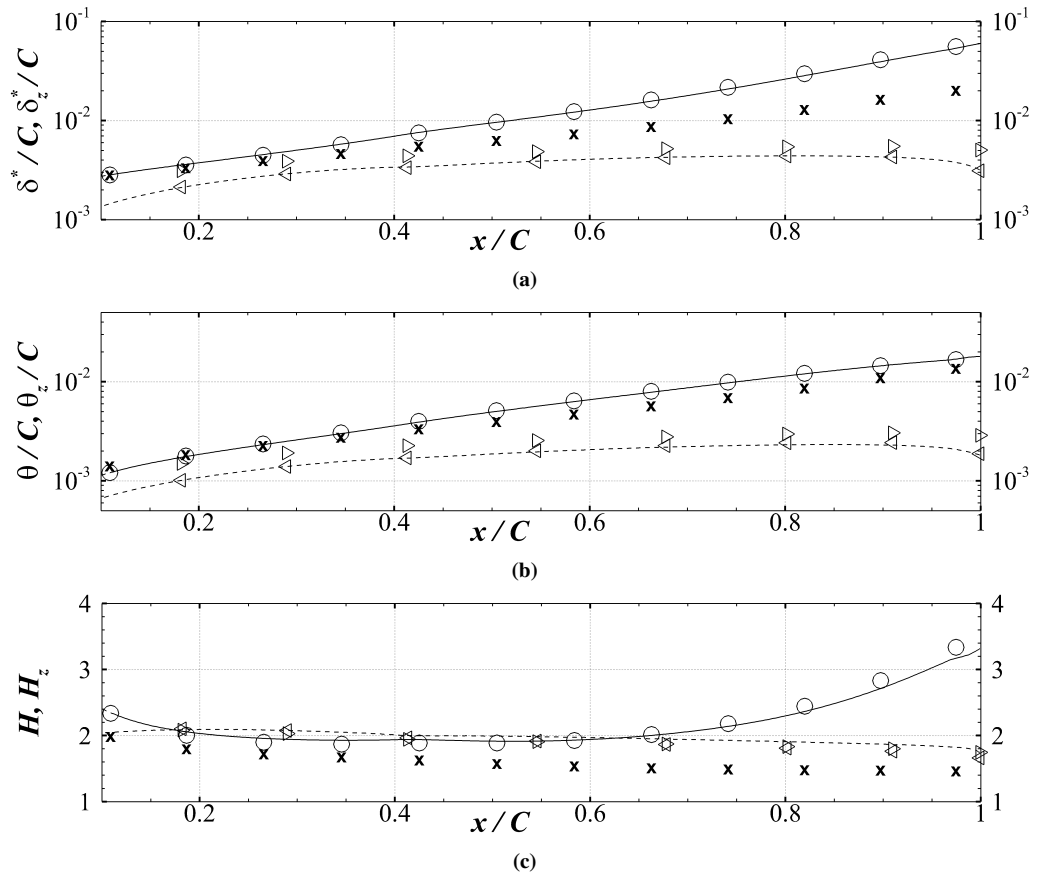
Figure 5.12: Distribution of non-dimensional integral quantities in the 10° incidence case with FST. Lines and symbols as in figure 5.11.

BL within the chordwise pressure gradient

As expected, for both loading conditions, the distribution of the shape factor along the chord is found to be specifically correlated to the strength of the chordwise pressure gradient regardless of the sweep. The suction side distribution of H for the low incidence case, not affected by the wing sweep, shows a linear behaviour in the initial 40% of the chord, while curvilinear with positive curvature afterwards (see figure 5.11c). In the higher incidence case, a similar monotonic increase along the whole chord is found, however, the growth does not follow a linear behaviour as it can be observed in figure 5.12c. The change in the functional behaviour of the shape factor is linked to the strength of the chordwise pressure gradient applied on the wing surface. The Clauser parameter (Clauser 1954) has been used to estimate the intensity of the pressure gradient. This is defined as $\beta = (\delta^*/u_\tau)dP_e/ds$ (note that dP_e/ds is the gradient of the pressure at the boundary layer edge in the direction tangential to the wing surface and lying in the chord plane). The Clauser parameter distribution is provided in figure 5.13a and 5.13b for the low and high incidence cases respectively. On the suction side it can be observed that β increases monotonically for both the incidences, although with a higher growth rate for the higher incidence. For the lower incidence case, it is found that $\beta > 2\rho Q_\infty$ (moderate adverse pressure gradient) for $x/C > 0.40$, i.e. from the location where the distribution of H switches between the linear and non-linear behaviour. For the low angle of attack case, $\beta > 2\rho Q_\infty$ from a location within the initial $10\%C$ with a H distribution that does not follow a linear growth. The described behaviours are found to be unaffected by the sweep.

Skin friction Reynolds number distribution

The skin friction Reynolds number (i.e. $Re_\tau = u_\tau\delta^*/\nu$) of the chordwise flow can be considered to correspond to a marginally turbulent condition along the chord for all the simulated cases. Its distribution appears to be independent of the crosswind for both incidences albeit an extended flow separation establishes on the wing surface. In figure 5.14 the distributions of Re_τ for both wing configurations are presented, for each incidence along the top and bottom side of the aerofoil. In the low incidence case, shown in figure 5.14a, both the distributions on the pressure and suction sides stay within the range $\Delta Re_\tau = [8-15]$. It can be observed that the sweep does not play any influence on the distribution of Re_τ. Similar observations can be made for the higher loading condition, shown in figure 5.14b. In this case, the distribution on the suction side allows to identify clearly the mean separation loca-

118
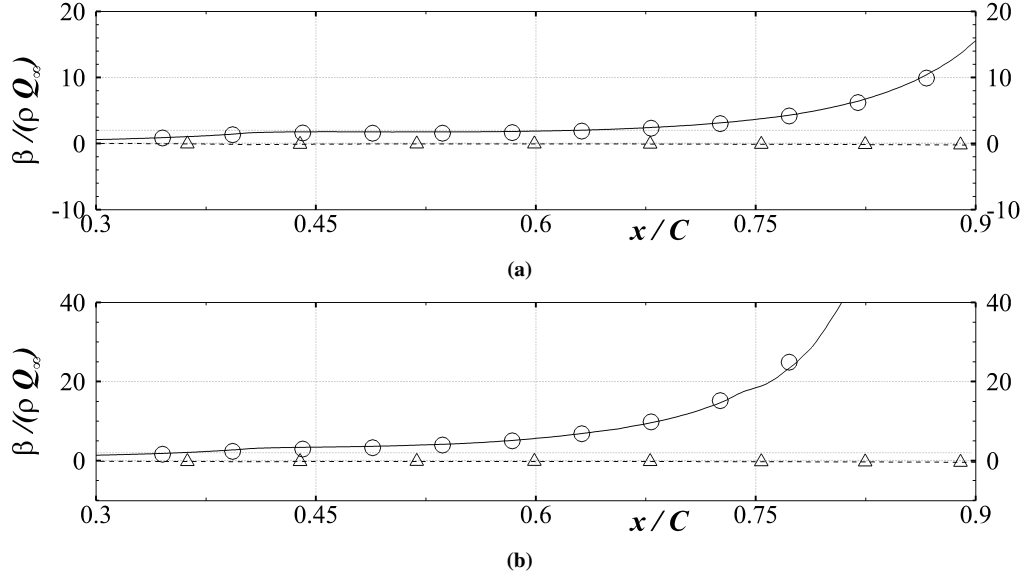
Figure 5.13: Distribution along the chord of $\beta/(\rho Q_\infty)$ for the (a) 5° incidence case with FST, (b) 10° incidence case with FST. The solid line is used for the suction side of the straight wing, while o are for the swept one. The dashed line is used for pressure side of the straight wing, ◁ for the swept case. The dotted lines correspond to $\beta = 0\rho Q_\infty$ and $\beta = 2\rho Q_\infty$.

tion at $x/C = 0.91$. It is also noticed that the values on the suction side span a wider range (i.e. $\Delta Re_\tau = [10 - 50]$) as compared to those of the lower loading condition.

The mean skin friction along the spanwise direction is not affected by an eventual separation, presenting a smooth behaviour along the whole chord. In particular, figure 5.14b reveals a monotonic increase of $Re_{\tau,z} = w_\tau \delta_z^*/v$ (an estimator of the spanwise friction, based on the spanwise friction velocity $w_\tau = \sqrt{\tau_{zn}^w/\rho}$. Here, τ_{zn}^w indicates the component in the spanwise plane, along the direction z (outlining the wing leading edge) of the wall stress vector $\vec{\tau^w}$ acting on the wing surface with normal n) moving downstream from the leading edge for the higher incidence case. It is noticed that also in the higher incidence case the distribution is only marginally affected by the separation of the chordwise flow, ranging between $Re_{\tau,z} = 8$ and $Re_{\tau,z} = 40$.

5.2.5 Lift and drag coefficients unsteadiness

Although the sweep does not influence the mean values and the *r.m.s.* of the C_l and C_{d_x} at both angles of attack, the crosswind has an impact on their time evolution playing a role in the modification of the large scale vortex shedding in the added FST regimes. While the mean and *r.m.s* values of the drag and lift coefficients can be found in section 5.1.2, here the focus is on their time history when the FST condition is considered. Figures 5.15a and 5.15d report the time variations of the C_l and C_{d_x} for the 5° incidence case, while those
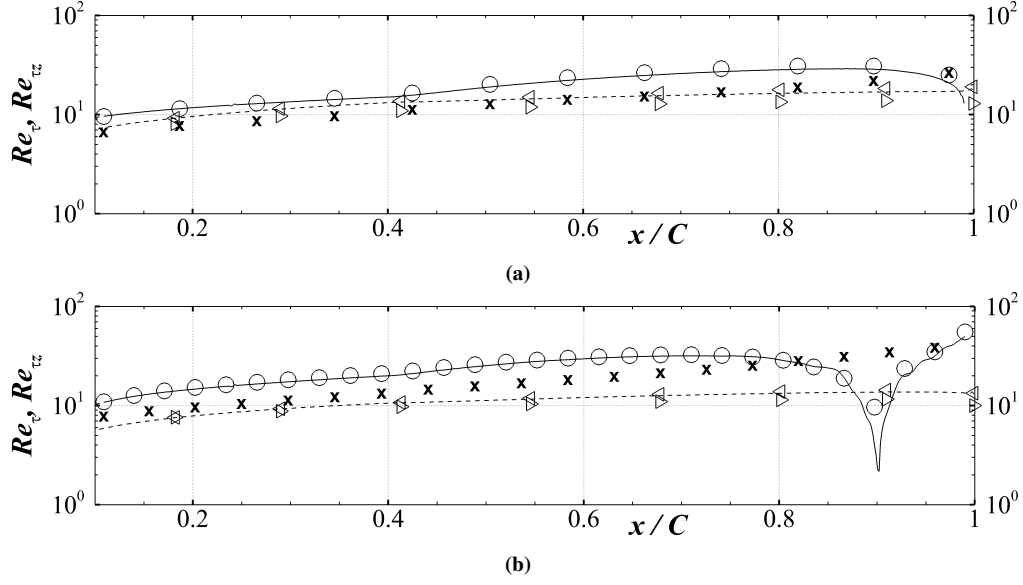
Figure 5.14: Re_τ distribution along the chord for (a) 5° incidence case with FST, (b) 10° incidence case with FST. The solid line without symbols is used for the straight wing on the suction side, while ∘ are used for the swept one. The dashed line with no symbols is used for the straight wing on the pressure side, while ◁ for the swept case. All the aforementioned quantities are related to the chordwise flow. The corresponding quantities for the spanwise flow Re_τ are shown with × on the suction side and ▷ on the pressure side.

of the higher incidence case are illustrated in 5.16a and 5.16d. Alongside the time history, the frequency content of each time signal is also provided to better understand the eventual dynamic modifications introduced by the sweep. In particular, the spectra of C_l and C_{d_x} time sequences ($PSD(C_l)$ and $PSD(C_{d_x})$) are shown in figures 5.15b and 5.15e for the low incidence case and in 5.16b and 5.16e for the higher loading condition. The sampling has been done with a frequency $f^* = 1.5 \times 10^4$ on a time window spanning $\Delta t^* = 70$ in the low loading condition, and $\Delta t^* = 30$ in the higher angle of attack case (the shorter time window for the higher angle of attack has been justified in the introduction of chapter 5). A difference in the energy content in the low frequency range can be recognized when varying the sweep for both loading conditions. At the lower angle of attack, the crosswind appears to trigger new flow dynamics, more than shifting those of the unswept case. In particular, new C_l modes at $f^* = 0.11$ and $f^* = 0.29$ (corresponding to a time period of $T^* = [9.09, 3.45]$) are detected. Similarly, also the C_{d_x} time series presents new peaks at $f^* = 0.11$ and $f^* = 0.19$ ($T^* = [9.09, 5.26]$). In the higher incidence case, the C_l modes at $f^* = 0.2$ and $f^* = 0.35$ ($T^* = [5, 2.85]$) are induced by the sweep. It is also observed that the mode at $f^* = [0.3]$ ($T^* = [3.33]$), present in the unswept case, is damped in both the C_l and C_{d_x} distributions by the crosswind. It is interesting to note that the sweep is found to modify the low frequency flow dynamics, without producing any effect on the mean flow.

Although the available time series spans a limited period of time, they still provide useful hints to unravel the underlying flow dynamics.

A rich dynamical behaviour can be appreciated from the the spectra of all the cases (figures 5.15b, 5.15e, 5.16b and 5.16e) in the frequency range $\Delta f^* = [5 - 8]$. However, the energy content of the mentioned frequency range is much smaller than the dominant ones that belong to the lower frequency range. In an attempt to understand the role of the small scale structures embedded in the flow (linked to the fast dynamic observed into the spectra) to the overall aerodynamic field, some instantaneous snapshots of the flow around the unswept wing have been sampled out. Some recurrent small scale vortex roll-ups within the boundary layer are observed to be entrained in the vortex shedding process, modifying the wake topology at different angles of attack. This phenomenon is visible considering the selected snapshots at 5° presented in figure 5.17. The snapshots show iso-contours of the instantaneous chordwise velocity, $u(x, y, z, t)$. The iso-lines have been chosen to facilitate the understanding of the flow pattern. In snapshots 5.17a and 5.17b, a large flow structure (highlighted by the red contour) with an height and width of approximately $6\%C$ (using the
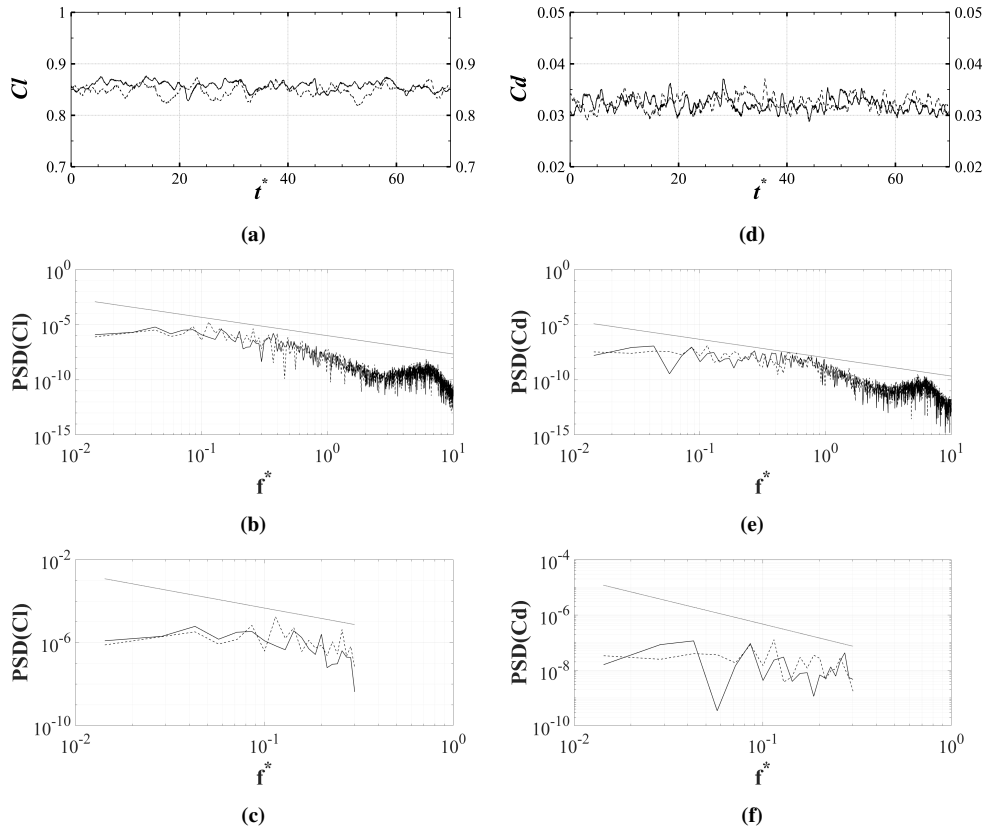
Figure 5.15: C_l and C_{d_x} time history for the 5° incidence cases with FST condition. The solid line is used for the straight wing, the dashed for the swept case. (a) Time history of C_l. (b) Corresponding $PSD(C_l)$. (c) Detail of the spectra in the low frequency range (only peaks containing at least 1% of the total energy). (d), (e) and (f) present the same analysis repeated for the C_{d_x}.

iso-line $u/Q_\infty = 0.6$ as an estimator) can be seen on top of the trailing edge during the roll-up process. The two snapshots are taken within a time interval $\Delta t^* = 0.01$. Another roll-up process on top of the trailing edge (highlighted by the blue-white contours) is shown in snapshots 5.17c and 5.17d, captured within the same time interval as before. The size of the structure is now smaller compared to the previous sequence, being around $2\%C$. The major difference between the roll-up processes illustrated in the aforementioned snapshots is the orientation of the axis about which the roll-up takes place. In particular, in the first type of roll-up process the rotation is clockwise, while in the second type of process the rotation is counter-clockwise. This explains the different colouration of the aforementioned flow structures, mainly red in the first case while blue in the second one. Similar roll-up processes, albeit bigger in size, are observed in the flow field of the higher loading condition. Visualisations of the instantaneous flow dynamics corresponding to the straight wing at 10° incidence with a time sequencing of $\Delta t^* = 0.02$ are presented in figure 5.18. Some clockwise roll-up processes can be seen on the suction side wall, at $x/C = 0.52$ in snapshot 5.18a or at $x/C = 0.78$ and $x/C = 0.88$ in snapshot 5.18d. Counter-clockwise rotations can be observed at $x/C = 0.90$ in panel 5.18b and between $\Delta x/C = [0.90 - 1.0]$ in panel 5.18c.
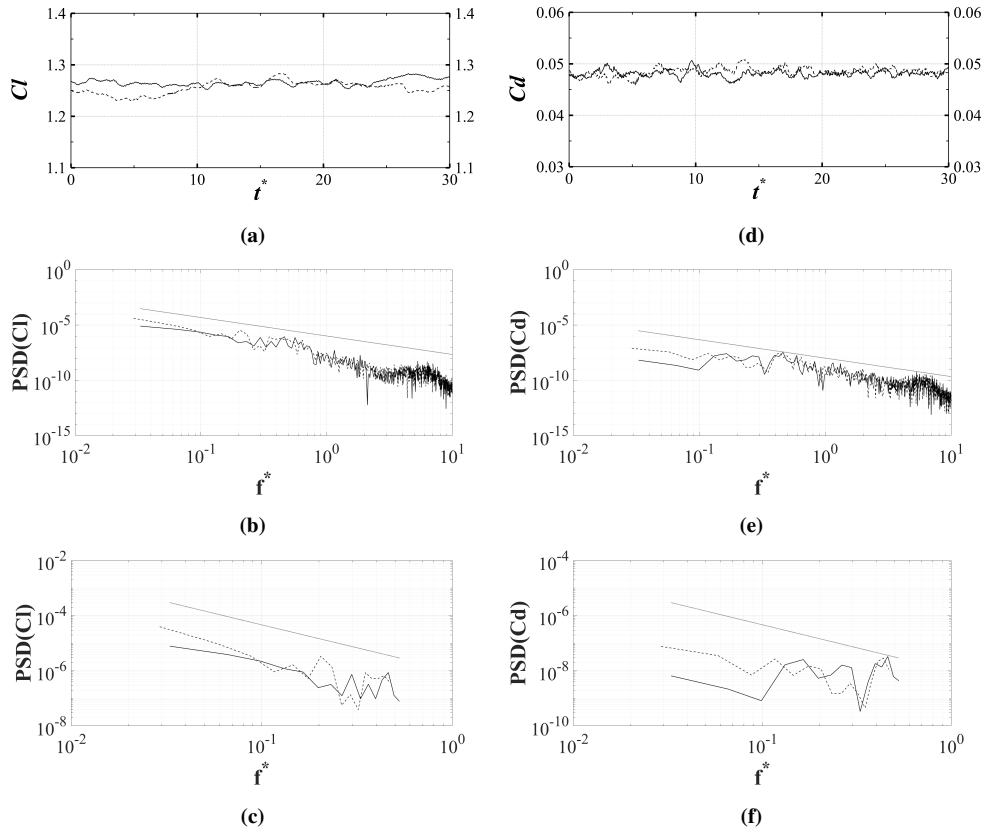
Figure 5.16: C_l and C_{d_x} time history for the 10° incidence case with FST condition. Legend and panels organisation as in figure 5.15.

The frequency range of all the described processes is contained in the range $\Delta f^* = [5 - 8]$ for all the wing configurations and incidences discussed in this work.

The instantaneous flow snapshots shown in 5.17 and 5.18 also provide a qualitative understanding of the flow manipulation carried out by the added FST. From the streamlines geometry it is noted that initially the FST impinges directly on the aerofoil nose and on the pressure side, without reaching the suction side. Therefore, the direct impact of the FST on the evolution of the upper side flow is reduced. The different manipulation induced by the FST on the two wing sides can be deduced by considering the residual flow perturbations found outside the boundary layer on the pressure side, that appear more frequently in the higher incidence case (i.e. flow perturbations localised within $\Delta x/C = [0.2 - 0.4]$ at $y/C = -0.05$ shown in panel 5.18b).
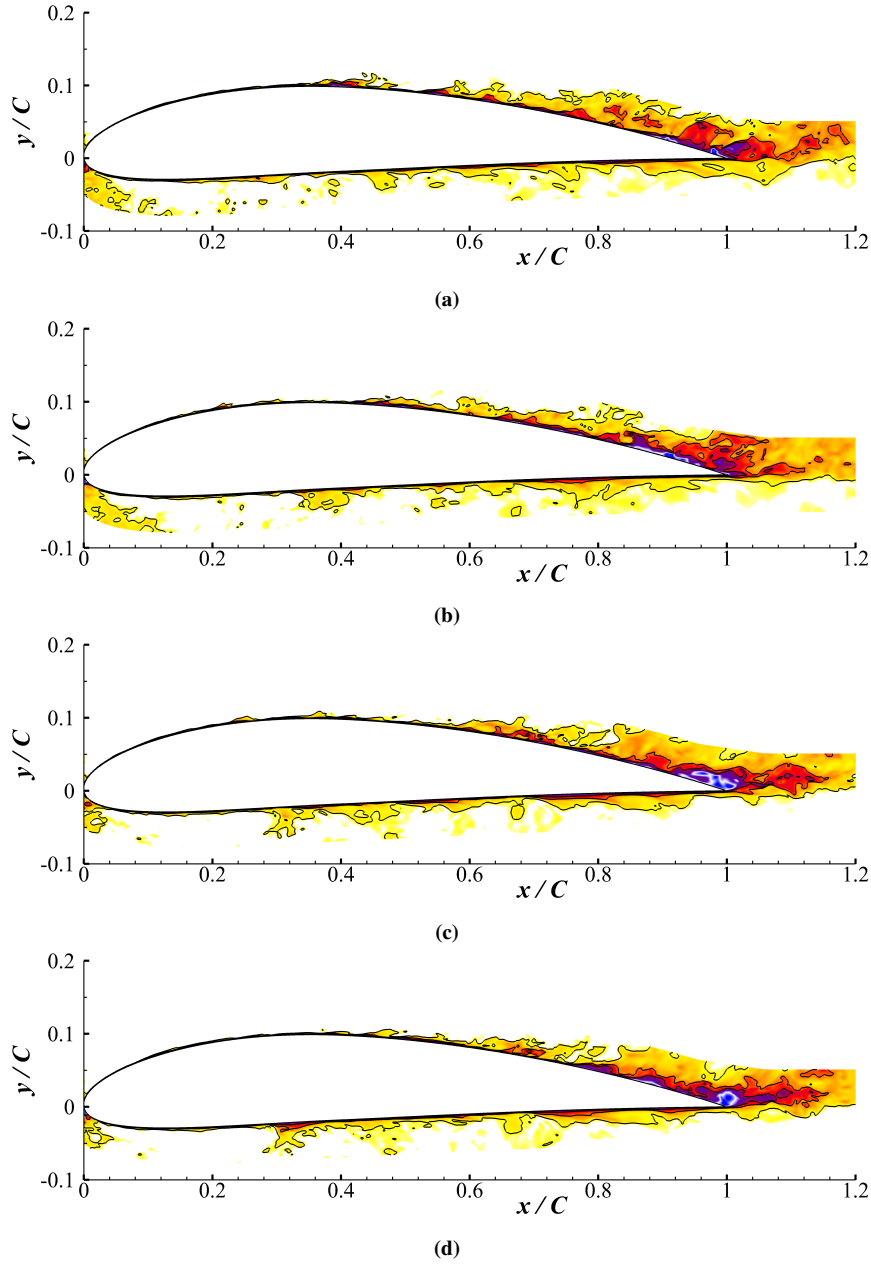
Figure 5.17: Iso-contours of u/Q_∞ for the 5° incidence case with FST condition. The contours are represented using a non-linear colour map in which the red scale indicates positive values and blue negative ones. The white colour is used for the velocity values close to zero and beyond $u/Q_\infty = 0.75$. The iso-lines correspond to $u = [0.2, 0.6, 0.8]Q_\infty$.
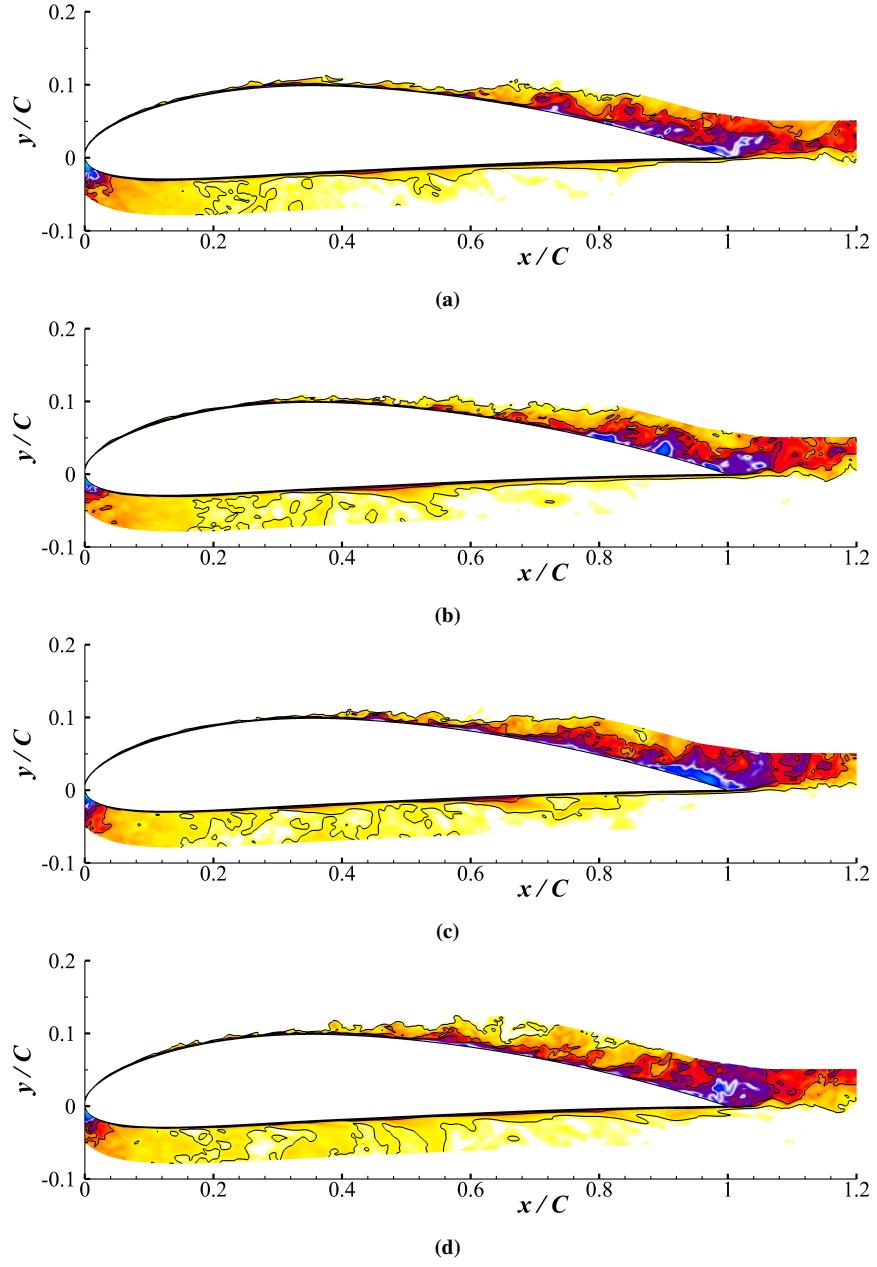
Figure 5.18: Iso-contours of u/Q_∞ for the 10° incidence case with FST condition. Legend as in figure 5.17.

5.3 Sweep effect to specific flow features

So far, the *Simple Sweep Theory* has been found to hold quite well for several quantities in both laminar and turbulent flow regimes. However, the *Simple Sweep Theory* may locally break down when substantial boundary layer separation takes place. This different behaviour of swept and unswept configurations is now characterised in more details by comparing the spectra of the velocity fluctuations. This analysis allows to detect and quantify the differences between the structures of the flow fields and to identify the initial formation of turbulent flow separation and the influence of the crosswind on it. The spectral analysis carried out in the following sections is based on a database obtained by recording flow snapshots over a time interval of $\Delta t^* \simeq 3$ for both swept and unswept configurations considering different wing portions.

5.3.1 Front wing portion

The energy containing modes of the perturbation field in the initial portion of the foil of the FST-injected-cases are found to be concentrated on specific wavelengths bands. The change in the energy distribution mainly depends on the incidence with a negligible effect of the sweep. In figure 5.19, the time-averaged spanwise energy spectrum of the non dimensional velocity fluctuations field $< \hat{E}^* >_t (x, y, k_z)$ premultiplied by the spanwise wavenumber k_z, $k_z < \hat{E}^* >_t (x, y, k_z)$ as defined in equation 4.5, is presented for both the wings configurations in the low incidence case with FST. The footprints of some small-scale spanwise-coherent structures ($0.01 < \lambda_z/C < 0.1$, with the energy peak recorded around $\lambda_z/C = 0.03$ corresponding to $\lambda_z^+ = \lambda_z u_\tau/\nu \simeq 85$) are visible within the first 30% of the chord on the suction side (recall that $x/C = 0.26$ corresponds to the location of mean laminar separation as seen in chapter 4). It is also noticed that the energy peak is at the same vertical location as the one found for the laminar inlet case, i.e. $y/C = 0.101$, which in the current turbulent boundary layer corresponds to $y^+ = y u_\tau/\nu \simeq 20$. The wavelength of the most energetic modes is reduced as compared to the one observed for the laminar case at the separation location, shown in figure 4.12 (in that case $\lambda_z/C > 0.2$). The crosswind slightly reduces the energy content of the most energetic modes, as it was also observed for the laminar inflow case. The partition of the energy between velocity components is not influenced by the perturbation applied upstream. This conclusion can be drawn by comparing the second, third and forth rows of the panels displayed in figure 5.19 with the corresponding panels in figure 4.12. In all cases, the energy is mainly concentrated in the chordwise fluctuations

Figure 5.19: Spanwise energy content of the fluctuating velocity field in the 5° incidence case with FST. The straight wing is illustrated in the left column, the swept one in the right column. The spectra are extracted at $x/C = 0.26$. The black diamonds are used to highlight the dominant modes of the unswept wing, while the white ones indicate the dominant modes of the swept case. Panels (a) and (e) correspond to iso-contours of $k_z < \hat{E}^* >_t C$. The grey-scale colour map is distributed non-linearly with the black regions corresponding to $k_z < \hat{E}^* >_t C > 3$. The iso-lines are sampled with an increment of $k_z < \Delta\hat{E}^* >_t C = 0.23$ starting from $k_z < \hat{E}^* >_t C = 0$. (b) and (f) Iso-contours of $< \hat{R}^*_{u'u'} >_t$. The grey-scale colour map is distributed non-linearly with the black regions corresponding to $< \hat{R}^*_{u'u'} >_t > 1$. The iso-lines are sampled with an increment of $< \hat{R}^*_{u'u'} >_t = 0.07$ starting from $< \hat{R}^*_{u'u'} >_t = 0$. (c) and (g) Iso-contours of $< \hat{R}^*_{v'v'} >_t$. Same legend as for $< \hat{R}^*_{u'u'} >_t$. (d) and (h) Iso-contours of $< \hat{R}^*_{w'w'} >_t$. Same legend as for $< \hat{R}^*_{u'u'} >_t$.

quantified by $< \hat{R}^*_{u'u'} >_t$, the spectrum of $< R^*_{u'u'} >_t$ (the latter defined in equation 4.6). At higher incidence, similar energy distributions are obtained as in the lower incidence case $(0.01 < \lambda_z/C < 0.1$, with the peak content slightly moved to $\lambda_z/C \simeq 0.025$ corresponding to $\lambda_z^+ \simeq 110)$. However, a new energy peak appears at a wavelength of about $\lambda_z/C \approx 0.2$ $(\lambda_z^+ \simeq 900)$. This peak is located well above the wall, at $y/C = 0.105$ $(y^+ \simeq 45)$.

The footprints of the active flow modes of the perturbation field can be visualised for each wing configuration using the instantaneous snapshots of the y-component of the vorticity perturbation $\omega'_y(x, y, z, t)$ on planes parallel to the suction wall. The snapshots corresponding to the lower angle of attack are presented in figure 5.21, while the ones corresponding to the higher loading condition are shown in 5.22. For each incidence the visualisations correspond

Figure 5.20: Spanwise energy content of the fluctuating velocity field in the 10° incidence case with FST. The straight wing is illustrated in the left column, the swept one in the right column. The spectra are extracted at $x/C = 0.26$. The black diamonds are used to highlight the dominant modes of the unswept wing, while the white ones indicate the dominant modes of the swept case. Panels (a) and (e) correspond to iso-contours of $k_z < \hat{E}^* >_t C$. The grey-scale colour map is distributed non-linearly with the black regions corresponding to $k_z < \hat{E}^* >_t C > 3$. The iso-lines are sampled with an increment of $k_z < \Delta\hat{E}^* >_t C = 0.3$ starting from $k_z < \hat{E}^* >_t C = 0.3$. (b) and (f) Iso-contours of $< \hat{R}^*_{u'u'} >_t$. The grey-scale colour map is distributed non-linearly with the black regions corresponding to $< \hat{R}^*_{u'u'} >_t > 1$. The iso-lines are sampled with an increment of $< \hat{R}^*_{u'u'} >_t = 0.1$ starting from $< \hat{R}^*_{u'u'} >_t = 0.1$. (c) and (g) Iso-contours of $< \hat{R}^*_{v'v'} >_t$. Same legend as for $< \hat{R}^*_{u'u'} >_t$. (d) and (h) Iso-contours of $< \hat{R}^*_{w'w'} >_t$. Same legend as for $< \hat{R}^*_{u'u'} >_t$.

to two cross-sectional planes above the suction side. One is extracted in the close-to-the-wall region, the other passes through the vertical location where the maximum perturbation intensity is recorded ($y/C = 0.101$, where the maximum of the fluctuating energy is attained for the location $x/C = 0.26$). The contours on the plane closer to the wall clearly show a set of streaky structures within the first portion of the wing. This streaky pattern can be observed for both incidences and wing configurations. The energy peaks with wavelength $0.02 < \lambda_z/C < 0.05$ detected in the premultiplied spectra $k_z < \hat{E}^* >_t$ are clearly related with this pattern and may represent the footprints of the Klebanoff mode governing the by-pass transition (Klebanoff 1971). Indeed, it is noticed a qualitative analogy of the aforementioned vorticity streaks pattern with that observed in the by-pass transition region by Brandt et al.
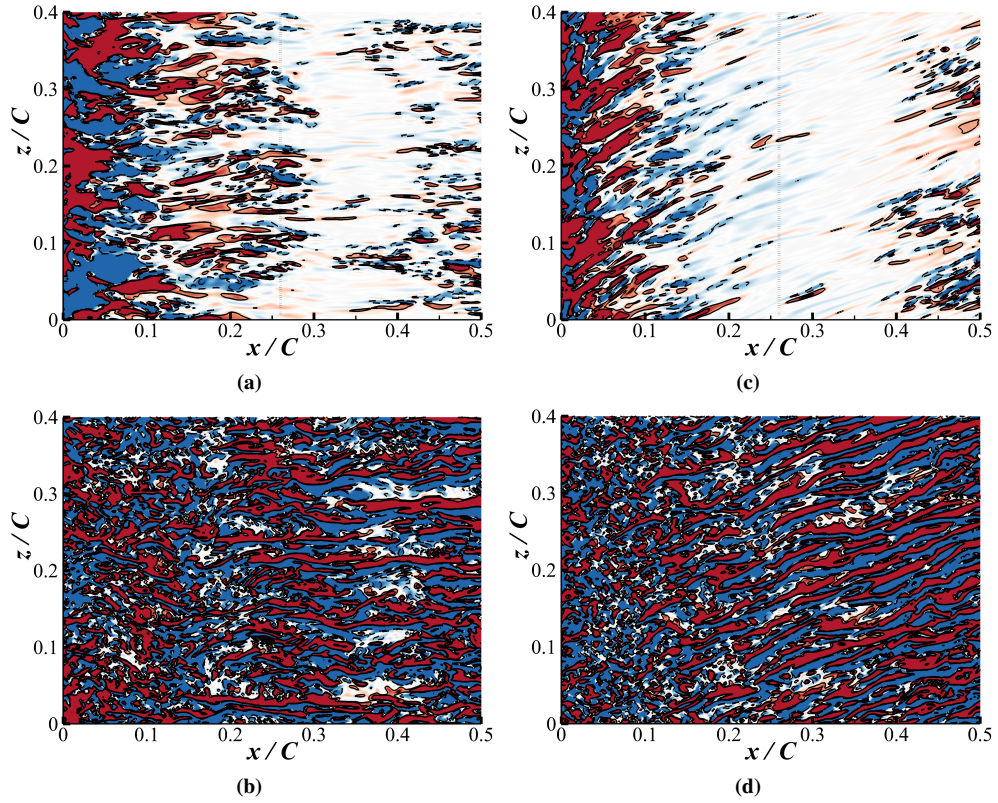
Figure 5.21: Iso-contours of $\omega'_y C/Q_\infty$ in the 5° incidence case with FST. Left column: straight wing; right column: swept wing. Panels (a) and (c): iso-contours on the suction side wall, top view, for the first half of the chord. (b) and (d): iso-contours on a plane parallel to the suction side wall and passing through $y/C = 0.101$ at $x/C = 0.26$. Red contours are for positive vorticity (i.e. $\omega'_y C/Q_\infty > 20$), blue for negative values (i.e. $\omega'_y C/Q_\infty < -20$) and white for vorticity close to zero. Selected iso-lines at $\omega'_y = [\pm 10 \pm 20]Q_\infty/C$ are represented with solid lines for positive values, dashed otherwise. The dotted lines indicate the locations of the mean separation line for $\alpha = 5^o$ incidence without FST.

(2004). Furthermore, it is possible to identify some flow structures footprints linked to the mode with $\lambda_z/C \simeq 0.2$ appearing in the $< \hat{R}^*_{u'u'} >_t$ spectra of the higher loading condition (figures 5.20b and 5.20f). Indeed, a coherent perturbation with a spanwise wavelength of about $20\%C$ in $\Delta z/C = [0.10, 0.30]$ with a chordwise amplitude of roughly $10\%C$ can be observed in panel 5.22c. The mild fluctuating energy content observed for $\lambda_z/C \simeq 0.2$ will be found in sections 5.3.2 and 5.3.3 to be linked to the appearance of a large scale separation of the boundary layer further downstream along the chord.

The flow visualisations also allow to reveal one of the effects of the crosswind into the wall velocity streaks related to the transition mechanism that is not revealed by the spanwise velocity spectra. In particular, for both incidences the flow visualisations in the planes closer to the wall (figure 5.21a and 5.21c for the low incidence, and figure 5.22a and 5.22c for the higher angle of attack) show how the crosswind bends in the spanwise direction the transitional streaks. The angle that the streaks form with the x direction is not constant and changes continuously as a function of the three Cartesian coordinates. Clearly, the intensity
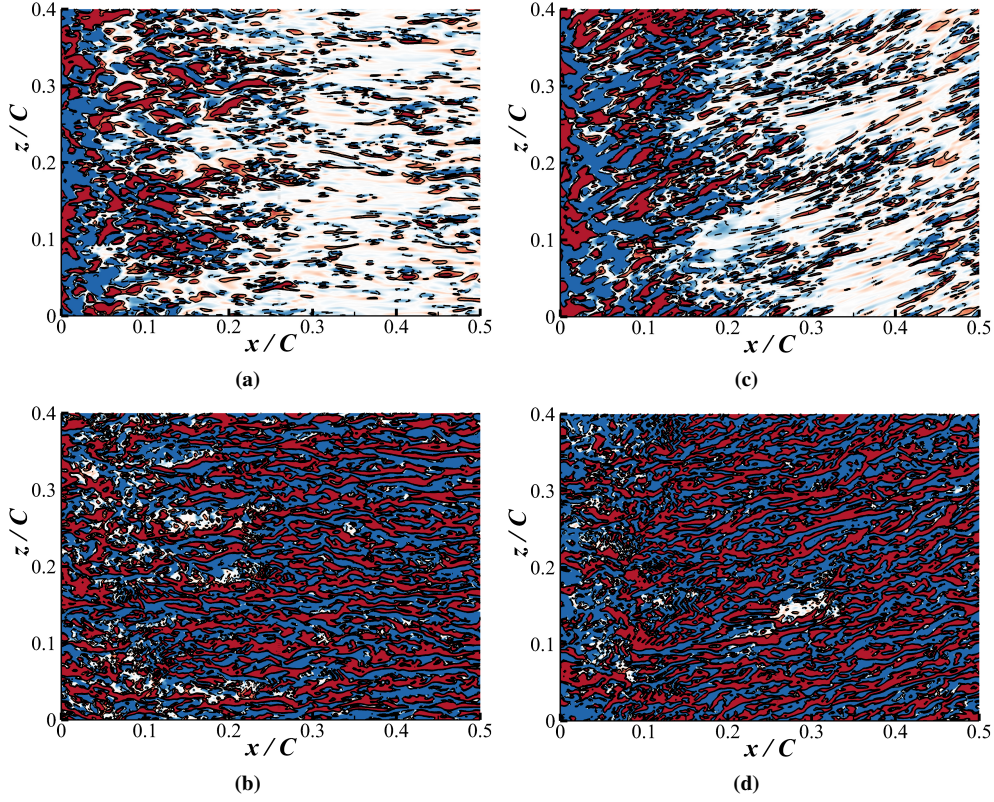
Figure 5.22: Iso-contours of $\omega'_y C/Q_\infty$ in the 10° incidence case with FST. Colour map and panels sequencing as in figure 5.21.

and directionality of the mean wind, which is responsible for the deflection of the streaks, depend on all the three space coordinates throughout the boundary layer as well (Vos & Farokhi 2015). In general, it is noticed that the streaks deflection is smaller for the higher incidence case, suggesting that the stronger chordwise pressure gradient gives an extra stretching of the structures along this direction. Moving further away from the wall, the velocity is expected to be aligned with that of the free stream, and therefore the dependency from the specific incidence is weakened.

5.3.2 Development of turbulent separation

When considering the unswept case, a similar fluctuating energy distribution is observed for both loading conditions in the regions close to the locations of the respective mean separations. This similarity can be observed in figure 5.23a and in figure 5.24a. From both figures one can notice that the strongest fluctuations are mostly contained within the wavelength band $\lambda_z/C = [0.01 - 0.1]$ (at $y/C \simeq 0.025$ in the low incidence case, at $y/C \simeq 0.05$ in the other incidence case). In the lowest incidence case the fluctuations are more intense towards the lower bound of the spanwise wavelengths range, while in the higher incidence case their

energy is preferentially accumulated at the other end. Another, less intense, peak is observed at $\lambda_z/C \simeq 0.2$ for both loading conditions (at $y/C \simeq 0.05$ in the low incidence case, at $y/C \simeq 0.07$ in the other incidence case). It is also remarked that the flow directionality of these large-scale spanwise perturbations (shown in figures 5.23b, c and d for the 5° case and in figures 5.24b, c and d for the higher angle of attack) corresponds roughly to the one observed in the laminar inflow case (in figures 4.12b, c and d). This similar behaviour, could be linked to the common baseline mechanisms that initiate and finally lead to the separation described by Kitsios et al. (2017). The fluctuating energy distribution can be observed to spread over different vertical ranges, due to the different sizes of the boundary layers in the two loading conditions. In the low incidence case the width of the wall normal range interested by the perturbation is bounded in height as $y/C < 0.05$, while it almost doubles its size in the higher angle of attack case. When the incidence is increased, a not uniform shift from the wall of the fluctuating energy contained in the wavelengths range $\Delta\lambda_z/C = [0.01 - 0.1]$ and that in wavelength $\lambda_z/C \simeq 0.2$ is also observed. As already mentioned, the energy contained in the small-scale moves upward from the location recorded in the lower incidence at $y/C \simeq 0.025$ to $y/C \simeq 0.05$ in the higher incidence case. The large-scale content moves from $y/C \simeq 0.05$ to $y/C \simeq 0.07$. It is remarked that the chord locations where the spectra have been computed differ for the two incidences. This choice has been taken to keep into account the different location of mean separation observed around $x/C = 1.0$ for the low incidence case, while at $x/C = 0.91$ for the other incidence.

A qualitative analysis of the structure of the perturbation field can be obtained by considering some selected instantaneous, fluctuating vorticity field visualisations. In particular, figure 5.26a shows an instantaneous snapshot of the chordwise vorticity perturbation $\omega'_x(x, y, z, t)$ field on a plane normal to the wall taken at the location of incipient separation for the unswept, low incidence case. Figure 5.26c shows a snapshot of ω'_y on a plane parallel to the suction side wall and in the vicinity of the latter for the same incidence. Figures 5.27a and 5.27c show snapshots corresponding to the other loading condition of the unswept wing. The ω'_x contours of alternating sign visible in the region close to the wall (range $\Delta y/C = [0 - 0.025]$ for the low incidence case and $\Delta y/C = [0.025 - 0.040]$ for the other incidence) and the spanwise sequencing of ω'_y (at chord location $x/C \simeq 1.0$ for the low incidence case and $x/C \simeq 0.91$ for the other) can be clearly associated with the wall turbulence velocity streaks (Kim et al. 1987), contributing to the energy content detected by the spectra in the bandwidth range $\Delta\lambda_z/C = [0.01 - 0.1]$. This turbulent streaky pattern is not to be confused with that observed in the front part of the wing, which is related to
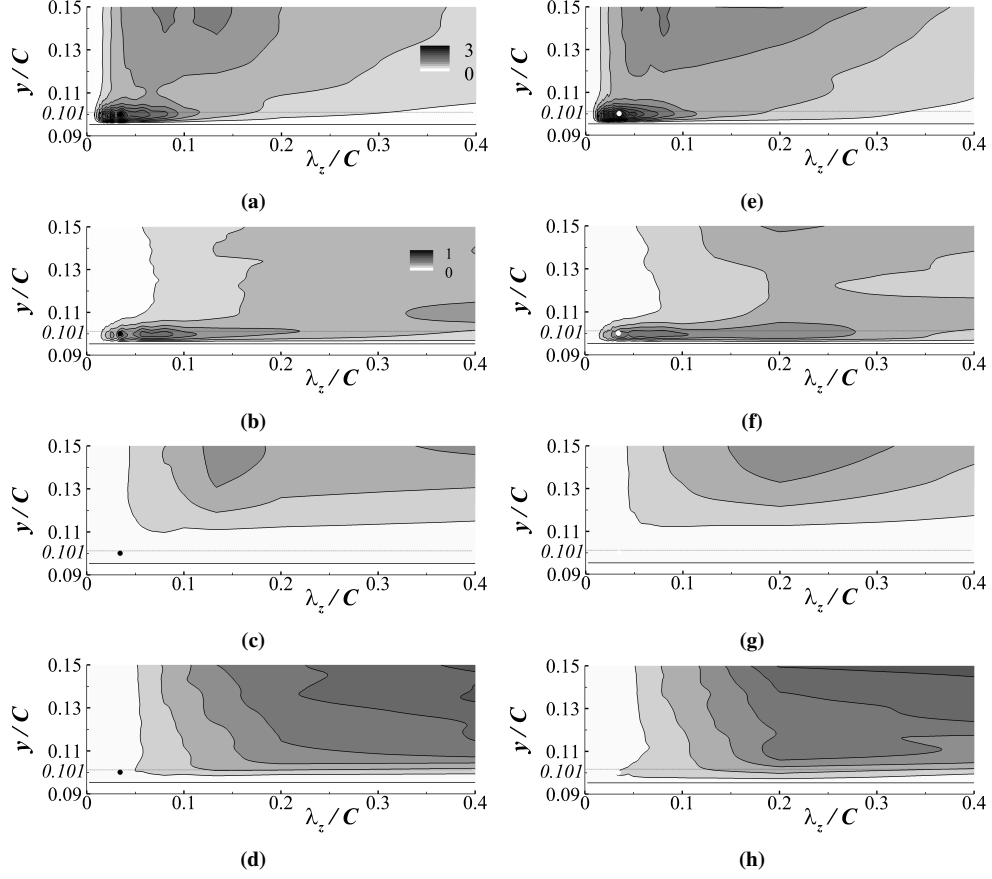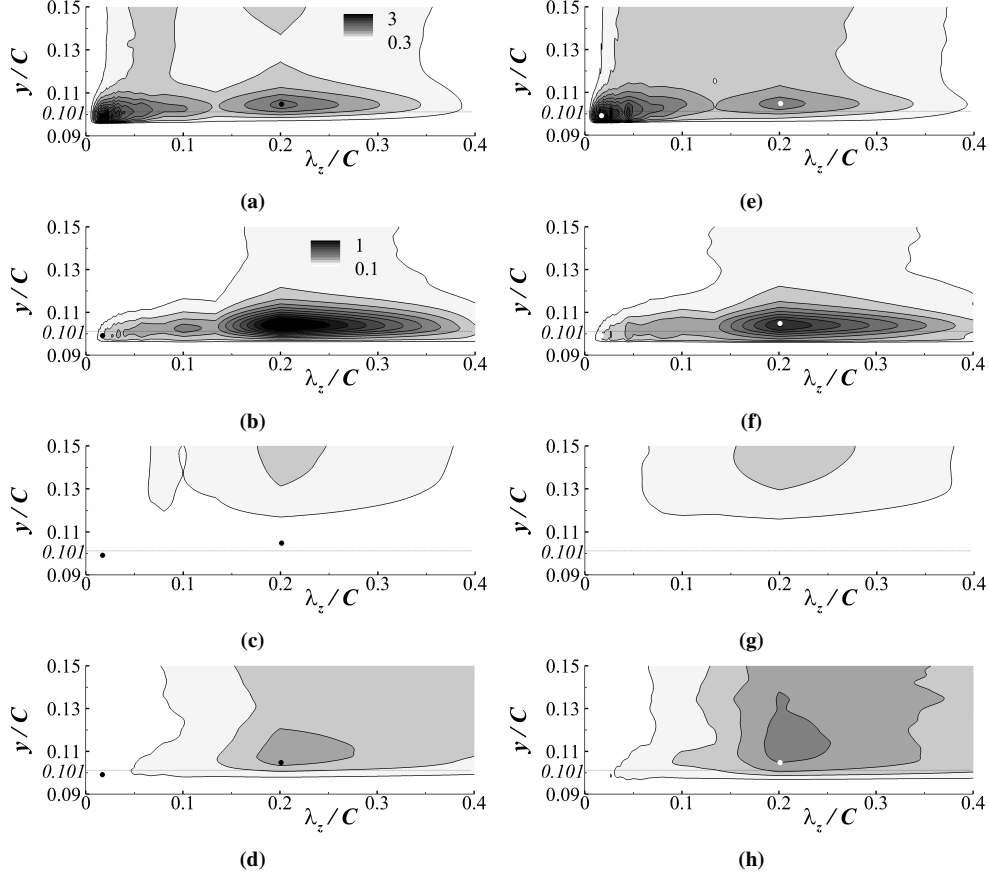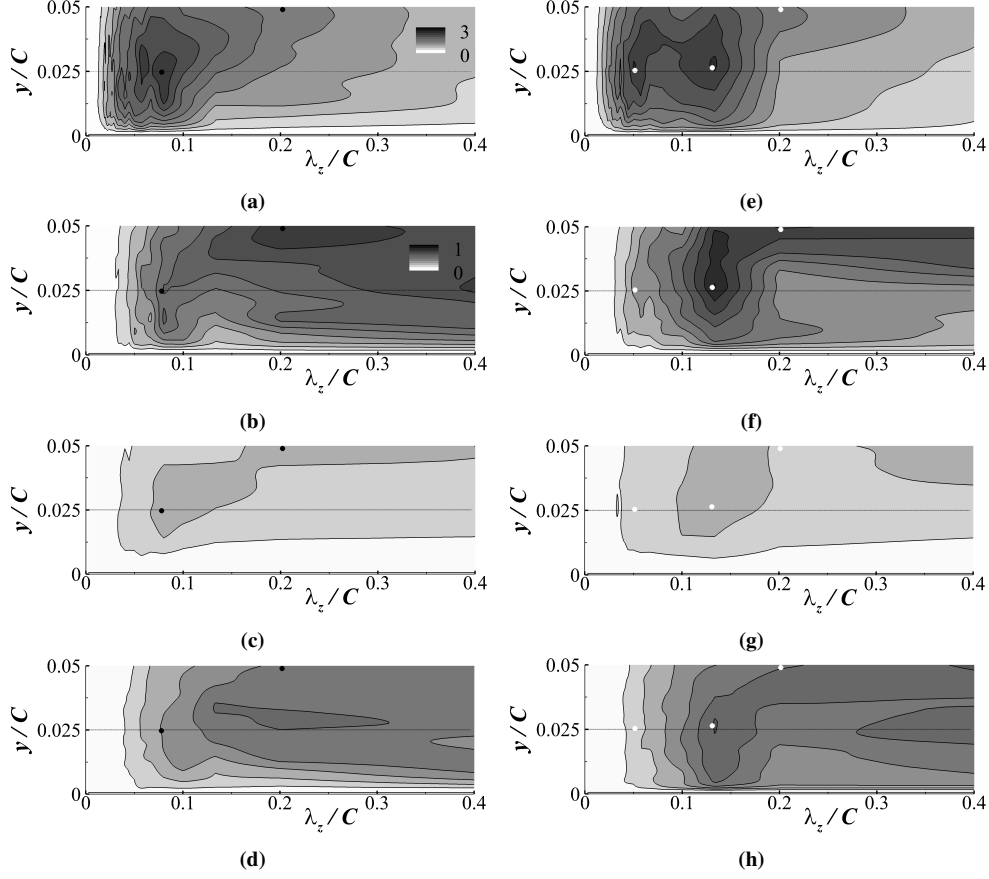
Figure 5.23: Spanwise energy content of the fluctuating velocity field in the 5° incidence case with FST. The straight wing is illustrated in the left column, the swept one in the right column. The spectra are extracted at $x/C = 1.0$. The black diamonds are used to highlight the dominant modes of the unswept wing, while the white ones indicate the dominant modes of the swept case. Panels (a) and (e) correspond to iso-contours of $k_z < \hat{E}^* >_t C$. The grey-scale colour map is distributed non-linearly with the black regions corresponding to $k_z < \hat{E}^* >_t C > 3$. The iso-lines are sampled with an increment of $k_z < \Delta\hat{E}^* >_t C = 0.23$ starting from $k_z < \hat{E}^* >_t C = 0$. (b) and (f) Iso-contours of $< \hat{R}^*_{u'u'} >_t$. The grey-scale colour map is distributed non-linearly with the black regions corresponding to $< \hat{R}^*_{u'u'} >_t > 1$. The iso-lines are sampled with an increment of $< \hat{R}^*_{u'u'} >_t = 0.07$ starting from $< \hat{R}^*_{u'u'} >_t = 0$. (c) and (g) Iso-contours of $< \hat{R}^*_{v'v'} >_t$. Same legend as for $< \hat{R}^*_{u'u'} >_t$. (d) and (h) Iso-contours of $< \hat{R}^*_{w'w'} >_t$. Same legend as for $< \hat{R}^*_{u'u'} >_t$.

the footprint of the Klebanoff mode governing the by-pass transition. The maps of ω'_y show how the turbulent streaks enlarge moving downstream towards the trailing edge. This effect is clearly related with the flow deceleration due to the increasing adverse pressure gradient (Lee & Sung 2009). As expected, this effect is more evident in the higher incidence case where the flow deceleration is stronger. The ω'_y maps also allow to recognise the footprints of the perturbations characterised by a spanwise wavelength $\lambda_z/C \simeq 0.2$. This is clearly visible in the flow pattern around a spanwise line at $x/C = 0.9$ for the low incidence case (figure 5.26c), and at $x/C = 0.65$ or $x/C = 0.90$ for the higher incidence case (figure 5.27c).

The sweep is found to have an impact to the perturbation fields at both the considered incidences. In particular, the crosswind appears to enhance the structures within the wall
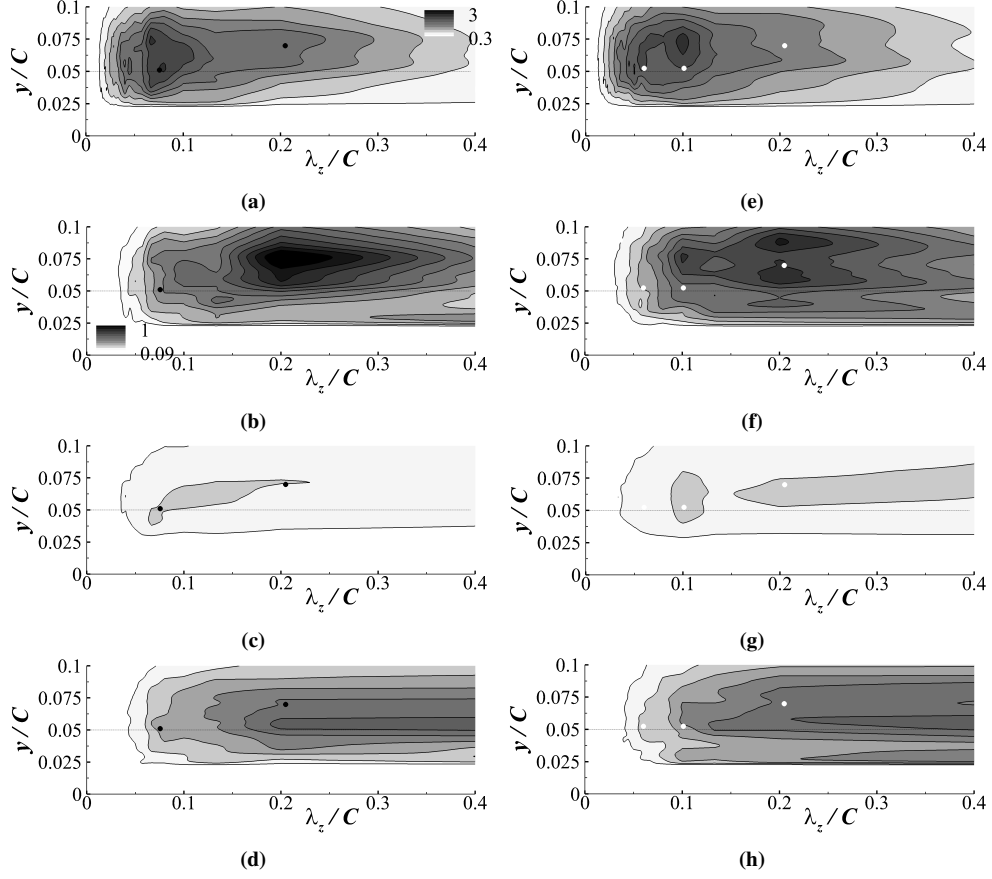
Figure 5.24: Spanwise energy content of the fluctuating velocity field in the 10° incidence case with FST. The straight wing is illustrated in the left column, the swept one in the right column. The spectra are extracted at $x/C = 0.92$. The black diamonds are used to highlight the dominant modes of the unswept wing, while the white ones indicate the dominant modes of the swept case. Panels (a) and (e) correspond to iso-contours of $k_z < \hat{E}^* >_t C$. The grey-scale colour map is distributed non-linearly with the black regions corresponding to $k_z < \hat{E}^* >_t C > 3$. The iso-lines are sampled with an increment of $k_z < \Delta\hat{E}^* >_t C = 0.3$ starting from $k_z < \hat{E}^* >_t C = 0.3$. (b) and (f) Iso-contours of $< \hat{R}^*_{u'u'} >_t$. The grey-scale colour map is distributed non-linearly with the black regions corresponding to $< \hat{R}^*_{u'u'} >_t > 1$. The iso-lines are sampled with an increment of $< \hat{R}^*_{u'u'} >_t = 0.09$ starting from $< \hat{R}^*_{u'u'} >_t = 0.09$. (c) and (g) Iso-contours of $< \hat{R}^*_{v'v'} >_t$. Same legend as for $< \hat{R}^*_{u'u'} >_t$. (d) and (h) Iso-contours of $< \hat{R}^*_{w'w'} >_t$. Same legend as for $< \hat{R}^*_{u'u'} >_t$.

buffer layer while slightly weakening those with large spanwise wavelength found further away from the wall. Comparing the perturbation spectra between the unswept and swept wings for the low incidence case (figure 5.23a and figure 5.23e), the energy linked to the wall turbulence in the swept case is observed to concentrate around two specific spanwise modes: $\lambda_z/C \approx 0.05$ and $\lambda_z/C \approx 0.15$. The mode with $\lambda_z/C \simeq 0.2$ is found to be fairly damped by the sweep. The vertical location of both peaks does not change with the sweep. A similar behaviour is observed when considering the other loading condition and comparing the energy spectrum of the unswept wing provided in figure 5.24a with the one of the swept wing in figure 5.24e. It is noticed that in the higher incidence case the mean crosswind of the swept configuration damps substantially the large scale energy content at the specific vertical
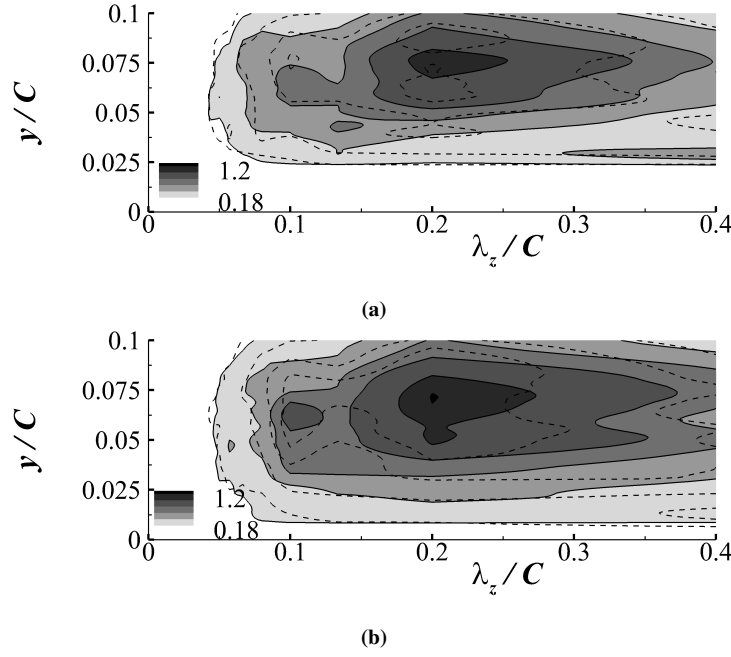
Figure 5.25: Comparison of $< \hat{R}^*_{u'u'} >_t$ between the unswept and swept wings in the 10° incidence case with FST. Spectra extracted at location (a) $x/C = 0.92$ and (b) at $x/C = 0.98$. The grey-scale colour map refers to the straight wing case with darker colours for higher values. Some iso-lines of $< \hat{R}^*_{u'u'} >_t$ correspond to $[0.18, 0.36, 0.54, 0.72, 1.0, 1.2]$. The solid lines are used for the unswept wing, while the dashed lines are used for the same iso-values obtained in the swept wing case.

location $y/C = 0.075$ as it can be observed in figure 5.24f from the energy content variation of the spanwise wavelength $\lambda_z/C \simeq 0.2$. The damping effect induced by the sweep on the large scale structures in the surroundings of the mean separation is more evident when the chordwise energy spectra of the straight and the swept wing are superimposed. In particular, figures 5.25a and 5.25b show this direct comparison for the subsequent locations $x/C = 0.92$ and $x/C = 0.98$. It can be observed that the energy peak of the swept wing at $y/C = 0.075$ is substantially reduced when location $x/C = 0.98$ is approached. Beyond this location, the energy content of the chordwise velocity fluctuations $< \hat{R}^*_{u'u'} >_t$ decays abruptly.

Through the visualisations of the instantaneous vorticity field some hints on the effect produced by the sweep on the flow structures embedded in the wall region can be obtained. From figures 5.26a and 5.26b and from figures 5.27a and 5.27b, one can observe how the top portion of the low speed streaks (vertical range within the $2 - 3\%C$ from the wall) appears to be stretched in the spanwise direction when comparing the visualisation of ω'_x for the swept and unswept wing configurations in both the low (figures 5.26a and 5.26b) and higher (figures 5.27a and 5.27b) incidence case. In the swept case the iso-contours spacing is observed to reduce leaving a thin high speed cushion to separate the low speed streaks. The energy content of the fluctuating field (shown in figure 5.23e or 5.24e) associated with

$\lambda_z/C \simeq 0.05$ corresponds to the narrow, high speed streaks, while the $\lambda_z/C \simeq 0.15$ one is related to the wide, low speed streaks. The width enlargement of the low speed streaks and the corresponding shrinking of the high speed ones can be attributed to the crosswind that deviates the streaks in the spanwise direction. The result of this imposed displacement are streaks bent in the spanwise direction easily observed with the swept/unswept comparative visualisation of ω'_y on planes parallel to the wall in figures 5.26c - 5.26d for the low incidence case. In figures 5.27c - 5.27d the same comparison is proposed for the higher incidence case. As an effect of this continuous deflection, the streaks become almost parallel to the trailing edge moving downstream towards a region affected by mean flow separation. This behaviour is even more striking for the higher loading condition shown in figure 5.27d. From the presented visualisations it can be concluded that the topology of the separated region past a swept wing is similar to the ones observed in other separating swept flows, being all of them characterised by spiralling streamlines oriented along the spanwise direction (Davis et al. 1987, Broadley 1998, Vos & Farokhi 2015, Ashill et al. 2005, Black 1952). This behaviour may be attributed to the superposition of the mean crosswind and the insurgence of a spanwise instability as discussed later.

For the higher incidence case, the mean flow of both the straight and swept wings at the location preceding the mean separation will be studied in a similar manner as it was done for the laminar inflow case in section 4.3.2. To this end, the mean wall-tangent and spanwise velocity profiles ($< u_{tg} >_{z,t} (x, n)$ and $< w >_{z,t} (x, n)$) extracted at location $x/C = 0.90$ are provided in figure 5.28a and 5.28b, alongside with their curvature distribution ($\partial^2 < u_{tg} >_{z,t} (x, n)/\partial n^2$ and $\partial^2 < w >_{z,t} (x, n)/\partial n^2$) in figure 5.28c and 5.28d. The wall-tangent velocity profile presents an inflection point at $n/C = 0.06$. This vertical location appears to be unaffected by the crosswind. As it was observed in the laminar separation scenario, the spanwise flow presents an inflection point at the same vertical location of the chordwise flow. The inflection point is observed to match the peak of the fluctuating energy content at the wavelength $\lambda_z/C \simeq 0.2$ observed in the spectra taken at location $x/C = 0.92$ and shown in figure 5.24. The presence of an inflection point for the chordwise flow may suggest the appearance of a Kelvin-Helmholtz instability contributing in modifying the large scale separation forming in the turbulent boundary layer promoted by the strong adverse pressure gradient. As already remarked for the laminar separation, the appearance of an inflection point also in the mean spanwise flow of the swept wing field suggests a redistribution of the fluctuating energy content reshaping the separation behaviour. This is in accordance with the difference in the large scale fluctuating energy between the straight and the swept wing
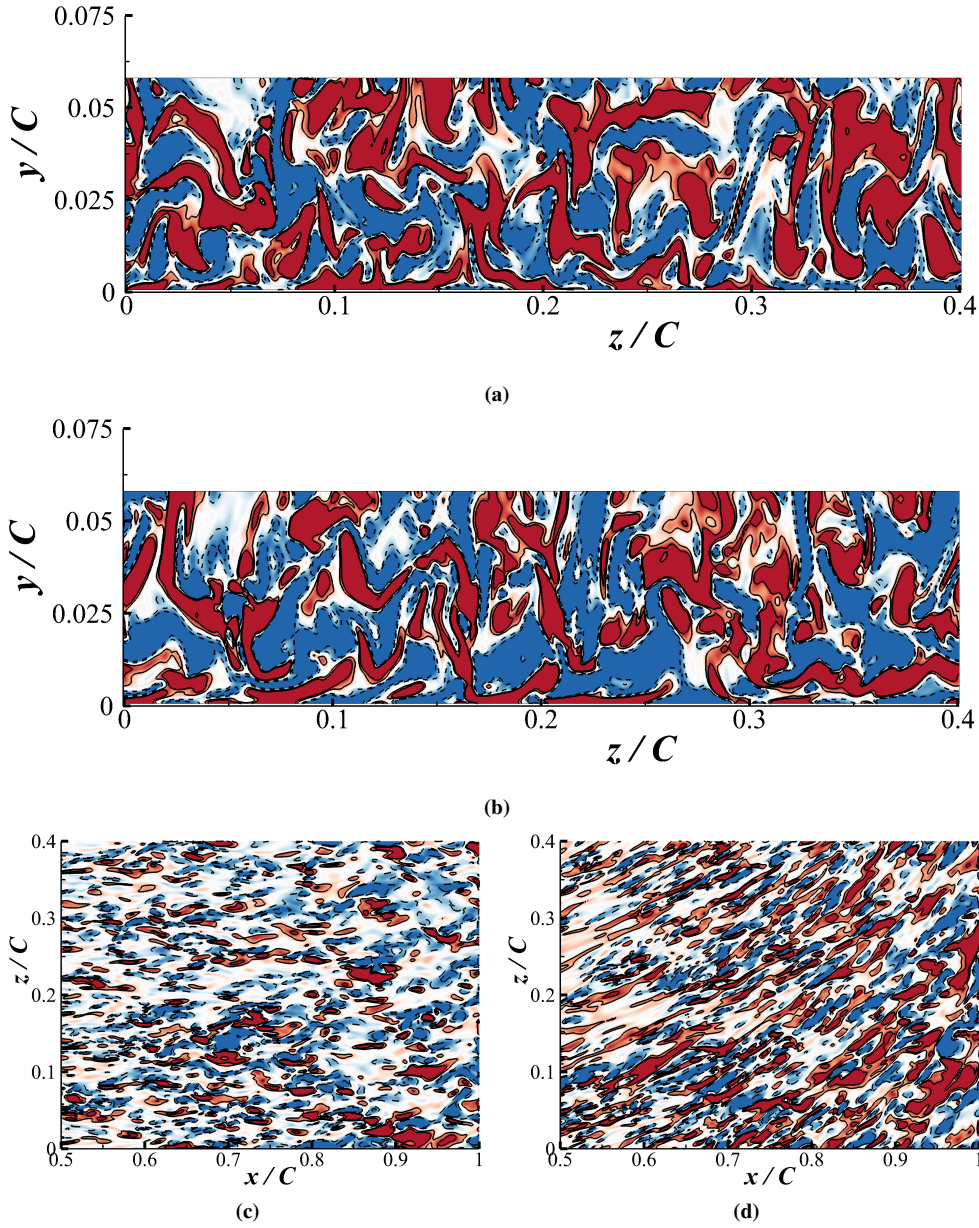
Figure 5.26: Iso-contours of the instantaneous fluctuations of the vorticity field in the 5° incidence case with FST. (a) and (b) Iso-contours of $\omega'_x C/Q_\infty$ extracted on a spanwise plane normal to the suction side wall at $x/C = 1.0$. Selected iso-lines at $\omega'_x = [\pm 10 \pm 20]Q_\infty/C$ are represented with solid lines for positive values, dashed otherwise. Top: straight wing; Bottom: swept wing. (c) and (d) Iso-contours of $\omega'_y C/Q_\infty$ on a plane parallel to the suction side wall and just on top of it, shown from mid chord onwards. Selected iso-lines at $\omega'_y = [\pm 10 \pm 20]Q_\infty/C$ are represented with solid lines for positive values, dashed otherwise. Left: straight wing; Right: swept wing. Red colour is used for positive vorticity perturbations (i.e. $\omega'_{\{\cdot\}} C/Q_\infty > 20$), blue for negative values (i.e. $\omega'_{\{\cdot\}} C/Q_\infty < -20$) and white for vorticity close to zero.

136

Figure 5.27: Iso-contours of the instantaneous fluctuations of the vorticity field in the 10° incidence case with FST. (a) and (b) Iso-contours of $\omega'_x C/Q_\infty$ extracted on a spanwise plane normal to the suction side wall at $x/C = 0.9$. Selected iso-lines at $\omega'_x = [\pm 10 \pm 20]Q_\infty/C$ are represented with solid lines for positive values, dashed otherwise. Top: straight wing; Bottom: swept wing. (c) and (d) Iso-contours of $\omega'_y C/Q_\infty$ on a plane parallel to the suction side wall and just on top of it, shown from mid chord onwards. Selected iso-lines at $\omega'_y = [\pm 10 \pm 20]Q_\infty/C$ are represented with solid lines for positive values, dashed otherwise. Left: straight wing; Right: swept wing. Red colour is used for positive vorticity perturbations (i.e. $\omega'_{\{\cdot\}} C/Q_\infty > 20$), blue for negative values (i.e. $\omega'_{\{\cdot\}} C/Q_\infty < -20$) and white for vorticity close to zero.

observed within the spectra of figure 5.25.

Concerning the characterisation of the flow field close to the separating region, figures 5.28e and 5.28f illustrate a comparison between the swept and unswept wing distribution of the *r.m.s* of the chordwise and spanwise velocity fluctuations ($< u'u' >_{z,t} (x,n)$ and $< w'w' >_{z,t} (x,n)$) for the 10° incidence case with FST. Figure 5.29a shows the same comparison for the Reynolds stress $< u'v' >_{z,t} (x,n)$. All the profiles have been extracted in proximity of the separation region at the same chord location $x/C = 0.9$. The Reynolds stresses linked to the chordwise flow do not show an appreciable difference in the location of the mean flow inflection point ($n/C \simeq 0.6$) when the crosswind is introduced. However, it is noticed that the crosswind due to the sweep enhances the fluctuating content in the cross-components Reynold stress $< u'w' >_{z,t} (x,n)$ (shown in figure 5.29b) in the vertical location $n/C \simeq 0.6$. This local increase may be related with the flow structures introduced by the interaction between the chordwise and spanwise flows inside the separating flow. Because of the chaotic nature of the turbulent separation, it was not possible to recognise flow structures embedded in the instantaneous flow field that could be directly linked with typical stages of the breakdown process leading to separation. This difficulty made impossible to directly diagnose the features that differentiate the turbulent separation on the swept and unswept case. However, in the profiles of $< w'w' >_{z,t}$ and $< u'w' >_{z,t}$ of the swept wing, the appearance of a peak close to the wall at $n/C \simeq 0.005$ is remarked. This local increase of the fluctuating activity can also be observed in the iso-contours of $< \hat{R}^{*}_{u'u'} >_{t}$ extracted further downstream, at $x/C = 0.98$, and shown in figure 5.25b, where the iso-lines corresponding to the swept wing flow allow to identify an energy peak with the wavelength $\lambda_{z}/C \simeq 0.4$ at vertical location $y/C \simeq 0.01$.
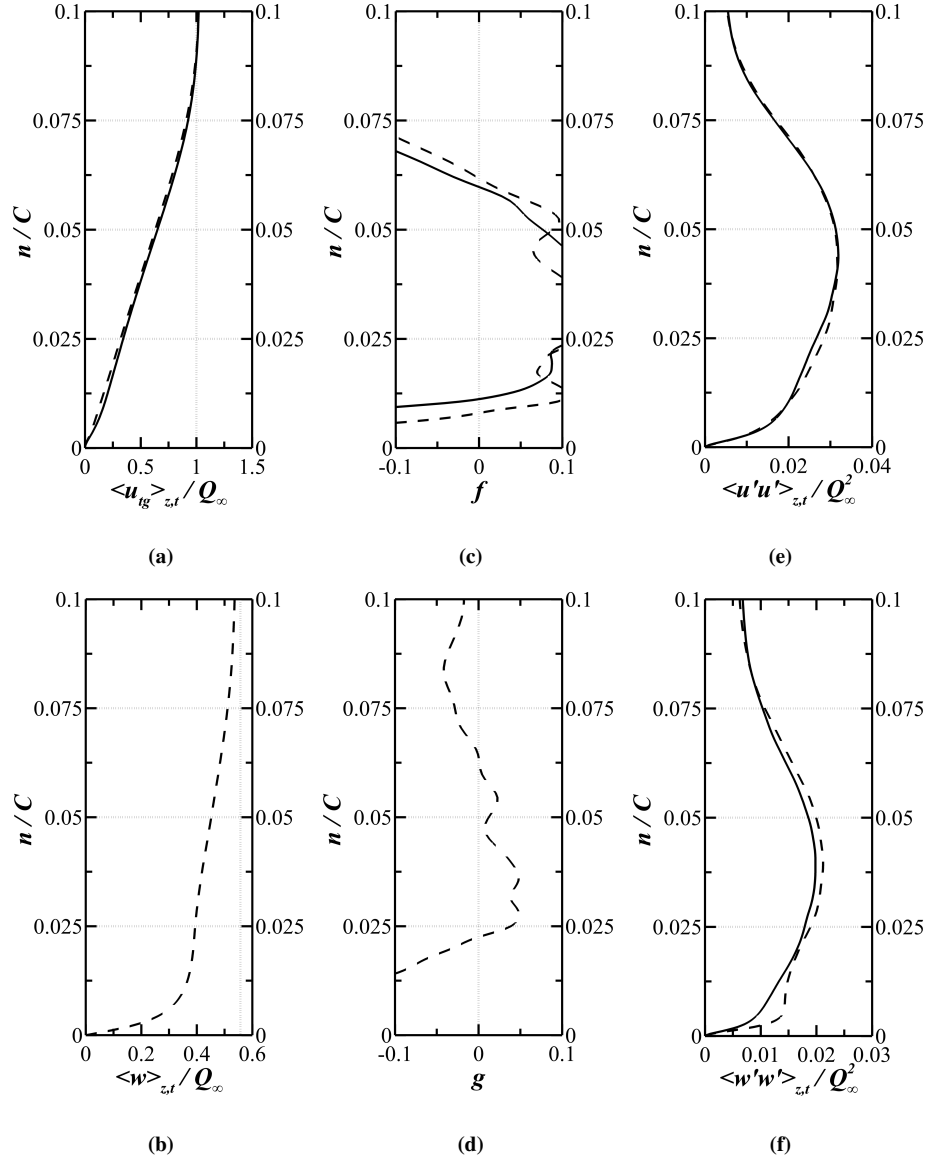
Figure 5.28: Mean chordwise and spanwise velocity field wall normal distributions extracted from the suction side at chord location $x/C = 0.9$ for both swept (dashed lines) and unswept (solid lines) configurations in the 10° incidence case with FST. Panel (a) $< u_{tg} >_{z,t} /Q_\infty$, (b) $< w >_{z,t} /Q_\infty$, (c) $f = (C^2/Q_\infty)\partial^2 < u_{tg} >_{z,t} /\partial n^2$, (d) $g = (C^2/Q_\infty)\partial^2 < w >_{z,t} /\partial n^2$, (e) $< u'u' >_{z,t} /Q_\infty^2$ and (f) $< w'w' >_{z,t} /Q_\infty^2$.
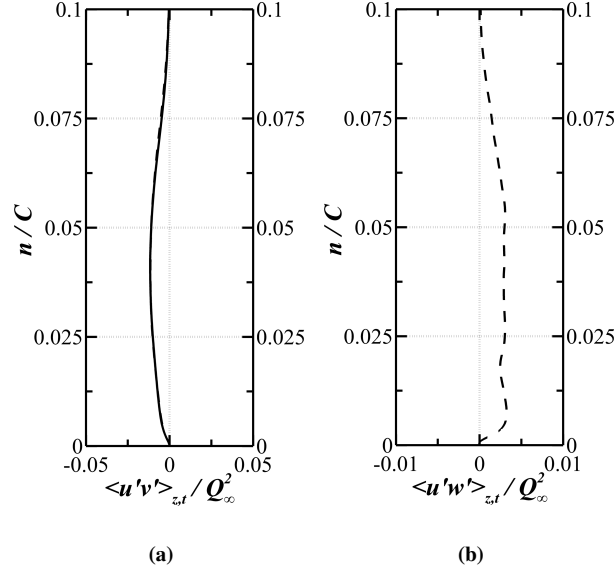
Figure 5.29: Cross-components Reynolds stress $< u'v' >_{z,t} /Q_\infty^2$ and $< u'w' >_{z,t} /Q_\infty^2$ in (a and b). All the profiles have been extracted from the suction side of the 10° incidence case with FST at $x/C = 0.90$. The solid line is used for the straight wing while the dashed line for the swept wing.

5.3.3 Statistical analysis of the reversed flow

An indication of the approaching separation of the turbulent boundary layer in the straight wing case can be found in the maps of the instantaneous chordwise wall friction $\tau_{sn}^{w}(x, y, z, t)$ on the suction side of the unswept wing. These are shown in figure 5.30a for the low incidence case and in figure 5.31a for the higher one. In this figures, the localised blue spots indicate the presence of separated nuclei. These nuclei preferentially line up following the low speed streaks. This behaviour has also been observed recently by Vinuesa, Örlü & Schlatter (2017). The width of the nuclei increases according to that of the low speed streaks where they are hosted, thus growing moving downstream due to the increasing adverse pressure gradient and reduced wall friction (Lee & Sung 2009). The initial appearance of the nuclei that represent locally reversed flow, is found at a very early stage of the wing ($x/C = 0.25$ for the 5° incidence case, $x/C = 0.05$ for the 10° case). It is interesting to note that the width of the nuclei increases up to $20\%C$ when the location of the mean separation on each wing is approached ($x/C = 1.0$ for the 5° incidence case, $x/C = 0.91$ for the other).

Thus, the separation of the turbulent boundary layer that develops on a straight wing appears to be a process that builds up moving downstream along the chord by the increased probability of finding longer and larger reversed flow spots. Under this perspective, the reverse flow nuclei could be seen as the precursor of the formation of a stall cell and the mean separation location just become a time-average quantity that has no instantaneous physical

(a)

(b)
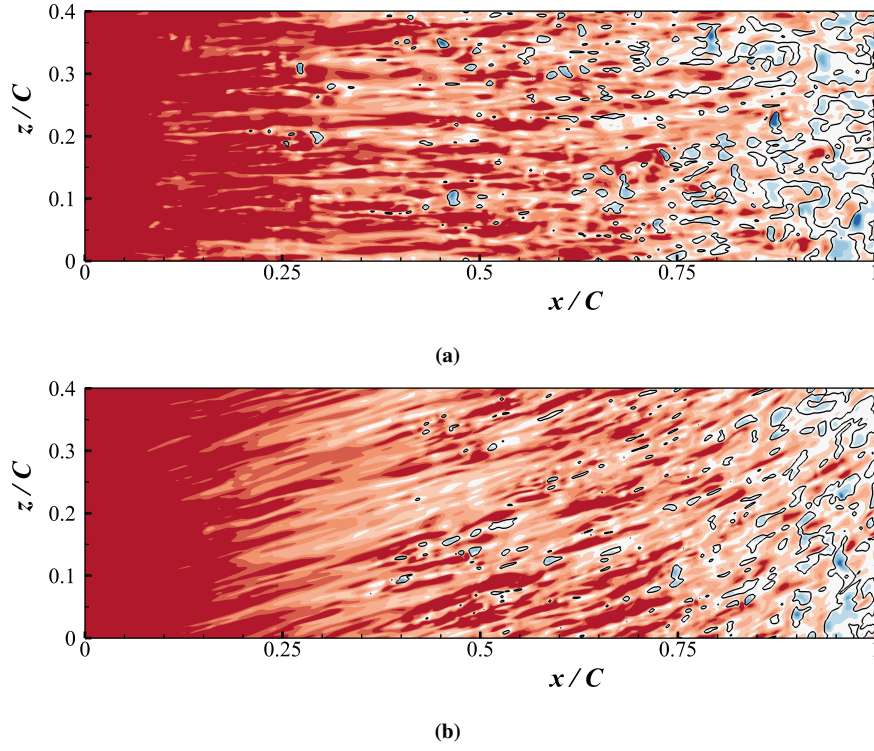
Figure 5.30: Iso-contours of $\tau_{sn}^w/(\rho Q_\infty^2)$ on the suction side wall for the 5° incidence case with FST. Top: straight wing; Bottom: swept wing. The red colour is used for positive friction values (the y axis is pointing upwards), blue for negative ones.

(a)

(b)
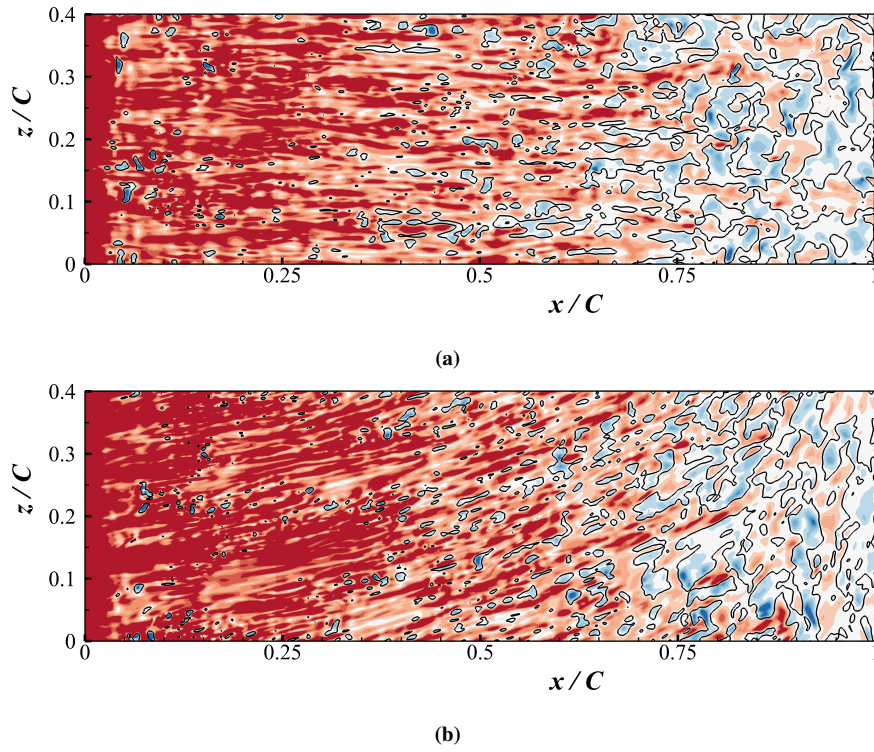
Figure 5.31: Iso-contours of $\tau_{sn}^w/(\rho Q_\infty^2)$ on the suction side wall for the 10° incidence case with FST. Panel descriptions and legend as in figure 5.30.
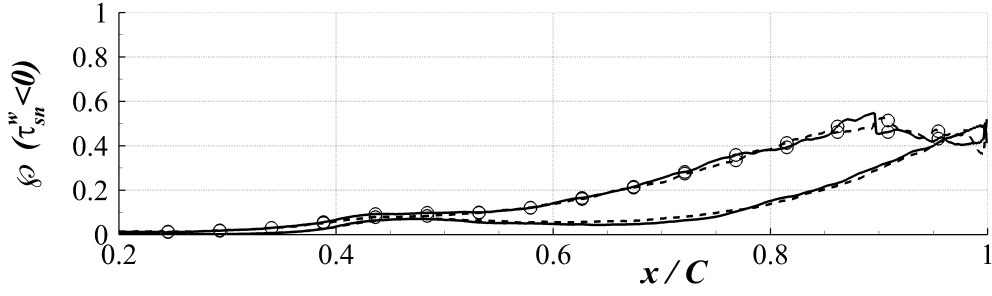
Figure 5.32: Distribution of $\wp(\tau_{sn}^w < 0)$ along the chord on the suction side wall. The solid line is used for the straight wing and the dashed line for the swept at 5° incidence, while the same lines with circles are used for the corresponding wings for the 10° incidence case.

meaning. This probabilistic picture of turbulent separation can be understood by looking at the colour distribution of the maps of figure 5.30 (the blue colour is used for the reversed flow), showing a continuously increasing probability of finding a region of localised reversed flow moving towards the trailing edge. This scenario becomes even more evident for the higher incidence case whose skin friction maps are shown in figure 5.31. To quantify the reversed flow, the time averaged cumulative probability to observe a backflow event along the span for all the chord stations along the wing $\wp(\tau_{sn}^w < 0)(x, n)$ (defined in equation 4.7) is shown in figure 5.32 (solid lines) for both incidences. As expected, the cumulative probability presents a continuous increase moving towards the trailing edge also showing a direct relation with the adverse pressure gradient distribution when quantified by the Clauser parameter (shown with the solid line in figure 5.13). It is also noticed that the probability to observe a backflow levels out at 0.5 when the location of the mean separation on each wing is approached ($x/C = 1.0$ for the 5° incidence case, $x/C = 0.91$ for the 10° case). From now on, it will be assumed that the location of the mean separation line can be estimated considering the chord location where more than 50% of the spanwise direction is occupied by reversed flow spots.

The fluctuating energy content contained in the spanwise wavelength $\lambda_z/C \simeq 0.20C$, which has been discussed when considering the spectra in sections 5.3.2, appears to be related with the local spanwise size of the separated front (i.e. the stall cell size). Indeed, the distribution of $\wp(\tau_{sn}^w < 0)$ saturates (independently of the incidence) at 50% chance of finding reversed flow and the flow structures containing reversed flow (blue spots indicating the stall cells) having spanwise extension of about $20\%C$ can be seen inside the area affected by mean separation in the flow visualisations proposed in figures 5.30a and 5.31a for both loading conditions.

The nature of the turbulent separation that has been described above, also offers an expla-

nation of the thickening layer of $<\omega_x>_{z,t}$ on the wing suction side at $x/C = 0.60$ presented in figures 5.8a and 5.8b. It is believed that the distribution portraits the footprint of an early incipient separation, which appears to lack a clear uniform separation (i.e. with a spanwise extension of $20\%C$) even for the high loading case. Also, the absence of a smooth shape for the $<\omega_x>_{z,t}$ layer in the 10° incidence case may be linked to the formation of the incipient separation. The process involves locally larger scales structures (although smaller than $20\%C$) which require a longer sampling time than the considered one (i.e. $\Delta t^* \simeq 30Q_\infty/C$ for the $<\omega_x>_{z,t}$) to produce statistically meaningful results.

In summary, the turbulent separation mechanism on the swept wings appears to follow a similar evolution as for the unswept case, whilst the flow topology of the inner boundary layer is greatly affected by the presence of the crosswind. Indeed, the distributions of $\wp(\tau_{sn}^w < 0)$ for both the swept wing loading conditions show similar behaviours as the one found for their unswept wing counterparts, as can be seen in figure 5.32.

It has been also observed that a strong difference in the flow field topology in the wall region takes place when the swept wing configuration is considered. In particular, by comparing the friction lines between the swept/unswept wing configurations, provided in figures 5.30a and 5.30b for the low incidence case (see figures 5.31a and 5.31b for the higher loading condition), one can easily observe the effect of the crosswind. In the low incidence case the lines that correspond to the low speed streaks are bent with an almost constant angle (imposed by the mean local flow) along the whole chord, except in the trailing edge region. Furthermore, the footprints of the low speed streaks at the wall appear narrower (considering the cross-section perpendicular to their elongation) than those observed in the unswept wing. This observation is confirmed when considering the width of the backflow nuclei that are channelled within the low speed streaks. Indeed, their size in the direction normal to the local velocity vector is observed to be qualitatively smaller when the crosswind is introduced. This observation is consistent with the experiments of Flack (1997), where narrower streaks were observed in a turbulent channel flow when a crosswind component is added to the mean flow. For the higher incidence case similar observations can be made, although the bending angle is not constant along the chord: close to the leading edge the flow is almost perpendicular to it, while it progressively turns to become almost parallel to the trailing edge when the location of mean separation, $x/C = 0.91$, is approached. A similar scenario has also been described in the discussion of turbulent separation given in Broadley (1998). As a final observation, it is noticed that beyond the mean separation location, the blobs containing reversed flow in a swept wing present a topology slightly more extended in the spanwise

direction than those on the unswept wing (the reader would compare the visualisations between the two wing configurations in figure 5.30 for the low incidence case and figure 5.31 for the other incidence). This observation is consistent with the modified large scale energy content observed in the spectra (figure 5.23 for the low incidence case and figure 5.24 and 5.25 for the other case) when the wing configuration with the crosswind is considered.

Chapter 6

Conclusions

High fidelity simulations of incompressible flows past infinite straight and swept wings featuring a $NACA-4412$ profile have been carried out. In both wing configurations, the chord Reynolds number has been kept constant at a value of 5×10^4. All the considered simulations involved cases with enough incidence to lead to a partial detachment of the suction side boundary layer. The aim of the present thesis has been to undertake a systematic comparison of the flow developing around swept and unswept wings to understand the effect of a mean crosswind on the flow fields. This exercise has been carried out considering both laminar and turbulent incoming flows. In particular, the assessment and the range of validity of the *Simple Sweep Theory* when flow detachment takes place was one of the primary research goals. Alongside this more applied task, a more basic objective concerning the characterisation of the separation mechanism from a fundamental perspective, highlighting analogies and differences between all the flow scenarios considered, has also been a central research topic. The flow scenarios that have been considered included a laminar inflow condition and a 10% intense turbulent free stream condition. In the laminar inflow case, a 5° angle of attack has been considered. In the turbulent inflow case, two distinct incidences have been considered, namely 5° and 10°. All the considered cases have been simulated using a straight and a 30° swept-back wing to allow a meaningful ground for cross-comparison.

All the configurations mentioned above share the appearance of a separated portion of the suction side boundary layer induced by the gradually increasing adverse pressure gradient that develops when moving towards the trailing edge. An original method is proposed

and used to extend the computation of the mean boundary layer integrals along the foil portion interested by the presence of flow detachment. This approach can be considered as an extension of the vorticity-vanishing criterion originally introduced by Vinuesa et al. (2016) for wings characterised by an attached boundary layer. This methodology has also been adopted to compute the integral properties of the boundary layers that develop on the swept wing configuration, i.e. in presence of a mean crosswind. In what follows, the conclusions have been organised accordingly to the various scenarios that have been considered.

6.1 Incoming uniform, laminar flow

6.1.1 Unswept wing flow

When a laminar inflow is considered, the unswept wing features a laminar separation bubble (LSB) on its suction side, while a laminar, attached boundary layer is observed on the pressure side. This is a well known scenario reported several times by other authors, e.g Gaster (1967), Jones et al. (2008), Yarusevych et al. (2009). The region interested by flow separation is bounded from above by a thin shear layer that, in the particular case considered here, detaches from the wall at the (spanwise and time) averaged location $x/C = 0.26$. This location is found to be marginally unsteady and weakly three-dimensional, therefore a probabilistic approach is not strictly necessary for its characterisation. A dividing streamline (Marxen & Henningson 2011), which envelopes the LSB, is also observed when the mean flow is considered.

The aforementioned detached shear layer undergoes a laminar to turbulence transition on the wing suction side. The transition originates from the inviscid instability of the chordwise flow component when entering the area interested by the reversing flow as demonstrated by Watmuff (1999) and observed by several other authors (e.g. Alam & Sandham (2000), Lang et al. (2004), Marxen et al. (2004), Jones et al. (2008), Hain et al. (2009), Marxen et al. (2012)).

On the suction side, the fluctuating flow field exhibits an intense energy content albeit mainly taking place around the dividing streamline. The shear layer is also observed to be modulated in the spanwise direction with a dominant mode appearing in correspondence of the mean separation location characterised by a wavelength $\lambda_z/C \simeq 0.2$. This flow mode is observed to be related with the detaching shear layer breakdown to turbulence.

6.1.2 Swept wing flow

The chordwise flow of the swept wing is found to follow the predictions obtained using the *Simple Sweep Theory* as long as the boundary layer remains attached to the wall. Conversely, the portion of the wing interested by detachment exhibits a chordwise flow that depends on the wing sweep. Clearly, in this condition the *Simple Sweep Theory* predictions are not valid and would require an eventual correction not proposed yet in the scientific literature. Although the deviation from the *Simple Sweep Theory* predictions are small for the low order statistics of the flow (i.e. mean flow fields of velocity and pressure and consequently the boundary layer integrals), they become non negligible for the higher order statistical quantities (i.e. flow fluctuating field and consequently the energy content of the developing turbulence, as well as the character of the reversed flow). It is also found that the sweep does not influence the mean wing performances, but the induced mean cross flow plays a role on the flow dynamic participating into the aerofoil wake. This effect has also an impact on the temporal behaviour of the wing performances, that are indeed influenced by the presence of the crosswind differently from what would be predicted by the *Simple Sweep Theory*. In this context, the result obtained in this thesis confirm the conclusions of former pioneering works of Uranga et al. (2011) and De Tullio & Sandham (2017). In particular, the crosswind is seen not to play any role in the determination of the separation location, however it modifies the process leading to transition by altering the unsteady behaviour of the detaching shear layer. The dominant spanwise mode leading to the turbulent breakdown of the shear layer in the case of a straight wing is characterised by a wavelength $\lambda_z/C \simeq 0.2$. This mode is marginally weakened in favour of larger spanwise modes in the swept wing scenario. The violation of the *Simple Sweep Theory* is observed especially downstream of the breakdown location. The modified energy content of the fluctuating field in the shear layer of the swept wing may be linked to the appearance of an inflection point in the crosswind mean velocity profile inside the reversed flow area. It is however noticed that the footprints of the fluctuating flow structures do not coincide with those observed in the literature of the conventional crossflow instabilities occurring on a swept wing for high Reynolds number, see for example Reed & Saric (1989).

The spanwise flow of the swept wing exhibits a distinct boundary layer with respect to that of the chordwise flow inside the separated flow area, as it remains attached everywhere along the chord. However, the spanwise flow feels the ongoing separation of the streamwise flow exhibiting the typical shape of a boundary layer over a porous wall (e.g. Monti et al.

(2019)), which suggests the LSB being a region with a varying effective viscosity for the spanwise flow.

Inside the separated flow region, the flow topologies of the straight and swept wings are different, especially close to the wall, with spanwise spiralling streamlines in accordance with the features already observed by other authors (e.g. Davis et al. (1987), Broadley (1998), Hetsch & Rist (2009). This set of vortices seems to originate from the combined action of the mean chordwise and spanwise flows, rather than being the results of an ongoing crossflow inflectional instability. A reasonable explanation for the spiralling character is the loss of chordwise momentum, giving a directionality preference to the reversing flow. In particular, in the swept configuration, the detached flow region is characterised by spanwise-coherent vortices.

6.2 Turbulent free stream

6.2.1 Unswept wing flow

For both the considered loading conditions, the increase of the turbulence level in the free stream deeply modifies the LSB scenario described above. A largely attached flow is the result of an enhanced turbulent mixing of momentum in the close to the wall region (Schlichting & Gersten 2000). The boundary layer on both the wing sides is triggered by the FST to a turbulent state via a by-pass mechanism from the very initial portion of the wing leading edge as observed by Brandt et al. (2004) for the case of the transition of a Blasius boundary layer on a flat plate. The turbulent boundary layer developing downstream features enough friction to remain attached to the wall for the most part of the aerofoil. In particular, in the lower incidence case, the average location of the separation front is found at the very end of the suction side, at $x/C = 1.0$. In the higher incidence case, the average location of the separation front is observed more upstream at location $x/C = 0.91$.

As expected, the wing lift of the FST injected cases is increased considerably, when compared to the laminar inflow case. The overall drag decreases is an obvious direct consequence of the LSB suppression that implies pressure drag reduction. The latter surpasses the friction drag increase of the turbulent boundary layer which is higher than its laminar counterpart. It is also noticed that the presence of turbulent boundary layer mitigates the unsteadiness of the integral aerodynamic coefficients.

For both the considered loading conditions, the fluctuating flow field near the wall, along the whole suction side, is characterised by an energy content in the spanwise modes having

wavelength in the range $0.01 < \lambda_z/C < 0.1$. This distribution of fluctuating energy in the spanwise direction can be linked to the development of the wall turbulence flow structures, in particular velocity streaks, along the foil. In the front part of the wing, the streaks are the product of the by-pass transition caused by the FST and may be linked to the Klebanoff mode, in agreement with what has been observed by other authors (Brandt et al. 2004). In the rear part of the wing, the streaks represent the turbulent low speed streaks and they present a varying spacing in accordance to the varying adverse pressure gradient condition. In particular, they widen moving towards the stronger adverse pressure gradient at trailing edge, confirming the conclusions made by Lee & Sung (2009), and consistently with a reduced value of the skin friction Reynolds number.

Apart from the broadband distribution of energy modes in the spanwise direction, a second peak of the fluctuating energy is observed on the suction side of the wing corresponding to a wavelength of $\lambda_z/C \simeq 0.2$. In the higher incidence case, this presence is recorded from a position which is upstream of the one corresponding to the lower angle of attack. The energy content of this large spanwise mode increases until reaching high values when the mean separation location is approached, for both the loading conditions. A similar appearance and growth of a spanwise mode that anticipates the separation has also been noticed in the laminar case. Inside the separated flow area, the wall normal location of the energy peak is observed to coincide with the location where an inflection point in the chordwise velocity profile appears, confirming the observations of Kitsios et al. (2017) made for a flat plate with strong adverse pressure gradient, on the verge of separation.

The turbulent detachment mechanism of the boundary layer appears to be a process that builds up continuously along the chord, starting from initially localised backflow nuclei, confirming the recent observation of Vinuesa, Örlü & Schlatter (2017). The size of the regions of locally reversed flow increases downstream. In particular, the probability of finding bigger reversed flow spots, channelled within the low speed streaks, increases as the adverse pressure gradient increases. To quantify this apparently stochastic behaviour of the appearance of separated nuclei, a probabilistic approach is clearly required and the location of the mean separation does not have any instantaneous physical meaning. This scenario is in accordance with what has been suggested by the pioneering work of Simpson (1989). In the present research, it has been noticed that the probability of observing a backflow spot along the chord correlates well with the intensity of the fluctuating activity of the flow mode $\lambda_z/C \simeq 0.2$. Also, this flow mode appears responsible for the maximum, averaged spanwise extension of the backflow spots. This is found to be $\simeq 0.2C$ when the average location of

the separation line is approached. This effect reflects in the fact that in the present $0.4C$ extended wing, the probability to find a reversed flow region along the spanwise direction levels out at 50%, once the mean separation location is approached.

6.2.2 Swept wing flow

For both the considered incidences, the mean chordwise flow field developing on the swept wing is well predicted by the *Simple Sweep Theory* , as long as the boundary layer is statistically attached to the wall. However, in the region neighbouring the average location of the separation of the chordwise flow, the swept and unswept wing flow fields start to deviate with a modality that differs from the one that would be predicted by the *Simple Sweep Theory* . In general, the wing performances, C_l and C_{d_x}, with their *r.m.s* are well predicted by the *Simple Sweep Theory* , even though some differences in the vortex shedding process and in the flow separation evolution are observed.

For both loading conditions, the probabilistic route to the chordwise turbulent separation is not strongly affected by the sweep, but its evolution is. The flow mode which influences the fluctuating flow during the detachment process of the unswept configurations, characterised by a spanwise wavelength of $\lambda_z/C \simeq 0.2$, is observed to be slightly weakened by the sweep that promotes fluctuating flow modes of larger spanwise extension. A similar effect of the mean crosswind was noticed for the laminar separation mechanism, too.

Despite the fact that for both the straight and the swept wings the evolution towards separation follows a similar pattern, the crosswind is observed to have an effect on the structure of the wall turbulence, along the whole chord in both the incidence cases. In particular, the velocity streaks appear to be bent and deformed in the mean crosswind direction which is not constant neither along the chord, nor inside the boundary layer. The spanwise deformation enhances the width of the low-speed streaks while narrowing the high speed ones. At the chord location where the mean separation occurs, the velocity streaks have been almost completely turned from an initial chordwise direction to a parallel-to-the trailing edge configuration. In this condition, their instantaneous spatial spacing appears to coincide with the size of the reversed flow spots, which in the present flow set up is $0.20C$ wide, on the average.

As observed for the laminar inflow case, also for the turbulent inflow case the swept wing shows boundary layers that evolve in the same manner for the chordwise and spanwise flows on the pressure side, while boundary layers with different features take place on the suction side. The chordwise flow on the suction side is exposed to an increasing probability

of separation, while on the pressure side the flow is always perfectly attached also when separation takes place on the opposite side of the foil. Again, as observed for the laminar case within the separated region, the spanwise velocity profile develops an inflection point coinciding with that of the chordwise flow. Also in the turbulent separation the spanwise flow develops a typical boundary layer of a flow over a porous media. No footprint of a conventional crossflow instability (as collected in Reed & Saric (1989)) is observed in the present turbulent boundary layer, probably because of the low value of the adopted Reynolds number. It is also possible that the technical difficulty in detecting the presence of travelling waves has not fully revealed the eventual presence of crossflow instabilities (Reed & Saric 1989) that may have also played a role.

6.3 Recommendations and future works suggestions

For both laminar and turbulent boundary layers, the *Simple Sweep Theory* can be safely used to predict the behaviour of a swept wing flow until the mean separation location is reached. Downstream of this location, the local behaviour of the flow field departs from those predictions. The baseline *Simple Sweep Theory* prescribes that a flow quantity of the two-dimensional chordwise flow of the swept case (e.g. $< C_{p_x} >_{z,t}$) can be predicted using the chordwise flow field of the correspondent straight wing ($< C_{p_x} >_{z,t}\big|_{\Lambda=0}$) when multiplied by the cosine function of the sweep angle Λ, i.e. $< C_{p_x} >_{z,t} = < C_{p_x} >_{z,t}\big|_{\Lambda=0} \cos(\Lambda)$. The simple sweep model is therefore linear with respect to the flow field quantities and non-linear with respect to the sweep. According to what mentioned above, to extend the theory when a separation takes place, a correction is required. This correction may be dependent to all the parameters that appear to govern the flow case, i.e. profile type and incidence (or consequently, the pressure distribution, $P(x)$), the Reynolds number Re_c, the sweep, the incoming turbulence intensity I, etc.. The corrected simple sweep model could be formally written

$$< C_{p_x} >_{z,t} = < C_{p_x} >_{z,t}\big|_{\Lambda=0} \cos(\Lambda) + f(P(x), Re_c, \Lambda, I), \qquad (6.1)$$

with the function f to be determined and taking on a non zero value only when a mean separation, either laminar or turbulent, takes place. However, the functional shape of the correction is presumably difficult to prescribe as linked to the non-linear character of the flow separation structure breakdown, which complexity has been discussed in this thesis.

For both laminar and turbulent boundary layers and for the considered wing configurations, the separation mechanism on an indefinitely extended wing is inherently unsteady

and three-dimensional, therefore requiring a time-dependent, three-dimensional probabilistic approach for its full investigation. In the case of the laminar boundary layer, the separation location is only marginally unsteady and weakly three-dimensional. Differently, the turbulent scenario is far more complex. A mean separation line at the wall can be defined using the spanwise and time averaged flow field for both the flow regimes (e.g. using the mean distribution of the skin friction coefficient). It is remarked that the mean separation line does not have any physical meaning in the instantaneous flow realisation when the turbulent separation is considered. Downstream of the mean separation location, a probabilistic approach is strictly necessary also for the laminar case in order to characterise the reversed flow. A simple model that prescribes a two-dimensional separation front at a specific wall location induced by the adverse pressure gradient can be profoundly misleading for the comprehension of the turbulent separation mechanism. In turn, the consequence of a poor comprehension of the turbulent boundary layer detachment mechanism would condition the development of turbulent separation control techniques towards the implementation of non effective strategies.

In particular, in the swept wing configuration, the crosswind has been observed to modify the structure of wall turbulence, even when fully attached turbulent boundary layers are considered. A priori, one could speculate that the crosswind influences the wall turbulence cycle (Jiménez & Pinelli 1999) also reshaping the outer logarithmic structures and their connection with close to the wall turbulence (Agostini & Leschziner 2014). To the best of the author's knowledge, the matter has been only marginally investigated with a limited use of highly-detailed flow methodologies. In this framework, a pioneering investigation was carried out by Flack (1997), who observed a slightly modified spacing between low speed streaks due to the crosswind, confirmed by the present investigation. It is clear that further investigations into the matter are required to unveil the modification of wall turbulence under the effect of a mean spanwise velocity component.

Another area that requires further research is the turbulent boundary layer separation process. The latter generates flow structures with an increasing size when moving downstream, until becoming comparable with that of the chord. The formation of this large structure is very unsteady and intermittent and a space-time average reveals very little of the ongoing physical process. A possible scenario that needs further investigation could be based on the conjecture that once the large-scale separating flow structures reach their maximum size (which appears governed by a specific fluctuating flow mode, differing between the straight and the swept wing), they go through a scale breakdown process sharing some analogies

with that one encountered during the breakdown of the laminar boundary layer separation to turbulence. This conceptual scenario is suggested after the similar effect introduced by the sweep to the fluctuating flow field during the breakdown process of the separating flow, independently of the boundary layer flow regime. Of course, further studies maybe formulated for simpler flow model problems are required to verify the proposed speculation on the analogy between the breakdown processes of the large-scale structures generated by the laminar and by the turbulent boundary layer separation mechanisms. This could be done using a detailed numerical simulations within a more controlled environment, e.g. an unswept flat plate with an imposed adverse pressure gradient, as done by many authors investigating the laminar separation phenomenon (e.g. Alam & Sandham (2000), Balzer & Fasel (2016)). In more controlled conditions, the breakdown process of the laminar and of the turbulent boundary layer separating flow structures could be characterised in an extremely detailed fashion. In the controlled scenario, sophisticate fundamental research could be carried out on the breakdown process, suppressing or enhancing flow modes in a numerical experiments as done for example by Jiménez & Pinelli (1999) to unveil the self generating mechanism of wall turbulence. These researches, carried out in simpler configurations, could also help in putting forward ideas for developing the corrections $f(P(x), Re_c, \Lambda, I)$, to extend the validity of the *Simple Sweep Theory* when a mean separation takes place.

Finally, it is important to mention that for both inflow scenarios considered in this thesis, the adopted methodology employing a spanwise wing extension of $0.4C$ with periodic boundary condition might have played an effect. This by forcing the dominant fluctuating mode to develop at an unphysical wavelength $\lambda_z/C \simeq 0.2$ for the straight wings that is ultimately observed to drive the breakdown of the the separation-generated flow structures. Furthermore, also the spanwise size of the computational box may have limited the extension of the dominant fluctuating mode, since the effect of the sweep to the large-spanwise fluctuating flow mode has been observed to be a moderate shift towards larger spanwise modes. However, independently of the effects of the computational domain, it is believed that this thesis has shed some light on the genuine physical breakdown process leading to separation, also highlighting some analogies between the laminar and the turbulent regimes and the differences between the straight and the swept wing configurations. Further computationally more expensive simulations considering the effect of the box size (i.e. larger spanwise extension or odd span/chord ratio) would provide a more solid evidence on the real-world validity of the present conclusions.

Appendix A

6.4   Peer-reviewed publications accepted

In the followings, the accepted publications based on the research carried out for the present thesis are attached.

The effect of the sweep angle to the turbulent flow past an infinite wing

C.A. Suardi, A. Pinelli, and M. Omidyeganeh

1 Introduction

Nowadays the majority of civil aircrafts employs swept-back wings. This configuration, proposed in the early 30's of last century, has been technologically motivated by the otherwise enhanced drag experienced in transonic cruise condition. Since its introduction, several studies have focused on the assessment of the aerodynamic behaviour of this wing configuration for a flow conditions resembling realistic, high Reynolds (Re) number cases of aeronautical interest [1, 2]. In these investigations, the boundary layer interesting the infinite wing undergoes an early transition inhibiting the appearence of any major separated regions for a moderate incidence and can thus considered a developing turbulent boundary layer (TBL) subject to a varying adverse pressure gradient (APG). In the present work, we also consider an infinite wing model at a modest angle of attack. However, because of the prohibiting computational cost of detailed simulations at a high Re number, we prefer to mimic this realistic conditions by superimposing free stream turbulence to the approaching clean stream. Indeed, this choice induces an early by-pass transition that prevent the eventual separation of the TBL, thus leading to a physical situation similar to the reference ones cited above. The high Re number regime, leading to an almost totally turbulent, attached boundary layer, is a quite interesting case for at least two reasons. The first one was put forward long ago and concerns the possibility of predicting the aerodynamic performances of a swept wing (lift and drag) in terms of the associated straight one, using a simple trigonometric function of the introduced sweep angle. This property, that has been verified experimentally and numerically by several authors, mainly holds for attached flows and is commonly termed as *Simple Sweep Theory*. Although this theory has been the working horse of swept wing design for decades, its exact applicability limits and its extention to other aerodynamic properties is still object of recent investigations. The second aspect that makes the TBL

C.A. Suardi · A. Pinelli · M. Omidyeganeh
City, University of London, London, UK, e-mail: `carlo.suardi@city.ac.uk`

on a swept wing an appealing research topic is related with the comprehension of the structure of the turbulent, wall bounded flow simultaneously exposed to an APG and to an imposed cross flow. An understanding on how these concomitant effects manipulate the structure of the TBL is the central topic of the present contribution. The region of primary interest is the one close to the trailing edge of the wing, where the pressure gradient is a strong adverse one and where the impact of the cross flow generated by the sweep angle is more evident. In particular, is accounted the effect of the sweep adoption on the appearence of *reversed flow nuclei*, similar to those reported into the literature for the high Reynolds TBL subject to zero pressure gradient (ZPG) [3] and for the moderate Re under an APG [7]. In general, our simulations on a straight wing, confirm the appearance of localised and unsteady local separated cores even for the case of an apparently fully attached boundary layer, due to the intense pressure gradient in the latter stage of the wing suction side for the aerofoil and incidence considered. When the 30° sweep-back angle is considered, we observe a mitigation of these reversed flow nuclei, alongside with a not trivial bending of the principal flow structures partecipating in the wall turbulence cycle. Due to the idea put forward by several authors suggesting an eventual link between the mentioned flow structures and the appearence of trailing edge flow separation on a wing, it is believed of great importance to understand how the sweep angle would affect this link. This in order to provide essential guidelines for the development of flow separation devices for the widely adopted swept wings.

2 Problem Formulation

The flow past an infinite swept wing is dealt with the 3D incompressible, Large Eddy Simulation equations (LES). The region close to the wing surface is fully resolved while the subgrid scale closure is achieved via the ILSA model proposed by Piomelli et al. [4]. The LES equations are space discretised via a co-located finite volume formulation on a structured mesh. The solver overall accuracy is second order in both space and time and the MPI library is used in the framework of a domain decomposition approach to exploit parallel, memory distributed computer architectures. The solver that incorporate all the aforementioned features (called *SUSA*) has been extensively validated in the past [5].The computational domain around each 2D aerofoil (NACA 4412) $x - y$ cross section is sketched in figure 1 alongside with tha wall resolution in inner units (being the friction velocity, u_τ, and the kinematic viscosity, v). On the $x - y$ plane, the domain is meshed using a body fitted C-grid which 3D extension is achieved extruding the 2D mesh in z using a uniform spacing. A zero velocity boundary condition is enforced at the solid walls, while on the outer boundary (i.e., the surface obtained when extruding the outer 2D boundary in z), we set an inlet/outlet condition that depends on the local, instantaneous direction of the computed flow (Dirichlet condition obtained from an irrotational solution if flow is incoming, non-reflective condition if outgoing) for the x and y velocity components. The swept/unswept wing configuration is simulated by setting a constant value for
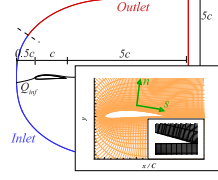
Fig. 1 Domain geometry for the computational study. z extension is 0.4 c (c being the chord size). The domain is assumed to be periodic in z.
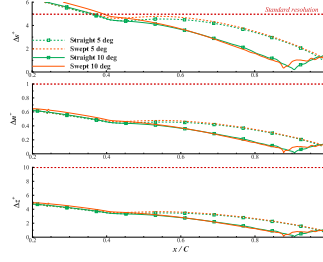
Fig. 2 Wall resolution in plus units for all the cases considered in this investigation, compared with the standard for a turbulent channel flow.

the z velocity component (parallel to the leading edge) on the outer boundary equal to $U_\infty tan(\beta)$, with the sweep angle β, equal to $30^o/0^o$ (U_∞ being the free-stream velocity component perpendiculat to the aerofoil LE). For both swept and unswept cases the chord Reynolds number is $Re_c = U_\infty c/\nu = 50 \times 10^3$, and two loading conditions have been considered setting the angle of attack to $\alpha = 5^o/10^o$. The boundary layer transition is triggered by superimposing to the incoming flow a turbulence field (10% intensity with integral length scale 0.045C) obtained through a twin, independent DNS of grid generated turbulence (Reynolds number based on grid spacing $Re_M = 2000$). In figure 3a is presented the turbulent kinetic energy spectrum of the perturbation introduced, as well as that of the resultant boundary layer in the buffer layer, ($y^+ \approx 25$), at a specific different suction side wing locations, $x/C \approx 0.75$ for the case of un-swept wing at 5° incidence. Inside the in-box it can be found an illustrative sketch of a portion of the grid turbulence introduced into the domain. The effect of the perturbation introduced is that of triggering the boundary layer transition to turbulence via a by-pass mechanism from the early stage of the wing. The energized boundary layer does not present a major separation from the wall for the considered incidences, condition otherwise faced in the absent of boundary layer perturbation [6]. Instead, it remains attached, by statistical mean, until the trailing edge. The coefficient of friction, shown in figure 3b for the case of un-swept wing and 5° incidence, clearly support this statement.

3 Results

A comparative study for the effect of a 30° sweep-back adoption on the flow field is made for the two different loading condition considered. Figure 4a presents the mean wall coefficient of pressure, whereas figure 4b presents some chord-wise velocity profile for two consequent chord-wise locations, $x/C = 0.4, 0.95$. The velocity profiles have been scaled with the inner units to make a comparison with the law of the wall in the case of a turbulent channel flow. A good match for both the
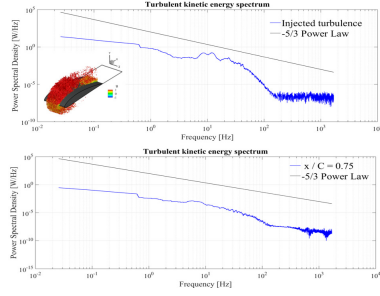
Fig. 3a Turbulent kinetic energy spectrum for the introduced perturbetion (Top) and into the buffer layer for late location on the wing suction side (Bottom). An illustration of the introduced grid turbulence and its effect on the boundary layer is presented into the the squared box.
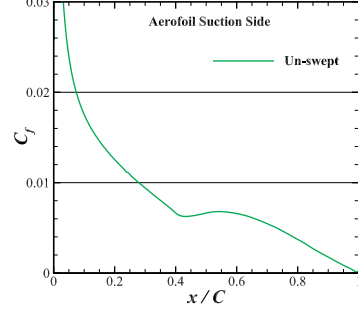
Fig. 3b Suction side wall friction coefficient along the chord.

incidences is found regardless the sweep angle adopted, supporting what has been already postulated as the simple sweep theory for the low order statistics of the turbulent attached flow past an infinite wing [1, 2].
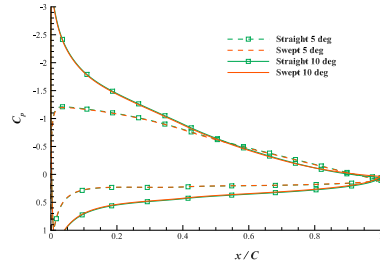
Fig. 4a Distribution of the wall coefficient of pressure for all the cases investigated.
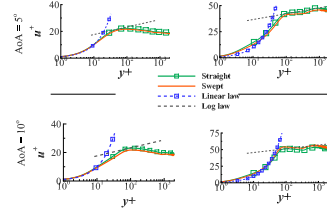
Fig. 4b Profiles of the chord-wise velocity in plus units for the 5° (Top) and 10° (Bottom) incidences, at the chord-wise location $x/C = 0.4$ (Left) and $x/C = 0.95$ (Right), respectively.

Even though some flow statistics has been found mildly affected by the adoption of the sweep angle, the flow dynamics of the turulent boundary layer results deeply modified. It is reported a varying distortion of the wall turbulence streaks moving toward the trailing edge, especially on the suction side. In figure 5 can be found the contours of the instantaneous wall-normal vorticity fluctuation on a surface above the wing suction side within the buffer layer for both the loading conditions, highlighting the streaks. The effect of the intensifying adverse pressure gradient seems to have a increasingly stronger impact as the streaks are thicker and present a more meandering pattern. Furthermore, a freshly new turbulent content is detected via the
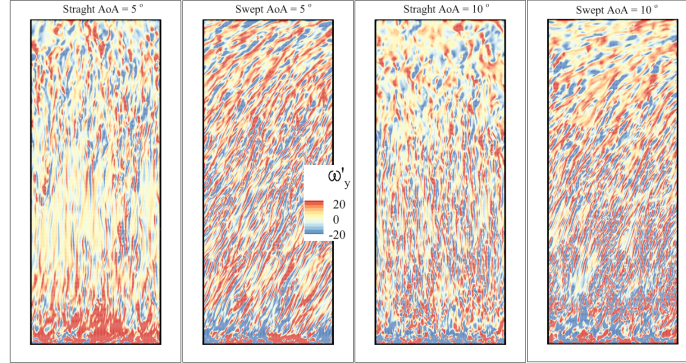
Fig. 5 Instantaneous iso-contours of the wall-normal component of the vorticity perturbation for the (Left) 5° and (Right) 10° case. The black line identifies the trailing edge. Suction side view. The flow is from bottom to top.

Reynolds stresses due to the introduced crosswind, for both the incidences, figure 6.
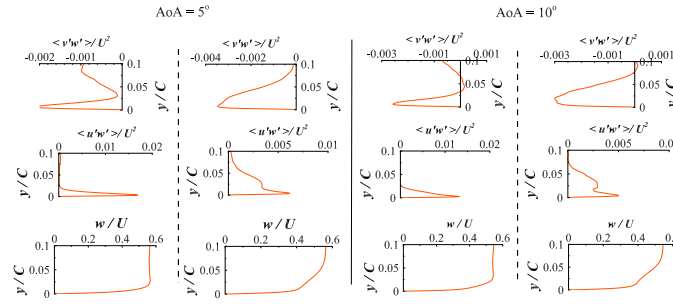
Fig. 6 Time and spanwise averaged profiles of quantities introduced purely by the crosswind for the (Left) 5° and (Right) 10° incidence case. Per each incidence are shown the profiles of the crosswind (Bottom), and two Reynold stresses (Centre and Top), extracted on the suction side at two consequent chord-wise locations, $x/C \approx 0.4$ (Left) and at $x/C \approx 0.95$ (Right).

The sweep angle is found to mitigate the reversed flow nuclei appearing inside the wing suction side boundary layer, and thus the portion of the wing interested by reversed flow. Figure 7a presents a map of the instantaneous skin friction on the suction side varying the sweep adopted, alongside with a quantitative account on the same side of the total probability to detect a reversed flow, with respect to the mean flow direction, moving along the chord, for the 5° (Top) and 10° (Bottom) incidence case. What can be qualitatively be observed by the friction map is clearly supported by the mitigated reversed flow region detected on the swept wing, regardless the incidence.
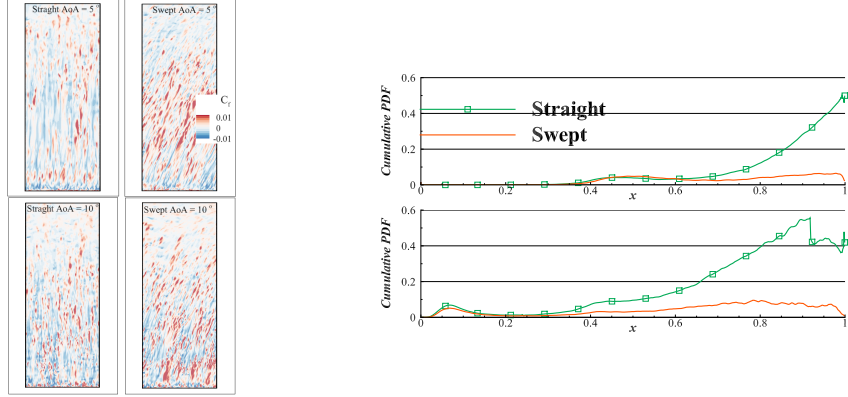
Fig. 7a (Left) Instantaneous iso-contours of the wall friction, flow from bottom to top, and (Right) total probability to detect a reversed flow along the chord for the suction side wall. The (Top) set refer to the 5° incidence case, the (Bottom) one for the 10° case.

References

1. J.M. Altman and N.L.F. Hayter. : A comparison of the Turbulent Boundary-Layer Growth on an Unswept and swept Wing. NACA Technical Note 2500 (1951)
2. Boltz, F. W. and Kenyon, G. C. and Allen, C. Q. : Effects of sweep angle on the boundary-layer stability characteristics of an untapered wing at low speeds. NASA D-338 (1960)
3. Brcker C.: Evidence of rare backflow and skin-friction critical points in near-wall turbulence using micropillar imaging. Phys Fluids. **27**, 031705 (2015)
4. Piomelli, U. and Rouhi, A. and Geurts, B. J.: A grid-independent length scale for large-eddy simulations. J.F.M. **766**, 499–527 (2015)
5. Rosti, M.: Direct numerical simulation of an aerofoil at high angle of attack and its control. City, University of London, London (2016)
6. C.A. Suardi and A. Pinelli and M. Omidyeganeh: Investigation of the Sweep Independence Principle for transitional regime of the flow past an aerofoil. EPSRC UK Turbulence Consortium Meeting, London (2018)
7. R. Vinuesa and R. rl and P. Schlatter: Characterisation of backflow events over a wing section. Jour. of Turb. **18.2**, 170–185 (2017)

Bibliography

Abbott, I. H., Von Doenhoff, A. E. & Stivers, L. J. (1945), Summary of airfoil data, Technical Report 824, National Advisory Committee for Aeronautics.

Ackeret, J., Degen, M. & Rott, N. (1951), Investigations on wings with and without sweepback at high subsonic speeds, Technical report, University of North Texas Libraries, Digital Library.

Agostini, L. & Leschziner, M. A. (2014), 'On the influence of outer large-scale structures on near-wall turbulence in channel flow', *Physics of Fluids* **26**(7), 075107.

Alam, M. & Sandham, N. D. (2000), 'Direct numerical simulation of 'short' laminar separation bubbles with turbulent reattachment', *Journal of Fluid Mechanics* **410**, 1–28.

Allen, L. & Burrows, F. M. (1956), Flight experiments on the boundary layer characteristics of a swept back wing, Technical report, The college of aeronautics Cranfield.

Altman, J. & Hayter, N. (1951), A comparison of the turbulent boundary-layer growth on an unswept and swept wing, Technical report, National Advisory Committee for Aeronautics. Ames Aeronautical Lab. Technical Note 2500.

Anderson Jr, J. D. (1990), *Modern compressible flow with historical perspective*, McGraw-Hill Publishing Company.

Anderson Jr, J. D. (1999), *A history of aerodynamics: and its impact on flying machines*, Vol. 8, Cambridge University Press.

Anscombe, A. & Illingworth, L. N. (1952), Wind tunnel observation of boundary-layer transition on a wing at various angles of sweepback, Technical Report 2968, Aeronautical Research Council, London.

ARCHER (2020), 'Archer kau calculator'.
  URL: *https://www.archer.ac.uk/access/au-calculator/*

Ashill, P. R., Fulker, J. L. & Hackett, K. C. (2005), 'A review of recent developments in flow control', *The Aeronautical Journal (1968)* **109**(1095), 205–232.

Auteri, F., Baron, A., Belan, M., Campanardi, G. & Quadrio, M. (2010), 'Experimental assessment of drag reduction by traveling waves in a turbulent pipe flow', *Phys. Fluids* **22**(11), 115103/14.

Balay, S., Abhyankar, S., Adams, M. F., Brown, J., Brune, P., Buschelman, K., Dalcin, L., Dener, A., Eijkhout, V., Gropp, W. D., Karpeyev, D., Kaushik, D., Knepley, M. G., May, D. A., McInnes, L. C., Mills, R. T., Munson, T., Rupp, K., Sanan, P., Smith, B. F., Zampini, S., Zhang, H. & Zhang, H. (2019), PETSc users manual, Technical Report ANL-95/11 - Revision 3.11, Argonne National Laboratory.
URL: *https://www.mcs.anl.gov/petsc*

Balzer, W. & Fasel, H. F. (2016), 'Numerical investigation of the role of free-stream turbulence in boundary-layer separation', *Journal of Fluid Mechanics* **801**, 289–321.

Bechert, D. W., Hage, W. & Meyer, R. C. (2006), *Self-actuating Flaps On Bird And Aircraft Wings*, Wit Press, pp. 435–446.

Black, J. (1952), 'A note on the vortex patterns in the boundary layer flow of a swept-back wing', *The Journal of the Royal Aeronautical Society* **56**(496), 279–285.

Böhmer, K., Hemker, P. W. & Stetter, H. J. (1984), *The Defect Correction Approach*, Springer Vienna, Vienna, pp. 1–32.

Boltz, F. W., Kenyon, G. C. & Allen, C. Q. (1960), Effects of sweep angle on the boundary-layer stability characteristics of an untapered wing at low speeds, Technical Report D-338, Nasa, Washington.

Bonfigli, G. & Kloker, M. (2007), 'Secondary instability of crossflow vortices: validation of the stability theory by direct numerical simulation', *Journal of Fluid Mechanics* **583**, 229–272.

Brandt, L., Schlatter, P. & Henningson, D. (2004), 'Transition in boundary layers subject to free-stream turbulence', *Journal of Fluid Mechanics* **517**, 167–198.

Brendel, M. & Mueller, T. J. (1988), 'Boundary-layer measurements on an airfoil at low Reynolds numbers', *Journal of Aircraft* **25**(7), 612–617.

Broadley, J. I. (1998), The control of trailing edge separation on highly swept wings using vortex generators, PhD thesis, Cranfield University.

Brücker, C. (2015), 'Evidence of rare backflow and skin-friction critical points in near-wall turbulence using micropillar imaging', *Physics of Fluids* **27**(3), 031705.

Brücker, C. & Weidner, C. (2014), 'Influence of self-adaptive hairy flaps on the stall delay of an airfoil in ramp-up motion', *Journal of Fluids and Structures* **47**, 31 – 40. Special Issue on Unsteady Separation in Fluid-Structure Interaction-l.
URL: *http://www.sciencedirect.com/science/article/pii/S088997461400036X*

Busemann, A. (1935), 'Aerodynamischer auftrieb bei ubershallgeschwindigkeit', *Luftfahrtforschung* **12**.

Cadieux, F., Domaradzki, J. A., Sayadi, T., T., B. S. & Duchaine, F. (2012), Dns and les of separated flows at moderate Reynolds numbers, *in* 'Proceedings of the 2012 Center for Turbulence Research Summer Program', Stanford University.

Carruthers, A. C., Thomas, A. L. R. & Taylor, G. K. (2007), 'Automatic aeroelastic devices in the wings of a steppe eagle aquila nipalensis', *Journal of Experimental Biology* **210**(23), 4136–4149.

Choi, K.-S. (2002), 'Near-wall structure of turbulent boundary layer with spanwise-wall oscillation', *Phys. Fluids* **14**(7), 2530–2542.

Clauser, F. (1954), 'Turbulent Boundary Layers in Adverse Pressure Gradients', *J. Aeronaut. Sci.* **21**, 91–108.

Cooke, J. C. (1950), 'The boundary layer of a class of infinite yawed cylinders', *Mathematical Proceedings of the Cambridge Philosophical Society* **46**(4), 645–648.

Crone, J. C. & Munday, L. B. (2014), Parallel performance of linear solvers and preconditioners, Technical report, U.S. Army Research Laboratory.

Dagenhart, J. R. (1992), Crossflow stability and transition experiments in a swept-wing flow, PhD thesis, Virginia Polytechnic Institute and State University. Collection nasa techdocs, Contributor NASA.

Davis, R. L., Carter, J. & Reshotko, E. (1987), 'Analysis of transitional separation bubbles on infinite swept wings', *AIAA Journal* **25**.

De Tullio, N. & Sandham, N. D. (2017), Transitional separation bubbles over swept wings, *in* '10th International Symposium on Turbulence and Shear Flow Phenomena', Chicago, USA.

Dmitriev, S. S. (1990), 'Mechanism of turbulent boundary layer separation from a smooth wall', *Fluid Dynamics* **25**, 867 – 874.

Drela, M. (1989), Xfoil: An analysis and design system for low Reynolds number airfoils, *in* T. J. Mueller, ed., 'Low Reynolds Number Aerodynamics', Springer Berlin Heidelberg, Berlin, Heidelberg, pp. 1–12.

Du, Y., Symeonidis, V. & Karniadakis, G. E. (2002), 'Drag reduction in wall-bounded turbulence via a transverse travelling wave', *J. Fluid Mech.* **457**, 1–34.

Duan, L., Choudhari, M. M., Li, F. & Wu, M. (2014), Dns of laminar-turbulent transition in swept-wing boundary layers, *in* 'Proceedings of the 43rd AIAA Fluid Dynamics Conference', AIAA.

EPSRC (2020), 'Engineering and physical sciences research council website'.
URL: *https://epsrc.ukri.org/*

European Union Aviation Safety Agency, European Environment Agency & EUROCONTROL (2019), 'European aviation environmental report 2019'.
URL: *https://ec.europa.eu/transport/sites/transport/files/2019-aviation-environmental-report.pdf*

Ferziger, J. H. & Peric, M. (2002), *Computational methods for fluid dynamics*, 3nd edn, Springer.

Flack, K. A. (1997), 'Near-wall structure of three-dimensional turbulent boundary layers', *Experiments in Fluids* **23**(4), 335–340.

Forum, M. P. (1994), Mpi: A message-passing interface standard, Technical report, University of Tennessee, Knoxville, TN, USA.

Fukagata, K., Iwamoto, K. & Kasagi, N. (2002), 'Contribution of Reynolds stress distribution to the skin friction in wall-bounded flows', *Phys. Fluids* **14**(11), L73–L76.

Gaster, M. (1967), 'On the flow along swept leading edges', *Aeronautical Quarterly* **18**(2), 165–184.

166

Germano, M., Piomelli, U., Moin, P. & Cabot, W. H. (1991), 'A dynamic subgrid scale eddy viscosity model', *Physics of Fluids A* **3**(7), 1760–17651.

Graver, B., Zhang, K. & Rutherford, D. (2018), 'Emissions from commercial aviation, 2018', *The International Council on Clean Transportation* .

Hain, R., Kahler, C. J. & Radespiel, R. (2009), 'Dynamics of laminar separation bubbles at low-Reynolds-number aerofoils', *Journal of Fluid Mechanics* **630**, 129–153.

Hess, J. & Smith, A. (1967), 'Calculation of potential flow about arbitrary bodies', *Progress in Aerospace Sciences* **8**, 1 – 138.

Hetsch, T. & Rist, U. (2009), 'An analysis of the structure of laminar separation bubbles in swept infinite geometries', *European Journal of Mechanics - B/Fluids* **28**(4), 486 – 493. **URL:** *http://www.sciencedirect.com/science/article/pii/S0997754609000375*

Horton, H. (1968), Laminar separation bubbles in two and three dimensional incompressible flow, PhD thesis, Queen Mary College.

Hosseinverdi, S. & Fasel, H. (2019), 'Numerical investigation of laminar-turbulent transition in laminar separation bubbles: The effect of free-stream turbulence', *Journal of Fluid Mechanics* **858**, 714–759.

Hosseinverdi, S. & Fasel, H. F. (2015), 'Laminar-turbulent transition in a laminar separation bubble in the presence of free-stream turbulence', *Procedia IUTAM* **14**, 570 – 579. **URL:** *http://www.sciencedirect.com/science/article/pii/S2210983815000929*

Howe, J. (1968), Some fluid mechanical problems related to subsonic and supersonic aircraft, Technical Report 183, NASA, National Aeronautics and Space Administration.

Hunt, J., Wray, A. & Moin, P. (1988), Eddies, stream and convergence zones in turbulent flows, Technical Report CTR-S88, Center for Turbulence Research.

International Energy Agency (2017), 'Co2 emissions by sector, world 1990-2017'.

Jacobs, E. & Sherman, A. (1937), Airfoil section characteristics as affected by variations of the Reynolds number, Technical Report 586, National Advisory Committee for Aeronautics.

Jagadeesh, C., Balthazar, M., Gross, A. & Fasel, H. (2013), Experimental investigation of the structure and dynamics of laminar separation bubbles at the onset of bursting, *in* '31st

AIAA Applied Aerodynamics Conference', American Institute of Aeronautics and Astronautics, San Diego, California.

Jiménez, J. & Pinelli, A. (1999), 'The autonomous cycle of near-wall turbulence', *J. Fluid Mech.* **389**, 335–359.

Johansson, G. (1988), An experimental study of the structure of a flat plate turbulent boundary layer, using laser-Doppler velocimetry, PhD thesis, Göteborg: Chalmers University of Technology.

Jones, L. E., Sandberg, R. D. & Sandham, N. D. (2008), 'Direct numerical simulations of forced and unforced separation bubbles on an airfoil at incidence', *Journal of Fluid Mechanics* **602**, 175–207.

Jones, R. (1947), Effects of sweepback on boundary layer and separation, Technical Report 884, Nasa, Ames Aeronautical Laboratory, Moffett Field, Calif.

Jones, R. (1989), *Adolf Busemann*, The National Academies Press, Washington, DC, pp. 62–67.
  URL: *https://www.nap.edu/catalog/1384/memorial-tributes-volume-3*

Jung, W., Mangiavacchi, N. & Akhavan, R. (1992), 'Suppression of turbulence in wall-bounded flows by high-frequency spanwise oscillations', *Phys. Fluids A* **4 (8)**, 1605–1607.

Kaltenbach, H. & Janke, G. (2000), 'Direct numerical simulation of flow separation behind a swept, rearward-facing step at reh=3000', *Physics of Fluids* **12**(9), 2320–2337.
  URL: *http://dx.doi.org/10.1063/1.1287338*

Kim, J. & Moin, P. (1985), 'Application of a fractional-step method to incompressible navier-stokes equations', *Journal of Computational Physics* **59**(2), 308 – 323.
  URL: *http://www.sciencedirect.com/science/article/pii/0021999185901482*

Kim, J., Moin, P. & Moser, R. (1987), 'Turbulence statistics in fully developed channel flow at low Reynolds number', *J. Fluid Mech.* **177**, 133–166.

Kitsios, V., Sekimoto, A., Atkinson, C., Sillero, J. A., Borrell, G., Gungor, A. G., Jiménez, J. & Soria, J. (2017), 'Direct numerical simulation of a self-similar adverse pressure gradient turbulent boundary layer at the verge of separation', *Journal of Fluid Mechanics* **829**, 392–419.

Klebanoff, P. (1971), Effect of free-stream turbulence on a laminar boundary layer, *in* 'Bulletin of the American Physical Society', Vol. 16, AMER INST PHYSICS 1305 WALT WHITMAN RD, STE 300, MELVILLE, NY 11747-4501 USA, pp. 1323–+.

Lang, M., Rist, U. & Wagner, S. (2004), 'Investigations on controlled transition development in a laminar separation bubble by means of lda and piv', *Experiments in Fluids* **36**(1), 43–52.

Lardeau, S. & Leschziner, M. (2013), 'The streamwise drag-reduction response of a boundary layer subjected to a sudden imposition of transverse oscillatory wall motion', *Phys. Fluids* **25**, 075109.

Lee, J. & Sung, H. J. (2009), 'Structures in turbulent boundary layers subjected to adverse pressure gradients', *Journal of Fluid Mechanics* **639**, 101–131.

Lenaers, P., Li, Q., Brethouwer, G., Schlatter, P. & Orlü, R. (2012), 'Rare backflow and extreme wall-normal velocity fluctuations in near-wall turbulence', *Phys. Fluids* **24**, 035110.

Leonard, A. (1975), 'Energy cascade in large-eddy simulations of turbulent fluid flows', *Advances in geophysics* **18**, 237–248.

Lin, J. C. (2002), 'Review of research on low-profile vortex generators to control boundary-layer separation', *Progress in Aerospace Sciences* **38**(4), 389 – 420.

Lopes, A. S., Piomelli, U. & Palma, J. M. L. M. (2006), 'Large-eddy simulation of the flow in an s-duct', *Journal of Turbulence* **7**, N11.
URL: *http://dx.doi.org/10.1080/14685240500331900*

Ludwieg, H. (1940), 'Pfeilflügel bei hohen geschwindigkeiten', *AVA, LGL-Bericht* **127**.

Marxen, O. & Henningson, D. S. (2011), 'The effect of small-amplitude convective disturbances on the size and bursting of a laminar separation bubble', *Journal of Fluid Mechanics* **671**, 1–33.

Marxen, O., Lang, M. & Rist, U. (2012), 'Discrete linear local eigenmodes in a separating laminar boundary layer', *Journal of Fluid Mechanics* **711**, 1–26.

Marxen, O., Lang, M. & Rist, U. (2013), 'Vortex formation and vortex breakup in a laminar separation bubble', *Journal of Fluid Mechanics* **728**, 58–90.

Marxen, O., Rist, U. & Wagner, S. (2004), 'Effect of spanwise-modulated disturbances on transition in a separated boundary layer', *AIAA Journal* **42**(5), 937–944.

Mcdonald, H. (1969), 'The effect of pressure gradient on the law of the wall in turbulent flow', *Journal of Fluid Mechanics* **35**(2), 311–336.

Mohamed, M. S. & Larue, J. C. (1990), 'The decay power law in grid-generated turbulence', *Journal of Fluid Mechanics* **219**, 195–214.

Monti, A. (2019), High-fidelity simulations of fully submerged, rigid canopy flows, PhD thesis, City, University of London.

Monti, A., Omidyeganeh, M. & Pinelli, A. (2019), 'Large-eddy simulation of an open-channel flow bounded by a semi-dense rigid filamentous canopy: Scaling and flow structure', *Physics of Fluids* **31**(6), 065108.

Monty, J., Harun, Z. & Marusic, I. (2011), 'A parametric study of adverse pressure gradient turbulent boundary layers', *International Journal of Heat and Fluid Flow* **32**(3), 575 – 585. 8th International Symposium on Engineering Turbulence Modelling and Measurements, Marseille, France,June 9 to 11, 2010.

Morkovin, M. V. (1993), *Bypass-Transition Research: Issues and Philosophy*, Springer Netherlands, Dordrecht, pp. 3–30.

Muzaferija, S. (1994), Adaptive Finite Volume method for flow prediction using unstructured meshes and multigrid approach, PhD thesis, University of London.

O'Meara, M. & Mueller, T. J. (1987), 'Laminar separation bubble characteristics on an airfoil at low Reynolds numbers', *AIAA Journal* **25**(8), 1033–1041.

Omidyeganeh, M. & Piomelli, U. (2011), 'Large-eddy simulation of two-dimensional dunes in a steady, unidirectional flow', *Journal of Turbulence* **12**, N42.
URL: *http://dx.doi.org/10.1080/14685248.2011.609820*

Orlandi, P. & Jiménez, J. (1994), 'On the generation of turbulent wall friction', *Phys. Fluids* **6**(2), 634–641.

Peskin, C. S. (1972), 'Flow patterns around heart valves: A numerical method', *Journal of Computational Physics* **10**(2), 252 – 271.
URL: *http://www.sciencedirect.com/science/article/pii/0021999172900654*

Pinkerton, R. (1938), The variation with Reynolds number of pressure distribution over an aerofoil section, Technical Report 613, National Advisory Committee for Aeronautics.

Piomelli, U., Rouhi, A. & Geurts, B. J. (2015), 'A grid-independent length scale for large-eddy simulations', *Journal of Fluid Mechanics* **766**, 499–527.

Pope, S. (2000), *Turbulent Flows*, Cambridge University Press, Cambridge.

Prandtl, L. (1946), 'On boundary layers in three-dimensional flow', *R. and T. No.64 British M. A. P. Volkerode* .

Quadrio, M., Ricco, P. & Viotti, C. (2009), 'Streamwise-traveling waves of spanwise wall velocity for turbulent drag reduction', *J. Fluid Mech.* **627**, 161–178.

Quarteroni, A., Sacco, R., Saleri, F. & Gervasio, P. (2014), *Matematica Numerica*, Springer-Verlag Mailand.

R., D. J. & Saric, W. S. (1999), Crossflow stability and transition experiments in swept-wing flow, Technical report, Nasa.

Reed, H. L. & Saric, W. S. (1989), 'Stability of three-dimensional boundary layers', *Annual Review of Fluid Mechanics* **21**(1), 235–284.
URL: *https://doi.org/10.1146/annurev.fl.21.010189.001315*

Rhie, C. M. & Chow, W. L. (1983), 'Numerical study of the turbulent flow past an airfoil with trailing edge separation', *AIAA Journal* **21**, 1525–1532.

Roberson, W. & Johns, J. A. (2008), 'Fuel conservation strategies: Takeoff and climb', *AERO, Boeing* **4**, 24 – 28.

Rosti, M. (2016), Direct numerical simulation of an aerofoil at high angle of attack and its control, PhD thesis, City, University of London.

Rosti, M. E., Omidyeganeh, M. & Pinelli, A. (2016), 'Direct numerical simulation of the flow around an aerofoil in ramp-up motion', *Physics of Fluids* **28**(2), 025106.
URL: *http://dx.doi.org/10.1063/1.4941529*

Rouhi, A., Piomelli, U. & Geurts, B. J. (2016), 'Dynamic subfilter-scale stress model for large-eddy simulations', *Phys. Rev. Fluids* **1**, 044401.

Saric, W. S., Reed, H. L. & White, E. B. (2003), 'Stability and transition of three-dimensional boundary layers', *Annual Review of Fluid Mechanics* **35**(1), 413–440.
URL: *https://doi.org/10.1146/annurev.fluid.35.101101.161045*

Schafer, F., Breuer, M. & Durst, F. (2009), 'The dynamics of the transitional flow over a backward-facing step', *Journal of Fluid Mechanics* **623**, 85–119.

Schlatter, P., Brandt, L., de Lange, H. C. & Henningson, D. S. (2008), 'On streak breakdown in bypass transition', *Physics of Fluids* **20**(10), 101505.

Schlichting, H. (1979), *Boundary-layer theory*, McGraw Hill.Inc.

Schlichting, H. & Gersten, K. (2000), *Boundary-Layer Theory*, Springer, Berlin.

Schlichting, H. & Truckenbrot, E. (1960), *Aerodynamik des Flugzeuges*, Springer, Heidelberg.

Sears, W. R. (1948), 'The boundary layer of yawed cylinders', *Journal of the Aeronautical Sciences* **15**, 49–52.
URL: *https://doi.org/10.2514/8.11499*

Selby, G. (1982), Phenomenological study of subsonic turbulent flow over a swept rearward-facing step, PhD thesis, University of Delaware.

Selby, G. (1983), 'Applicability of the independence principle to subsonic turbulent flow over a swept rearward-facing step', *AIAA Journal* **21**(11), 1603–1604.

Simpson, R. L. (1989), 'Turbulent boundary-layer separation', *Annual Review of Fluid Mechanics* **21**(1), 205–232.

Simpson, R. L. (1996), 'Aspects of turbulent boundary-layer separation', *Progress in Aerospace Sciences* **32**(5), 457 – 521.

Smith, C. (1996), *Coherent flow structures in smooth-wall turbulent boundary layers: Facts, mechanisms and speculation*, John Wiley and Sons Ltd., pp. 1–39.

Smith, C. R., Walker, J. D. A., Haidari, A. H. & Sobrun, U. (1991), 'On the dynamics of near-wall turbulence', *Philosophical Transactions: Physical Sciences and Engineering* **336**(1641).

Suardi, C., Pinelli, A. & Omidyeganeh, M. (2019), The effect of the sweep angle to the turbulent flow past an infinite wing, *in* B. Geurts & M. V. Salvetti, eds, 'Proceedings of the 12th Ercoftac Workshop Direct And Large Eddy Simulation', Springer.

Talay, T. A. (1975), Introduction to the aerodynamics of flight, Technical Report 367, NASA, National Aeronautics and Space Administration.

Uranga, A., Persson, P., Drela, M. & Peraire, J. (2011), Preliminary investigation into the effects of cross-flow on low Reynolds number transition, *in* '20th AIAA Computational Fluid Dynamics Conference', American Institute of Aeronautics and Astronautics, Honolulu, Hawaii.

Vila, C., Örlü, R., Vinuesa, R., Schlatter, P., Ianiro, A. & Discetti, S. (2017), 'Adverse-pressure-gradient effects on turbulent boundary layers: Statistics and flow-field organization', *Flow, turbulence and combustion* **99**(3), 589—612.
URL: *https://europepmc.org/articles/PMC6044292*

Vinuesa, R., Bobke, A., Örlü, R. & Schlatter, P. (2016), 'On determining characteristic length scales in pressure-gradient turbulent boundary layers', *Phys. Fluids* **28**(055101).

Vinuesa, R., Hosseini, S. M., Hanifi, A., Henningson, D. S. & Schlatter, P. (2017), 'Pressure-gradient turbulent boundary layers developing around a wing section', *Flow, Turbulence and Combustion* **99**(3), 613–641.

Vinuesa, R., Negi, P., Atzori, M., Hanifi, A., Henningson, D. & Schlatter, P. (2018), 'Turbulent boundary layers around wing sections up to rec=1,000,000', *International Journal of Heat and Fluid Flow* **72**, 86 – 99.

Vinuesa, R., Örlü, R. & Schlatter, P. (2017), 'Characterisation of backflow events over a wing section', *Journal of Turbulence* **18**(2), 170–185.

Viotti, C., Quadrio, M. & Luchini, P. (2009), 'Streamwise oscillation of spanwise velocity at the wall of a channel for turbulent drag reduction', *Phys. Fluids* **21**, 115109.

Vos, R. & Farokhi, S. (2015), *Aerodynamics of Swept Wings*, Springer Netherlands, Dordrecht, pp. 427–511.

Wassermann, P. & Kloker, M. (2003), 'Transition mechanisms induced by travelling cross-flow vortices in a three-dimensional boundary layer', *Journal of Fluid Mechanics* **483**, 67–89.

Watmuff, J. H. (1999), 'Evolution of a wave packet into vortex loops in a laminar separation bubble', *Journal of Fluid Mechanics* **397**, 119–169.

White, E., Saric, W., Gladden, R. & Gabet, P. (n.d.), Stages of swept-wing transition, *in* '39th Aerospace Sciences Meeting and Exhibit', AIAA, pp. 1–10.

Wild, J. M. (1949), 'The boundary layer of yawed infinite wings', *Journal of the Aeronautical Sciences* **16**, 41–45.

Yarusevych, S., Sullivan, P. E. & Kawall, J. G. (2009), 'On vortex shedding from an airfoil in low-Reynolds-number flows', *Journal of Fluid Mechanics* **632**, 245–271.

Zaki, T. A., Wissink, J. G., Rodi, W. & Durbin, P. A. (2010), 'Direct numerical simulations of transition in a compressor cascade: the influence of free-stream turbulence', *Journal of Fluid Mechanics* **665**, 57–98.